School of Physics
and Astronomy

Applications of coherent anti-Stokes Raman scattering (CARS) microscopy to cell biology

Arnica Karuna

PhD Thesis

05-05-2016

Declaration and Statements

Declaration

This work has not been submitted in substance for any other degree or award at this or any other university or place of learning, nor is being submitted concurrently in candidature for any degree or other award.

Signed ..... (candidate) Date.....

Statement 1

This thesis is submitted in partial fulfilment of the requirements for the degree of Doctor of Philosophy.

Signed ..... (Candidate) Date.....

Statement 2

This thesis is a result of my own independent work/investigation except where otherwise stated. Other sources are acknowledged by explicit references. The views expressed are my own.

Signed ..... (Candidate) Date.....

Statement 3

I hereby give consent for my thesis, if accepted, to be available for photocopying and for inter-library loan, and for the title and summary to be made available to outside organizations.

Signed ..... (Candidate) Date.....

Statement 4

I hereby give consent for my thesis, if accepted, to be available online in the University‘s Open Access repository and for inter-library loans after expiry of a bar on access previously approved by the Academic Standards & Quality Committee.

Signed ..... (Candidate) Date.....

Dedicated to my parents for their unwavering support

Acknowledgements

All glory comes from daring to begin. -Eugene Ware

I would like to thank my supervisor Prof. Wolfgang Langbein for encouraging me to make the leap of faith (and quite a big one all the way from India) which changed my entire outlook to research and indeed life in general, and gave me the much needed direction when I needed it the most. Thank you for always making time and great effort for discussions throughout my PhD, especially in the beginning and the towards the end of the research. I am grateful to my other supervisors, Prof. Paola Borri and Prof. Rachel Errington for moulding my PhD experience expertly with their professional guidance and providing excellent motivation. I am thankful to Mrs. Sally Chappell and Mrs. Marie Wiltshire for preparing the samples on which this work is based.

Thanks are due to Dr. Francesco Masia- my postdoctoral mentor and Dr. Iestyn Pope for their indispensable help in introducing me to the lab techniques and the analysis methods. I owe a lot of my scientific understanding and the ability to present this thesis to Dr. Masia for his unflinching support at all times. My colleagues in Schools of Physics and Biosciences shared their PhD journeys with me, assuring me that all roads lead to Rome; except the ones where we stop moving-thank you! I am grateful to Dr. Kenneth Ewan, Dr. Andrew Hollins and Dr. Anika Offergeld for valuable discussions about all things related to the biology of organoids.

I thank Dr. Valentina Cesari and the children of the Masia family for making my stay in Cardiff comfortable and bringing a dash of acceptance, love and support to my experience.

This work would not have been possible without my family who always encouraged me to aim high, and supported my moving 5000 miles away from them for this research. It is due to them that I have dreamed since the age of 14 to do a PhD in pure science. I would also at this stage like to thank Dr. Cherian from St. Stephen's college, Delhi who has been my mentor and advisor since our first acquaintance, for sharing his valuable time and experience with me. Thanks are due to my amazing friends for their love, support and lots of laughs. Finally, big thanks to my little niece, for reintroducing me to childlike fearlessness in daring to begin.

Introduction

Traditionally, many advances in the field of biology have been driven by optical microscopy based techniques which reveal morphological information about the samples under study [1, 2, 3, 4]. The scope of the applications of these methods is limited due to the lack of contrast from most biological materials (cells and tissues) which are transparent to visible light. The introduction of extraneous materials (such as fluorescent quantum dots or other fluorescent proteins/labels) with affinity towards certain sub-cellular components which are then imaged, has emerged as a popular and powerful method to image biological materials. Fluorescence microscopy using visible wavelengths in its simplest application includes the identification and imaging of interesting features of a sample which are fluorescently labelled in a structurally/chemically specific way. In more recent developments, fluorescence lifetimes have been imaged. Fluorescence based techniques can also be applied to track protein dynamics or drug delivery in live samples. Despite the benefits of imaging samples with labels, and a host of associated applications, the issues of photobleaching and induced phototoxicity remain. Another very important aspect which gains relevance in live sample imaging is that the system dynamics may be influenced by the introduction of fluorescent labels.

Spectroscopy techniques, which rely on the material resonances are chemically specific, sensitive, and if combined with microscopy, bridge the gap between non-invasive imaging and fluorescence microscopy. Instead of an extraneous label, the contrast generated originates from molecular transitions of the chemical species in the sample. Coherent Raman scattering (CRS) based techniques rely on the chemical contrast generated due to molecular vibrations and have been applied to biology [5]. One CRS technique, stimulated Raman scattering (SRS) has been used to distinguish between the macromolecular constituents of cells [6, 7] and tissues [8]. Additionally, quantitative hyperspectral SRS has been demonstrated in polymer and lipid mixtures [6]. Another type of CRS, coherent anti-Stokes Raman scattering (CARS) [9] was reported in 1965, nearly half a decade before SRS. However, due to difficulties in implementation, CARS was not readily put to application. Since its revival in 1999 [10], CARS has emerged as a label-free, chemically specific microscopy technique and has been applied to image various biological materials [11, 12]. In addition to the studies of lipid rich samples [13, 14], spectral differences between the cytosol and the nucleus have been reported using CARS microscopy [15, 16]. However, none of the previous works in this field present full 3D hyperspectral data, or make quantitative volumetric estimates of the various chemical components present in the sample. With respect to biomedical/biochemical application based studies, literature suffers from a paucity of examples investigating the effects of drugs on biological materials using CARS microscopy. This project aims to overcome these

shortcomings. In this work, CARS microscopy is applied to single cells (osteosarcoma, U-2OS which are lipid poor due to their functional profile) with volumetric quantitative analysis to determine the absolute masses of the component species. For the first time in our knowledge, full 3D hyperspectral data has been acquired and analyzed. Correlative fluorescence imaging to ascertain the origin of various components of the cells as imaged with CARS was also performed. Furthermore, reports of no observed (with CARS) correlation in protein content in the intranuclear region with the mitotic stage in cells in one publication [16] have been disproved, shown in this thesis. Osteosarcoma is a rare type of cancer, most commonly diagnosed in children and adolescents. However, due to its rarity, it is not well researched. The usual line of treatment includes surgery followed by chemotherapy, of which Taxol (microtubule stabilizer) and ICRF-193 (topoisomerase II poison) form an important part. The effects of these drugs on cells are often investigated in literature using a range of techniques, of which, the most non-invasive one is chemically non-specific optical microscopy [17, 18]. Among the chemically specific methods used to perform such studies, flow cytometry [19, 20, 21] is one of the most commonly employed; and the most invasive methods, also in widespread use, are Western blotting and gel electrophoresis [22]. This means that in the best case scenario, we can perform optical microscopy on the cells with no chemical specificity or sensitivity, or sacrifice non-invasiveness for chemical information. Identifying a need for label-free methods to study the effects of these drugs, we applied CARS microscopy to study the effects of Taxol and ICRF-193 on U-2OS cells. This was done to determine whether CARS microscopy is suitable for population phenotyping and profiling the effects of anti-cancer drugs over a period of time, following treatment. Also for the first time, in this project, CARS microscopy has been demonstrated with chemical specificity and sensitivity on structurally and functionally multicellular 3D assemblies, organoids. In the past, other groups have reported studies on organoids, their metabolism and drug interactions using fluorescence microscopy [23, 24, 25], with the already mentioned shortcomings and pitfalls of photodamage and photobleaching.

This thesis is structured into five chapters. The required background is given in the first two chapters. The first chapter introduces optical spectroscopy with emphasis on CARS, including a discussion of the theory and the various implementations of CARS microscopy. The second chapter contains the biology background in cells and cell division requisite for this project. An overview of the current state of the art in imaging techniques is also given.

The set-up and analysis techniques used to acquire and analyze the data presented in this work are described in the third chapter, along with a characterization of the effects of the imaging optics and the sample's refractive index on the analysis method and the quantitative calculations, using polystyrene and poymethymethacrylate beads of different sizes.

The next two chapters describe the applications of CARS microscopy to fixed U-2OS cells and organoids. In chapter four, the results of CARS imaging and spectral analysis of U-2OS cells correlated with two-photon fluorescence are shown. Furthermore, applications of CARS to study the effects of two kinds of anti-cancer drugs i.e, Taxol and ICRF-193 on U-2OS cells are demonstrated. Additionally, a side project not related to CARS microscopy, but presenting a simple method to quantitatively

investigate the number of eGFP molecules attached to cyc-B, across the cell cycle is also described in this chapter. Chapter five demonstrates the suitability of CARS microscopy to image higher levels of biological organization, specifically organoids which are miniature lab grown 3D models of organs.

The summary and outlook of this project are given in the last chapter, which is followed by the Appendices including additional detailed information referenced in the thesis.

All 3D data are available as videos in the data DOI related to this thesis.

Contents

Chapter 1

Background

1.1 Introduction

Einstein adapted Planck's law to explain the photoelectric effect by applying the principle of quantization of energy, interpreting light as a stream of photons of discrete quanta of energies, hν.
Let us consider a two state system shown in Fig. 1.1, with two energy levels corresponding to an energy difference of ΔE.

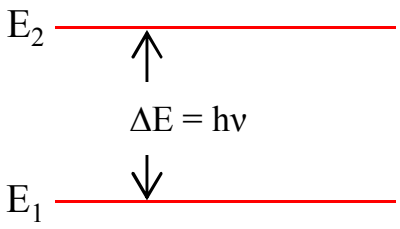

Figure 1.1: Two state system showing ground state, E_1 and excited state E_2. The energy difference between the two states is ΔE.

In such a system, a molecule in the ground state, E_1 may absorb an energy ΔE from an incident photon, and transition to the excited state, E_2. The spectrum of a broadband radiation measured after its interaction with the molecule shows absorption at frequency ν, corresponding to the frequency of a photon of energy ΔE. Conversely, if the molecule is already in E_2, it can loose ΔE (by emitting a photon), and relax to E_1, resulting in an emission spectrum. This process is known as spontaneous emission. Additionally, a third type of interaction known as stimulated emission can occur at the same time. In this case, in response to the incident photons of energy ΔE, the molecules relax to E_1, emitting photons of energy ΔE to the same state as the incident photons.
The approximate scales for the rotational, vibrational and electronic quanta of energy are given in Table 1.1, and show that electronic transitions have the highest energy, followed by vibrational and then rotational transitions. On examining the orders of magnitudes of the excitation energies for the various kinds of molecular motion, we deduce that the structure of the energy levels in a molecule is such that associated with each electronic energy level[28], there is a set of vibrational levels, each of which include a set of rotational energy levels. By probing molecular responses to excitation (in the form of rotational, vibration or electronic transitions), one can identify the composition of unknown substances and also elucidate the struc-

Level Type	E (kJ/mol)	E (eV)	ν (Hz)	E (cm^{-1})	Spectral region
Rotational	10^{-1}	10^{-3}	10^{11}	1	Microwave
Vibrational	10^{1}	10^{-1}	10^{13}	10^{3}	IR/Fingerprint
Electronic	10^{2}	10^{1}	10^{14}	10^{4}	Visible and UV

Table 1.1: Typical energy spacing for rotational, vibrational and electronic transitions [26, 27]

ture of the constituent molecules.

Despite its failure to explain experimental observations like the photoelectric effect, blackbody radiation and the Compton effect, the classical theory of radiation-matter interaction is the foundation of light interaction with matter from which the quantum theory of light is developed. In the Lorentz oscillator model [29], an atom is regarded as a dipole oscillator with negatively charged electrons attached to the positively charged nucleus through springs which follow Hooke's law. In presence of an electric field $\mathbf{E}(\omega)$, the electrons undergo vibrational motion at the frequency of the driving field, which can be modelled as a driven harmonic oscillator [29, 30] to explain the response of atoms to an electromagnetic field, as discussed in the following section.

1.2 Classical theory of light matter interaction

1.2.1 Lorentz oscillator model of an atom

The theory of a damped driven oscillator is applicable to the light matter interaction problem [29] by assuming that the electrons undergo oscillatory motion in response to an applied field. The equation of motion of an atom under the influence of an electromagnetic field $\mathbf{E} = \mathcal{E}_0 \cos(\omega t + \phi)$ is written as

$$m\ddot{x} + m\gamma\,\dot{x} + m\omega_0^2\,x = mq\mathcal{E}_0\,\cos(\omega t + \phi) \tag{1.1}$$

$$= mq\mathcal{E}_0 \Re(e^{-i(\omega t+\phi)}) \tag{1.2}$$

where m is the mass of the electron, γ is the damping coefficient, q is the charge of an electron, x is the displacement of the electron from its equilibrium position, $q\,\mathcal{E}_0$ is the amplitude of the electric force and ϕ is the phase of light. The solution of equation 1.2 is given by

$$x = x_0 \Re(e^{-i(\omega t+\phi)}) \tag{1.3}$$

Substituting equation 1.3 in equation 1.2, we get the amplitude of the oscillations,

$$x_0 = -\frac{q\mathcal{E}_0}{m(\omega_0^2 - \omega^2 - i\gamma\omega)} \tag{1.4}$$

The corresponding phase is given by

$$\tan\phi = \frac{\gamma\omega}{\omega_0^2 - \omega^2} \tag{1.5}$$

Under the influence of an external electric field, a dielectric material experiences polarization due to the orientation of its atomic dipoles parallel to the external field

(as in the case of polar dielectrics) or due to an alteration of the charge distribution in the material. This separation of charges/ rotation of dipole moments produces an internal field, the polarization, **P** which is defined as the volume density of the dipole moments within the material. In an isotropic medium, **P** is parallel to the external electric field. Therefore, $\mathbf{P} = \epsilon_0 \chi \mathbf{E}$, where ϵ_0 is the electric permittivity and χ is the electric susceptibility of the dielectric medium. The displacement field, **D** which accounts for the effect of free and bound charge within a material is directly proportional to the applied field and polarization. Therefore, $\mathbf{D} = \epsilon_0 \mathbf{E} + \mathbf{P} = \epsilon_0(1+\chi)\mathbf{E}$. The dielectric constant, ϵ_r is defined as $1 + \chi = \epsilon_\mathrm{r}$.

The dipoles are oriented parallel to the applied electric field and oscillate with amplitudes [29] calculated using Lorentz oscillator model. The amplitude of the dipole moment of one such oscillator is given by

$$p = q x_0 \tag{1.6}$$

$$= \frac{q^2 \mathcal{E}_0}{m(\omega_0^2 - \omega^2 - i\gamma\omega)} \tag{1.7}$$

The susceptibility associated with this polarization is χ_R, where the subscript R is to indicate that the oscillators are driven close to resonance and N is the number density of oscillators in the material.

$$\chi_\mathrm{R} = N \frac{q^2}{\epsilon_0 m(\omega_0^2 - \omega^2 - i\gamma\omega)} \tag{1.8}$$

In an optical medium, generally, several resonances of different types may be present. An analysis of equation 1.8 is useful to understand how typical materials respond to an electromagnetic field. In the low frequency limit, $\chi_\mathrm{R} = Nq^2/m\omega_0^2$. This susceptibility creates a background from the higher energy resonances. At resonance, $\chi_\mathrm{R} = -iNq^2/m\gamma\omega_0$, a finite value. However, when the driving force oscillates much faster than the resonance, $\chi_\mathrm{R} = 0$. The total susceptibility of a material is a result of all three of these cases.
The treatment shown in this section is valid only in the linear regime. When high intensities of light are incident on a material, **P** has significant contributions of higher orders in **E**. This is the non-linear realm of optics and will be discussed in section 1.3.

1.2.2 Absorption and scattering

Light incident on a material may be absorbed or scattered. The absorbed light can excite the medium and may consequently result in re-emission as fluorescence or phosphorescence, described in section 1.2.3.1. The phenomena of scattering and absorption, described below, form the bases of various types of spectroscopies.
Based on experimental observations, light propagating through a homogeneous medium is absorbed as per Beer-Lambert's law [26], i.e.

$$\log \frac{I_0}{I} = \beta \mathcal{C} \ell \tag{1.9}$$

where I_0 is the incident intensity, I is the resultant intensity of light after propagating through a distance ℓ in the absorbing medium, β is the molar extinction coefficient

and $\mathcal{C}$ is the concentration of the medium.
An electric field propagating along the z direction is expressed as

$$\mathbf{E} = \mathcal{E}_0 e^{i(kz-\omega t)}$$

in the complex form. Also, n is the refractive index of the medium with real and complex parts such that

$$n = n_1 + in_2$$

Therefore,

$$\mathbf{E} = \mathcal{E}_0 e^{-n_2\omega z/c}\, e^{i(n_1\omega z/c-\omega t)}$$

On comparing with Beer's law in equation 1.9, we get

$$\beta' = 2n_2\omega/c$$

where $\beta' = 2.303\,\beta\mathcal{C}$, indicating that n_2 is related to absorption.
In a medium with impurities of size much smaller than the incident wavelength, Rayleigh scattering is observed. In this scattering, the propagating light shows intensity dependence of ω^4. In the next section, a light matter interaction, Raman scattering will be described which includes not only the elastic (Rayleigh scattering) but also inelastic components of scattering.

1.2.3 Examples of light matter interactions

Generally, the processes of absorption, scattering and emission occur simultaneously in a sample in response to incident light. In the following discussion, two types of light-matter interactions, luminescence comprising fluorescence and phosphorescence, and Raman scattering, which form the bases of the techniques used to study the samples of interest in this project will be discussed.

1.2.3.1 Fluorescence and Phosphorescence

Luminescence includes the absorption and incoherent emission of light. In fluorescence, the incident photons are absorbed by molecules in their electronic ground state to transition into an excited electronic state and subsequently relax within the molecular states via non-radiative interactions with the environment. The subsequent emission of photons by the molecules to relax to the electronic ground state is called fluorescence or phosphorescence. As shown in Fig. 1.2 for an organic fluorophore, an incoming photon excites the molecule to a higher electronic state. The molecule then 'fluoresces' by emitting a photon in order to relax to the ground state. The process of fluorescence occurs over a few tens of ns [26, 28].
In Fig. 1.2, the dashed arrow shows inter-system crossing in which a molecule in the excited singlet state, S_1 transitions to the triplet state, T (of typically lower energy). From the triplet state, the molecule relaxes to the ground state, S_0 by emitting a photon. This process is called phosphorescence and occurs over a time scale of μs to hours [28].

1.2.3.2 Rotational spectra

The molecular response to excitation is a result of the interaction of the modes of rotation/vibration/electronic transition with the applied field. In general, the total degrees of freedom of a non-linear molecule comprising N atoms is 3N [26]. Such a

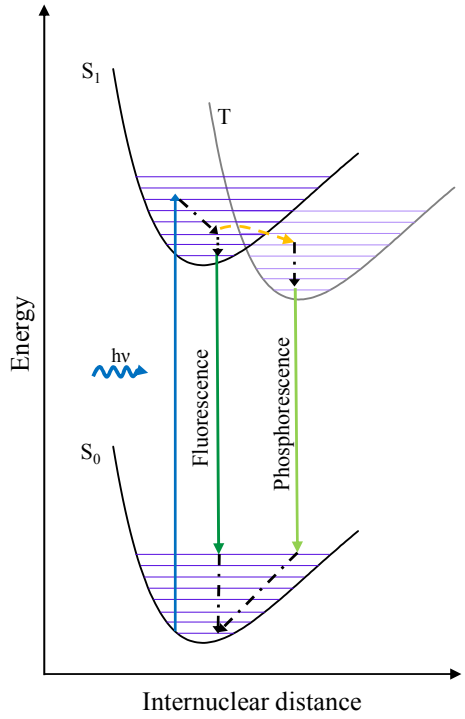

Figure 1.2: Jablonski diagram showing transitions in a molecule showing fluorescence. Electronic states are shown in black modelled on Lennard-Jones potentials, while purple lines represent vibrational/rotational energy levels. S_0 is the singlet ground state, S_1 is the first excited singlet state and T is a triplet state. The transition of the fluorophore in response to excitation with a photon of energy corresponding to S_1 - S_0, from S_0 to S_1 is shown with the blue arrow. The dashed-dotted lines show non-radiative internal conversion in which the fluorophore relaxes from a high vibrational energy state to a lower vibrational state losing energy thermally to the surroundings. The dark green arrow represents the transition of the molecule from S_1 ground vibrational state to S_0 excited vibrational state, corresponding to the process of fluorescence emission. Following this, the molecule relaxes to the ground vibrational state of S_0 through non-radiative transfer, shown by dotted lines. The process of phosphorescence (light green arrow) which occurs subsequent to inter-system crossing (yellow dashed arrow) wherein the molecule transitions to a triplet state from the excited singlet is also shown. Adapted and redrawn from Figures 2.10 a, b in reference [31] with permission from SPIE and Dr. Michiel Müller.

molecule can translate through space with 3 degrees of freedom corresponding to its motion in x, y, z directions. The molecule can rotate about each of the three axes, resulting in 3 degrees of rotational freedom. This leaves 3N-6 vibrational modes [32]. The various molecular vibrations can be described as symmetric/asymmetric stretch, scissoring, wagging, rocking and twisting, to name a few. If the electric dipole moment or the polarizability of the molecules changes in any of these modes, the molecular modes can interact with the applied field.
In rotational(vibrational) spectroscopy, microwaves (infra-red radiation) interact with the molecule and set it into rotational (vibrational) modes of motion. If any of the modes of rotation (vibration) of this molecule result in a change in its dipole moment, the mode is said to be microwave (infrared) active.
As a detailed overview of various kinds of spectroscopy can be found in literature

[26, 30], we restrict ourselves to a brief description of the general topic while focussing in detail on Raman spectroscopy. We model the rotational energy transitions of a diatomic molecule using the rigid rotor model. Quantum mechanically, the rotational energy states of a diatomic molecule are described by

$$E_{\mathrm{J}} = \frac{\hbar^2 J(J+1)}{2\mathcal{J}}$$

where E is the energy of the molecule in a rotational level given by the rotational quantum number J which takes integral values (0, 1, 2...) and $\mathcal{J}$ is the moment of inertia of the molecule in the particular mode of rotation (along the bond axis or end over end in plane of the molecule or end over end perpendicular to plane of the molecule).
The selection rules for these transitions, determined by the quantum mechanical treatment of this system allow transitions in which the change in the rotational quantum number, $\Delta J = \pm 1$. The rigid rotor approximation does not take into account the change in bond-lengths with changes in J (due to elasticity of bonds).

1.2.3.3 Vibrational spectra

A vibrating diatomic molecule is most simply treated in Hooke's law approximation as a simple harmonic oscillator of frequency $\omega = \sqrt{k/\mu}$, where k is the force constant and μ is the reduced mass of the vibration, given by $1/(m_1^{-1} + m_2^{-1})$ where m_1 and m_2 are the masses of the nuclei [26].
In quantum mechanics, the energy of such a harmonic oscillator is quantized as,

$$\epsilon_v = \hbar \left(v + \frac{1}{2}\right) \omega$$

with the vibrational quantum number, v. The change in v in a vibrational transition is given by $\Delta v = \pm 1$.
Real molecules do not follow Hooke's law of elastic bonds and dissociate if compression/extensions beyond a certain threshold are applied, leading to an anharmonic shape of the vibrational potential, and therefore,

$$\epsilon_v = \hbar \left(v + \frac{1}{2}\right) \omega_e - \hbar \left(v + \frac{1}{2}\right)^2 \omega_e x_e$$

where ω_e is the equilibrium frequency of the anharmonic oscillator, and x_e is the anharmonicity constant given by $\omega_e/4D_e$. D_e, the dissociation energy, is the amplitude of the anharmonic potential. There are no selection rules for anharmonic vibrational transitions.

1.2.3.4 Raman scattering

Raman scattering, reported in 1928 by Raman and Krishnan [33] is the inelastic scattering of light (in addition to Rayleigh scattering) into higher and lower energies (compared to incident monochromatic radiation) when passing through a transparent medium.
We recall that the electric dipole moment $\mathbf{p}$ is given by $\mathbf{p} = \alpha \mathbf{E}$, where α is the electronic polarizability. In the absence of nuclear motion, $\alpha = \alpha_0$ while the presence of nuclear motion introduces a first order correction of polarizability in this expression, $\partial\alpha/\partial Q$, where $Q(t)$ is the nuclear coordinate. It is this component which is critical

to a molecular vibrational mode being Raman active. If there is a change in the electronic polarizability corresponding to a nuclear mode, the molecule is Raman active. The expression for the polarizability is

$$\alpha(t) = \alpha_0 + (\partial\alpha/\partial Q)_0 + ... \tag{1.10}$$

Nuclear motion is modelled as a simple harmonic oscillation given by

$$Q(t) = Q_0 \left(e^{i\omega_v t} + c.c.\right) \tag{1.11}$$

where *c.c.* stands for complex conjugate. When a beam of light

$$\Re(\mathbf{E}) = \mathcal{E}_0\, e^{-i\omega_1 t} + c.c$$

is incident on a molecule, the induced dipole moment is given by

$$\mathbf{p}(t) = \alpha \left(\mathcal{E}_0\, e^{i\omega_1 t} + c.c.\right)$$

Substituting equation 1.10 for polarizability up to the first order derivative, we get

$$\mathbf{p}(t) = (\alpha_0 + \partial\alpha/\partial Q)\, \mathcal{E}_0\, e^{i\omega_1 t} + c.c. \tag{1.12}$$

$$= \alpha_0 \mathcal{E}_0\, e^{-i\omega_1 t} + \mathcal{E}_0\, Q_0\, (\partial\alpha/\partial Q)_0\, (e^{-i(\omega_1+\omega_v)t} + e^{-i(\omega_1-\omega_v)t}) + c.c. \tag{1.13}$$

The first term in equation 1.13 corresponds to Rayleigh scattering while the second term represents inelastic scattering, with $\omega_1 + \omega_v$ (Stokes) and $\omega_1 - \omega_v$ (anti-Stokes) components.
Quantum mechanically, we explain Raman scattering by considering a light of frequency, ν_0 passing through the sample [26]. The incident photons undergo elastic collisions with the sample's molecules without exchanging energy, and are scattered. The scattered photons at ν_0 correspond to Rayleigh scattering. To explain the side bands (Stokes, S and anti-Stokes, AS lines) shown in Fig. 1.3, we recall the discrete structure of energy levels and the concept of quanta introduced earlier in this chapter. Molecules of the sample respond to incident light by either absorbing quanta

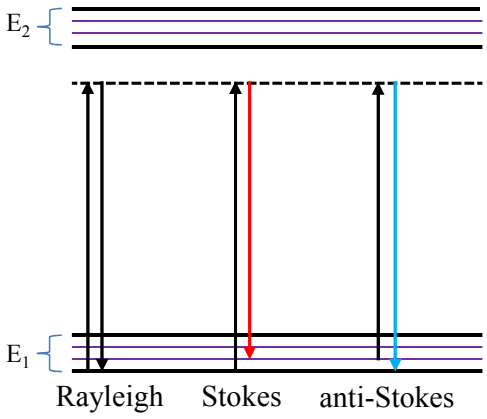

Figure 1.3: Energy level diagram of Raman scattering showing Rayleigh, Stokes and anti-Stokes lines. Energy states, E_1 and E_2 are shown. The purple lines represent the vibrational states within the electronic energy states. Black arrows indicate the excitation (also the transition with energy corresponding to Rayleigh scattering). The Stokes line is shown in red and anti-Stokes in blue.

corresponding to an energy transition (Stokes), or relax to a lower energy level by emission of some quantum of energy (anti-Stokes).
Referring to Boltzmann's distribution law ($N_u = N_l\, e^{-\Delta E/kT}$, where N_u and N_l are the numbers of molecules in the upper and lower energy states respectively, ΔE is the energy difference between the two states, k is Boltzmann's constant and T is temperature in Kelvin), Stokes scattering is more intense than anti-Stokes. Raman active vibrational transitions are described by $\Delta v = 0, \pm 1, \pm 2, \pm 3...$ and so on, the same as those for infra-red spectroscopy but the selection rules and strengths are different.
The chemical specificity of Raman scattering makes it useful in diagnostic and sensing applications. However, the typical Raman cross sections are of the order of $10^{-29}\,\mathrm{cm}^{-2}$/mode, a factor of 10^{14} smaller than that corresponding to electronic transitions, (including fluorescence) which have cross sections in the order of $10^{-15}\,\mathrm{cm}^{-2}$. This leads to a weak signal, thus limiting the application of spontaneous Raman scattering in biological samples which are sensitive to photo-damage. A significant improvement in the signal to noise ratio, (S/N) is achieved in non-linear, coherent anti-Stokes Raman scattering, which will be described in section 1.4.

1.3 Non-linear optics

In the previous section, the theory of a damped driven harmonic oscillator has been applied resulting in linear optics i.e., $\mathbf{P}$ linearly dependent on $\mathbf{E}$. For high intensities of electric field, as has become possible with the advent of lasers, one finds additional terms having a non-linear dependence of $\mathbf{P}$ and consequently χ on $\mathbf{E}$, resulting in a range of interesting phenomena, some of which will be described in this chapter with primary focus on the third-order non-linearity which is the mainstay of CARS microscopy. We recall that the interaction between the electrons and nucleus in an atom is approximated by Hooke's law. In case of large oscillations induced in the atom as a result of the high magnitude of the applied field, the linear approximation of Hooke's law breaks down and we observe anharmonicity giving rise to non-linearities in the atom's response to applied field. The interatomic fields are typically of the order of $10^{10} - 10^{11}\,\mathrm{V/m}$. This means that we should expect that the non-linearities are of a similar magnitude as the linear response when the excitation field magnitudes are comparable to the interatomic fields [29, 34].
As a result, for a medium placed in a high external electric field, the relation of $\mathbf{P}$ with $\mathbf{E}$ is no longer restricted to first-order linear dependence. Therefore, we additionally have the non-linear polarization

$$\mathbf{P}_{\mathrm{NL}} = \mathbf{P}^{(2)} + \mathbf{P}^{(3)} + \mathbf{P}^{(4)} + ... \tag{1.14}$$

where $\mathbf{P}^{(\mathrm{n})}$ represents the n-th order polarization given by $\epsilon_0 \chi^{(\mathrm{n})} \mathbf{E}^{\mathrm{n}}$. In terms of susceptibility, the non-linear polarization is written as,

$$\mathbf{P}_{\mathrm{NL}} = \epsilon_0 (\chi^{(2)} \mathbf{E}^2 + \chi^{(3)} \mathbf{E}^3 + ...) \tag{1.15}$$

Imaging methods like second harmonic generation (SHG) and two-photon fluorescence (TPF) rely on the second-order non-linearity, while Kerr effect and coherent Raman scattering are third-order non-linear effects. SHG and Kerr effect will be briefly touched upon in the following sections. Since CARS and TPF are the imaging techniques used to study the samples in this project, these will be discussed in more detail in the applications section.

1.3.1 Second-order non-linearity

The second-order non-linear response of a material is used in imaging techniques like SHG and TPF. The most general case of three wave mixing in a second-order non-linear medium is discussed in the next section. Special cases of this frequency mixing, SHG and TPF will then be discussed in subsequent sections.

1.3.1.1 Frequency mixing

Frequency mixing by the second-order non-linear terms can be discussed by considering the application of an electric field of form $\mathbf{E}(t) = \Re(\mathcal{E}_1 e^{i\omega_1 t} + \mathcal{E}_2 e^{i\omega_2 t})$ to a non-linear medium [34]. By substituting this expression of electric field in equation 1.16 for the second order non-linear term, we observe that the material response includes terms with frequencies 0, $2\omega_1$, $2\omega_2$, $\omega_1 + \omega_2$ and $\omega_1 - \omega_2$. The frequencies $2\omega_1$ and $2\omega_2$ correspond to second harmonic generation. Frequency up-conversion, or sum frequency generation is given by the $\omega_1 + \omega_2$ term, while frequency down conversion or difference frequency generation term is given by the $\omega_1 - \omega_2$ term.

1.3.1.2 Second harmonic generation

Using only a single excitation frequency, the electric field is, $\mathbf{E}(t) = \Re(\mathcal{E}(\omega)e^{i\omega t}) = \mathcal{E}(\omega)e^{i\omega t} + \mathcal{E}^*(\omega)e^{-i\omega t}$. From equation 1.15, the second-order non-linear polarization is given by $\mathbf{P}^{(2)} = \chi^{(2)}\mathbf{E}^2$. Substituting $\mathbf{E}(t)^2 = 2\mathcal{E}(\omega)\mathcal{E}^*(\omega) + \mathcal{E}(\omega)^2 e^{2i\omega t} + \mathcal{E}^{*2}(\omega)e^{-2i\omega t}$ in this equation, we get

$$\mathbf{P}_{\mathrm{NL}} = \chi^{(2)}\mathcal{E}(\omega)\mathcal{E}^*(\omega) + \chi^{(2)}[\mathcal{E}^2(\omega)e^{2i\omega t} + \mathcal{E}^*(\omega)^2 e^{-2i\omega t}] \tag{1.16}$$

$$= \underbrace{\chi^{(2)}|\mathcal{E}(\omega)|^2}_{\mathbf{P}_{\mathrm{NL}}(0)} + \underbrace{\chi^{(2)}\Re(\mathcal{E}(\omega)^2}_{\mathbf{P}_{\mathrm{NL}(2\omega)}} e^{2i\omega t}) \tag{1.17}$$

$$\tag{1.18}$$

In equation 1.18), the first term, $\mathbf{P}_{\mathrm{NL}}(0)$ represents the non-oscillating rectification of the oscillating field. The second term, $\mathbf{P}_{\mathrm{NL}}(2\omega)e^{2i\omega t}$ corresponds to second harmonic generation at twice the frequency of the incident wave. For a centrosymmetric medium, the smallest order of non-linearity is 3 [34], i.e., no SHG occurs.

1.3.1.3 Phase matching

Before proceeding further, an important aspect of implemention of these techniques, phase matching must be discussed. Let us consider the process of SHG. The refractive index of the medium experienced by the frequency doubled waves generated in the SHG process is different from that experienced by the fundamental wave. We consider a block of medium. The SHG waves generated at the front of this block arrive at the back of the block at a different time compared to the fundamental waves. Consequently, the SHG waves generated at the back of the block are not in phase with the SHG waves generated in the front and these waves can destructively interfere, reducing the SHG intensity.
The condition for phase matching can be determined as follows. We consider that since the refractive index of the medium is different at frequencies 2ω and ω, the propagation vectors of the two waves are also different. If we impose a constraint such that $\mathbf{k}(2\omega) = 2\mathbf{k}(\omega)$, since the second-order non-linearity scales as $\mathbf{E}^2$; the waves' propagation vectors are matched. This corresponds to the conservation of

momentum.
In the most general case for a three-wave mixing process with the applied field comprising harmonics at ω_1 and ω_2 as in section 1.3.1.1, the phase matching condition is satisfied if $\mathbf{k}_1 + \mathbf{k}_2 = \mathbf{k}_3$ where $\mathbf{k}_3$ is the generated wave's propagation vector.

1.3.1.4 Two-photon fluorescence

As already discussed in section 1.2, a particular class of molecules called fluorophores emit photons in response to excitation by photons of suitable energy. Maria Göppert-Mayer predicted theoretically that a fluorescent molecule can be excited by using two incident photons arriving at the sample within attoseconds of each other [35, 36], if their additive energy equals that required for the transition. The Jablonski diagram of the process is shown in Fig. 1.4.
The fluorescence emission processes followed by a molecule excited by either two or one photon are the same. The point spread function (PSF, defined as the spread of light in the image of an infinitesimally small object) of TPF is the square of that of the one-photon fluorescence, the z-dependence of signal in the former goes as z^{-4}. The area scales as z^2, resulting in the signal from bulk varying as z^{-2} [28], which gives 3D sectioning capability to the process of TPF. The 3D sectioning capability and its compatibility with the implementation of other non-linear techniques makes TPF a preferred imaging modality over single photon fluorescence for some applications.

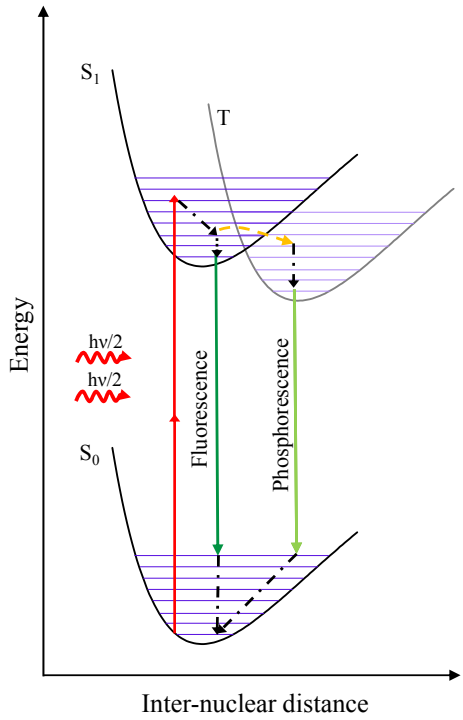

Figure 1.4: Jablonski diagram showing two-photon fluorescence. The states and transitions are the same as Fig. 1.2 with the exception that instead of one exciting photon of frequency ν, two photons of frequency $\nu/2$ each are used. Adapted and redrawn from Figures 2.10 a, b in reference [31] with permission from SPIE and Dr. Michiel Müller.

1.3.2 Third-order non-linearity

In this section, third-order non-linearities will be discussed. A similar analysis as in the previous section will be applied. The third-order non-linear susceptibility $\chi^{(3)}$ is the physical quantity of interest in Kerr effect and CARS microscopy.

1.3.2.1 Optical Kerr effect

The optical Kerr effect is observed as a third-order non-linear response of a medium to a single frequency incident beam. The expression for dielectric constant including the third order non-linear term is

$$\epsilon_r = 1 + \chi + \chi^{(3)}\,\mathbf{E}^3 \tag{1.19}$$

The part of the dielectric constant corresponding to the third-order non-linearity is $\chi^{(3)}\mathbf{E}^2$. In the non-linear regime, from equation 1.19, we observe that the dielectric constant and consequently, the refractive index show a dependence on the field intensity. The phase matching condition is always fulfilled as the response is generated at the same frequency as the excitation field.

1.3.2.2 Coherent Raman scattering (CRS)

Spontaneous Raman scattering as already explained in section 1.2.3.4, is a weak effect due to the small scattering cross section. Additionally, in spontaneous Raman scattering, the sample's molecules in the focal volume of the excitation beam vibrate at random phases with each other, resulting in a weak total Raman signal. In contrast, coherent Raman scattering generates coherent signals by exciting the sample in the third-order non-linear regime using an excitation profile comprising two frequency components, i.e., the pump and Stokes. The response of the sample to this excitation is expressed as:

$$\mathbf{P}^{(3)} = \chi^{(3)}\Re((\mathbf{E}_\mathrm{p} + \mathbf{E}_\mathrm{s}))^3 \tag{1.20}$$

The expanded form of the excitation field in CARS is given by

$$\Re(\mathbf{E}) = \mathcal{E}_{0p}e^{i\omega_\mathrm{p}t} + \mathcal{E}_\mathrm{s}e^{i\omega_\mathrm{s}t} + c.c \tag{1.21}$$

From equation 1.20, we obtain $P^{(3)}$ components at various frequencies, which are listed in Table 1.2 [32] along with their frequency and amplitude. The different components of CRS correspond to coherent anti-Stokes Raman scattering (CARS), stimulated Raman loss (SRL), stimulated Raman gain (SRG) and coherent Stokes Raman scattering (CSRS). Of these components, the CARS and CSRS signals are

Component	Frequency	Amplitude
SRL	ω_p	$\mathcal{E}_\mathrm{p}\mathcal{E}_\mathrm{s}\mathcal{E}_\mathrm{s}^* + c.c$
SRG	ω_s	$\mathcal{E}_\mathrm{p}\mathcal{E}_\mathrm{p}^*\mathcal{E}_\mathrm{s} + c.c$
CARS	$2\omega_\mathrm{p} - \omega_\mathrm{s}$	$\mathcal{E}_\mathrm{p}\mathcal{E}_\mathrm{p}\mathcal{E}_\mathrm{s}^* + c.c$
CSRS	$2\omega_\mathrm{s} - \omega_\mathrm{p}$	$\mathcal{E}_\mathrm{s}\mathcal{E}_\mathrm{s}\mathcal{E}_\mathrm{p}^* + c.c$

Table 1.2: Components of $\mathbf{P}^{(3)}$ in response to pump-Stokes excitations at ω_p and ω_s respectively [32].

generated at frequencies well separated from that of the excitation beams. Furthermore, CARS is detected at a higher frequency compared to the one-photon excited fluorescence emission, thus preventing cross-talk between the two processes and eliminating the autofluorescence background (which constitutes a part of the response of a typical biological sample). Therefore, CARS is advantageous over CSRS which is spectrally overlapping with fluorescence and spontaneous Raman scattering. These factors and the fact that photodetectors have higher quantum efficiencies at higher frequencies make CARS an easier and more advantageous signal to detect compared to CSRS. The other two components, i.e., SRL and SRG are degenerate with the pump and Stokes beams respectively, and therefore, their detection involves additional steps to discriminate the emitted signal from the exciting beam. In SRS (the responsible interaction for SRL and SRG), the pump and Stokes beams induce stimulated Raman scattering in the sample, leading to an enhanced signal when the driving fields are matched with the molecular vibrational frequencies. The terms 'loss' and 'gain' in the names of the associated processes, i.e., SRL and SRG correspond to the loss in the pump intensity due to the transition of molecules in the ground state to an excited state in response to the driving fields; and the gain in the Stokes intensity due to the Raman signal generated at the Stokes frequency. Consequently, there is no SRS signal when the driving field frequency is not matched with the vibrational transitions of the molecule. We compare this with the CARS process in which the sample response comprises resonant and non-resonant components, the latter of purely electronic origins. This non-resonant background is a subject of much speculation in the CARS community as it hinders meaningful interpretation of the CARS signal. In fact, the non-resonant background limits the usability of CARS microscopy in the imaging of certain samples such as plants which are strongly autofluorescent. For such samples, SRS is a viable technique for label-free, chemically specific and sensitive imaging, as demonstrated by Mansfield et al. [37], using phase sensitive detection. SRS has also been used to study cuticular waxes [38] and lipid accumulation [39] in plants. However, despite the non-resonant background, CARS microscopy has also been successfully applied to study plants, as demonstrated in various studies [40, 41, 42], using various methods (such as frequency modulation) to separate the autofluorescence background from the CARS signal.
The various nuances of the theory of CARS microscopy will be described in the next section, along with a longer discussion about the non-resonant background and various technical modifications in current use to work around it.

1.4 CARS

The energy level diagram of CARS given in Fig. 1.5 shows the molecular transitions occurring in CARS excitation and emission. The pump and Stokes fields interfere and drive the vibrational energy state transition through virtual states. While the transitions associated with the CARS process occur as a result of four-wave mixing and relate the induced third-order molecular polarization to the excitation field through $\chi^{(3)}$, the description provided below treats them sequentially for a more intuitive understanding [27]. In the first step of the process, the pump field couples the vibrational state V_1 with the virtual state Γ_1. The Stokes field then couples V_2 with Γ_1. A second pump field then couples V_2 to Γ_2. The resulting polarization leads to the anti-Stokes emission at $\omega_{as} = 2\omega_p - \omega_s$.

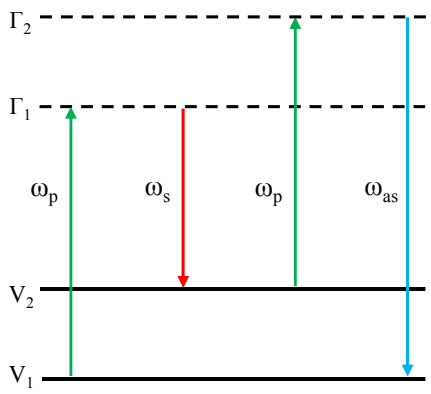

Figure 1.5: Energy level diagram describing molecular transitions in CARS. Vibrational states V_0 and V_1 within the same electronic state are shown in black solid lines. The dotted lines represent virtual states Γ_1 and Γ_2. The green (red) arrow represents transition corresponding to energy $\hbar\omega_p$ ($\hbar\omega_s$). The transition which gives rise to the anti-Stokes signal is shown by the blue arrow. Adapted from Figure 6.7 in reference [27] with permission from John Wiley & Sons.

1.4.1 The CARS signal

We recall from our discussion in section 1.3.2.2 that in CRS, two fields (pump and Stokes) drive the sample molecules in the focal volume to vibrate at $\Omega = \omega_p - \omega_s$. This vibration of the molecules presents an oscillating susceptibility to a third beam, called the probe. The molecular vibrations are modulated onto the probe beam of frequency ω_{pr}, of which one component, designated as the CARS signal [43] is emitted at the frequency $\omega_{as} = \omega_p - \omega_s + \omega_{pr}$, where the subscript as refers to the anti-Stokes signal. The condition of resonance is realized when $\Omega \sim \Omega_0$, where Ω_0 corresponds to a vibrational transition of the molecule.
Mathematically, the induced dipole moments in the molecules due to CARS excitation are similar to that shown for spontaneous Raman scattering in section 1.2.3.4. The excitation field given by $\mathbf{E}_p + \mathbf{E}_s$ induces atomic polarization and drives the electron motion, which in turn interacts with the nuclear modes through a perturbation in polarizability represented by $\partial\alpha/\partial Q$. Through this perturbation term (recall equation 1.10), the field exerts a force, F on the molecule which is given by

$$F = \left(\frac{\partial\alpha}{\partial Q}\right)_0 \mathcal{E}_p \mathcal{E}_s^* e^{-i(\omega_p - \omega_s)t} \tag{1.22}$$

Substituting equation 1.22 as the source in the equation of motion of Lorentz harmonic oscillator (equation 1.2), we obtain a solution for the vibrational modes as [43] $Q(t) = Q(\Omega)e^{i\Omega t} + c.c$, where $Q(\Omega)$ is the spatial component (and the amplitude) of the nuclear motion, given by

$$Q(\Omega) = \left(\frac{\partial\alpha}{\partial Q}\right)_0 \frac{\mathcal{E}_p \mathcal{E}_s^*/m}{\Omega_0^2 - \Omega^2 - i\Omega\gamma} \tag{1.23}$$

Since the polarization and consequently, the susceptibility are related to the polarizability, we have for CARS signal, the third-order polarization,

$$\mathbf{P}^{(3)}(t) = \mathrm{P}^{(3)}(\omega_{\mathrm{as}})\mathrm{e}^{-\mathrm{i}\omega_{\mathrm{as}}\mathrm{t}} + \mathrm{c.c} \qquad \text{And,} \tag{1.24}$$

$$\tag{1.25}$$

$$P^{(3)}\omega_{\mathrm{as}} = N\left(\frac{\partial\alpha}{\partial Q}\right)_0^2 \frac{\mathcal{E}_{\mathrm{p}}^2\mathcal{E}_{\mathrm{s}}^*/m}{\Omega_0^2 - \Omega^2 - i\Omega\gamma} \tag{1.26}$$

$$\tag{1.27}$$

$$= 6\epsilon_0\chi_{\mathrm{R}}^{(3)}(\Omega)\mathcal{E}_{\mathrm{p}}^2\mathcal{E}_{\mathrm{s}}^* \tag{1.28}$$

In the focal volume of the exciting beams, the sample typically comprises several modes from 0 to J and the individual susceptibilities of the constituent molecules are summed over in the phase matched direction as,

$$\chi_{\mathrm{R}}^{(3)}(\Omega) = \sum_{j=0}^{\mathrm{J}} \frac{R_j/6\epsilon_0}{\Omega_{0j}^2 - \Omega^2 - i\Omega\gamma_j} \tag{1.29}$$

where the oscillator strengths, R_j are given by $(\partial\alpha/\partial Q)^2/m$ and account for various molecular transition probabilities [29]. The line widths of the resonances are given by γ_j and represent the damping in the system. From equation 1.29, we obtain the real and imaginary parts of $\chi^{(3)}$ as

$$\Re\left(\chi^{(3)_{\mathrm{R}}}\right) = \sum_{j=0}^{\mathrm{J}} \frac{R_j(\Omega_{0j}^2 - \Omega^2)}{(\Omega_j^2 - \Omega^2)^2 + \Omega^2\gamma_j^2} \tag{1.30}$$

$$\Im\left(\chi_{\mathrm{R}}^{(3)}\right) = \sum_{j=0}^{\mathrm{J}} \frac{R_j\Omega\gamma_j}{(\Omega_{0j}^2 - \Omega^2)^2 + \Omega^2\gamma_j^2} \tag{1.31}$$

Unlike SRS and SRL, the CARS and CSRS signals are generated even in conditions of non-resonant excitation. This means that the CARS susceptibility $\chi^{(3)}$ includes resonant and non-resonant components [32, 44] and can be written as,

$$\chi^{(3)} = \chi_{\mathrm{R}}^{(3)} + \chi_{\mathrm{NR}}^{(3)} \tag{1.32}$$

where the subscripts R(NR) stand for resonant (non-resonant). The resonant component is a result of the vibrational transitions of the molecule and therefore is the interesting component. The non-resonant component of the susceptibility is purely electronic in origin [32, 44, 45, 46] and given by the Kerr effect [47]. However, transitions far below the resonance also give a non-resonant contribution, such as the CH_2 resonances in the 2800 cm^{-1} range give a background in the fingerprint regions [47]. The CARS intensity, I_{C} is expressed in terms of resonant and non-resonant components as

$$I_{\mathrm{C}} \propto |\chi_{\mathrm{R}}|^2 + 2\Re(\chi_{\mathrm{R}}\chi_{\mathrm{NR}}) + |\chi_{\mathrm{NR}}|^2 \tag{1.33}$$

The three components of I_{C} are plotted in Fig. 1.6. In equation (1.33), the first term on the RHS arises from the resonant part of the third-order susceptibility and the third term originates from the non-resonant component of $\chi^{(3)}$ and is constant. The middle term which is the mixing of resonant and non-resonant susceptibilities is dispersive. Through this term, the non-resonant background (NRB) changes the

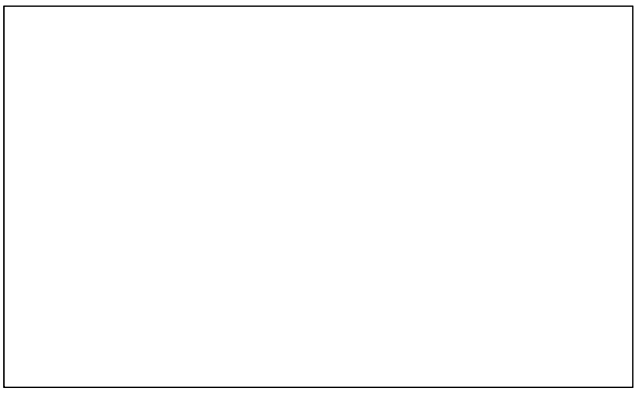

Figure 1.6: Components of the CARS intensity, (I_C) normalized to its non-resonant part. The solid black line shows the Lorentian shape of the resonant component of the CARS intensity. The spectrally constant non-resonant component is shown as a dotted line. The mixing term of the resonant and non-resonant components is shown as a dashed curve. This figure (appearing as Figure 3 a in reference [46]) has been redacted for copyright reasons.

lineshape of the CARS resonances. Moreover, since the CARS intensity is proportional to N^2 [32], where N is the number of oscillators generating the signal, the dispersive term in the expression for I_C becomes more important when probing molecular species in low concentrations because in such a case, the resonant signal is weak and the non-resonant component dominates the detected intensities.

1.4.2 Phase matching

In CARS, we actively drive the molecules to vibrate in a fixed phase and a strong CARS signal is emitted under conditions of phase matching. To obtain this condition we match the wave vectors (represented by k with appropriate subscripts for different waves) as previously done in section 1.3.1.3. For the CARS process, we obtain the phase matching condition:

$$\Delta\mathbf{k} \leq \mathbf{k}_{\mathrm{as}} - (2\mathbf{k}_{\mathrm{p}} - \mathbf{k}_{\mathrm{s}}) \tag{1.34}$$

where $\Delta\mathbf{k}$ is the wave vector mismatch between the anti-Stokes wave and the CARS polarization, and $\mathbf{k}_{\mathrm{as}}$ is the anti-Stokes wave vector.
Alternately, in terms of the interaction length l over which the signal constructively interferes, we write equation 1.34 as

$$l|\Delta\mathbf{k}| = \pi \tag{1.35}$$

From equation 1.35, we observe that phase mismatch is minimised if the interaction length is small. This condition is readily satisfied by using high numerical aperture (NA) lenses (NA > 0.2) [46] to tightly focus the pump and Stokes beams onto the focal volume [10], also ensuring high excitation field intensities in the focal volume which are necessary for CARS signal generation.

1.4.3 Implementation of CARS microscopy

While the phenomenon of CARS was reported in 1965 by Maker and Terhune [9], it was not until 1982 that the first CARS microscope was developed by Duncan

et al. [48] to study onion skin cells using two dye lasers, implementing the phase matching condition i.e., $\Delta\mathbf{k} = 0$ with a non-collinear geometry. It was observed that the phase matching condition was not critical while studying thin samples. However, the use of non-collinear geometry in these experiments made the implementation of CARS microscopy complicated, and discouraged its wider use. Nearly a decade later, the phase matching condition given in equation 1.35, was implemented by Zumbusch et al. by using tightly focussed infrared beams in collinear geometry using a 1.4 NA lens [10]. The improved spatial resolution and primarily, the relative ease of implementation of the technique in collinear geometry marked the revival of CARS microscopy, opening up interesting possibilities to explore the applications of CARS, wherein samples could be studied with spatial and spectral resolution. Since the work of Zumbusch et al., several implementations of CARS microscopy (typically using two lasers, one for pump and the other for Stokes) have been reported, to perform several variations of the technique, which will be discussed in the following sections, along with some aspects of the implementation of CARS microscopy.

1.4.4 Non-resonant background

In the broadest sense, various implementations of CARS microscopy can be classified as either broadband/hyperspectral or single frequency. In single frequency CARS, lasers are tuned to an interesting frequency and the CARS response of the sample at that frequency is detected. In hyperspectral CARS, the sample response over a large frequency range is probed. Hyperspectral CARS provides complete information about a sample's response over a spectral range, and is therefore used to study unknown samples; while single frequency CARS is often used as a fast imaging method for known samples. In both these cases, the issue of non-resonant background merits discussion. The reason non-resonant background is important is because CARS resonance lineshapes are asymmetric due to the mixing of the resonant and non-resonant components of the signal as already shown in equation 1.33. Consequently, the ratio of the resonant and non-resonant components of the signal is an important factor in any application of CARS microscopy. In the case of hyperspectral CARS, the non-resonant background (typically, glass which is non-resonant in 1200 - 3600 cm^{-1} range) is also measured and then used to calculate the resonant part of the signal [49, 50, 51, 52]. In single frequency CARS, it is difficult to differentiate between the resonant and non-resonant components of the signal, and therefore it is recommended to suppress the non-resonant background. Some of the methods to reduce non-resonant background are described below.

1) **Polarization CARS** One way to reject the non-resonant signal is through an implementation called polarization CARS in which the polarization differences of resonant and non-resonant signals of the material are used to differentiate between the resonant and non-resonant components of the signal and then selectively reject the non-resonant part. In this technique, the pump and Stokes beams are linearly polarized [44, 53]. The pump beam is polarized along a direction perpendicular to its propagation vector and the Stokes beam is polarized at an angle to the pump. On detecting the CARS signal with an analyzer that is crossed with the polarization of non-resonant signal, the non-resonant background is eliminated from the detection [44], assuming a homogeneous medium as background. However, this method has the disadvantage that the total signal detected is low due to rejection of a part of resonant signal and all of non-resonant signal before detection.

2) **Time-resolved CARS** Time-resolved CARS microscopy relies on the time-scales of response of the electrons and nuclei to the applied fields. Electrons which are responsible for the non-resonant background follow the driving field instantaneously, while the relatively heavier nuclei which are responsible for the resonant component of the signal, lag in their response, depending on the line widths of the resonances they show [54]. By rejecting the first temporal part of the signal, one can reject the non-resonant component. However, similar to the case of polarization CARS, this method also reduces the signal intensity because temporally rejecting even 1 ps of the signal results in a reduced resonant component as the vibrational line widths are of the order of a few ps [44].

3) **Interferometry** As discussed in section 1.4.1, the $\chi^{(3)}$ non-resonant background is real, while the imaginary part of $\chi^{(3)}$ is comparable to spontaneous Raman scattering. Based on this distinction between resonant and non-resonant components of $\chi^{(3)}$, spectral interferometry [55] is another method to reject non-resonant background. In this technique, the CARS signal is mixed with a local oscillator field (typically the response of a non-resonant material). $\Im(\chi)$ varies sinusoidally with the phase difference between the CARS signal and the local oscillator field [56]. On the other hand, $\Re(\chi)$ varies as cosine of the phase. By setting the phase to 0° or 90°, one can suppress the imaginary or real part of susceptibility respectively. This technique is superior to polarization and time-resolved CARS because the signal is not suppressed, only split into two components. Using the spectral information, we can retrieve the phase, and discriminate the resonant and non-resonant parts of the signal.
These methods, although demonstrably useful for standard samples, are complicated to implement in the case of complex samples such as cells and other biological materials [57] due to various issues, such as the weak CARS response of biological samples, especially in the fingerprint region, and the relative paucity of distinguishing peaks in the CH-stretch region. Therefore, any loss of signal as experienced in polarization CARS and time resolved CARS is undesirable. The third method discussed above, i.e., interferometry requires additional optical components. In contrast to all of these methods, the correctness of the analysis and interpretation of the CARS data is maintained if one uses digital non-resonant background correction algorithms as mentioned earlier and as will be discussed in section 3.3, without losing any part of the signal.

1.4.5 Choice of excitation sources for CARS microscopy

Above and beyond the issue of non-resonant background, the pump beam in typical CARS set-ups ($\sim$ 650 nm) can induce multiphoton damage in the sample. Laser characteristics such as the repetition rate govern the speed of acquisition, with faster speeds corresponding to lesser photodamage. Therefore, in order to ensure optimum operation of the CARS microscope, the importance of careful choice of laser sources cannot be overlooked. Laser wavelength, pulse width, and repetition rate all bear an effect on the resonant and non-resonant CARS signals, as described below.

1.4.5.1 Effect of wavelength

When excitation fields in the visible region of the spectrum are used to study typical materials, such as in the CARS microscope built by Duncan et al. [48], the electronic resonances are two-photon excited. This leads to a build up of the non-resonant signal [58] in the sample, and consequently photodamage, which hampers the detection of the resonant signal. These undesirable effects can be avoided if near-infrared excitation (infrared excitation causes heat damage to the sample as water absorbs strongly in this region) is used, which also improves the spatial resolution in imaging compared to the infrared, while reducing the Rayleigh scattering (biological window $\sim$ 650 - 1350 nm, i.e., light in this wavelength range has the maximum penetration depth in tissues) and thus enables the imaging of thick samples [10].

1.4.5.2 Effect of pulse width

Typical vibrational resonances of biological molecules in water have a width $\sim$ 10 - 20 cm^{-1} [46]. A laser pulse (in the case of CARS, the interference between Fourier limited pump and Stokes fields) with spectral width larger than that of the vibrational resonance will excite not only the vibration, but also the non-resonant background. The behaviour of the resonant and non-resonant components of the CARS signal with pulse width can be qualitatively summed up as follows. The resonant component increases with pulse width but saturates when the pulse spectral width matches the spectral width of the vibrational resonance. However, assuming Fourier-limited pulses (i.e., pulse duration $\sim$ 1/spectral width), the non-resonant signal rises quadratically with the pulse spectral width since it is not dependent on the resonances but is a result of inefficient driving of the electronic transitions. Therefore, the ratio of the resonant to the non-resonant components of the CARS signal decreases as the pulse width increases [44, 46]. To balance the signal/noise ratio and the signal power, pulse durations of $\sim$ 2 ps are ideal.

1.4.5.3 Effect of pulse repetition rate

Since CARS is a third-order effect, high peak excitation powers and low repetition rates provided by pulsed lasers are ideal to produce a large non-linear response from the sample while limiting the heating due to absorption. However, the laser power and repetition rates must be adjusted to limit the damage to the sample and attain reasonable acquisition speed respectively [59].

1.4.6 CARS signal propagation

In the development of this chapter, we have regarded the CARS signal generated by the molecules in response to an appropriate excitation by treating the constituent atoms as dipoles. This means that the CARS signals generated by the molecules should follow the same trends as does a Hertzian dipole, which radiates in forward and backward directions [46]. The backward directed CARS signal was first reported by Volkmer et al. [60]

We call the CARS signal propagating in the backward direction (opposite to the excitation beams in a collinear geometry) as epi-CARS or E-CARS, while the forward signal is referred to as forward CARS or F-CARS. The CARS signal from larger scatterers is forward propagating. The epi-CARS signal originates from scatterers smaller than the excitation wavelength and propagates in the forward and backward

directions, due to incomplete destructive interference of the signal generated in epi. In this case, the backward propagating CARS signal remains phase matched despite large $\mathbf{\Delta k}$ due to the small interaction length [61, 62].
Aside from the small interaction length in the case of small scatterers and consequent satisfaction of the phase matching condition, the epi-CARS signal can also arise due to sharp discontinuities in $\chi^{(3)}$ which are equivalent to small objects in the focal volume samples [59, 62].
In addition to these, refractive index mismatch typically seen at interfaces between medium and specimen [63] can result in back-reflection of the forward propagating CARS signal, resulting in an epi-component.
Understanding the epi-data in a quantitative way is difficult due to oscillations in the signal as a result of interference with the large wave-vector mismatch [62]. Despite the difficulty in quantitative interpretation of epi-CARS signal, the advantage of collecting epi-signal in imaging small structures without a large signal from the medium, makes it a useful scheme of detection [64, 65].

1.5 Summary

In this chapter, starting from linear optics, a general overview of spectroscopy with special attention to Raman scattering been given. The third-order non-linear susceptibility, which is the physical basis of CARS microscopy has been discussed along with the theory of CARS. Furthermore, some implementations of CARS microscopy have also been discussed, together with their merits and demerits. In our multimodal set-up, described in the third chapter, we enable hyperspectral CARS using a single femtosecond, broadband Ti:Sa laser with a high repetition rate, thus reducing photodamage to the samples, while maintaining $5\,\mathrm{cm}^{-1}$ resolution. To access a large spectral range (1200 - $3800\,\mathrm{cm}^{-1}$), we have implemented a novel technique called spectral focussing which allows us to perform hyperspectral measurements without tuning the laser. However, before delving into the specifics of our implementation, in the next chapter we present an introduction to the underlying biology relevant to this project along with a discussion on the present state of the art of cell imaging.

Chapter 2

The mammalian cell and somatic cell division

2.1 The Cell

With typical sizes of a few tens of micrometers in prokaryotes and a hundred micrometers in eukaryotes, cells, the basic units of life, are too small to be seen by the unaided eye [66]. In fact, cells remained undiscovered until the development of simple microscopes. The discovery of cells in 1665 is credited to Robert Hooke who reported observing honeycomb like structures in cork using a handmade microscope [67]. Around the same time (1675), Antonie van Leeuwenhoek had observed bacteria in water using his microscope and called them *animalcules* [2, 67]. Leeuwenhoek's claims were met with much scepticism until Hooke verified them. In the light of these discoveries and many more studies and observations of cells from different organisms, the cell theory was proposed in 1838 - 39 by Matthias Schleiden and Theodor Schwann, i.e., 1) All organisms are made of cells, and 2) The cell is the structural unit of life. Following several independent experiments to disprove spontaneous generation (continuity between living and non-living things), Rudolf Virchow added a third tenet to the cell theory, that new cells can only be produced from pre-existing cells [2, 67].
Indeed, due to the complexity of mammalian cells, most of the progress in cell biology was, and is, driven by research on either plant or lower animal (yeast or bacteria) cells. However, the knowledge acquired by studying simpler systems is also applicable to the more complex systems. With improvements in the techniques of microscopy, and the development of dyes, sub-cellular organelles such as nucleus, endoplasmic reticulum (ER), golgi apparatus and mitochondria were discovered in the late nineteenth century [2]. These organelles differ from each other functionally and morphologically [68], and play specific roles in maintaining the cellular biochemistry to enable the cell to perform various processes like respiration, reproduction, absorption of nutrients and apoptosis, which are fundamentally essential to life. Some of the major subcellular mammalian organelles and their functions are described in the following discussion [69, 70].

2.1.1 Intracellular organelles

One important cell constituent is the cytoskeleton. Comprising three types of fibres - actin filaments, intermediate filaments, and microtubules, the cytoskeleton main-

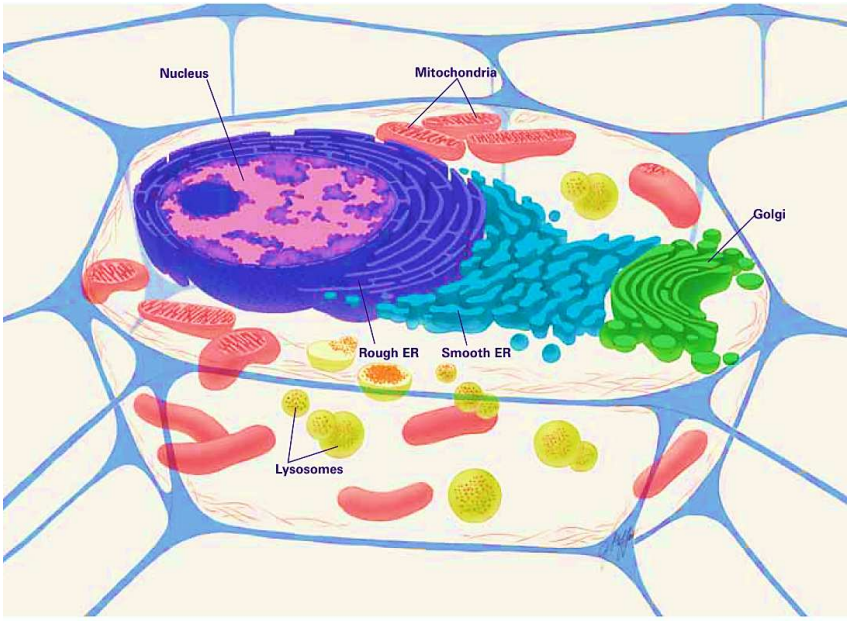

Figure 2.1: Schematic representation of a mammalian cell transverse section showing the various intracellular organelles. Reprinted from page 6 in NIH publication [70].

tains the shape, size and facilitates the movement of the intracellular organelles and the cell as a whole (actin filaments). The microtubules are strong fibres which orchestrate the chromosome segregation during mitosis while the properties of the intermediate filaments vary depending on their location making these filaments suitable markers for the origins of metastatic cancer tumours [70].
A cell can broadly be classified to comprise two parts, 1) the genetic material or the DNA enclosed within an organelle called the nucleus, and 2) the cytoplasm in which a host of intracellular organelles specialized for performing specific functions are interspersed, as shown in Fig. 2.1.

The nucleus (1 in each cell) is the most prominent and conspicuous sub-cellular organelle and contains the cell's genetic material (DNA) and RNA (within nucleoli) enclosed within a double membrane. The region contoured by the inner membrane is called the nucleus. The outer membrane of the nucleus is continuous with the lumen of the endoplasmic reticulum (ER, 1 in each cell) to enable the transport of ribosomal RNA produced in the nucleoli to the ribosomes on the ER. The labyrinth structure of the ER (outwards from the lumen) comprises two parts, i.e., 1) the rough ER (RER, dotted with ribosomes which produce proteins from rRNA) which transitions into 2) the smooth ER (SER). The ribosomes on RER are the sites of protein synthesis while SER is the site of lipid synthesis.
The proteins produced in RER are transported in small vesicles which bud off from the parts of RER devoid of ribosomes and fuse with the golgi apparatus (1 in each cell) [71]. The golgi apparatus consists of several sacs of enclosed membranes, which further package the proteins received from RER into vesicles, set to be transported to their intracellular or extracellular destinations.
Lysosomes (many in each cell) are enzyme filled sacs which degrade/digest the obsolete intracellular materials and convert them to proteins to be recycled and/or waste to be degraded. Peroxisomes (many in each cell) contain enzymes to break down

fatty acids and toxic materials into water and oxygen, which are used in biosynthesis.
To perform all these functions, the cellular reactions are driven by ATP (adenosine triphosphate) to ADP (adenosine diphosphate) conversions. In the first step of cellular respiration which occurs in the cytoplasm, ATP is anaerobically used to convert glucose to pyruvate and ADP. In the mitochondria (double membraned, many in each cell) pyruvate, glucose and fatty acids are oxidised. The inner membrane of a mitochondrion possesses many folds called cristae, which increase the membrane surface available for the production of ATP from ADP.
The organelles play specific and significant roles in various cell functions as already mentioned. One particularly interesting process undergone by the cells is that of cell division which is the basis of growth, repair, development and most of all, our very existence as multicellular organisms. The details of the cell cycle are given in the next section.

2.2 The Cell Cycle

Cells undergo division to supplement the growth and repair of injured tissues. The process of cellular reproduction includes duplication of the genetic content and its subsequent distribution to two daughter cells. This sequence of duplication and copying of the genetic content of the cell from one generation to the next is known as the cell cycle and can be subdivided into four phases as shown in Fig. 2.2. A diploid cell with genetic content represented by 2x (representing two identical sets of chromosomes) responds to cell division promoting stimuli while it is in the first gap G_1 stage and passes into the synthesis (S) stage of the cell cycle during which the genetic material of the cell is duplicated. At the end of the S phase, the genetic content of the cell has doubled to 4x and the cell enters the second gap stage, called G_2 in which protein and microtubule production takes place. Additionally in this phase, duplication of the genetic content is verified. In somatic cells, G_2 is followed by the mitotic (M) phase of the cell cycle at the end of which two daughter cells are produced, each containing one copy of the 2x genetic material. The daughter cells can then undergo their own cell cycles [73, 74].

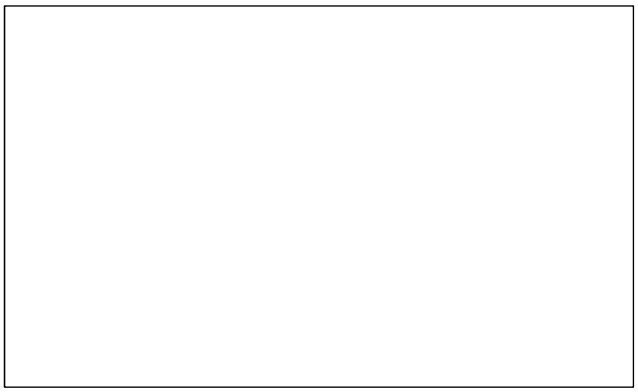

Figure 2.2: Schematic illustration of the cell cycle. Stage G_0 is not shown. Copyright (2008) from Molecular Biology of the Cell by (Bruce Alberts et al. This figure (appearing as Figure 17.4 in reference [72]) has been redacted for copyright reasons.

The phases that the cell passes through from its creation till the onset of the M

phase are collectively known as interphase. In the absence of mitotic signals, a cell may enter and stay arrested in the G_0 phase, or may differentiate or undergo apopstosis. A G_0 cell may re-enter the G_1 phase when stimulated to undergo growth and subsequently divide [74]. The M-phase comprises a set of sub-stages, at the end of which two genetically identical daughter cells are produced.

2.2.1 The M-Phase

During interphase, in response to mitotic signals, the cells duplicate their genetic content along with some organelles and macromolecules in preparation of the mitotic stage of the cycle during which the cell components are distributed to two daughter cells. This process occurs in a set of substages which are summarized in Fig. 2.3 and described as follows [72, 75, 76].
The first step in mitosis is prophase which is marked by the condensation of the genetic material into chromosomes, which are rod-like in appearance. It is known that the condensation (supercoiling) of DNA into chromosomes is attributed to histone proteins which are the cores around which the DNA is wrapped [77]. Additionally, another class of proteins, the non-histones form the scaffolds required to maintain the chromosome structure [78, 79]. Typically, in chromosomes, DNA and histones exist in a 1:1 mass ratio. However, the non-histone content varies from 1-2 times that of DNA by mass [80]. This means, that for a typical cell, the protein content in chromosomes is 2-3 times that of DNA.
In prophase, the nuclear membrane begins disintegrating and the centrosomes duplicated during the S phase of interphase begin migrating towards the opposite poles of the cell.
In prometaphase, the breakdown of the nuclear membrane is completed and the centrosomes align at the opposite poles of the cell. The spindle fibres emanate from the centrosomes. The spindle apparatus plays an important role in cell division by facilitating the movement of the chromosomes and other organelles around the cell to ensure equal distribution of the genetic and non-genetic materials to the daughter cells.
Metaphase is characterized by the sister chromatids' (two copies of each chromosome duplicated during the S phase) alignment on the equatorial plane of the cell. Specifically, each member of the sister chromosome pair, or dyad, is joined at the centromere. The spindle fibres grow in the cell volume, and attach to the sister chro-

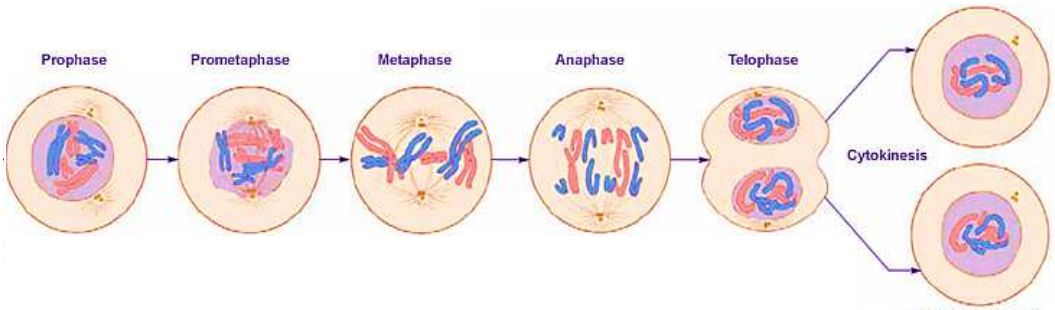

Figure 2.3: Schematic illustration of the substages of mitosis. Reprinted from pages 50 - 51 in NIH publication [75].

matids at their kinetochores, with the dyads oriented towards the opposite poles of the cell.
In the next stage of mitosis, called anaphase, the sister chromatids are pulled towards the opposite poles of the cell. Once at the poles, in telophase, the chromatids decondense into chromatin. Reconstitution of the nuclear envelope around the two sets of chromatin at the poles of the cell occurs and a furrow perpendicular to the equatorial plane of the cell at the outer edge of the cell membrane begins forming. Additionally, the mitotic spindle starts disassembling.
The final substage of mitosis is called cytokinesis in which the division of cytoplasm and consequently, the cytoplasmic organelles (discussed in the following section) takes place. At the end of cytokinesis, two genetically identical daughter cells are formed, which proceed on their own cell cycles.

2.2.2 Inheritance of organelles in somatic cell division

In the process of cell division, not only is the genetic material duplicated and transferred to the daughter cells, but also, organelles and other macromolecules like proteins are duplicated and inherited by the daughter cells. In the absence of this duplication, the cells would get smaller with each cycle [72]. Indeed, volume changes during the M-Phase have been reported [3], with the cells being at their smallest volume in metaphase and increasing their volume after cytokinesis to be the same as the volume of the mother cell in prophase.
If the distribution of the organelles fails and the daughter cells cannot regenerate the lost organelles, the functioning of the affected cells is impaired and typically leads to cell death. Moreover, some organelles play an important role in the process of cell division, and therefore, their inheritance is necessary for the process of division to complete [81].
The duplication of organelles to the two daughters at the end of mitosis is particularly important for organelles like mitochondria which contain genetic material, which once lost cannot be regenerated by the cell. Some organelles which do not contain their own genome, for example, the endoplasmic reticulum and the golgi apparatus [81, 82] can not be regenerated by the cell if lost. Two schemes of inheritance of genetic and non-genetic intracellular organelles were proposed by Warren and Wickner [83], i.e., regulated and stochastic. The organelles which play an important role in cell division and/or are present only in small numbers in the cell are inherited following a controlled, regulated process. Examples of these organelles include the nucleus containing genetic material and the centrioles, which organize the spindle apparatus critical for the process of mitosis. Other organelles, which are not essential to the process of cell division but play other roles in cellular life processes, are stochastically distributed to the two daughter cells as vesicles which regenerate the organelles at the end of mitosis. The golgi apparatus, lysosomes and the ER follow this scheme of division [82].

2.2.3 Cell cycle check points

The progression of the cell along the cell cycle is monitored and controlled by biochemical factors which respond to various intra and extracellular signals at three specific cell cycle checkpoints as described below [72].
The first checkpoint is called the restriction point which occurs in late G_1 to control the cell's (which is originally in early G_1 or G_0) entry into the S phase and the con-

sequent chromosome duplication in the S phase. At this checkpoint, the cell checks for DNA damage and in case of no damage, duplicates the genetic material even on removal of mitotic signals. The second checkpoint, called the G_2/M checkpoint occurs before the cell commits to mitosis. The purpose of this checkpoint is to prevent the progression of the cell into the M phase if genetic material is not duplicated in its entirety or there are chromosomal defects. The third and last checkpoint is called the metaphase/anaphase transition checkpoint which exists to ensure that the chromosomes (which now appear as sister chromatids connected at the centromere) are attached to a well formed spindle apparatus, and aligned on the equatorial plate, ready to be split into two copies, each to migrate towards the opposite poles of the cell. Depending on the degree of damage or failure to satisfy the checkpoints, the cell might be arrested in the phase of damage detection and a repair may be attempted, or the cell cycle is aborted [74].
The cell cycle and the quality checkpoints are moderated by various proteins. The chemical basis of cell cycle control and regulation will be discussed in the next section.

2.2.4 Chemical control of the cell cycle

The events of the cell cycle are catalyzed by a class of proteins, of which the most important ones are called cyclin dependent kinases (CDKs) [72, 84]. Different CDKs are activated at different stages of the cell cycle by their corresponding cyclins, the levels of which increase or decrease in each phase of the cell cycle. CDK-cyclin complexes activate specific protein substrates which guide the cell through each phase of the cell cycle- by either promoting DNA duplication in the S phase or the alignment of chromosomes on the spindle apparatus to promote the metaphase/anaphase transition [74].

2.2.4.1 CDK-cyclin control of the cell cycle

The control of the cell cycle is mediated by CDK-cyclin complexes. The binding of a specific cyclin to the CDK followed by phosphorylation of the CDK by a CDK activating kinase (CAK) activates the CDK [72, 85]. Fig. 2.4 shows the CDK-cyclin combinations which become active during the various stages of the cell cycle. Importantly, CDK 7-cyc H complex is the CAK which is active throughout the duration of the cell cycle. At the various checkpoints described in section 2.2.3, the interruption of the cell cycle (in response to DNA damage or improper alignment of the chromosomes on the mitotic spindle) occurs through deactivation of the CDKs that promote the cell's progression from one phase of the cell cycle to the next. The proteins that mediate the deactivation of the CDKs are called CDK inhibitors or CKIs [74, 85].
Due to their activation at specific stages of the cell cycle, various cyclins and CDKs or CDK-cyclin complexes provide cell biologists a means to probe the cell cycle from a chemical point of view, serving as markers of the cell stage.

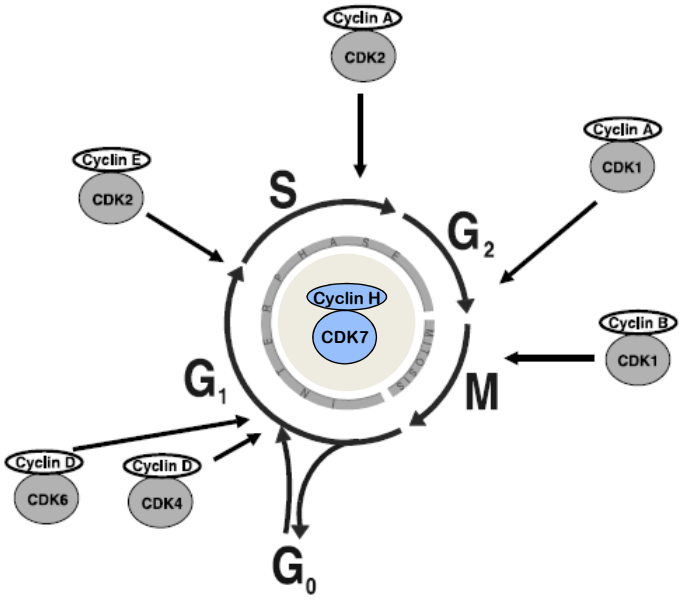

Figure 2.4: CDK-cyclin dependent control of the cell cycle. The figure shows the CDK-cyclin complexes active during various stages of the cell cycle. Modified from Figure 1 in reference [85] with permission from John Wiley & Sons.

2.3 State of the art

This section is split into two parts. In the first part, a general overview of microscopy techniques in current practice to study cells and other biological materials is given. In the second part, the current state of the art of the imaging methods applied specifically to study the cell cycle, the main thrust of this project is described.

2.3.1 Cell imaging: From optical microscopy to label-free techniques

Biologists rely on optical microscopy techniques [4, 86] to further their understanding of the subject, employing contrast generating mechanisms like phase contrast, differential interference contrast (DIC) and fluorescence microscopy to image biological material which is transparent to visible light. Of these methods, phase contrast and DIC microscopy are not chemically specific. Nevertheless, quantitative variants of phase contrast [3, 87, 88, 89] and DIC [90] have been used to study cells and make advances in the field of cytology. However, despite the quantitative aspect of these imaging methods, they are not chemically specific.
In answer to the shortcomings of the techniques mentioned above, fluorescence based microscopies are chemically specific due to the selectivity of the fluorophore binding sites. These methods however, suffer from significant challenges of photobleaching and phototoxicity. A fluorophore in its excited singlet state might cross over to an excited triplet state (inter-system crossing) resulting in the fluorophore permanently losing its ability to fluoresce (see section 1.2.3.1). Phototoxicity is caused by the molecules of the fluorophores in the triplet states undergoing reactions with other molecules and releasing free radicals which could be toxic to the cellular machinery. Alternatively, the fluorophore in its triplet state may undergo non-radiative relaxation by vibrations or phosphoresce i.e., relax to the ground state over a longer

time-scale (milliseconds) as compared to fluorescence (nanoseconds) [91] (see section 1.2.3.1). Additionally, introducing extraneous molecules to study the sample with fluorescent microscopy induces biochemical changes in the sample. Despite these drawbacks, fluorescence based methods, e.g. TPF microscopy [36, 92, 93] and fluorescence life-time imaging microscopy [94] (FLIM) are in wide use to study cellular processes like protein interactions and metabolism [95]. In contrast with fluorescence microscopy in which the fluorescence intensity is proportional to the concentration of the fluorophores, FLIM measurements rely on environment dependent changes in the fluorophore's emission lifetime or the different lifetimes of different fluorophores.
Recently, the technique of light sheet fluorescence microscopy [96] which enables high-speed and high-resolution imaging of fluorescent samples with reduced photodamage has been developed. This is achieved by exciting the sample in thin focal planes to prevent photobleaching and phototoxicity in bulk. While FLIM and light sheet fluorescence microscopy address the aspects of time-resolved chemical specificity and photobleaching respectively, the process of fluorescence staining is itself cumbersome. Some fluorophores like the green fluorescent protein (GFP) and its derivatives are genetically encoded and can be transfected to stably express in cells. Chalfie et. al showed in 1994, that enhanced GFP (eGFP, a variant of GFP, produced by altering the genetic sequence of GFP to improve the reporter protein sensitivity [97]) can be stably expressed in *E coli* possessing an eGFP encoded plasmid [98]. These fluorescent proteins are 'built in' in the organism and therefore, this method nullifies the need for exogenous labels, but requires genetic modification of the organisms. Such expressed fluorophores can be used to study gene expression, protein localization and dynamics in live cells. However, in order to study molecules other than proteins, non-protein organic fluorophores are required [99]. Organic fluorophores are easy to use due to the relative simplicity of the staining procedure compared to the genetic engineering required in the use of fluorescent proteins. Typically, in the process of staining the samples with non-protein organic fluorophores, the samples must be washed and/or treated with quenchers to remove the excess fluorophores to allow background-free visualization of the cell structure. To enable a simpler method of sample preparation for fluorescence microscopy, recently, no-wash fluorescent labels have been developed and used to label proteins [100].
Despite these advances in the various imaging techniques relying on the use of fluorophores, the introduction of extraneous molecules in the sample is undesirable as it might induce changes in the sample chemistry in addition to posing the problems of phototoxicity and photobleaching. Other considerations such as the size of the protein of interest (not useful to stain proteins similar to or smaller than the fluorophore) limit the usability of fluorophores. For example, eGFP (molecular weight $\sim 33\,\mathrm{KDa}$) cannot be used to label insulin (molecular weight $\sim 0.6\,\mathrm{KDa}$). Aside from small proteins, lipid-rich organelles are difficult to stain due to a lack of hydrophobic fluorophores. To avoid the pitfalls associated with fluorescence based imaging methods, label-free techniques outlined in the following discussion have been demonstrated as applied to biological materials. Various Raman microspectroscopy based publications including references [101, 102, 103] (spontaneous Raman imaging of cell cycle), references [7, 37, 104] (SRS) and references [11, 15, 16, 46, 64, 105] (CARS) report the development and application of chemically specific and sensitive imaging methods, to study cells and tissues. Furthermore, second harmonic generation (SHG) has also been used to provide specific information about collagen [106]

and structural proteins [107] in cells. While the use of fluorescence based methods cannot be completely done away with due to the versatility and the vast applications of fluorescent labels, as well as the limitations of CARS, SRS, SHG and other microscopies, specifically in probing proteins and nucleic acids (since it is difficult to differentiate between different types of cellular proteins and nucleic acids with commonly used label-free methods), the advantage of label-free methods becomes more evident when imaging lipids for which hydrophobic fluorescent labels need to be developed.
In this project, fixed mitotic U-2OS cells which are poor in lipid content were imaged with CARS, to push this microscopy technique beyond its well established niche of lipid related studies. The next part of this discussion aims to put our work in context.

2.3.2 Imaging the cell cycle

Optical microscopy techniques such as quantitative phase contrast have been applied to monitor the cell size during mitosis [3] and to study the changes in the optical density of the nucleus as a function of cell cycle stage using quantitative DIC [108]. Despite its associated issues as discussed in the previous section, it is worth mentioning that fluorescence microscopy has also been used to study the cell cycle [109, 110, 111] using high throughput confocal microscopy, and indeed forms the basis of several other application based studies in biology [112]. More directly related to this project, there are several reports on label-free imaging of the cell cycle which will be briefly reviewed in this section.
Matthaus et al. [101, 113] studied the mitotic phase of the cell cycle (live HeLa cells) and showed that the Raman spectra (500 - 1800 cm^{-1}) at individual points in the cytosol and the nuclear region/chromatin are characteristically different in the fingerprint region. Furthermore, they reported the results of infrared microspectroscopy (900 - 1800 cm^{-1}) on the same samples, demonstrating differences between the cytosol and the nuclear content. All of these measurements were taken on commercial microscopes. However, due to the weak Raman signals, the images of the cells shown in these works were acquired at specific frequencies, and the spectra presented were taken at specific spatial regions. Notwithstanding the fact that these data are not hyperspectral, they were the first to demonstrate that label-free Raman imaging of cells is useful for differentiating the chemical composition of the cytosol and chromatin. Swain et al. reported in reference [102] that the composition of live human osteosarcoma cells (MG63) changes from a relatively high lipid content in G_0/G_1 to a relatively high protein/nucleic acid content in G_2/M phase of the cell cycle, using Raman microspectroscopy to acquire and average the spectra (600 - 1800 cm^{-1}) at several lateral positions at the middle axial plane of the cell. Klein et al. [103] demonstrated that confocal Raman microscopy of live cells (acquiring Raman spectra over a single focal plane) correlates well with immunofluorescence staining of various sub-cellular compartments, i.e., the golgi bodies, actin filaments and the cell nucleus. The Raman microspectroscopy images (spectral range $\sim$80 - 3040 cm^{-1}) at a single axial plane shown in this work required 45-60 minutes for acquisition. While all these pieces of work present new results and breakthroughs in the field of label-free imaging, it should be noted that none of them provide full hyperspectral information about the cells due to the long acquisition times required for such measurements, which are not compatible with biological material imaging. To counter the low signal strengths and the associated long integration times partic-

ular to spontaneous Raman experiments, SRS has been employed to study cells and tissues with results that differentiate between the cytosol and the nucleus [114], and different types of lipids [104]. Furthermore, in one study [7], the authors determined the cell cycle phase of cells relying on the morpho-chemical contrast generated by SRS to ascertain the presence of the nucleus/nucleolus in the early stages of the cell cycle and the condensation of the nuclear material in mitosis. However, the implementation complexity of SRS is evident and requires the use of three lasers as well as other equipments/optics to isolate the SRS signal from the frequency degenerate pump and Stokes fields, as already discussed in section 1.3.2.2. Moreover, the most important merit of SRS over CARS, i.e., background-free detection is not necessarily an advantage because the non-resonant background amplifies the total signal, enabling the detection of weakly resonant materials in the sample [15]. Furthermore, several authors have already shown applications of CARS microscopy to live cell imaging in various publications as referenced in the previous discussion. Of these, Parekh et al. [15] in 2010, demonstrated differences between the spectra at points within the cytoplasmic and nuclear regions using broadband CARS (500 - 3200 cm^{-1}). Another paper also published in 2010 by Pliss et al. [16] reported the use of CARS microspectroscopy in the fingerprint region (500 - 1800 cm^{-1}) to study mitotic cells and make conclusions about the transport of macromolecules by the nucleus. They also showed results with no correlation between chromosome compaction/ DNA condensation and local concentration of proteins, in contrast with the known role of proteins in chromosome compaction. As will be demonstrated in chapter 4, our calculations made using a robust volumetric quantification process (also explained in chapter 4) suggest a clear correlation between the cells' mitotic stage and the concentration of intranuclear proteins.
In this project, we will aim to affirm the suitability of CARS to differentiate between subcellular compartments in the CH-stretch range using the FSC^3 algorithm (next chapter) to factorize hyperspectral CARS data in full 3D into various components (see section 3.3), and correlate the components to specific subcellular compartments using TPF imaging. Furthermore, we will quantitatively ascertain the masses of the various components and apply this method of imaging and analysis to study cell populations treated with two types of anti-cancer drugs in clinical concentrations, with two distinct modes of action. These results are presented in chapter 4.

Chapter 3

Set-up and Analysis

3.1 Multimodal CARS microscopy set-up

The theory of coherent Raman scattering has been discussed in the first chapter. CARS microscopy, a subclass of coherent Raman scattering is best performed using picosecond pulses which are ideal for performing CARS but not well suited for SHG and TPF imaging, which are optimized for 10-100 fs excitation. Our multimodal set-up with CARS, SHG and TPF functionality employs a 5 fs broadband (660-970 nm) Ti:Sa laser (Venteon, Pulse:One, PE) with 80 MHz repetition rate. The laser output is split into appropriate components to provide three excitation beams i.e., TPF/SHG (>900 nm), pump (<730 nm,) and Stokes (730-900 nm). Using a single laser is an economic and ergonomic advantage over a typical two laser system employed to perform two beam experiments. The narrow pump (65 nm bandwidth at 10% maximum intensity) and the broad Stokes (200 nm at 10% maximum intensity) beams are centered at 682 nm and 806 nm respectively. CARS excitation is implemented by the interference of the pump and Stokes beams, using spectral focussing with glass dispersion [115, 116]. This technique is specifically employed in our set-up to access a wide spectral range without the need for tuning the lasers. An introduction to spectral focussing is given below, along with the specifics as used in our set-up.

3.1.1 Spectral focussing

The refractive index of a medium depends on the wavelength, λ of the light propagating through it. Therefore, different wavelengths are slowed down to different extents while traversing the medium. The time τ taken by the light pulse to travel a length L in a medium of refractive index $n(\lambda)$ is given by [117]

$$\tau = -\frac{L}{c}\left(\lambda\frac{dn}{d\lambda}\right) \tag{3.1}$$

where c is the speed of light. This relation is derived using the group velocity (velocity of the envelope) of the pulse given by $\Delta\omega/\Delta k$. This is in contrast to the phase velocity which is given by ω/k. From equation 3.2, and considering a medium with normal dispersion, i.e., $dn/d\lambda < 0$, we observe that the longer wavelength pulses are travelling faster. This means that a pulse travelling through a medium

will be elongated due to dispersion and the broadening is given by $\Delta\tau$

$$\Delta\tau = -\frac{L\Delta\lambda}{\lambda c}\left(\lambda^2\frac{d^2n}{d\lambda^2}\right) \tag{3.2}$$

We consider a Gaussian electric field $\mathbf{E}(t) = \mathcal{E}_0\exp(-t^2/\tau_{\mathrm{G}_0}^2 + i\omega_0 t)$. The pulse duration (FWHM intensity) is $\tau_0 = \tau_{\mathrm{G}_0}\sqrt{2\ln 2}$. The field of the pulse after propagation through the medium is given by [116, 118]

$$\mathbf{E}(t) = \mathcal{E}_0\left(-(t/\tau_G)^2 + it(\omega_0 + \beta t)\right) \quad \text{where,} \tag{3.3}$$

$$\beta = \frac{2k''L}{\tau_{\mathrm{G}_0}^2\tau_{\mathrm{G}}^2} \quad \text{and} \tag{3.4}$$

$$k'' = \frac{\lambda^3}{2\pi c^2}\frac{d^2n}{d\lambda^2} \tag{3.5}$$

where β is the chirp parameter and k'' is the group velocity dispersion. τ_{G} (τ_{G_0}) is the width of the pulse after (before) dispersion and ω_0 is the central frequency of the Gaussian pulse. The pulse width after dispersion is given by

$$\tau_G = \tau_{\mathrm{G}_0}\sqrt{1 + \left(\frac{2k''L}{\tau_{\mathrm{G}_0}^2}\right)^2} \tag{3.6}$$

The molecular vibration at the beat frequency of the pump and Stokes beams is therefore elongated to $\tau_{\mathrm{G}} \sim$ few ps.
From equation 3.3, we observe that the instantaneous frequency is given by $\omega(t) = \omega_0 + 2\beta t$. As shown in Fig. 3.1, a pulse with temporal-spectral profile as shown in (A) is elongated in time, keeping the spectral range constant after passing through a dispersive medium (B). By applying an equal linear chirp to both the pump and Stokes pulses, we introduce an equal instantaneous frequency difference (IFD) between them, as shown in (C). The temporal delay between the two pulses can be tuned to access different IFDs, as depicted in (D). This method enables tunable excitation in the picosecond regime, suitable for resolving vibrational resonances. Detailed specifications of the set-up (schematic shown in Fig. 3.2) can be found elsewhere [119]. A brief description of the set-up modalities used in this project follows.

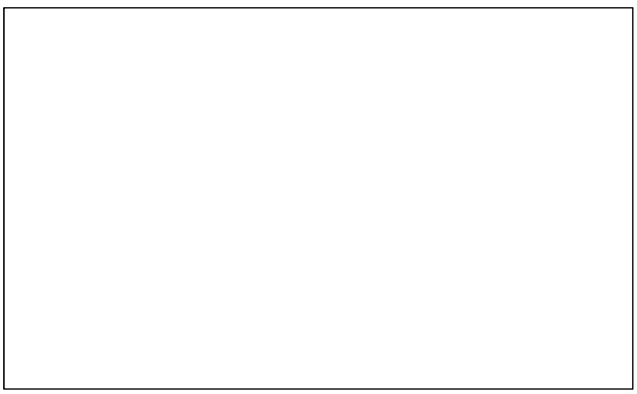

Figure 3.1: Representative diagram showing pulse broadening using spectral focussing. The pump and Stokes pulses are chirped to introduce a constant instantaneous frequency difference between them. This figure (appearing as Figure 14.4 b, c, d in reference [118]) has been redacted for copyright reasons.

3.1.2 The set-up

Referring to Fig. 3.2, a short-pass dichroic mirror DM1a (Eksma Optics) reflects the components of the laser spectrum >900 nm to be used for SHG/TPF excitation, while transmitting the rest of the wavelengths for use in CARS excitation. We use a long-pass dichroic mirror, DM2 (CVI Melles Griot) to further split the laser component designated for CARS excitation into pump (centered at 680 nm) and Stokes (centered at 804 nm) wavelengths. In our single femtosecond laser set-up, the pump and Stokes pulses are linearly chirped (the extent of the chirp is controlled by varying the length of SF57 glass blocks) equally to elongate the pulses to the picosecond range (the pump duration is $\sim$1.5 ps) and to introduce a constant IFD between the two pulses and allows a spectral range of 1200 - 3800 cm^{-1} to be scanned by varying the time delay between the pump and Stokes beams, eliminating the need for tuning the laser for scanning across the spectrum [115, 116]. This technique is called spectral focussing and has been discussed in the previous section. When switching to the fingerprint region of the spectrum (1200 - 2400 cm^{-1}), we also need to change the glass thickness to maintain a constant chirp between the two spectral ranges. The TPF/SHG beam is compressed to $\sim$30 fs at the sample using a prism compressor and then, the beams (TPF/SHG, pump and Stokes) are recombined by DM1a before impinging on the sample. The microscope in the set-up (Nikon Ti-U inverted) is equipped with various objectives and condensers as well as optics/filters to perform various standard optical microscopies i.e., DIC, bright-field, dark-field

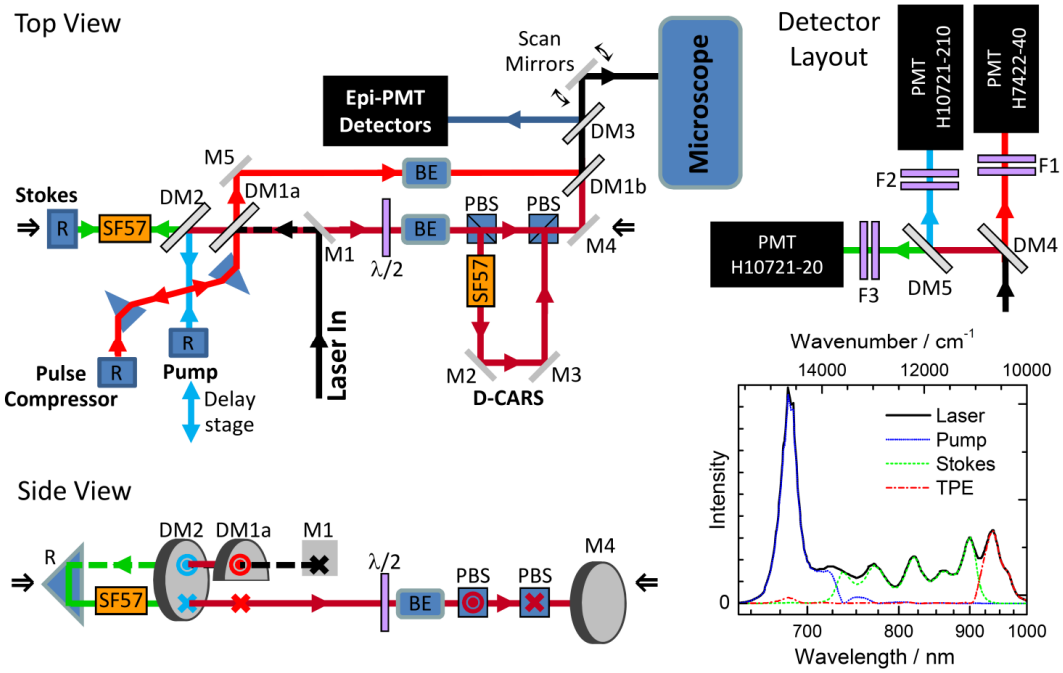

Figure 3.2: Schematic of our multi-modal CARS microscope. The positions of reflectors (R), dichroic mirrors (DM), mirrors (M), beam expanders (BE) and glass blocks (SF57) are shown. Polarizing beam splitters (PBS) and a half-wave plate ($\lambda/2$) were used to implement D-CARS, which was not used in this work. In the detection scheme, photomultiplier tubes (PMT) and filters (F) were used along with dichroic mirrors to detect CARS, SHG and TPF signals in both the forward and the epi directions. Reprinted from [119]) with permission from OSA.

and epi-fluorescence (lamp: Prior Lumen 200). For performing epi-fluorescence imaging, the microscope is equipped with various filter cubes (containing dichroic, emitter and exciter components) suitable for imaging various fluorescent dyes as follows.

1.) Semrock GFP-A-Basic-NTE: suitable for imaging of fluorescent dyes emitting green wavelengths, eg. eGFP. This filter cube comprises an exciter (FF01-469/35-25), an emitter (FF01-525/39-25) and a dichroic (FF497-Di01-25×36).

2.) Semrock Custom Blue 40-LP-A-NTE: suitable for imaging of fluorescent dyes emitting blue wavelengths, eg. DAPI. This filter cube comprises an exciter (FF01-370/36-25), an emitter (FF02-447/60-25) and a dichroic (FF409-Di03-25×36).

3.) Semrock mCherry: suitable for imaging of fluorescent dyes emitting red wavelengths, eg. mitotracker orange. This filter cube comprises an exciter (FF01-562/40-25), an emitter (FF01-593/LP-25) and a dichroic (FF593-Di03-25×36).

Standard optical microscopy images are recorded by a monochrome CCD camera (Hamamatsu Orca) with a pixel size of $6.45 \times 6.45\,\mu$m.
In the forward direction, the signal from the sample is collected by the condenser. This is then split into its CARS, SHG and TPF components using long-pass dichroic mirrors (DM4 : Semrock FF520-Di02; to transmit the CARS signal (>540 nm) and DM5 : Chroma t4951p; to transmit the TPF (>510 nm) and reflect the SHG (<470 nm) components of the signal). After filtering out the excitation beams using the Semrock filters placed at the positions (see Fig. 3.2) F1 (CARS), F2 (SHG), F3 (TPF) in the forward direction, the signals are projected onto PMTs to discriminate the CARS (Hamamatsu H7422-40), SHG (Hamamatsu H107210-210) and TPF (Hamamatsu H10770A-40) parts of the signal. The filter specifications are as follows.

1.) F1: Two FF01-562/40 filters with transmission range 542 - 582 nm (corresponding to the CARS signal in the CH stretch range), and two FF01-609/57 filters with transmission range 582 - 630 nm (corresponding to the CARS signal in the fingerprint region).

2.) F2: Two FF01-469/35 filters with transmission range 449 - 488 nm to discriminate the SHG signal.

3.) F3: To discriminate forward and epi TPF signal, two FF01-510/84 filters with transmission range 496 - 544 nm.

The epi-signal is collected by the objective, transmitted along the excitation pathway and deflected by DM3 (Semrock FF660 Di02) towards an assembly of filters and PMTs similar to that in the forward scheme of detection, with the exception that for epi-CARS detection in the fingerprint region, we use one FF01-609/57 and one FF01-609/54 filter giving a transmission range of 582 - 637 nm.

3.2 Data collection and reconstruction

To acquire the data, the laser beam is raster scanned across the sample's xy dimensions while the z scan is enabled by a stepper motor (Prior ProScan III) controlling

the motion of the focus of the objective. A separate motorized stage can be used to move the sample in xy dimensions, but for data acquisition, it is preferable to scan the laser beam in xy and move the objective in z, keeping the sample undisturbed. The overall control of the set-up is accomplished through MultiCARS, an in-house software developed by Prof. W. Langbein et al. (Cardiff University, School of Physics and Astronomy) to enable the acquisition and reconstruction of CARS data. The data is collected and stored as a scan output repetition (sor) comprising time traces of position and signal.
To transform the sor data into easily analyzable data, we convert the time-dependent data into a regular grid, resulting in an up to 4D data cube with characteristic voxel properties. A set of these voxels constitutes a regularized data set with a nominal IFD axis (determined by the acquisition settings i.e., the chirp and the time delay between the pump and Stokes beams). To calibrate the delay offset, the known Raman spectrum of polystyrene (PS) at $3050\,\mathrm{cm}^{-1}$ is compared with the Raman like spectrum retrieved from a CARS measurement on a bulk polystyrene sample. The PS spectrum is measured on each day of measurement of CARS data. The calibrated data are exported into ASCII files which are processed further to retrieve the Raman like spectra of the samples, their concentrations and spatial distributions.

3.3 Data analysis

CARS intensity data is analyzed using the hyperspectral image analysis (HIA) software developed by Dr. F. Masia and Prof. W. Langbein (Cardiff University, School of Physics and Astronomy)[49, 120, 121]. A brief discussion of the analysis methodology is given in this section.
The CARS response is measured as CARS intensity, I_{C}, the interference between the resonant and non-resonant components as described in the previous chapter. For background reference, we acquire CARS data with zero pump-Stokes overlap (hereon referred to as zero pulse overlap). The first step in HIA is the denoising (based on singular value decomposition, SVD) performed on background subtracted $\sqrt{I_{\mathrm{C}}}$ which contains value independent noise. In this part of the analysis, unsupervised denoising is performed by decomposing the data matrix D given by $\sqrt{I_{\mathrm{C}}}$ into a spectral basis as $D = U\,\Sigma\,V^{\mathrm{T}}$ where U is the new spectral basis ($s \times s$ unitary matrix), Σ is the importance matrix ($s \times s$ diagonal matrix) containing the singular values of each element of U, and V^{T} (conjugate transpose of V) is a $s \times p$ unitary matrix representing the data in the new spectral basis. The extent of the

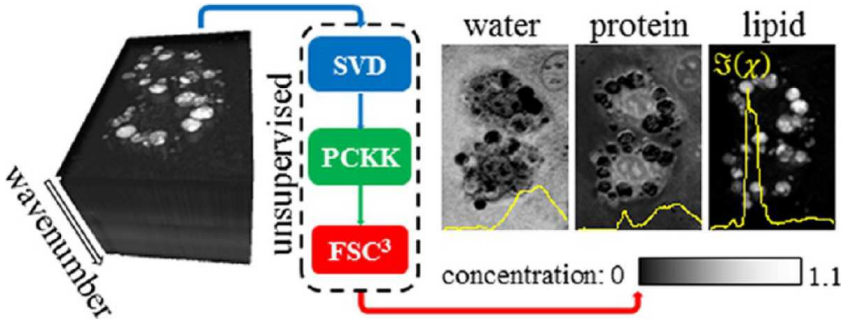

Figure 3.3: Schematic of the analysis of hyperspectral CARS data as performed in HIA. Reprinted from [49] with permission from ACS Publications.

noise-filtering is defined by the maximum index (referred to as the number of SVD components) of the Σ components which are retained, with the retention of smaller indices (fewer SVD components) corresponding to greater noise filtering. The default value for the number of Σ components is determined by fitting the second half of Σ linearly (since the singular values of Gaussian noise are linearly dependent on index in the large index regime). Components of the importance matrix $\sqrt{2}$ above this linear fit are designated as dominated by signal and are retained. The other components with index larger than the chosen number of SVD components are set to zero in Σ_{nf} (see Fig. 3.4). The noise-filtered data is expressed as $D_{\mathrm{nf}} = U\,\Sigma_{\mathrm{nf}}\,V^{\mathrm{T}}$. In the analysis included in this thesis, the index of the singular values (components of Σ) was set to 5 for the analysis of polymers, and 10 for the cells and organoids, therefore designating the first 5 or 10 singular values as signal dominated in the two cases respectively.

$\bar{I}_{\mathrm{C}}$, the ratio of the denoised background corrected intensity to the non-resonant CARS intensity (to account for the system response) is used to determine the complex susceptibility, χ in the frequency domain. We recall that $\bar{I}_{\mathrm{C}} = |\chi/\chi_{\mathrm{ref}}|^2 = |\bar{\chi}|^2$. In the next step, called phase corrected Kramer's Kronig (PCKK- a method of phase retrieval) the analysis retrieves the real and imaginary parts of $\bar{\chi}$ in the following way.

Since $\ln\sqrt{\bar{I}_{\mathrm{C}}} = \Re(\ln(\bar{\chi}))$ and the susceptibility is a complex quantity expressed as $\bar{\chi} = |\bar{\chi}|e^{i\phi}$, we infer that $\Im(\ln\,\bar{\chi}) = \phi$. In PCKK, we retrieve the phase ϕ by applying causality (through the use of a Heaviside function, $\theta(t)$) which leads to the KK relations, on the Fourier transform (denoted by $\mathcal{F}$) of $\ln(\bar{I}_{\mathrm{C}})$ i.e.,

$$\phi = \Im(\mathcal{F}(\theta(t)\mathcal{F}^{-1}(\ln\bar{I}_{\mathrm{C}})))$$

In addition to the time domain filtering using $\theta(t)$, we also perform phase correction to determine the offset in phase. As a consequence of this formulation, the real and imaginary components of $\bar{\chi}$ are determined as

$$\Re(\bar{\chi}) = \sqrt{\bar{I}_{\mathrm{C}}}\,\cos\,\phi \tag{3.7}$$

$$\Im(\bar{\chi}) = \sqrt{\bar{I}_{\mathrm{C}}}\,\sin\,\phi. \tag{3.8}$$

Having retrieved the imaginary component of the CARS susceptibility, we factorize $\Im(\bar{\chi})$ into a number of independent chemical concentrations, in the FSC^3 (factorization into susceptibilities and concentrations of chemical components) step of HIA. To do this, we perform non-negative matrix factorization (NMF) of $\Im(\bar{\chi})$ with a concentration constraint to account for the fact that the measured sample volume is filled with material, with an option to include $\langle\Re(\bar{\chi})\rangle$ (the spectral average of $\Re(\bar{\chi})$) which is similar to the Kerr non-linearity [47]. NMF is a minimization routine in which the data matrix D is expressed as a function of C ($n \times p$, the concentration matrix) and S ($s \times n$, the spectral matrix) as $D = C \times S^T + E$, where n is the number of components into which the data is factorized. In this factorization, the norm of the error, $E(s \times p$ matrix$) = D - C \times S^{\mathrm{T}}$ is iteratively minimized by rescaling the concentrations and spectra by a factor, α. We consider one FSC^3 iteration to comprise three steps as enumerated below. An FSC^3 analysis comprises many of these iterations. In the first iteration, we start with a random guess for the spectra S and concentrations C.

1. Keeping C fixed, minimize $||E||$ by changing the spectra, to get new spectra, S'.

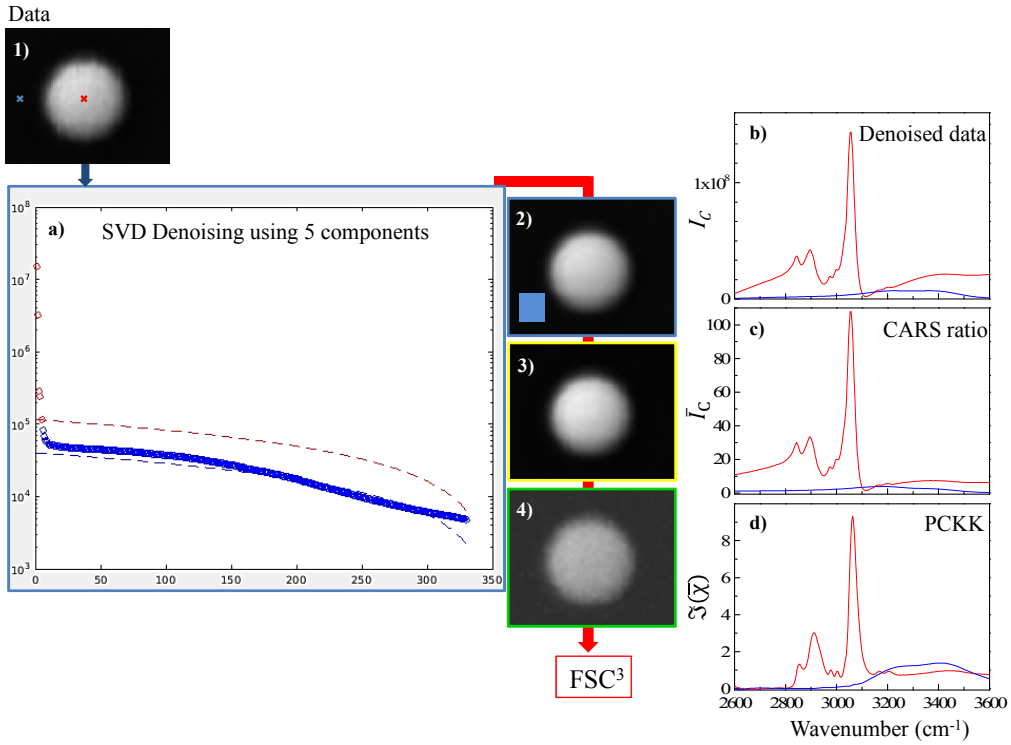

Figure 3.4: Steps of analysis of CARS images using HIA. 1) is the background subtracted data which is denoised to retain the first 5 SVD components. a) is the SVD plot of index k (number of components of Σ) on the x axis and the values Σ_{kk} on the y axis. The blue dashed line shows the linear fit of Σ_{kk} from $k =$ 150 to 330. The red dashed line is a factor of 2.9 larger than the fit shown in blue. This line would be a factor of $\sqrt{2}$ higher than the blue one if k was chosen automatically (which would give $k = 9$) for this analysis. The first 5 indices shown in red were considered noise-free. 2) shows the denoised data. The blue region in 2) defines the region corresponding to water considered in the calculation of CARS ratio, $\bar{I}_C$ shown in 3). The data after phase retrieval is shown in 4). b), c) and d) show the spectra of 2), 3) and 4) respectively at the two points indicated by crosses, colour coded in 1) .

2. Keeping S' fixed, we change the concentrations to minimize $||E||$ and obtain new concentrations, C'.

3. The third step is the concentration constraint in which the factors α_i are calculated by minimizing $||E_{C,j}||$ where, $E_{C,j} = 1 - \Sigma_{i=1}^{n} \alpha_i C_{i,j}$, j is the index of positions and has a maximum value p, and i is the index of the NMF spectra, with a maximum value n. The new concentrations are calculated as $C''_{i,j} = \alpha_i C'_{i,j}$ and the new spectra $S''_i = S'_i/\alpha_i$.

The spectra and concentrations (S'' and C'', respectively) from the first iteration of the analysis are then used as initial values in the next iteration to improve the spectra and concentrations by minimizing the errors. This is repeated for the set number of iterations (user defined) at the end of which, the factorized spectra and concentrations are displayed. For the analysis shown in this work, the number of FSC^3 components, n, is user defined, but can also be automatically determined [121]. Fig. 3.4 shows an example of the steps of this analysis for a 3 μm PS bead imaged using the immersion optics.

3.4 CARS microscopy and HIA characterization using polystyrene (PS) and poly-methyl-methacrylate (PMMA) beads

To demonstrate the applicability of the HIA analysis method to determine absolute volumes of chemical components in hyperspectral CARS imaging, PS and PMMA beads of known sizes were studied [122] using both 0.75 NA (dry optics) and 1.27 NA (immersion optics) microscope objectives (see section A.1). We used two different polymers and two sets of imaging optics in order to characterise the effects of refractive index and imaging optics on the quantitative calculations. The polymer beads dispersed in a 2% agar solution were pipetted into an imaging chamber of 9 mm diameter, created by a 0.12 mm thick imaging spacer (Grace BioLabs) affixed to a microscope slide, and subsequently covered with a #1 coverslip. Hyperspectral 3D CARS data of the beads were acquired in the CH stretch (2400 - 3800 cm^{-1}) region of the spectrum with IFD step size of 3 cm^{-1}. The pixel dwell times unless otherwise specified were 10 μs.
3D data are located in the data DOI and available for viewing.

3.4.1 Effects of refractive index and imaging optics on FSC^3 analysis

In Fig. 3.5 the results of an FSC^3 analysis on the CARS hyperspectral data of a 3 μm PS bead acquired using the immersion optics are shown. The analysis settings are as specified in Table D.2. The two FSC^3 components obtained were identified as water and PS by their spatial distribution and $\Im(\bar{\chi})$ spectra. The spatial distribution of E_C is shown, with brighter regions corresponding to positive concentration error. It is observed that the highest $|E_C|$ appears at the edges and in the wake of the bead. Additionally, laser fluctuations (see *xz* sections of FSC^3 components 2, E_C and E_S) result in randomly distributed spikes in the image. These fluctuations were excluded from the analysis. The concentration error at the edges and in the wake of the bead is a consequence of the changes in the refractive index of the media that the excitation beams encounter at the water to PS interface with refractive index values of 1.33 and 1.59 respectively. The effects of such refractive index steps on CARS intensity spectra and contrast have been investigated and reported in literature [123, 124]. In the following discussion, the influence of refractive index contrast on the PCKK analysis and subsequent FSC^3 factorization, as studied in this project is described. The concentration error shown in Fig. 3.5 is -24% at the bead edge and +10% in the centre of the bead in the *xy* plane of the middle of the bead. Note the inhomogeneous distribution of the concentration error with respect to both its sign and magnitude. At the edges and the wake of the bead, the excitation beams suffer distortion, resulting in a negative concentration error due to reduced intensity at focus and consequently, the CARS signal. On the other hand, the center of the bead shows positive concentration error due to the bead presenting a spherical distribution of high refractive index (as compared to water) and thus acting as a solid immersion lens to focus the excitation beams. A positive concentration error is also seen in front of the bead due to the beams reflected by the bead, with an amplitude of 9%. Qualitatively similar but weaker effects have been reported in measurements of lipid droplets in cells [49, 125]. In Fig. 3.5, the spectral error E_S is shown. E_S remains generally small (few % range) and is maximum at the edge of

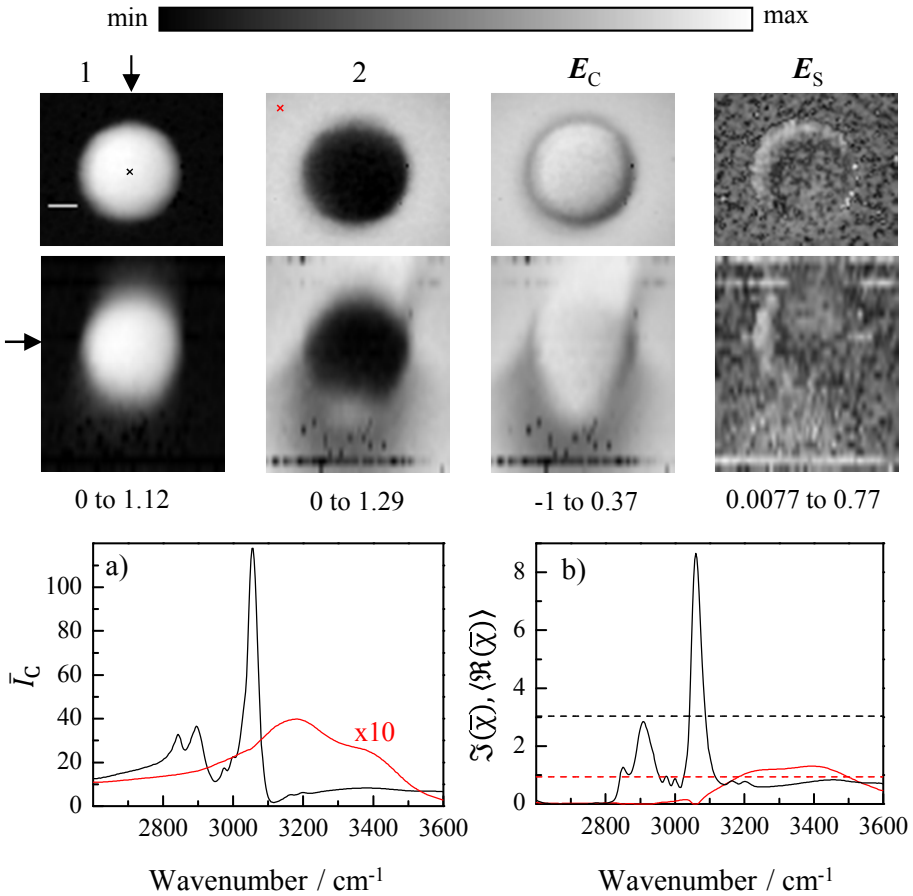

Figure 3.5: Results of a FSC^3 analysis of CARS hyperspectral volumetric images of a 3 μm PS bead taken with about 10 (6) mW pump (Stokes) power at the sample. Top: xy distribution of the concentrations of the FSC^3 components 1 and 2, and the concentration error E_C on a linear grayscale and the spectral error E_S on a logarithmic grayscale. Middle: Corresponding xz sections. The z and y-positions of the xy and xz sections are indicated by an arrow in the xz and xy sections. The grayscales ranges are given below the images. The scale bar is 1 μm. a) CARS ratio $\bar{I}_C$ spectra of water (red) and the PS bead (black) taken at positions indicated by the cross in the top left images. The maximum detected CARS intensity I_C in polystyrene was about 10^8 photoelectrons/s. b) FSC^3 spectra of component 1 (black) and component 2 (red), with $\Im(\bar{\chi})$ and $\langle\Re(\bar{\chi})\rangle$ as solid and dashed lines, respectively. Reprinted from [122] with permission from John Wiley & Sons.

the bead ($\sim$ 10%).

To study the effect of refractive index on FSC^3 and PCKK data, PMMA beads were also investigated, chosen due to their refractive index of 1.49 which is similar to typical lipids (1.43 - 1.49), smaller than that of PS. The results of a FSC^3 analysis of a 2.6 μm PMMA bead are given in Fig. 3.6, and show two components with FSC^3 spectra corresponding to water and PMMA. A significant fraction of water is also observed in the FSC^3 component spectrum corresponding to PMMA due to the small size of the bead. The PSF of concentration is a coherent field PSF with larger width, as opposed to the CARS intensity PSF. Typically, the properties of the intensity PSF are quoted as resolution in the literature. Here we report the PSF of the concentrations. Quantitatively, for the 0.2 μm PS bead shown later the

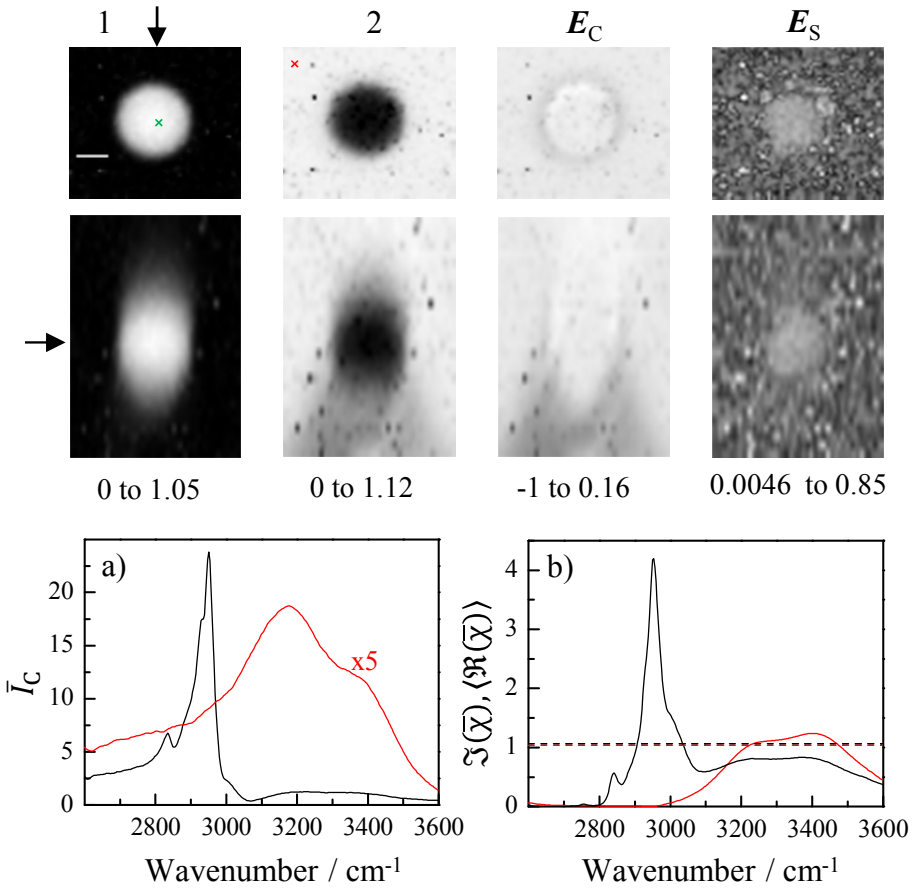

Figure 3.6: Same as Fig. 3.5, but for a 2.6 μm PMMA bead. The maximum CARS intensity in PMMA was about 2×10^7 photoelectrons/s. Grayscales as in Fig. 3.5. Reprinted from [122] with permission from John Wiley & Sons.

FWHM of the concentration distribution is calculated as 0.32 (0.93) μm in the lateral (axial) direction. It is seen that a significant part of the field PSF is in water even when imaging the center of the bead, mostly due to the lower resolution in the axial direction. The concentration error due to refraction is much smaller as compared to PS, approximately -3% at the edge of the bead and +6% at the centre, for the xy plane through the middle of the bead. Note that despite the significant effects of refraction on the concentration error as observed for FSC^3 analysis of CARS data of both the polymers with different refractive indices, the retrieved spectra are correctly calculated as refraction is only weakly dependent on excitation wavelength. The effect of numerical aperture of the imaging optics on FSC^3 analysis of CARS data was also investigated. The data shown earlier were taken with a 1.27 NA objective in excitation with a fill factor 0.98 and 1.4 NA in collection and corresponding opening angle 73° (90°) in excitation (detection). The fill factor, F is defined as

$$F = \frac{w_0}{\mathrm{NA} \times f} \tag{3.9}$$

where w_0 is the width of the Gaussian beam entering the lens, NA and f are the numerical aperture and focal lengths of the lens respectively. Fig. 3.7 shows the results of a FSC^3 analysis of hyperspectral CARS data of a 3 μm PS bead. This data was taken with a fill factor of 0.55 resulting in opening angles of 18° and 33°

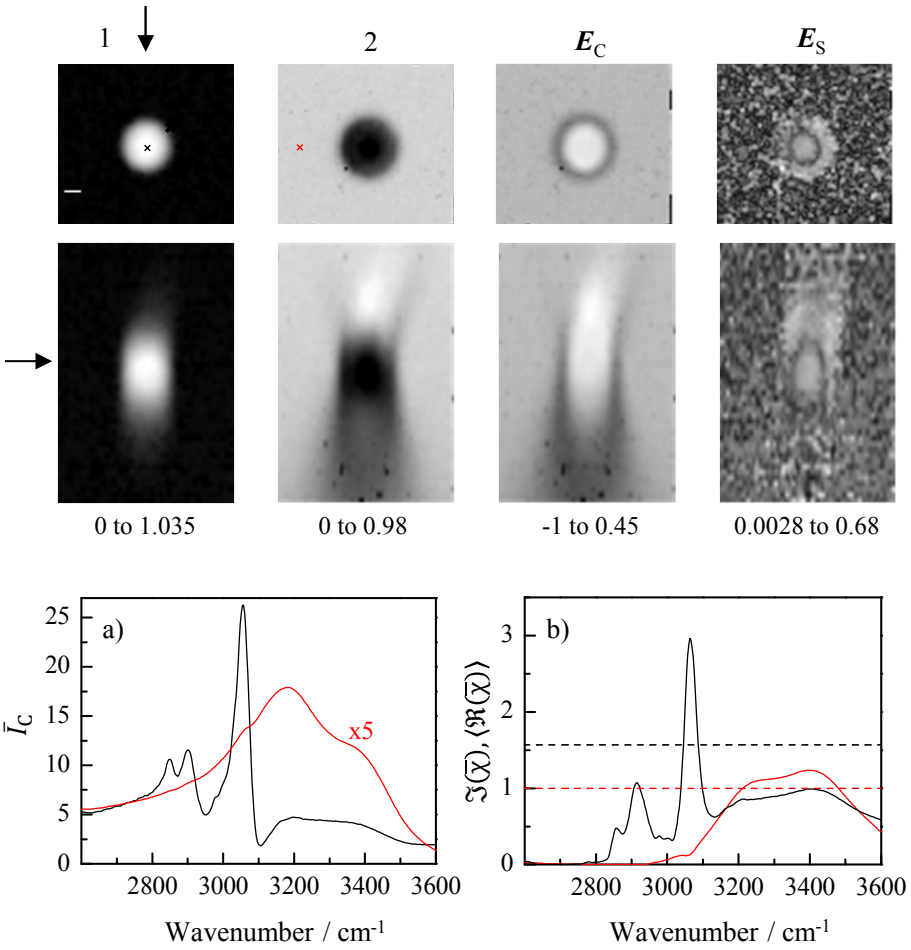

Figure 3.7: Same as Fig. 3.5 but for measurements obtained using a 0.75 NA objective, fill factor 0.55, and a 0.72 NA condenser, using 15 (10) mW pump (Stokes) powers at the sample. The maximum detected CARS intensity in the PS bead was about 5×10^7 photoelectrons/s. Grayscales as in Fig. 3.5. Reprinted from [122] with permission from John Wiley & Sons.

in excitation and detection respectively. The angles θ were calculated using

$$\theta = \arcsin\left(\frac{F \times NA}{n}\right) \tag{3.10}$$

It is expected that the refraction effects in the dry optics should be more relevant since the opening angle is smaller compared to refraction angles. On examining the concentration error, it is observed that while the error is -25% at the bead's edge and qualitatively similar to that of the data acquired using immersion optics in Fig. 3.5; it is significantly larger, +29%, at the centre of the bead. The smaller excitation NA in these optics leads to a larger PSF extension resulting in larger regions corresponding to water getting detected along with the spectra of FSC^3 component corresponding to PS.

3.4.2 Quantitative verification of HIA by volumetric studies on polymer beads

To verify the suitability of FSC^3 analysis of CARS data to quantitative determination of concentrations in volumetric images, CARS images of PS beads of nominal

diameters (3.004 ± 0.065) μm, (1.02 ± 0.01) μm and (0.20 ± 0.01) μm were analyzed. The CARS data for the 0.2 μm bead was acquired using a pixel dwell time of 100 μs. The hyperspectral data of the three beads were then analysed simultaneously using FSC^3 to obtain a common factorization of spectral components. The results are shown in Fig. 3.8.

The volumes of the beads were calculated using the concentration maps corresponding to the PS component obtained by the FSC^3 analysis. A bounding cuboid of volume V was defined, with a lateral extension across $\pm(r + \delta r)$ from the centre of the bead, where r is the nominal radius of the bead and $\delta r = 0.28\,\mu$m is an additional width to accommodate the PSF size. The axial limits of the cuboid were defined by $\pm\,(r + \delta z)$, where $\delta z = 0.9\,\mu$m. To determine the absolute PS, a fraction $\gamma = 0.77$ in the PS component was introduced in the calculation, defined as the ratio of the areas of the FSC^3 component compared to bulk PS [49] in the spectral range 3020 - 3120 cm^{-1}. This factor was introduced in the calculation to account for the PSF at the center of the beads extending into water regions of the image and subsequently resulting in water getting co-detected in the FSC^3 component corresponding to PS. The background concentration C_{w} was calculated to be of the order of a few %, defined as the average of the PS component in the spatial regions corresponding to water. The total volume of the PS bead was then expressed as $V_{\mathrm{PS}} = \gamma \int_V (C_{\mathrm{PS}} - C_{\mathrm{w}}) dV$. To estimate the error of V_{PS}, a 10% relative error and a 1% absolute error of the concentration were considered. Therefore, the error in calculated volumes was estimated to be $\sqrt{(0.1 \times V_{\mathrm{PS}})^2 + (0.01 \times V)^2}$. Fig. 3.8 shows the calculated volumes as a function of the nominal size (diameter) of the beads. It is apparent that the volumes calculated using FSC^3 results are consistent with the nominal volumes, notably so, even for the smallest bead ($r = 0.1\,\mu$m) which is smaller than the spatial resolution. With these results, the accuracy and applicability of hyperspectral CARS imaging and FSC^3 analysis to quantitatively determine the chemical composition of structures in three dimensions is demonstrated.
The effects of imaging NA on the spatial PSF of the concentration in the FSC^3 analysis of the beads analyzed above are shown in Fig. 3.9. Concentration profiles of PS beads using both immersion and dry optics are plotted with fill factors 0.93 and 0.55 as used before. In the case of imaging with immersion optics, the 0.2 μm bead data shows a lateral (axial) FWHM of 0.31 (0.9) μm. In case of dry optics, for the 1 μm bead a lateral (axial) FWHM of 1.0 (3.3) μm was calculated. In the dry optics, the refractive index of water in the sample which the excitation beams traverse in the axial direction is accounted for by multiplying the axial scale with the refractive index of water (1.33) resulting in a FWHM of 4.4 μm. From the theory of optics, it is known that the lateral resolution scales linearly with NA, while the axial resolution scales as NA^2. In the calculations shown, this scaling is not exactly reproduced due to underfilled dry (low) NA optics. Fill factors above 0.7 optimize the resolution of the imaging system [126]. To mathematically describe the effect of fill factor, F on the resolution achieved, we approximate the effective NA as

$$\mathrm{NA}_{\mathrm{eff}} = \left(\left(\frac{w_0}{F \times f} \right)^{-2} + \mathrm{NA}_{\mathrm{o}}^{-2} \right)^{-1/2}$$

where f is the focal length of the objective and NA_{o} is the NA of the objective.
Using this equation which reproduces the dependence of the resolution on effective NA shown in [127], we obtain the effective NA for the 1.27 NA objective as 1.13 and

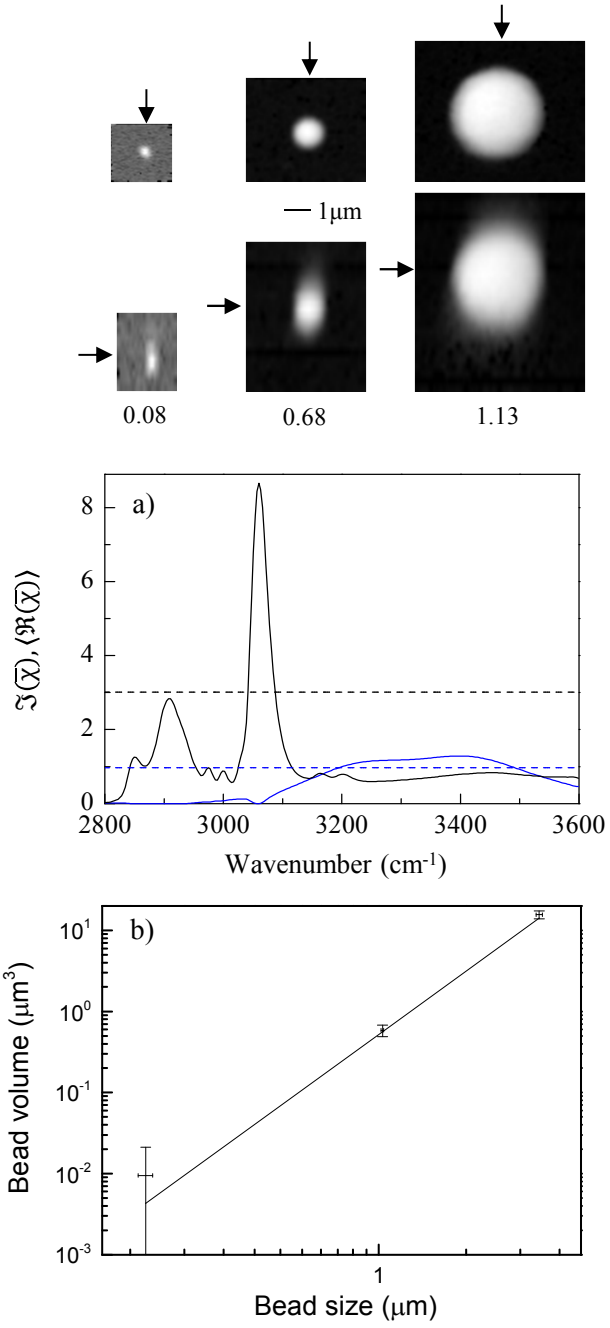

Figure 3.8: Results of the FSC^3 analysis of CARS hyperspectral images of PS beads of various nominal sizes. The top (middle) row shows xy (xz) maps of the concentration of the PS component, at the z (y) positions indicated by the arrows. a) FSC^3 spectra. b) volumes of beads measured from the FSC^3 concentrations (V_{PS}, symbols, error bars see text) and their nominal sizes (solid line), versus nominal bead radius. Grayscales as in Fig. 3.5. Reprinted from [122] with permission from John Wiley & Sons.

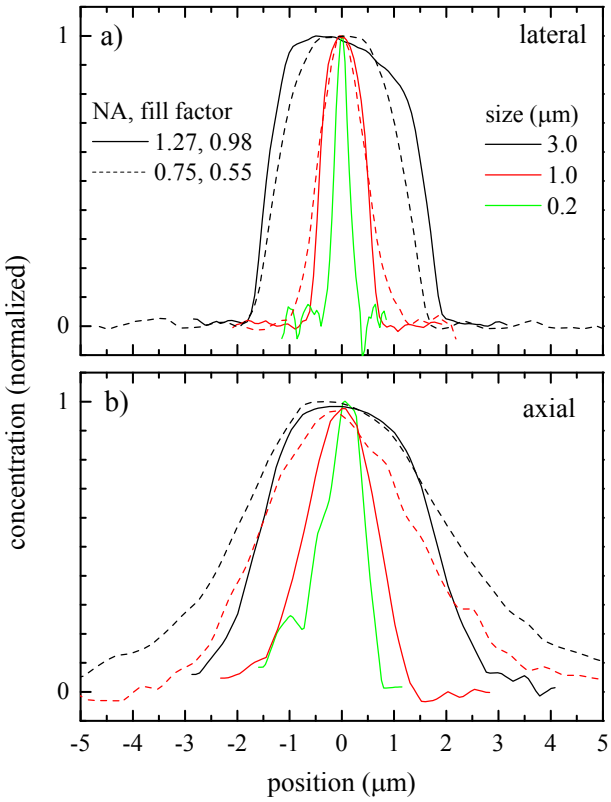

Figure 3.9: Normalized concentration profiles of PS beads in lateral (a) and axial (b) direction. Optics 1.27 NA (solid lines, fill factor 0.98), 0.75 NA (dashed lines, fill factor 0.55). Bead sizes 3 μm (black), 1 μm (red) and 0.2 μm (green). Reprinted from [122] with permission from John Wiley & Sons.

for the 0.75 NA objective as 0.53.

3.4.3 NaCl as a non-resonant material standard

The data of beads shown in the previous section were analysed using cover-slip glass (Schott D263M comprised of 65% fused silica plus other oxides) as non-resonant reference material. This glass shows vibrational resonances at frequencies below 1000 cm^{-1}, which are not relevant for our set-up. However, at lower IFDs, using glass as the non-resonant standard introduces artefacts Ref. [128]. Additionally, glass is an amorphous material with a composition varying between different manufacturers. Therefore, different glass types (even with similar refractive indices) show different vibrational spectra, thus limiting their applicability as universal non-resonant materials for CARS data analysis. This motivates a search for a better non-resonant standard. NaCl with vibrational Raman spectra devoid of resonances above 10 cm^{-1} is a suitable non-resonant material. Although second-order Raman scattering has been observed for NaCl at $< 400\,cm^{-1}$ it is negligible in CARS. Additionally, the band-gap of NaCl (9 eV [129]) is much larger than the excitation photon energy of 1 - 1.7 eV in the CH stretch region, typically used in CARS imaging, resulting in a purely off-resonant electronic background. This results in a third-order susceptibility virtually independent of the photon energies in the biological window. A highly saturated solution of pure NaCl (Sigma Aldrich) was prepared with deionized water as solvent. 15 μL of this solution was drop cast onto a microscope slide

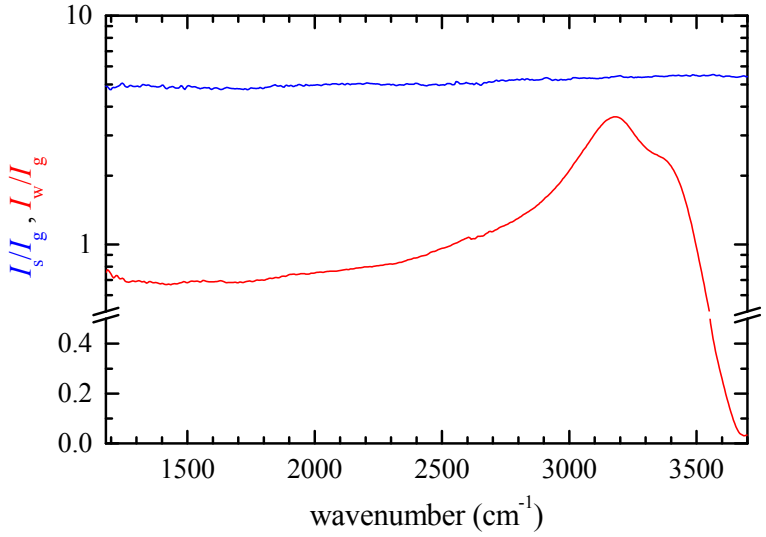

Figure 3.10: CARS intensity ratio spectra between NaCl and glass I_s/I_g (blue) and between water and glass I_w/I_g (red). Reprinted from [122] with permission from John Wiley & Sons.

which was then covered with a #1 coverslip. This was then placed in a fridge, at 4° C and water was allowed to evaporate over a period of 3 weeks. Following this method, formation of NaCl crystals of thickness ~ 10 - $20\,\mu$m was accomplished. CARS data of NaCl crystals were acquired using 0.75 NA optics over a full spectral range of our set-up (1200 - 3800 cm^{-1}).

In Fig. 3.10 the ratio of the CARS intensities measured in a NaCl crystal (I_s) and the glass slide (I_g) is shown, exhibiting a weak frequency dependence in the range 1200 - 3700 cm^{-1} with approximately 10% variation, which is similar to the estimated measurement systematics. The measured value of the salt-glass ratio of about 5 is consistent with theoretical expectations assuming Kerr non-linearity, expressed as $(\chi_s^{(3)}/\chi_g^{(3)})^2$. Since $\chi^{(3)} \propto n_0 n_2$, where n_0 is the linear refractive index and n_2 is the non-linear refractive index [130], on substituting the n_2 values 1.59×10^{-13} esu of NaCl and 0.85×10^{-13} esu for fused silica [130], and the n_0 values 1.539 for NaCl [131] and 1.456 for fused silica [132] at the central wavelength of the pump beam, a CARS intensity ratio of 3.9 is obtained. In Fig. 3.10, the ratio between CARS intensities of water (I_w) and glass is also shown. The ratio shows the OH resonance around 3200 cm^{-1} and reduces close to zero at 3700 cm^{-1} due to the out of phase contributions between resonant and non-resonant parts.
Despite its uniform non-resonant response, using NaCl as an *in situ* reference material is disadvantageous as compared to the use of glass because it is not present in a typical microscopy sample. However, considering its easy availability and the possibilities to create cubic crystals of NaCl with uniform composition using a simple preparation method, it presents a convenient standard medium for quantitative calibration of measured CARS responses. This can be done by introducing an additional step in the calibration procedure, measuring the NaCl to glass ratio for the specific glass type used, as well as the corresponding glass to water (or other buffer medium in the sample) ratio. Then, the glass (or buffer) measured within the data can be used as reference by correcting it to the NaCl reference which is well defined and non-resonant and therefore, a good standard.

3.5 Conclusions

In this chapter, we have focussed on the specifics of CARS microscopy as performed in our group and established the accuracy of our methods. Specifically, our home-built multimodal CARS microscopy set-up and analysis have been described. This set-up and analysis method were used to image and analyze all the data shown in this thesis. The effects of the imaging NA and refractive index of the sample on the FSC^3 analysis have been investigated and reported in this chapter. Importantly, the accuracy of quantitative analysis on polymer beads of different nominal sizes has been demonstrated, regardless of the imaging optics or the refractive index of the material imaged. This establishes the robustness of our imaging and analysis methods, which means that the quantitative concentrations resulting from FSC^3 analysis can be used to ascertain the volumetric composition of biological samples, which will be discussed in detail in the following chapters. Furthermore, investigative studies on NaCl have demonstrated the suitability of sodium chloride as a non-resonant reference material due to its resonance-free spectral profile in the frequency range $1200 - 3800\,\mathrm{cm}^{-1}$, easy availability and uniform composition as compared to glasses.

Chapter 4

CARS imaging of the cell cycle

As described in chapter 2, cells- the basic units of biology play a critical role in the continuity of life. To understand how cells function is fundamental to answering a number of questions pertinent to disease models and development of treatment strategies. A label-free imaging method to study cells with quantitative and qualitative aspects is much in demand. CARS micro-spectroscopy, a sensitive method with chemical specificity is beneficial over conventional fluorescence microscopy techniques because it provides chemically specific information about the samples without the need for introducing extrinsic labels.
In this chapter, cell biology applications of CARS microscopy are discussed. 3D data is located in the data DOI and available for viewing.

4.1 Methods

The CARS microscopy set-up and the analysis software- HIA discussed in the previous chapter were used to acquire and analyse the CARS measurements on osteosarcoma cells, U-2OS (ATCC HTB-96) cell line, transfected with a G2M Cell Cycle Phase Marker (GE Healthcare, UK). In other words, the cells were transfected with eGFP attached to cyc B1 which is an indicator of the mitotic phase of the cell cycle (see section 2.2.4) in order to facilitate identification of the cells in mitosis. Samples fixed with formaldehyde did not show eGFP fluorescence due to denaturation of the fluorophore as a result of its interaction with formaldehyde. To study the eGFP expression of the cells, a mild fixative agent (details below) was used.

4.1.1 Sample preparation

The samples of unlabelled U-2OS cells for imaging cyc B1 - eGFP expression were prepared by Mrs. S. Chappell and Prof. R. Errington, School of Medicine, Cardiff University. All other cell samples were prepared by Mrs. M. Wiltshire and Prof. R. Errington, School of Medicine, Cardiff University.
U-2OS cells were seeded and grown for 24 hours on a set of #1 cover-slips placed in five six-well plates A, B, C, D1 and D2 containing phosphate buffer solution (PBS) as medium. The cells in plates D1 and D2 were treated with clinically significant concentrations of drugs, i.e., 5 nM Taxol and 7.2 μM ICRF-193 respectively for 24 hours to study the effects of drug treatments on the cell population.
The cells in well plate A were used to image the eGFP-B1 complex and were fixed in BD CytoFix (Becton Dickinson), a mild fixative agent that maintains the eGFP

structure and fluorescence.
The cells in well plates B (control), D1 and D2 which were in various stages of the cell cycle were fixed for 30 minutes in 4% paraformaldehyde (PFA) following which the samples were immersed in phosphate buffer solution (PBS). In well plate D2, PFA was added to the different wells at different times to allow the cells to grow without ICRF-193 in the medium for a set number of days prior to fixation (details in section 4.5.2). Following preparation, all the well plates were covered and kept refrigerated at 4° C until imaging.
The cells in well plate C were stained with mitotracker-orange prior to and DAPI (4',6-diamidino-2-phenylindole) after fixation. Mitotracker-orange [133] diffuses across the plasma membrane of a live cell by passive transport and accumulates in the mitochondria. DAPI binds to the minor groove of DNA, specifically the adenine and thymine rich regions of the DNA [134]. Mitotracker-orange (CMTMRos Thermo Fisher Scientific) in a dilution of 10^{-5} v/v of the purchased product to PBS was added to the wells for a few minutes before washing with PBS to remove the excess fluorescent staining solution, and subsequently fixed for 30 minutes in 4% paraformaldehyde (PFA). The cells were then washed a few times with PBS. In the next step, 10^{-3} v/v of DAPI solution (NucBlue Fixed Cell ReadyProbes, Thermo Fisher Scientific) to PBS was added to the wells to stain the DNA. The cells were again washed a few times with PBS to remove excess DAPI. The well plates were then covered and stored at 4° C until imaging. The concentrations of the fluorescent labels were chosen to prevent cross talk between fluorescence and CARS imaging, as described in section 4.4.1.
To mount the cells for imaging under the microscope, approximately 13 μL of PBS was pipetted into a well created by the 13 mm diameter opening of a 0.12 mm thick adhesive imaging spacer on a 1 mm thick microscope slide (Fisher Scientific). The region of the cover-slip expected to lie over the adhesive of the spacer was wiped with clean room wipes to facilitate the adhesion of the cover-slip with the spacer. The cover-slip was then inverted over the medium filled well on the slide, and pressed to seal.
A summary of the well plates and the sample types they contain, is given in Table 4.1.

Sample type	Fixative	Well plate #
G2M eGFP	BD Cytofix	A
G2M eGFP	PFA	B
G2M eGFP, Mitotracker-orange, DAPI	PFA	C
G2M eGFP, 5 nM Taxol	PFA	D1
G2M eGFP, 7.2 μM ICRF-193	PFA	D2

Table 4.1: Table listing the various samples with their corresponding well plates.

4.1.2 Imaging

Epi-fluorescence images

Epi-fluorescence imaging of e-GFP in the cells from well plate A was done using the fluorescence lamp, with the GFP filter cube and the dry optics. The camera exposure times were set to either 5 s or 1.5 s. The details of these pieces of equipment are given

in section 3.1.2. This imaging was an exercise to get acquainted with the mitotic cells' morphology in order to identify the interesting (mitotic) cells for CARS microscopy (see sections 4.3 onwards). Additionally, a simple method to quantify eGFP and consequently, cyc B1 concentration in cells, using epi-fluorescence imaging was also developed, as demonstrated in section 4.2.

Two photon fluorescence (TPF) for labelled cells

To image the fluorescence from cells labelled with DAPI and mitotracker-orange (well plate C), DAPI was two-photon excited by the pump beam and detected using the filter set F2 and the PMT designated for SHG imaging. To excite mitotracker-orange the TPF beam was used and the fluorescence was detected with the same filter (F1)/PMT set as for the CARS signal. The filter sets and PMT models are mentioned in the set-up description given in the previous chapter. Following the imaging of fluorescently labelled DNA and mitochondria, hyperspectral CARS measurements were made on the samples to avoid photobleaching by CARS excitation before the measurement of fluorescence. TPF images were acquired with a pixel dwell time of 10 μs.

CARS

Hyperspectral CARS images of the cells in various stages of mitosis were acquired with 10 μs pixel dwell time (unless specified otherwise), as a function of the IFD in the CH stretch region (2400 - 3600) cm^{-1} with an IFD step size of 5 cm^{-1} unless otherwise specified. An image of the background intensities, at zero pulse overlap was also taken for each data. The pixel size in the measurements taken using dry optics was set to $\sim$ 450 nm in *xy*, and 1 μm in *z*. For these optics, the FWHM of the PSF as already mentioned in section 3.4.1 is approximately 1000 nm in lateral and 3 μm in axial direction. According to Nyquist sampling criterion, we should use a lateral step size of $<$ 500 nm and axial step size of $<$1.5 μm.
For the data acquired using the immersion optics, the *xy* step size was set to $\sim$ 150 nm and *z* step size to $\sim$ 0.5 μm unless otherwise specified. The FWHM of the PSF for these optics in the lateral and axial directions is 300 nm and 0.9 μm as discussed in section 3.4.1. Note that for some measurements, we undersample in the axial direction (using a step size of 0.7 or 1 μm) in the interest of acquisition speed and to avoid damaging the sample. To address the undersampling in acquisition, during processing and analysis we assume a homogeneous density of the chemical components in each voxel.

4.2 e-GFP quantification across the cell cycle

As discussed in section 2.2.4, the protein cyc B1 is active in the mitotic stage of the cell cycle. Qualitative and quantitative fluorescence imaging of eGFP-B1 transfected cells enables discrimination of the mitotic cells (well plate A) from a large population of cells in various stages of the cell cycle. In this section, results of quantitative analysis of epi-fluorescence are presented. The data were acquired using the dry optics.
A method to absolutely quantify the concentration of eGFP in the cells was developed and is detailed in the following discussion.

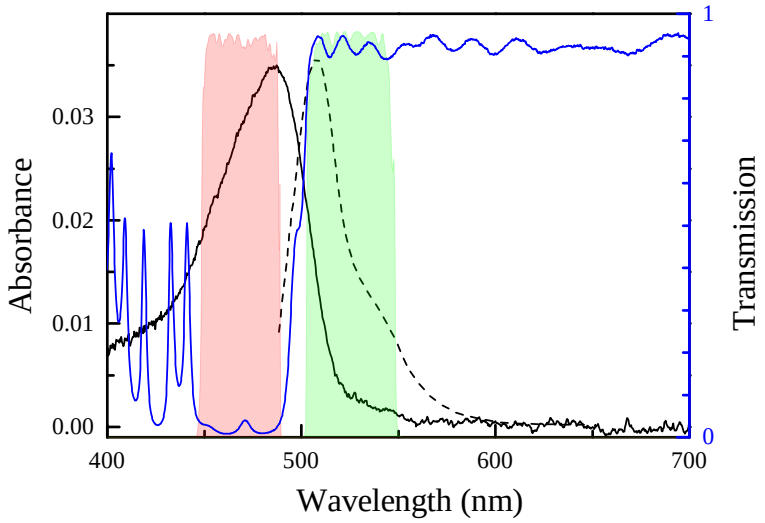

Figure 4.1: Absorbance spectrum of the eGFP solution acquired using the Ocean Optics set-up described in text. The nominal emission spectrum of eGFP is shown as dashed line (as reported in and adapted from [135] with permission from Elsevier). The filter cube dichroic, exciter and emitter transmission profiles are shown in blue, red and green respectively (as per the manufacturer's specifications).

4.2.1 Calibration sample preparation and measurements

A calibration sample was prepared with approximately 10 μL pure eGFP solution obtained from Dr. D. Jones, School of Biosciences, Cardiff university. The eGFP solution was pipetted to fill the 9 mm diameter opening of a 0.12 mm thick imaging spacer. A #1 cover-slip was inverted over the spacer, thus making a sealed well of eGFP.
The absorption spectrum of the sample was measured on a UV-vis spectrometer (USB2000-FLG Ocean Optics) with an operation range of 380 - 1050 nm. The light source in this set-up is a lamp (HL-2000-FHSA Ocean Optics).

4.2.2 Results

We calculate the absorbance A, of eGFP solution using the relation

$$A = -\log_{10}\left(\frac{S-R}{L-D}\right) \tag{4.1}$$

Where S refers to the intensity spectrum of the sample (eGFP), R refers to the intensity spectrum of the reference (water), L refers to the lamp spectrum and D is the dark spectrum (taken with the lamp switched off). Using Lambert-Beer's law (see equation 1.9), $A = \beta\,\mathcal{C}\,l$, where $\mathcal{C}$ is the molar concentration, β is the molar extinction coefficient and l is the pathlength that the incident light travels through the solution, the concentration $\mathcal{C}$ of eGFP in the solution can be determined. The resulting absorbance spectrum of eGFP, having a maximum value of 3.46% at $\sim$ 488 nm is shown in Fig. 4.1. The extinction coefficient β of eGFP at $\lambda =$ 488 nm is 53,000/mol/cm^2 [135], and the pathlength l is 120.8 μm (measured using the microscope stage).
On substituting these values in Lambert-Beer's law, the concentration of eGFP in the

solution is obtained as $54 \pm 7\,\mu$M by considering 10% relative error in absorbance, 8% error in the extinction coefficient [135] and 1% error due to standard deviation plus approximately 0.5% error due to the microscope systematics in the measurement of the gasket height (pathlength). The relative error in concentration is dominated by the errors in the absorbance and the extinction coefficient, and expressed as $\sqrt{0.1^2 + 0.08^2}$. The number of eGFP molecules per area, n, is calculated using the relation

$$n = \mathcal{C}\, N_{\mathrm{A}}\, l \tag{4.2}$$

where N_{A} is Avogadro's number. The error in the number density is dominated by a relative error of 13% in concentration. Therefore, the number density is $n = (3.9 \pm 0.5) \times 10^{14}/\mathrm{cm}^2$. These values were then used to quantify the eGFP in cells as follows.

The data from the epi-fluorescence imaging was analysed using ImageJ to calculate the sum of intensities, I_{c} of pixels enclosed within a contour defining the boundary of the cell. These intensities were then normalized with the fluorescence of the eGFP sample imaged under otherwise identical conditions to calculate the number of eGFP molecules in the cells, N_{c}, as

$$N_{\mathrm{c}} = \frac{n I_{\mathrm{c}} \tau_{\mathrm{p}} A_0}{\overline{I}_{\mathrm{p}} \tau_{\mathrm{c}}} \tag{4.3}$$

where $\tau_{\mathrm{p}} = 0.6\,\mathrm{ms}$ and $\tau_{\mathrm{c}} = 5\,\mathrm{s}$ (unless otherwise specified) are the exposure times used to acquire the image of the eGFP sample and the cells respectively. $\overline{I}_{\mathrm{p}}$ is the mean intensity measured over an area of the image of the pure eGFP sample and A_0 is the pixel area of the camera ($0.104\,\mu m^2$ for $20\times$ magnification).

In Fig. 4.2, the so determined N_{c} is plotted against cell stage identifier, showing a distribution wherein the cells in metaphase are sorted at/near the peak of the distribution while the ones in other stages of their cycle are present at the edges of the distribution. The cell stage identifier is a number assigned to the cells, depending on their morphological appearance and their eGFP expression in various stages of the cell cycle. To assign the cell stage number, we recall that cyc B1 is produced during the S phase, in the rough endoplasmic reticulum. Metaphase promoting factor (MPF) i.e., cyc B1 + CDK1 is localized in the cytosol during interphase (G_2) and gets transported to the nucleus before the disintegration of the nuclear envelope in prophase, marking the onset of mitosis [136]. After the chromosome alignment on the metaphasic plate [137] cyc B1 degradation begins.

In the samples studied, the eGFP emission was found to be stronger in the cytoplasmic or the nuclear region of the cell depending on the cell cycle stage. The distribution of cyc B1-eGFP across various stages of the cell cycle is summarized as follows:

The concentration of cyc B1 at each stage of the cell cycle varies across the individuals of the cell population. Smith et al. have reported a typical relative decrease of cyc B1 - eGFP expression of approx. 35% in U-2OS cells in metaphase over two consecutive cell cycles [21]. This variation in cyc B1 expression makes it difficult to compare cells in broadly classified substages of interphase.

For the analysis presented in this section, epi-fluorescence images of 36 fixed U-2OS cells were taken. The assignment of stage identifiers to the cells was done using the eGFP expression described in Table 4.2 and by identifying the morphological features of the cells at various stages of the cell cycle, considering the spatial distribution of eGFP in the cells. The numbering is taken as chronological along the cell

Cell cycle stage	cyc B1-eGFP localization
Interphase (S, G_2)	Cytosol, microtubules
Late G_2	Cytosol, centrosomes
Prophase	Nucleus
Prometaphase	Spindles
Late metaphase onwards	Progressive degradation

Table 4.2: Localization of cyc B1- eGFP throughout the cell cycle in fixed cells [136, 137, 138].

cycle, starting with interphase.
Specifically, the cells were first sorted into interphase and the substages of mitosis by observing their morphology. Flat cells were designated as interphase cells while the cells showing a spherical morphology were considered mitotic. Within mitosis, the cell morphology changes from metaphase to cytokinesis and therefore, this was also taken into account. Finally, within the identified stages, the cells were arranged in either increasing or decreasing order of eGFP concentrations according to the expected trend. In the leading and trailing regions of the curve shown in Fig. 4.2, we observe that the daughter cells which appear attached to each other (cells 1-4, 6, 8) with or without apparent cytoplasmic division are given lower identifier numbers than cell 25 which appears to be in early stages of cytokinesis. This was done due to the higher eGFP concentration in the set of cells compared to cell 25, relying on the knowledge that cyc B1 levels reach a maximum in metaphase following which they decline (cyc B1 expression is actually the net rate of production of the protein, but the expression level generally refers to the number of proteins, represented here by the fluorescence intensity of the eGFP attached to the protein).
Conversely, the eGFP concentration in cell 11 is lower than that of cells 9 and 10. Despite this, cell 11 is given a higher identifier number due to its mitotic morphology. Such correlations were applied over the entire set of cells imaged and the resulting plot given in Fig. 4.2 shows the variation of cyc B1 concentrations with the number of eGFP molecules/cell, over various cells fixed in different stages of the cell cycle. The graph shows that the eGFP concentrations increase by an order of magnitude to about 10^5 molecules/cell as the cells approach mitosis, peak at metaphase and progressively decline thereafter until the next cell cycle commences.
The maximum number of eGFP molecules/μm^2 displayed in the image grayscales shown in Fig. 4.2 is calculated using the relation

$$n_{\max} = \frac{nI_{\max}\tau_{\mathrm{p}}}{\bar{I}_{\mathrm{p}}\tau_{\mathrm{c}}} \tag{4.4}$$

where $I_{\max}$ is the maximum pixel value in the region of interest defined by the cell's boundary.
The result of this analysis is a model of eGFP expressions during the cell cycle which matches the known behaviour of cyc B1 as described in section 2.2.4.
Using a cell volume of 4000 μm^3 [139], the molar concentration of eGFP in mitotic cells with 1.3×10^5 eGFP molecules is $0.063 \pm 0.008\,\mu$M.
Fig. 4.3 shows higher resolution images of the cells which were previously shown adjacent to the datapoints in Fig. 4.2 and also includes the total number of photo-

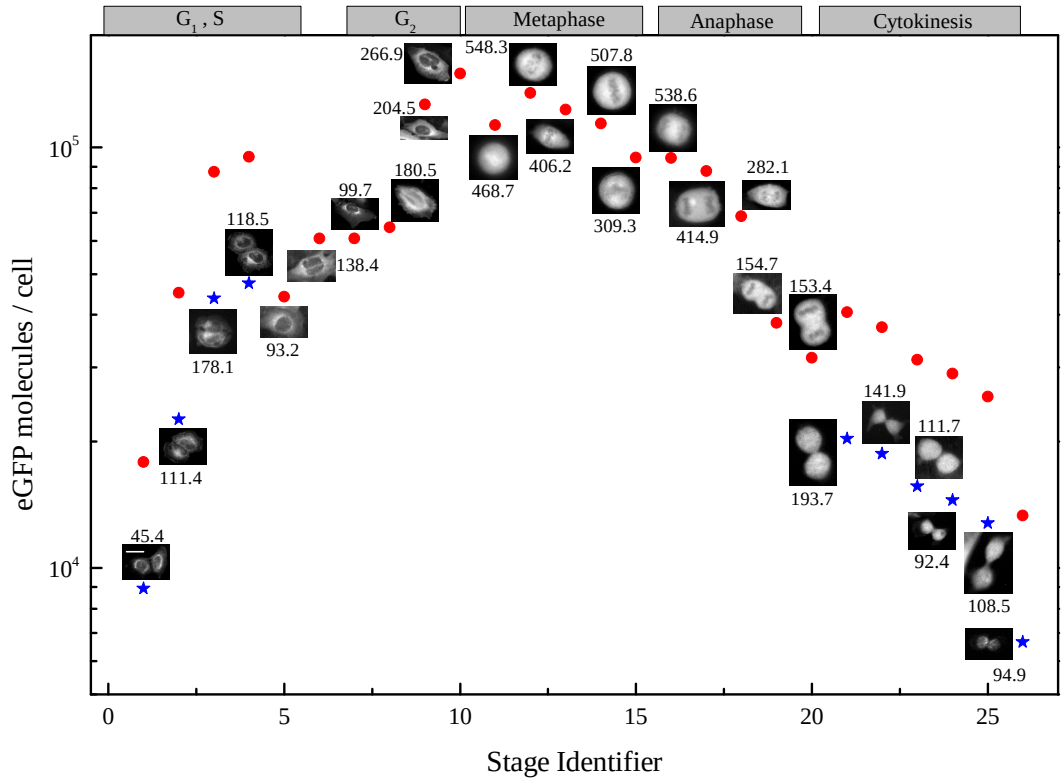

Figure 4.2: Quantitative analysis of eGFP expression along the cell cycle. Cells 3, 11, 15, 21 and 26 were imaged using 1.5 s exposure time (images of cells are placed beside the data points). The scale bar shown on the first cell is 10 μm and is valid for all images shown in the plot. Data points represented by blue stars correspond to the images which show two cells not fully separated for which the total number of eGFP molecules in the two cells was evaluated across both the cells, and then divided by two. The numbers next to the images are the maximum displayed area concentrations of the grayscale used (black (0) to white (maximum)), in units of molecules/μm^2.

electrons detected per second over the cell. These were calculated as

$$N_{\mathrm{p}} = 4.42\, I_{\mathrm{c}}/\tau_c \tag{4.5}$$

using the camera gain, 4.42 electrons/count. Other parameters i.e., the detection efficiency and the illumination power density at the sample are calculated as shown in Appendix B.

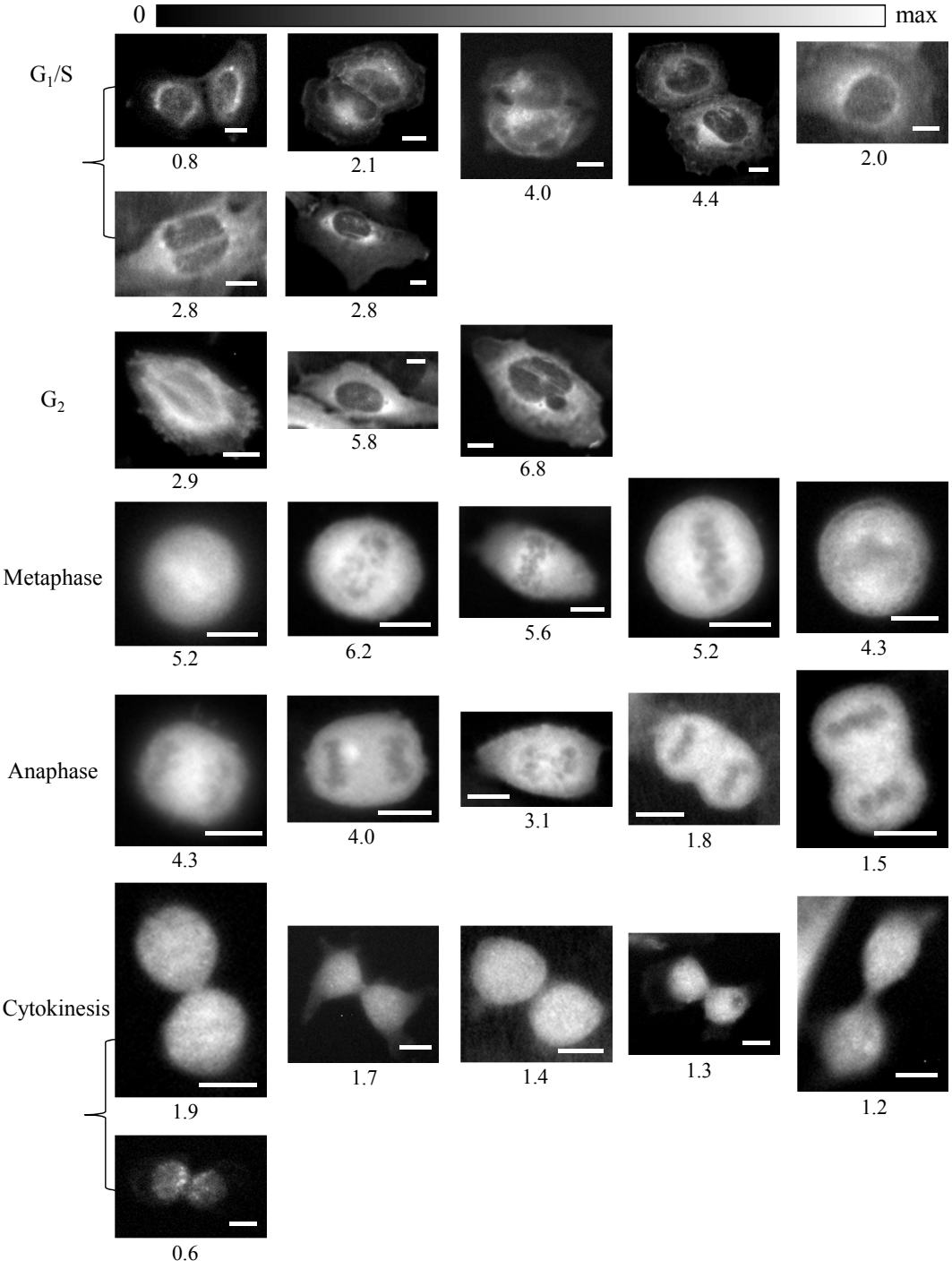

Figure 4.3: Epi-fluorescence images of the cells shown in Fig. 4.2 arranged in order of increasing stage identifier from left to right in each stage of the cell cycle (top to bottom). The numbers underneath the images are the photoelectron rates integrated over the cell in the units of 10^6 el/s. The scale bars shown are $10\,\mu$m.

In literature, a 1:1 correspondence between the numbers of eGFP and cyc B1 molecules in U-2OS cells has been reported [140] using flow cytometry. Specifically, in G_1 cells, 5000 and in G_2 cells, 7000 molecules of eGFP and cyc B1 each were calculated [140]. It is expected that the number of eGFP and cyc B1 molecules will

increase in the subsequent mitotic stages. In comparison to these values on live cells, we obtain for fixed cells, molecule numbers of the order of $(0.9\text{-}5)\times10^4$ in G_1 and G_2 and around 10^5 in the mitotic stage of the cell cycle. The differences in the results are explained as due to the variability in the cyc B1 expression across different cells in a population and over subsequent cell cycles. Additionally, differences in the number of molecules of cyc B1 in HeLa cells depending on the counting method used have been reported [141] (using Western blotting), which is possibly supporting of the hypothesis that such differences are due to the variability of cyc B1 expression across different cells in a population.
In contrast to Western blotting and flow cytometry (which are also technically invasive and complex) our method detailed in this section using epi-fluorescence imaging presents a relatively fast, direct and simple technique which facilitates eGFP/cyc B1 concentration determination, requiring only conventional and readily available optical microscopy components.
Having characterized the eGFP/cyc B1 expression as described in this section, we correlated it with the cell morphology (using DIC) as a learning exercise in order to identify mitotic cells as they appear in the two kinds of imaging modalities. While the data shown in this section and the next were measured on cells retaining their eGFP fluorescence after fixation (well plate A), the samples shown in sections 4.4 onwards, in this chapter were fixed in PFA (well plates B, C, D1, D2), which denatures the eGFP and therefore prevents it from fluorescing. For such samples, which are effectively unlabelled with respect to the eGFP/cyc B1 complex, and therefore are ideal samples to establish the use of CARS in a label-free way, we used DIC microscopy to select the mitotic cells.

4.3 CARS imaging of cyclin B-eGFP tagged cells

In line with the goals of this project, CARS microscopy of U-2OS cells was performed. Progressing from the characterization and quantification of eGFP as discussed in the previous section, the results of FSC^3 analysis (over a spectral range of 2750 - 3100 cm^{-1}) of hyperspectral CARS images of a few cells (well plate A) in various stages of mitosis are shown in this section. Some of the cells from the previous section were selected for CARS imaging, to study the chemical composition of mitotic cancer cells.
In Fig. 4.4 - Fig. 4.6, the results of simultaneous FSC^3 analysis (settings given in Table D.3) of three cells imaged using the dry optics are shown. These data were chosen for analysis specifically due to the cells being in different stages of mitosis. On simultaneously analyzing the data, a common factorization of the chemical composition of the data is obtained, along with the respective concentration maps of the corresponding FSC^3 components. This method of simultaneous factorization of several data is particularly useful to identify differences in the chemical composition as well as spatial distribution of the components in each data set.
From a total of nine FSC^3 components used, only three are shown in this section, corresponding to protein, lipid and chromatin (1,2,3 respectively). The other components, comprising four attributed to water and one each for glass and systematics are shown in Fig. D.1 - Fig. D.3. The water in the cells imaged is split by FSC^3 analysis into several components as an analysis artefact. Additionally, the water component is modified slightly due to the presence of cellular organic material, which also contributes to the splitting of the water into several components. The component corresponding to sum water (W) for all the data shown in this work was digitally prepared by adding the different FSC^3 water components and the corresponding spectrum was obtained by using a weighted average of the water components, as

$$W_{\text{sum}} = \frac{\sum_i a_i \times W_i}{\sum_i a_i} \tag{4.6}$$

where a_i is the average concentration and W_i is the spectrum of the i-th water component.
The first two figures show the results of the analysis of hyperspectral CARS data obtained over a large spatial region of the cover-slip of the same lateral field of view at two different z planes, as a representative typical field of view of the samples imaged. In Fig. 4.4, an FSC^3 analysis of this field of view (FOV) containing cells in various stages of mitosis is shown over a spectral range of 2750 - 3100 cm^{-1}. In the xy plot, at the z plane shown in Fig. 4.4, cell 1 which is in early stages of cytokinesis, is in focus. The FSC^3 components correspond to sum water, protein, chromatin and lipid as shown in images W,1,2,3 and their respective spectra in b).

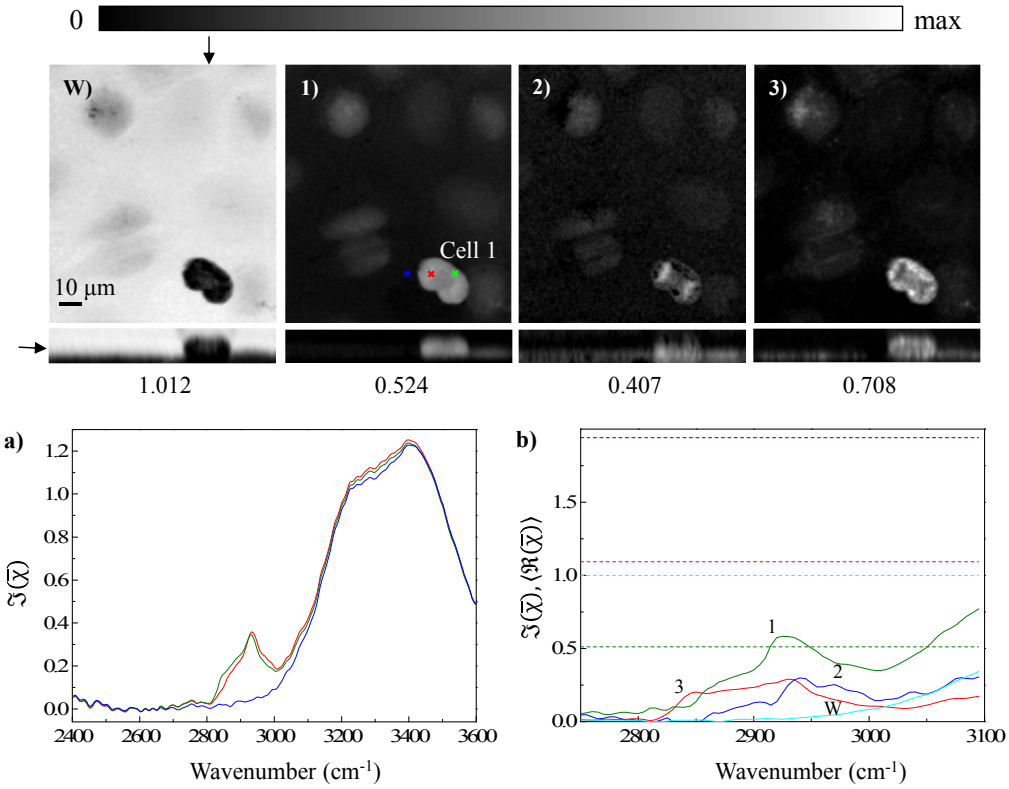

Figure 4.4: FOV 1 at $z = 3\,\mu m$ above the glass surface: images W,1,2,3 show the xy distributions of various FSC^3 components corresponding to sum water, protein, chromatin and lipid respectively, with their corresponding xz sections shown underneath. The arrows mark the positions at which the sections were taken. The scale of concentrations displayed in the images (grayscale bar) goes from 0 to maximum, the latter indicated underneath each xz section. a) shows the PCKK spectra taken at the positions colour coded on image 1. The FSC^3 spectra i.e., $\Im(\bar{\chi})$ and $\langle\Re(\bar{\chi})\rangle$ in solid and dashed lines respectively are shown in b).

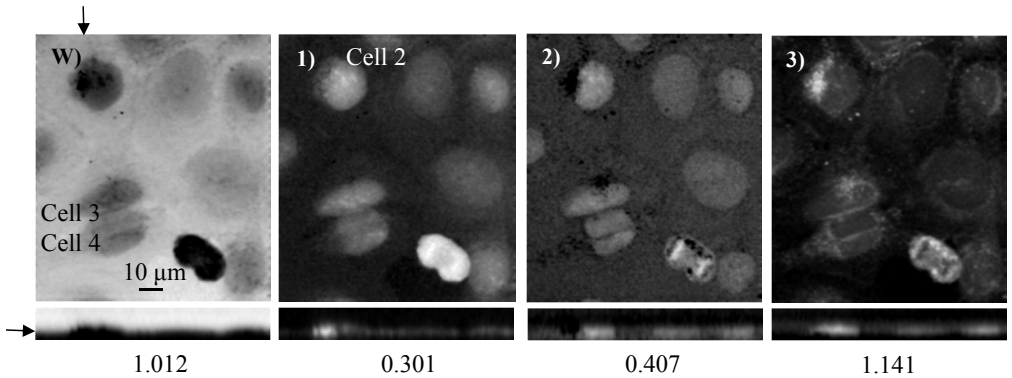

Figure 4.5: FOV 1 at $z = 1\,\mu$m above the glass surface: FSC^3 analysis of data shown in Fig. 4.4 at a different z plane. Images W,1,2,3 are the xy and xz sections of concentrations of FSC^3 components corresponding to sum water, protein, chromatin and lipid respectively. The arrows indicate the positions at which the sections were taken. Grayscales as in Fig. 4.4. The spectra corresponding to the components are given in Fig. 4.4 b) .

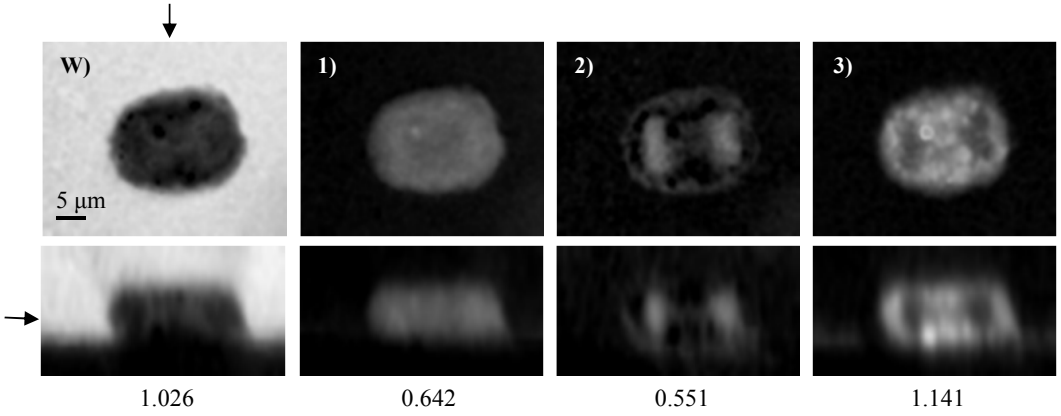

Figure 4.6: FOV 2: FSC^3 concentrations (xy and xz sections) corresponding to sum water, protein, chromatin and lipid respectively, of a U-2OS cell in late anaphase. Grayscales as in Fig. 4.4. The component spectra are shown in Fig. 4.4 b).

In Fig. 4.5, a different z section of the same data as in Fig. 4.4 is shown. Cell 2 in this FOV is in the early mitotic stage as determined from its rounded shape and homogeneously distributed FSC^3 components. $\mathcal{C}_3$ in this cell (corresponding to lipid) appears colocalized with the golgi apparatus.
The eGFP expression of cells 1, 3 and 4 are shown in Fig. 4.2 (stage identifiers 4 and 5).
FOV 2 shown in Fig. 4.6 shows the concentrations obtained from an FSC^3 analysis of a late anaphase cell, the eGFP expression of which is shown in Fig. 4.2 at stage identifier 17. In FOV 3, (Fig. 4.7), two cells in the cytokinesis stage are visible. The cells have not yet separated, but the nuclear material is no longer showing a chromatin like (filamentous) distribution as observed in cell 1 in FOV 1 (Fig. 4.4). These cells are identified to be in cytokinesis due to their spherical appearance and the eGFP characteristics shown in Fig. 4.2, at stage identifier 23. An interesting feature in the late anaphase cell shown in Fig. 4.6 is that the FSC^3 component corresponding to lipid, $\mathcal{C}_3$ is homogeneously distributed across the cytosol showing a

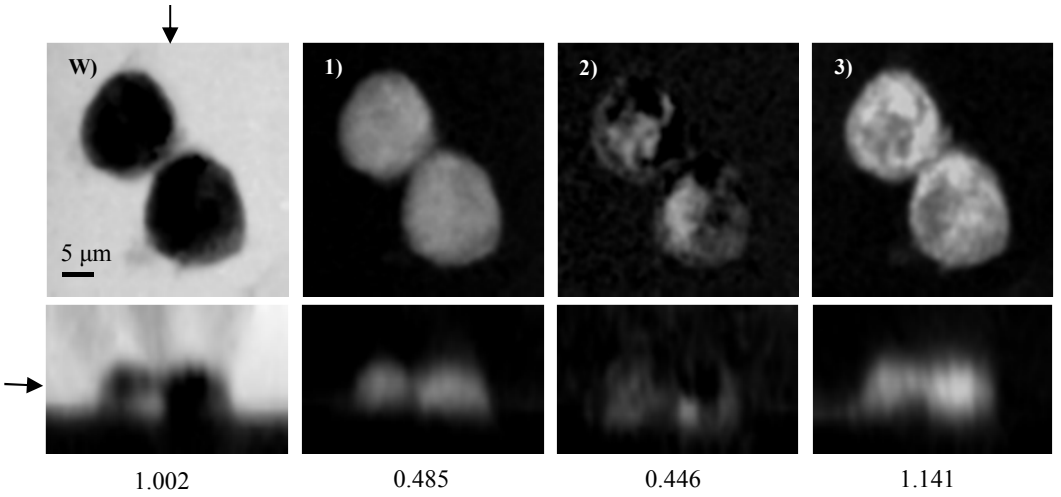

Figure 4.7: FOV 3: FSC^3 concentrations (xy and xz sections) corresponding to sum water, protein, chromatin and lipid respectively, of a U-2OS cell in cytokinesis. Grayscales as in Fig. 4.4. The component spectra are shown in Fig. 4.4 b).

granular appearance. This appears to demonstrate the vesicular distribution of the cell organelles during mitosis as mentioned in section 2.2.2.

In the following analysis, we show 2D data taken using the immersion optics (for higher resolution and signal/noise ratio compared to that in the case of dry optics) and analyzed individually. In Fig. 4.8, a metaphase cell is shown. The factorization settings used in this analysis are given in Table D.4. Of the ten FSC^3 components used, five are shown, with two corresponding to protein (1,2), two to lipid (4,5) and one component to chromatin (3). The sum water (as described for FSC^3 analysis of cells previously shown in this chapter) component, W is also shown. The components not shown here correspond to water (three components) and systematics (two components) and are given in Fig. D.4. Such a large number of FSC^3 components was used in order to factorize chromatin as a separate component, which is otherwise not obtained.

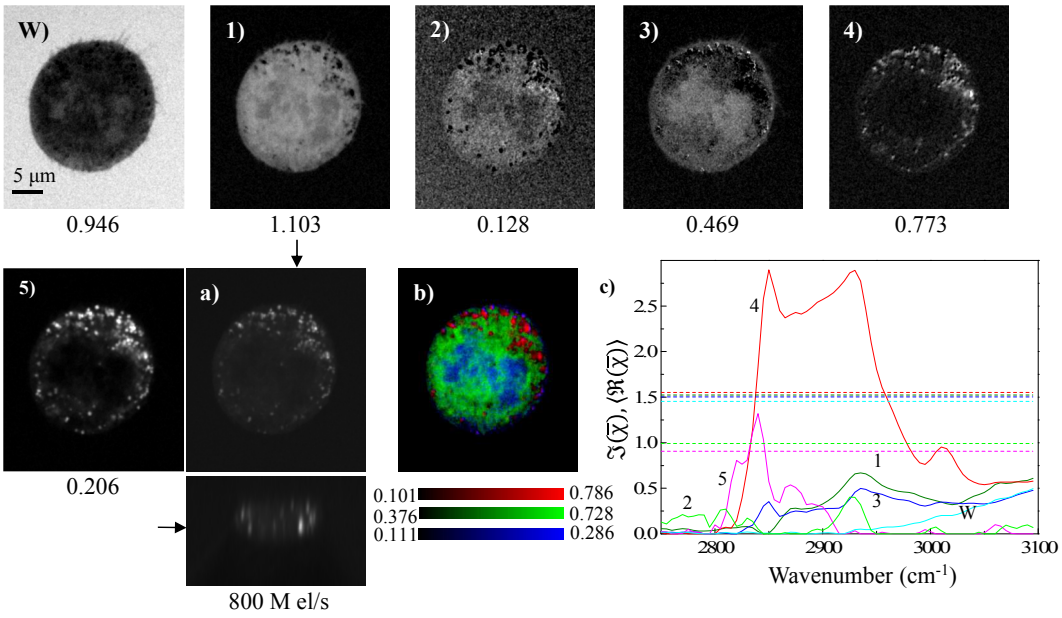

Figure 4.8: FOV 4: FSC concentrations (xy sections) of a prophase cell in the middle z plane of the cell are shown. Grayscales as in Fig. 4.4. a) shows the xy and xz sections of CARS intensity acquired at 2830 cm^{-1}, with arrows marking the positions of the sections at which the images are shown. The FSC^3 spectra of the concentrations W,1,2,3,4,5 corresponding to sum water, protein, protein, chromatin, lipid and lipid respectively are shown in c). b) is a colour overlay with FSC^3 components 4, 1 and 3 plotted in red, green and blue channels respectively, with value scales as shown.

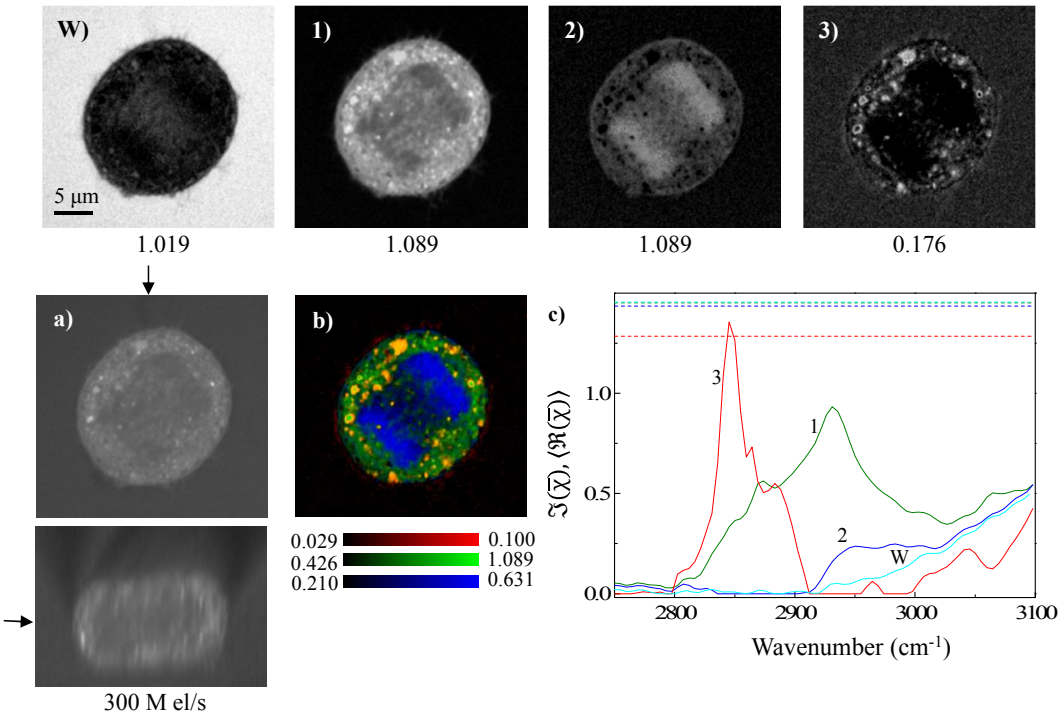

Figure 4.9: FOV 5: *xy* sections of FSC^3 concentrations of a cell in anaphase at the centre *z* plane. Components W,1,2,3 corresponding to sum water, protein, chromatin and lipid respectively, and their spectra are shown in c). Image a) shows the *xy* and *xz* sections of CARS intensity acquired at 2830 cm^{-1} with arrows marking the positions of the sections at which the images are shown. Image b) is a colour overlay with components 3, 1 and 2 plotted in red, green and blue channels respectively.

An anaphase cell is shown in Fig. 4.9 which was analyzed using six FSC^3 components. The analysis settings are given in Table D.5. Only three relevant components are shown, corresponding to protein, chromatin and lipid. Sum water, W is also given. The individual components corresponding to water (three) are shown in Fig. D.5. In Fig. 4.9, the FSC^3 component $\mathcal{C}_3$ corresponding to lipid shows granular appearance, in cytosol. These lipid rich regions also appear as bright blobs in $\mathcal{C}_1$ which corresponds to protein.

Note on the nomenclature of the FSC^3 components: We emphasize that the factorization algorithm does not give pure, but nevertheless spectrally distinct components. The 'chromatin' component appears more DNA like than protein, and the protein/lipid components are more proteic/lipidic than anything else. With respect to the chromatin component, only one of the four DNA bases (thymine) has peaks in the spectral range analyzed. Therefore, we refer to $\mathcal{C}_3$ as chromatin (and not DNA) because it is not pure DNA and this fact assumes a far greater importance in the case of this component rather than in the case of other components because only one of the four DNA bases are detected by CARS in the spectral range used. So, we hypothesize that this component is even less pure than the other species detected, justifying its nomenclature. Furthermore, small components, such as chromatin are harder to reproduce as their signal/noise ratio is low and they are, therefore not well factorized by the FSC^3 method. The lipids are needless to say, the purest (as indicated by their spectral signature and spatial distribution) of all the components

factorized using FSC^3 due to the large number of CH bonds.

4.4 CARS and TPF imaging of mitotracker and DAPI labelled cells

The data shown in the previous section demonstrate the capability of CARS microscopy to discriminate between two sub-cellular compartments, one colocalized with the cytosol ($\mathcal{C}_1$) and the other within the nuclear region ($\mathcal{C}_2$), based on the differences in their chemical composition. Additionally, the distribution of lipids was also imaged in the cells, which in some cases was found to be colocalized with the golgi apparatus (see image 3 in Fig. 4.4 and Fig. 4.5). Previously, other authors have reported studies on mammalian cell lines (MCF-7 and HEK-293) to image nucleic acids using SRS [7] at selected energies in the fingerprint region. Matthaus et al. have shown Raman microspectroscopy of HeLa cells in the fingerprint region, with nuclear contrast [101] demonstrated through characteristic DNA peaks. Additionally, SRS imaging of A549 cells reveals an intranuclear spectrum [104] similar to what we observe in U-2OS cells as already shown in this work. CARS has been used by Parekh et al. [15] to demonstrate the differences in the average spectra of the nuclear and extranuclear regions of L929 cells. As also discussed in section 2.3, none of these reports show factorized components (or their quantitative volumetry) of the CARS spectra, or full 3D hyperspectral information in the CH-stretch region. Through the work in this thesis, we aim to show, for the first time in our knowledge, with quantitative specificity, the chemical signature of the U-2OS cells (3D hyperspectral CARS images), factorized into distinct spectra with intranuclear, cytoplasmic and lipid localizations. We start by verifying that $\mathcal{C}_2$ as shown in the previous section (and also similar to the average nuclear spectra shown in the works cited above) is indeed colocalized with the nucleus. To do this, we performed correlative TPF imaging followed by CARS imaging of the cells stained with DAPI (well plate C). The granular appearance of the protein and lipid components as seen in Fig. 4.8 and Fig. 4.9 was also checked for correlation with the distribution of mitochondria, using correlative TPF imaging of mitotracker-orange. The results of this analysis on three cells stained with both DAPI and mitotracker-orange (from well plate C), in various stages of mitosis are shown in this section. The cells were identified using DIC and imaged with CARS and TPF using immersion optics. The concentrations of the fluorescent labels used were carefully selected to ensure no two-photon excitation by the pump beam, which would contribute to a CARS non-resonant background. Before presenting the FSC^3 results, a description of the process to determine the suitable concentrations of the fluorescent labels for imaging is given below.

4.4.1 Determination of suitable concentrations of fluorescent labels

Two-photon emission/excitation profiles [142] of Alexa 546 dye which is similar to the one photon emission/excitation of mitotracker-orange, and DAPI are shown in Fig. 4.10. The detection ranges of CARS (red) and SHG (blue) channels are also shown. As seen in Fig. 4.10, DAPI has a non-zero excitation at 680 nm. Therefore, it can be two photon excited by the pump (see section 3.1.2). However, while the TPF cross section of mitotracker-orange is not known at the wavelength of the pump beam (680 nm), we observe a weak background in CARS colocalized with the mitochondria. We attribute this background to a weak two-photon excitation of

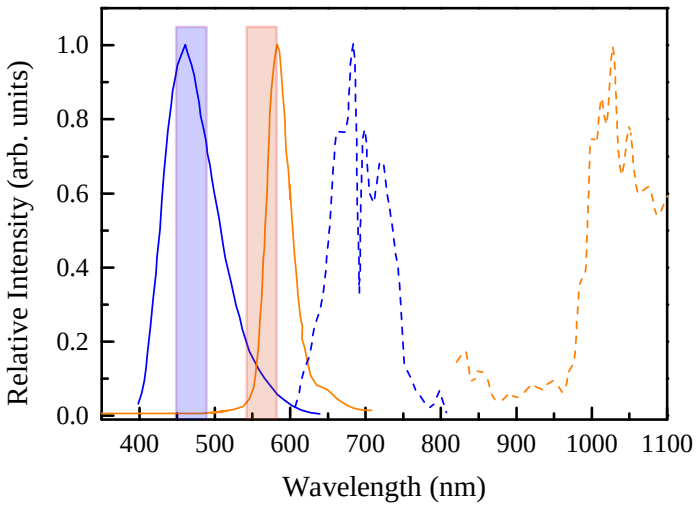

Figure 4.10: Two photon excitation (dashed) and emission (solid) spectra of Alexa 546 in orange and DAPI in blue. Adapted from [142] with permission from John Wiley & Sons.

mitotracker-orange by the pump. Therefore, the concentrations of the fluorescent labels were carefully chosen to ensure that their fluorescence had negligible influence on the CARS measurements. To determine suitable concentrations of fluorophores for imaging of these cells, a dilution series of DAPI was characterized using the dry optics. Assuming that the uptake of DAPI is similar across different cell lines, A549 (lung cancer, specifically adenocarcinomic human alveolar basal epithelial) cells were fixed as per the procedure already described for U-2OS cells in five wells (1-5) of a six well plate.

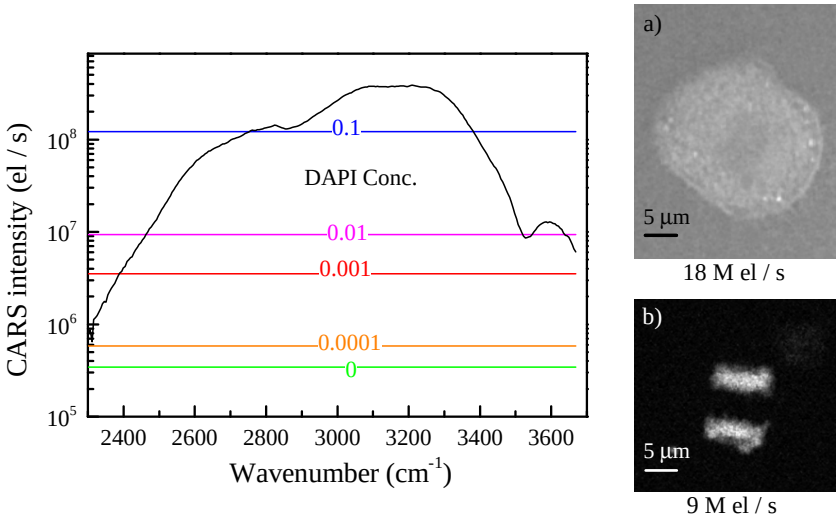

Figure 4.11: Figure showing graph giving the average CARS intensity (black) over the nuclear region in the control sample. The coloured lines show the CARS intensity backgrounds at zero pulse overlap averaged over the nuclear region in cells stained with different concentrations of DAPI as indicated. a) shows the spatially resolved CARS channel intensity at 2850 cm^{-1} of a control sample. b) shows the background at zero pulse overlap, due to the TPF of DAPI of a cell stained with 0.1 v/v concentration of DAPI.

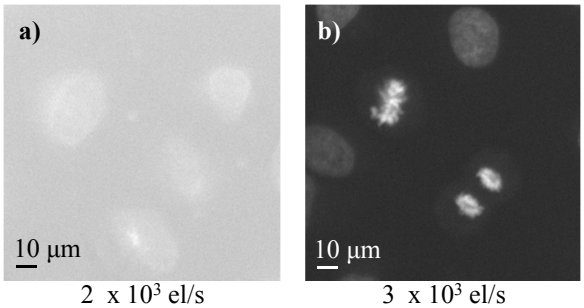

Figure 4.12: Epi-fluorescence images of cells stained with DAPI imaged using the dry optics with acquisition time of 2 s. a) cells stained with 10^{-4} v/v DAPI/PBS. b) cells stained with 10^{-3} v/v DAPI/PBS. Grayscales as in Fig. 4.4 with black = 0 and white = the maximum number of photoelectrons/second/pixel displayed below the images.

The cells in wells 1-4 of the well plate were then labelled with DAPI in concentrations $10^{-1}, 10^{-2}, 10^{-3}$ and 10^{-4} v/v of the stock solution of DAPI from the manufacturer (concentration unknown) to PBS. Well 5 was kept unstained, as the control. The cells on the cover-slips were then mounted on slides as already described in section 4.1.1 and imaged in the CARS microscope. In Fig. 4.11, the graph shows CARS intensity of an unstained cell in black, averaged over the nuclear region of one cell from the control sample (well 5). The coloured lines show the non-resonant background at zero pump-Stokes pulse overlap, averaged over the nuclear region in the cells from wells 1-5 of the well plate. The unstained sample (green) shows a background intensity of the order of 10^5 el/s. Compared to this, the sample stained with the maximum concentration of DAPI (10^{-1} v/v shown in blue) shows a background intensity of 10^8 el/s, which is of the same order as that of the CARS intensity in the CH-stretch region.
Using very low concentrations of DAPI does not allow TPF imaging of the fluorescence. Fig. 4.12 shows epi-fluorescence images (1-2) of A549 cells stained with 10^{-4} and 10^{-3} v/v concentration of DAPI/PBS.
Detectable DAPI fluorescence confined to nuclear regions is not observed in the sample stained with 10^{-4} concentration (Fig. 4.12 a). Since the experiment requires correlative imaging of TPF and CARS, this concentration is not suitable for imaging. The sample stained with 10^{-3} concentration shown in Fig. 4.12 b is suitable for both TPF and CARS imaging, since the nucleus is visible and the background is about 1% of the CARS intensity. Note that the background was subtracted before the CARS analysis, so that the remaining effect is estimated to be in the 10^{-3} range which can be neglected. The optimum concentration of mitotracker was determined in the same fashion as the DAPI staining discussed. Samples prepared using 10^{-4} v/v mitotracker-orange/PBS were found suitable for our experiment.

4.4.2 Factorization over extended IFD range

We show the results of FSC^3 analysis of hyperspectral CARS images of a fluorescently labelled cell (with label concentrations as discussed above) in Fig. 4.13. An FSC^3 analysis of a metaphase cell, over a spectral range including the dominating water peak at 3100 - 3600 cm^{-1} is shown. The factorization settings are given in Table D.6. The spectral composition of the cell was factorized into eight FSC^3 components, of which four relevant ones are shown (images 1-4), with their corresponding

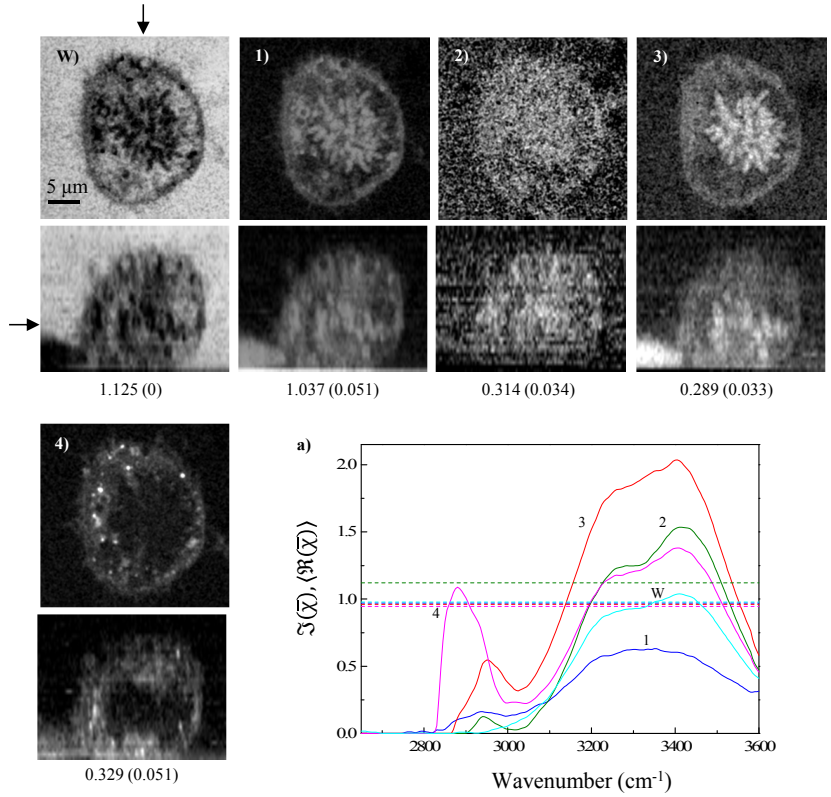

Figure 4.13: FOV 6: FSC^3 analysis of a metaphase U-2OS cell factorized over the IFD range (2650 - 3600) cm^{-1}. Images W,1,2,3,4 show *xy* and *xz* sections of FSC^3 concentrations corresponding to sum water, protein, protein, chromatin and lipid respectively with grayscales as in Fig. 4.4. The arrows mark the positions at which the sections were taken. The dry component concentrations are given in parenthesis below each image. a) shows the FSC^3 spectra of images W,1,2,3,4.

spectra shown in b). The sum water component is also given (W). The images 1-4 correspond to the concentration distributions of the components attributed to protein (1,2), chromatin (3) and lipid (4). In all the components' spectra, a sizeable contribution of the water resonance at 3150 - 3160 cm^{-1} (since organic materials have no significant $\Im(\chi)$ above 3200 cm^{-1}) is observed. This is due to the small concentrations of materials in the system (a typical cell contains $\sim$ 70% water [72]). The four components not shown here are attributed to water and given in Fig. D.6.

4.4.2.1 Calculation of dry factors

As the first step towards interpreting the results in a quantitative way, the procedure for calculating the dry factors which represent the fraction of pure, dry organic material within the individual FSC^3 components (which include organic material as well as water) is described below.
Dry factors, γ_{dry} are calculated for each FSC^3 component localized within the cells. The sum water component ($\mathcal{C}_{\text{W}}$) is rescaled by a constant multiplier, α to match the considered FSC^3 component ($\mathcal{C}_i$, corresponding to protein, lipid or chromatin) in the IFD range 3050 - 3200 cm^{-1}. By doing this, we estimate the 'pure' water component corresponding to each $\mathcal{C}_i$. The rescaled water component is then subtracted from

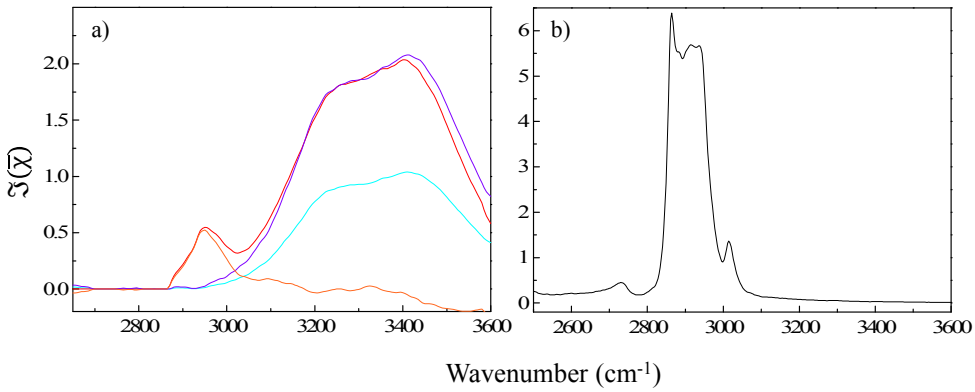

Figure 4.14: a) Plot showing the FSC^3 components corresponding to water (cyan) and chromatin (red) of the factorization shown in Fig. 4.13. The spectrum in purple is the water spectrum scaled by a factor of 2. The dry spectrum of the FSC^3 component corresponding to chromatin is shown in orange. b) Oleic acid (pure CH material, courtesy, Dr. F. Masia, School of Physics and Astronomy, Cardiff University) spectrum

$\mathcal{C}_i$, giving the dry spectrum of $\mathcal{C}_i$. In the example shown in Fig. 4.14, the sum water component, W in Fig. 4.13, $\mathcal{C}_{\rm w}$ (cyan), was rescaled by a factor of $\alpha = 2$ to match with the chromatin component, $\mathcal{C}_3$ (red) in the IFD range of 3050 - 3200 cm^{-1}. The rescaled water spectrum is shown in purple and the dry spectrum of $\mathcal{C}_3$ in orange.

The dry spectrum is then integrated over the IFD range corresponding to the CH region (in this case, 2860 - 3050 cm^{-1}), giving the area $\mathrm{A}_3 = 50\,\mathrm{cm}^{-1}$. In order to estimate the volume associated with a given area of $\Im(\bar{\chi})$ in the CH stretch region, we normalize the area A_3 by the area of a pure material, here oleic acid (OA, measured by Dr. F. Masia, School of Physics and Astronomy, Cardiff University). The normalized area is multiplied by a factor, F_3 which is calculated assuming that the area integrals are proportional to the number of Raman active -H bonds in the material in the analyzed spectral range. We can express the factor, F_3 as

$$F_3 = \frac{b_{\rm OA}/m_{\rm OA}}{b_3/m_3}\,\frac{\rho_{\rm OA}}{\rho_3} \tag{4.7}$$

where $b_{\rm OA}$ (b_3) is the number of Raman active bonds in OA (chromatin) in the IFD range measured, $m_{\rm OA}$, m_3 is the molecular weight of OA (chromatin) and $\rho_{\rm OA}$ (ρ_3) is the density of OA (chromatin). The area of the OA spectrum in the IFD range 2650 - 3100 cm^{-1} is 797 cm^{-1}, $b_{\rm OA}/m_{\rm OA} = 0.12$ and $\rho_{\rm OA} = 0.895\,\mathrm{g}/\mu\mathrm{m}^3$. The dry factor, for the i-th FSC^3 component is defined as

$$\gamma_{\rm dry} = \frac{\mathrm{A}_i}{\mathrm{A}_{\rm OA}} F_i \tag{4.8}$$

Table 4.3 shows the bonds/molecular weight, b/m of three cellular macromolecules i.e., protein, DNA and oleic acid. The bond structures and the counting of the Raman active bonds in these molecules are exemplified in Appendix C. In these calculations, the four constituent bases of DNA were considered to occur in equal proportions. While calculating the b/m for the protein component, relative abundance of twenty amino acids [143] which make up the proteins were taken into account. The b/m of the most common lipids in cells, palmitic acid (PA) and stearic

acid (SA) [144] are also given. The spectral ranges of integration vary for different

Macromolecule	b	m (a.m.u)	b/m (1/a.m.u)
Protein	6	128.44	0.047
DNA/base-pair	18	651.52	0.027
Palmitic acid	31	256.42	0.121
Stearic acid	35	284.48	0.123
Oleic acid	33	282.46	0.117

Table 4.3: Number of bonds b, molecular weights m and the number of bonds/molecular weight for protein, DNA, and some common lipids (palmitic, stearic and oleic acids) in cells.

FSC^3 components to include the organic component of the respective component. The rescaling factors α, the areas A_i over the specified IFD range, the factors F and the dry factors γ_{dry} corresponding to the FSC^3 components 1-4 shown in Fig. 4.13 are given in Table 4.4. Chromatin, corresponding to $\mathcal{C}_3$ is a mixture of protein and DNA in a 2:1 ratio [80]. The factor F_3 was calculated using the density of chromatin estimated to be $1.5\,\text{pg}/\mu\text{m}^3$ as a weighted average of the protein density, $1.3\,\text{pg}/\mu\text{m}^3$ [145] and DNA density, $2\,\text{pg}/\mu\text{m}^3$ [145]. For lipids, F_4 was calculated using an average of the densities of OA, PA and SA. As listed on PubChem (National Center for Biotechnology Information), palmitic [146] (stearic [147]) acid has a density of $0.85\,\text{pg}/\mu\text{m}^3$ ($0.94\,\text{pg}/\mu\text{m}^3$) resulting in an average density of $0.89\,\text{pg}/\mu\text{m}^3$ which is similar to the density of oleic acid, $0.89\,\text{pg}/\mu\text{m}^3$. The factors F remain the same for the respective components attributed to protein, chromatin or lipid in all calculations shown henceforth while the areas and consequently, γ_{dry} vary.

$\mathcal{C}_i$	α	IFD range (cm^{-1})	A_i (cm^{-1})	F_i	γ_{dry}	Localization
$\mathcal{C}_1$	0.68	2815 - 3050	22	1.76	0.049	Protein
$\mathcal{C}_2$	1.15	2910 - 2985	4.95	1.76	0.011	Protein
$\mathcal{C}_3$	2	2860 - 3050	50	1.78	0.113	Chromatin
$\mathcal{C}_4$	1.3	2815 - 3050	124	1	0.156	Lipid

Table 4.4: Calculation parameters and dry factors corresponding to the FSC^3 components 1-4 shown in Fig. 4.13 corresponding to protein ($\mathcal{C}_{1,2}$), chromatin ($\mathcal{C}_3$) and lipid ($\mathcal{C}_4$).

4.4.3 Simultaneous factorization over limited IFD range

The factorization over a large spectral range of data as exemplified in Fig. 4.13 is dominated by the water resonance. Additionally, simultaneous factorization of data using an extended IFD range does not converge to one spectral basis due to small differences in the water/dry component ratio attributed to the small differences between individuals of the cell population. It has been discovered through experience that limiting the IFD range of the FSC^3 analysis is one way to reduce the influence of the dominant water component in favour of the dry components of interest. Therefore, in all the subsequent analysis shown in this work, we choose the spectral range analyzed with FSC^3 to exclude most of the water response.
The results of a simultaneous factorization of three data sets corresponding to cells

in metaphase (shown in Fig. 4.13), anaphase and cytokinesis over a limited IFD range of 2750 - 3200 cm^{-1} are shown and discussed below. The settings used for this factorization are given in Table D.7. The total number of FSC^3 components used in this factorization was seven, of which only four are shown in this section. The other components (shown in Fig. D.7 - Fig. D.9) include the two components attributed to water and one to systematics.

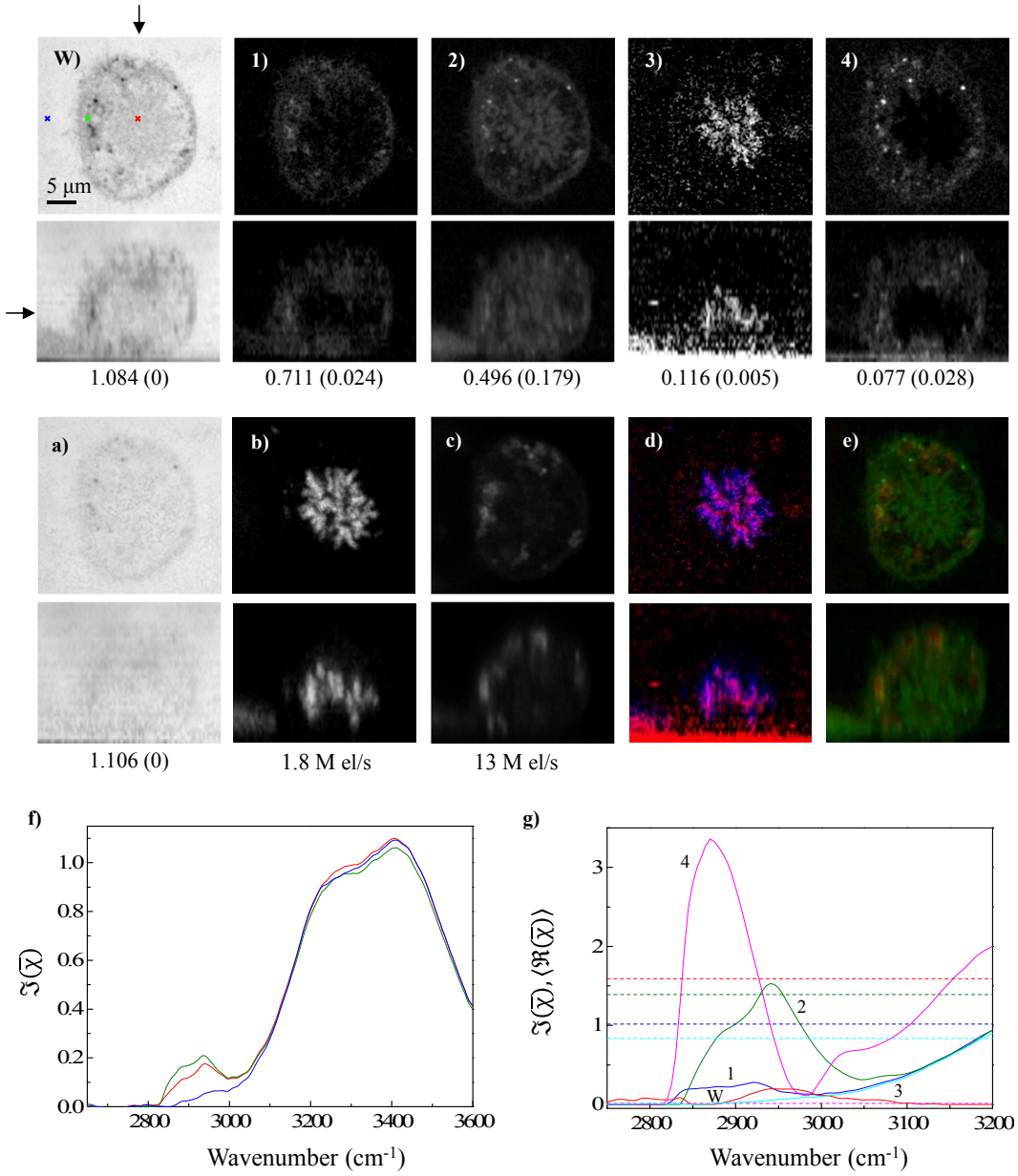

Figure 4.15: FOV 6: FSC^3 concentrations and spectra of a U-2OS cell in metaphase. *xy* and *xz* sections of concentrations of components W,1,2,3,4, corresponding to sum water, lipid, protein, chromatin and lipid respectively. Grayscales as in Fig. 4.4. Image a) shows the total concentration of water in the sample. Images b), c) : TPF of DAPI and Mitotracker respectively. d) is a colour overlay of 3 in red and b in blue channel respectively. e) shows 2 in green and c in red channel. The PCKK spectra taken at the colour coded points marked on image W are given in f). g) shows the FSC^3 spectra corresponding to images W,1,2,3,4.

In Fig. 4.15, a U-2OS cell in metaphase (stage evident by the shape of the cell and the condensed chromatin in the middle of the cell) is visible. The four relevant components corresponding to two components of lipid (1, 4), and one component each corresponding to protein (2) and chromatin (3) are shown. The sum water spectrum is given in W. f) shows the retrieved spectra at the three points colour coded in W. While spectral differences at this stage of the analysis are subtle, they become more apparent after factorization using FSC^3 as shown in g). Image a) in Fig. 4.15 is the total concentration map of water, calculated by adding the $\mathcal{C}_{\mathrm{W}}$ and the wet factors (γ_{wet}) weighted images 1, 2, 3 and 4. γ_{wet} were calculated complementary to the dry factors as, $\gamma_{\mathrm{wet}} = 1 - \gamma_{\mathrm{dry}}$. γ_{dry} for this factorization calculated as described in section 4.4.2.1 and are given in Table 4.5. The wet factors were calculated for the various organic components 1-4 of this FSC^3 analysis as 96%, 62%, 94% and 62%. a) shows a homogeneous distribution across the cell with a slightly negative contrast in the regions corresponding to the lipid and chromatin components. A comparison of the results of TPF and FSC^3 analysis of CARS is shown in images b)-e) in Fig. 4.15. Good colocalization of the spatial concentration map of $\mathcal{C}_3$ (shown on red channel) with the DAPI fluorescence image (blue channel) is observed in d). The colour overlay of mitotracker-orange fluorescence (red channel) and $\mathcal{C}_2$ (green channel) shown in image e) shows that mitochondria are not detected in FSC^3 as a specific chemical component, but as a part of the protein component, localized in the cytosol.

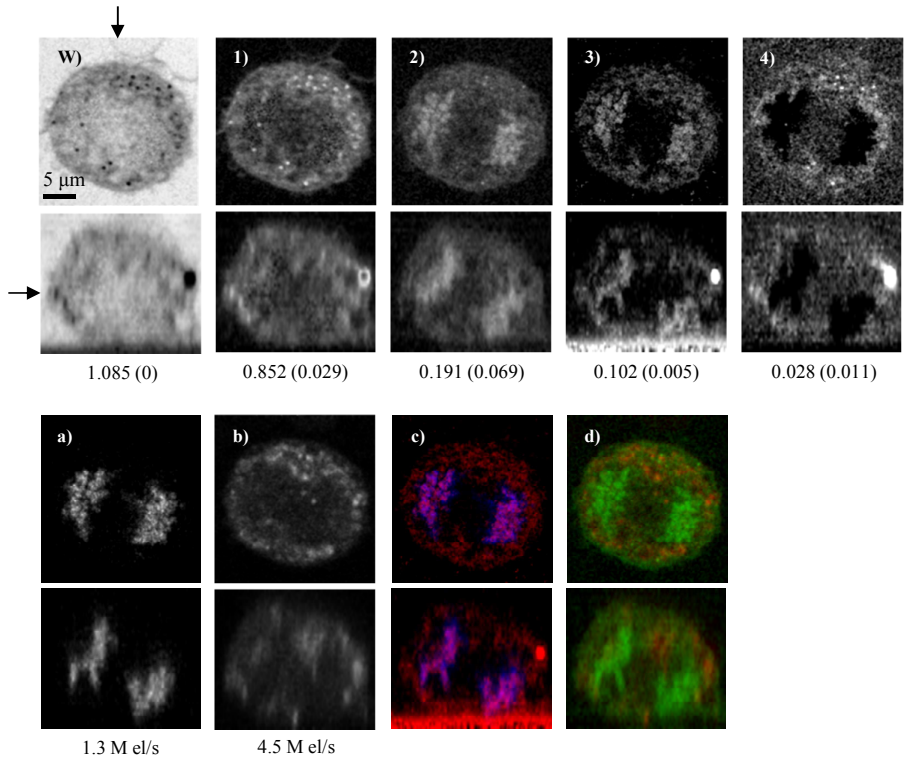

Figure 4.16: FOV 7: FSC^3 analysis and TPF imaging of a U-2OS cell in anaphase. Images W,1,2,3,4 (sum water, lipid, protein, chromatin and lipid respectively) are the *xy* and *xz* sections of FSC^3 components corresponding to the spectra shown in Fig. 4.15 g). Grayscales as in Fig. 4.4. Images a) and b) are the *xy* and *xz* sections of the TPF images of DAPI and mitotracker-orange respectively. c) shows the TPF image of DAPI in blue and $\mathcal{C}_3$ in red. d) is a colour overlay of mitotracker-orange TPF (red) and $\mathcal{C}_2$ (green).

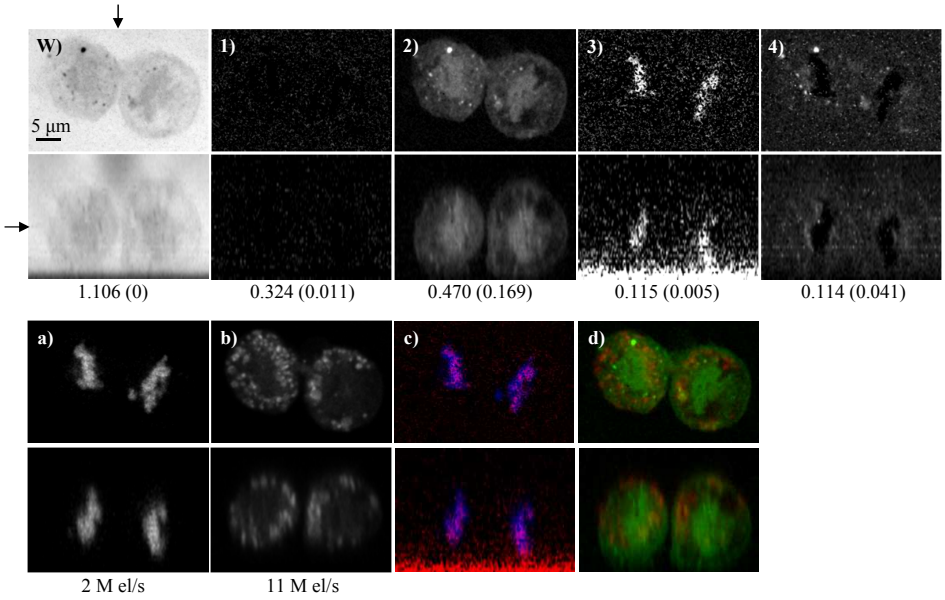

Figure 4.17: FOV 8: FSC^3 components W,1,2,3,4 corresponding to sum water, lipid, protein, chromatin and lipid respectively, and TPF images of U-2OS cells in cytokinesis. Panel description same as Fig. 4.16. Aqcuired using 6 cm^{-1} IFD step size.

In Fig. 4.16, a cell in anaphase is shown, analyzed simultaneously with the metaphase cell shown in Fig. 4.15. The genetic material is distributed at the two poles of the slightly oval shaped cell- a characteristic feature of cells in this stage of mitosis.
Fig. 4.17 shows two recently divided cells still connected to each other by the midbody, also known as the Flemming body. The midbody often appears between two daughter cells shortly before cytokinesis is completed [111]. As observed for the cells in metaphase and anaphase shown previously, for the cells in cytokinesis also, the FSC^3 concentration distribution of component 3 is well correlated with the fluorescence image of DAPI.

4.4.3.1 Volumetric calculations

Volume calculations to estimate the mass of the organic FSC^3 components in all the cells were made in two sets corresponding to two regions of interest i.e., 1) nuclear volume and 2) whole cell volume. The TPF images of DAPI were used to define the region of interest (ROI) to include only the regions corresponding to DNA (or chromatin), and measure (using ImageJ) the integrated value of each z slice over the specific ROI. To define full cell volumes, the cell perimeters visible in $\mathcal{C}_2$ were used. The raw intensities are defined as the sum of the gray values of pixels contained in the ROI. When summed over the z-stack, the raw intensities represent the dry volume concentrations, V_i of the FSC^3 component $\mathcal{C}_i$ as

$$V_i = \frac{c\, I_i\, V_0}{65535} \gamma_{\mathrm{dry},i} \tag{4.9}$$

where I_i is the sum of the pixel values over the z stack of $\mathcal{C}_i$, c is the maximum concentration (in this factorization $c = 1.106$), V_0 is the pixel volume, 65535 is the maximum pixel value in the 16 bit image and $\gamma_{\mathrm{dry,i}}$ is the dry factor for the particular FSC^3 component. The areas of the dry spectra of the FSC^3 components were

calculated over an IFD range of 2750 - 3050 cm^{-1} for $\mathcal{C}_{1,2,4}$ and over 2860 - 3050 cm^{-1} for $\mathcal{C}_3$. The dry weights of the interesting FSC^3 components, given by $M_i = V_i\,\rho_i$ were then calculated.
The results of these volumetric calculations over the nuclear and whole cell ROIs are tabulated in Table 4.5 and Table 4.6 respectively. The v/v concentrations representing the ratio of V_i to the ROI volume, V_{ROI} are also given.
One error in these volumetric calculations is due to an inexact matching of the average water spectrum with the water part of the component spectra. This is shown in Fig. 4.14, where the rescaled water spectrum (purple) generally matches the water part of the FSC^3 component corresponding to chromatin but is slightly unmatched at certain wavenumbers (3050 -3150 cm^{-1}). This results in an error, $\Delta\mathrm{A}_i$ in the area of the dry parts of the components,

$$\Delta\mathrm{A}_i = \mathrm{A}_{\mathrm{W}\alpha}\,U \tag{4.10}$$

where $\mathrm{A}_{\mathrm{W}\alpha}$ is the area of the rescaled water spectrum in the IFD range over which the dry areas are calculated, and U is the relative error in the matching of the rescaled water with the water part of the component spectra. The errors in dry volumes are calculated as $\Delta V_i = V_i\Delta\mathrm{A}_i/\mathrm{A}_i$.
Note that the values of the dry volumes reported for the cells in cytokinesis (Fig. 4.17) are divided by two to present the results for each of the daughter cells. From here onwards, the volumetric results for all the cells which are treated as two due to their being in cytokinesis (or more for showing more than one distinct nucleus) will be marked with an $*$. Additionally (for this calculation and the others shown in this thesis), α and A_i in the relevant IFD ranges for the intracellularly localized FSC^3 components are given in Appendix C. Table 4.5 shows that as expected, the nuclei contain low levels of lipids by mass. We observe that the composition of the intranuclear region in the cells is actually dominated by protein ($\mathcal{C}_2$) and not chromatin ($\mathcal{C}_3$). On the other hand, the chromatin component occurs colocalized within

Data	$\mathcal{C}_i$	γ_{dry}	$V_i \pm \Delta V_i$ ($\mu\mathrm{m}^3$)	V_i/V_{ROI} (%)	Mass (pg)	Localization
Fig. 4.15	1	0.034	1.72 ± 0.02	0.18	1.5	Lipid
(Metaphase)	2	0.360	32.4 ± 0.3	3.29	42.1	Protein
	3	0.047	1.0 ± 0	0.1	1.5	Chromatin
	4	0.363	1.74 ± 0.04	0.18	1.6	Lipid
Fig. 4.16	1	0.034	5.95 ± 0.06	0.88	5.3	Lipid
(Anaphase)	2	0.360	17.6 ± 0.2	2.60	22.8	Protein
	3	0.047	0.92 ± 0	0.14	1.4	Chromatin
	4	0.363	0.81 ± 0.02	0.12	0.7	Lipid
Fig. 4.17 $*$	1	0.034	0.0387 ± 0.0004	0.01	0.03	Lipid
(Cytokinesis)	2	0.360	18.1 ± 0.2	5.70	23.5	Protein
	3	0.047	0.34 ± 0	0.11	0.5	Chromatin
	4	0.363	1.00 ± 0.02	0.32	0.9	Lipid

Table 4.5: Results of the volumetric calculations of $\mathcal{C}_1, \mathcal{C}_2, \mathcal{C}_3$ and $\mathcal{C}_4$ of labelled U-2OS cells in various stages of mitosis, over the nuclear volume. The last column shows the cell compartments to which the respective FSC^3 components are attributed. * indicates that the values reported are in units of value/cell as there is more than one cell in the field of view.

the nucleus, but with a mass of ~ 1 pg, which is significantly lower than the known DNA content of a diploid cell (5 - 7 pg before, and 10 - 14 pg after the S phase [80]). We attribute this to the fact that only one of the four DNA bases (thymine) are detected using CARS in the spectral range analyzed. We observe that (see Table 4.5) the intranuclear protein content is the maximum in the metaphase cell (twice that in the case of anaphase and cytokinesis cells which have similar intranuclear protein masses). This is consistent with the fact that the metaphase chromosomes are the most condensed (recall that DNA condensation is accomplished through different types of proteins); and in contrast with the work of Pliss et al. [16] who reported no CARS observable correlation between intranuclear protein content and the mitotic stage of the cell. On examining the sum of the masses of the intranuclear protein and chromatin components, we calculate 43.6 pg for the metaphase, 24.2 pg for the anaphase and 24 pg for the cytokinesis cells. As described in section 2.2, and considering the ratio of DNA : Protein (1:2) in chromatin, used in the calculation of the dry factors detailed in section 4.4.2.1, the mass of chromatin in mitotic cells (with double the DNA content compared to a diploid G_1 cell), varies between 30 - 42 pg (considering 10 - 14 pg of DNA per mitotic cell). Despite the factorization of the cell composition into impure components, the sum of the masses of the FSC^3 components corresponding to chromatin and protein within the nuclear volumes in all the three cells, are in close agreement with the literature values of the mass of chromatin in a cell. Furthermore, the masses of the protein content over the nuclear volume are also consistent with the known biological facts about mitosis.
On considering the full cell volumes for volumetric and mass calculations (see Table 4.6), we find that as expected, protein dominates the cell composition followed by lipids. Furthermore, the metaphase cell shows the maximum proteic content in the sample set, even over the entire cell volume. The masses of the chromatin component are larger than those shown in Table 4.5 due to the fact that this is a particularly noisy component (see the concentration maps) and also not well factorized. The other two components are relatively purer and can be trusted more.

Data	$\mathcal{C}_i$	γ_{dry}	$V_i \pm \Delta V_i$ (μm^3)	V_i/V_{ROI} (%)	Mass (pg)	Localization
Fig. 4.15 (Metaphase)	1	0.034	10.81 ± 0.1	0.22	9.7	Lipid
	2	0.360	133 ± 1	2.69	173	Protein
	3	0.047	2.52 ± 0	0.05	3.8	Chromatin
	4	0.363	17.2 ± 0.4	0.35	15.4	Lipid
Fig. 4.16 (Anaphase)	1	0.034	40.9 ± 0.4	0.85	36.6	Lipid
	2	0.360	74.1 ± 0.6	1.55	96.3	Protein
	3	0.047	4.04 ± 0	0.08	6.1	Chromatin
	4	0.363	11.7 ± 0.3	0.25	10.5	Lipid
Fig. 4.17* (Cytokinesis)	1	0.034	0.487 ± 0.005	0.02	0.4	Lipid
	2	0.360	87.2 ± 0.7	3.11	113.3	Protein
	3	0.047	1.72 ± 0	0.06	2.6	Chromatin
	4	0.363	16.5 ± 0.4	0.59	14.7	Lipid

Table 4.6: Results of the volumetric calculations of $\mathcal{C}_1, \mathcal{C}_2, \mathcal{C}_3$ and $\mathcal{C}_4$ of labelled U-2OS cells in various stages of mitosis, over the full cell volume. * indicates that the values reported are in units of value/cell as there is more than one cell in the field of view.

As shown in this section, we can use CARS microscopy and FSC^3 analysis to confirm the already known information about the chemical composition of cells in a label-free, non-invasive way. Typically, highly invasive and destructive methods like mass spectrometry which involve centrifugation of the samples are used to determine such masses. Therefore, CARS microscopy in the form presented in this work is a significant advancement in the field of biology, producing quantitative results demonstrably consistent with the known facts. However, the components detected are impure as already discussed, making the interpretation of the results difficult. Furthermore, the FSC^3 spectra and the corresponding concentration maps are expected to vary especially for the chemical species with low signal to noise ratio, for example chromatin. Consequently, two different factorizations cannot be compared and it becomes necessary to analyze all the data which require a comparative analysis simultaneously. This will be demonstrated in the next section through an alternate simultaneous factorization of the three data sets.

4.4.3.2 CARS-TPF correlation

To study the correlation between $\mathcal{C}_3$ colocalized to the nuclear region/DNA ($\mathcal{C}_2$ homogeneous over the cell) and DAPI (mitotracker-orange) TPF, background subtracted TPF intensities were plotted against component concentrations. The region of interest for this analysis was chosen to exclude the area outside the cells. The correlation plots (analyzed using 50×50 bins) for the cell in metaphase (FSC^3 analysis in Fig. 4.15) are shown in Fig. 4.18. Fig. 4.18 a (b) shows the correlation of DAPI fluorescence with $\mathcal{C}_3(\mathcal{C}_2)$, respectively. While plot a shows the correlation between DAPI and $\mathcal{C}_3$, b shows some correlation between mitotracker and $\mathcal{C}_2$. Plot c compares $\mathcal{C}_3$ with mitotracker-orange TPF intensities, and shows little correlation between the two, as expected because $\mathcal{C}_3$ is localized within the nuclear regions while mitotracker-orange is specific to mitochondria.

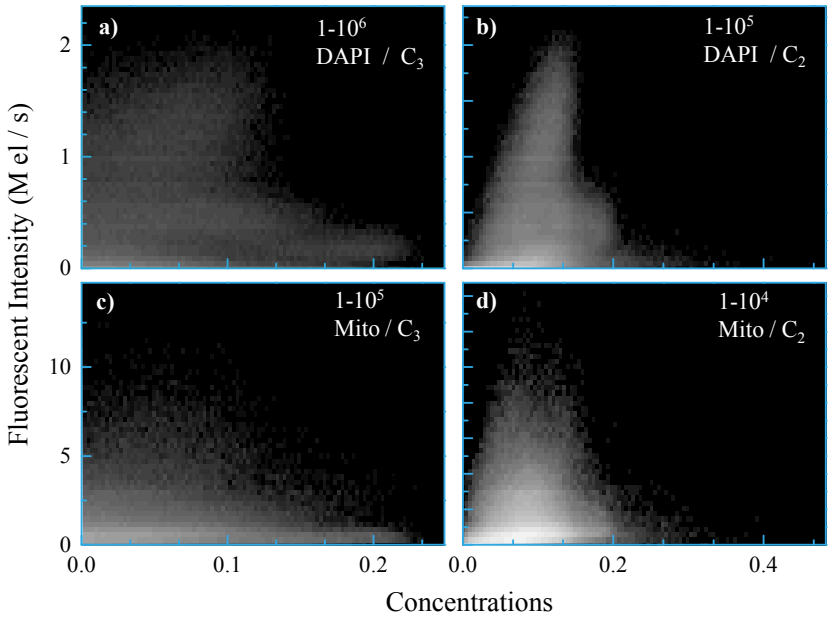

Figure 4.18: Colocalization analysis of TPF and FSC^3 components for the U-2OS cell in metaphase, shown in Fig. 4.15. Logarithmic grayscales with ranges as indicated. a) and b): DAPI TPF versus FSC^3 component $\mathcal{C}_3$ and $\mathcal{C}_2$ respectively. c) and d): mitotracker-orange TPF versus $\mathcal{C}_3$ and $\mathcal{C}_2$ respectively.

The mitotracker/$\mathcal{C}_2$ plot (d) shows correlation between the two images, which is attributed to the homogeneously distributed $\mathcal{C}_2$, and mitochondria specific mitotracker.
The results of a similar analysis for the cells in anaphase and cytokinesis are shown in Fig. 4.19 and Fig. 4.20 respectively.

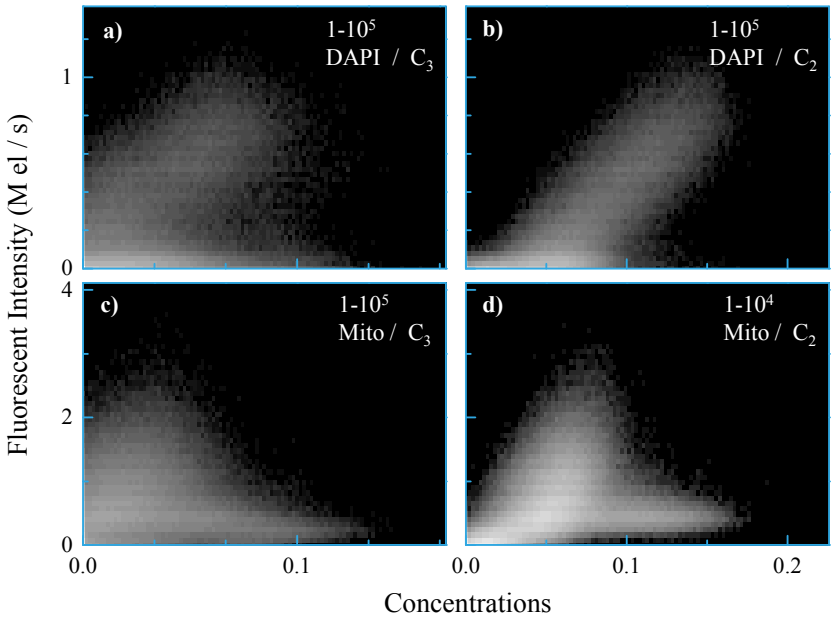

Figure 4.19: Colocalization analysis of TPF and FSC[3] components for the anaphase cell shown in Fig. 4.16. Layout as Fig. 4.18.

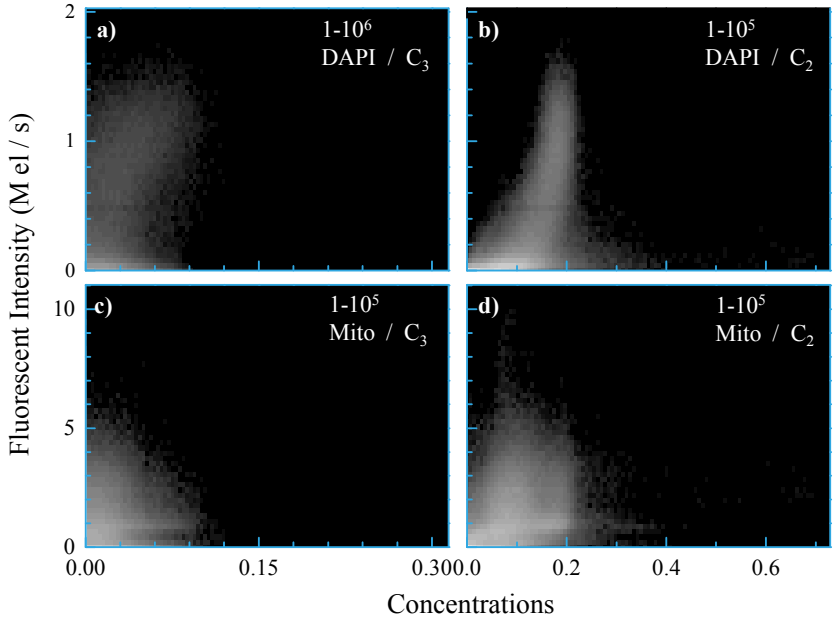

Figure 4.20: Colocalization analysis of TPF and FSC[3] components for the cytokinesis cells shown in Fig. 4.17. Layout as Fig. 4.18.

Alternate FSC^3 factorization of data analyzed simultaneously

Systematic errors present in the data can dominate the small fractions of the organic components, leading to significant errors in the factorized components. Since these systematic errors are not following the constraints of the factorization, they can also lead to non-convergence of the FSC^3 algorithm. To demonstrate the possible variability of the resultant factorization owing to random initial guesses as well as the systematic errors which become important specifically for components with small signal to noise ratio (example, chromatin), another factorization of the three data sets analyzed together is shown with a spectral range of 2750 - 3100 cm^{-1}.
As in the previous results shown in this work, we factorize the chemical composition of the cells into a total of seven components of which three components shown (images 1-3 in Fig. 4.21) correspond to protein, chromatin and lipid respectively. The sum water component, W is also shown. The factorization settings used in this analysis are given in Table D.8. The components attributed to water (two), glass (one) and systematics (one) are shown in Fig. D.10 - Fig. D.12.

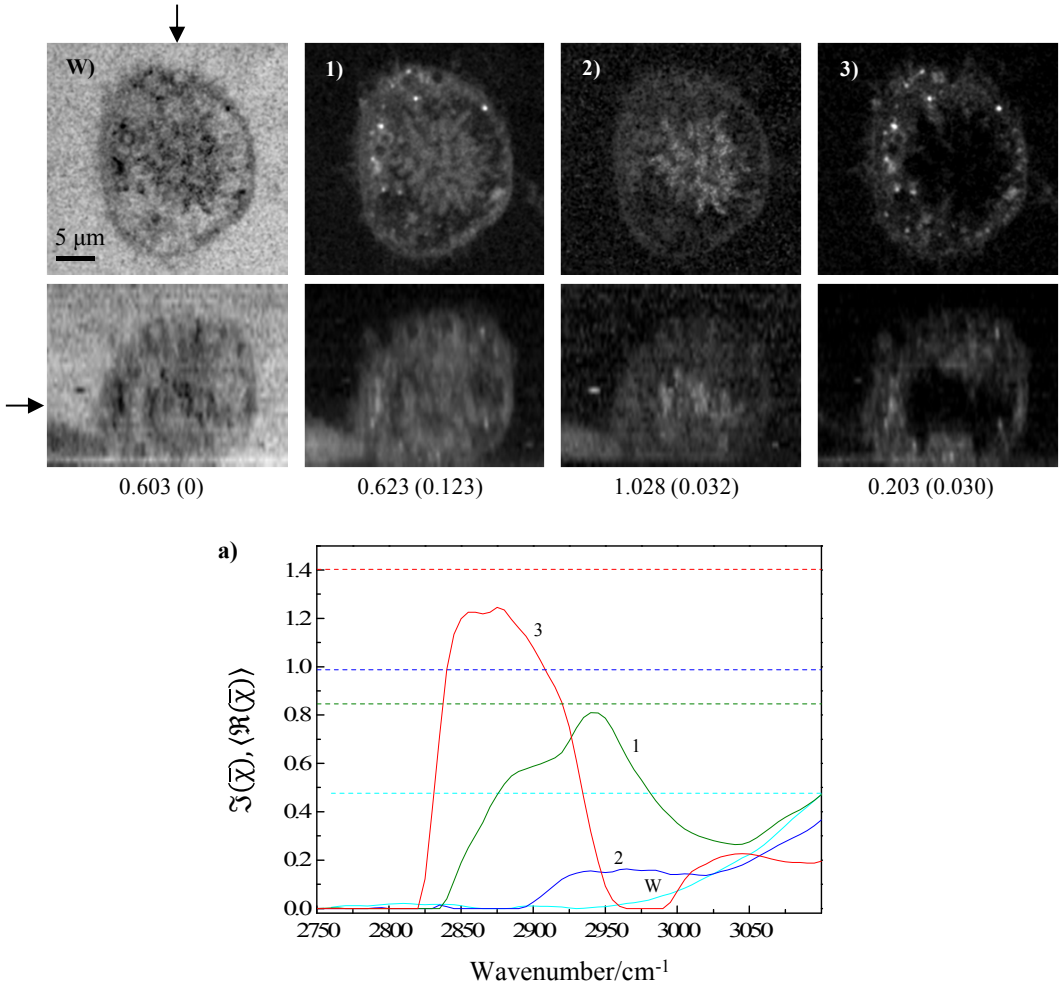

Figure 4.21: FSC^3 concentrations and spectra of a U-2OS cell in metaphase. Images W,1,2,3 are the *xy* and *xz* sections of FSC^3 concentrations attributed to sum water, protein, chromatin and lipid respectively. Grayscales as in Fig. 4.4. FSC^3 spectra corresponding to the images are shown in a).

The other two cells simultaneously analyzed with the metaphase cell are shown in Fig. 4.22 and Fig. 4.23.

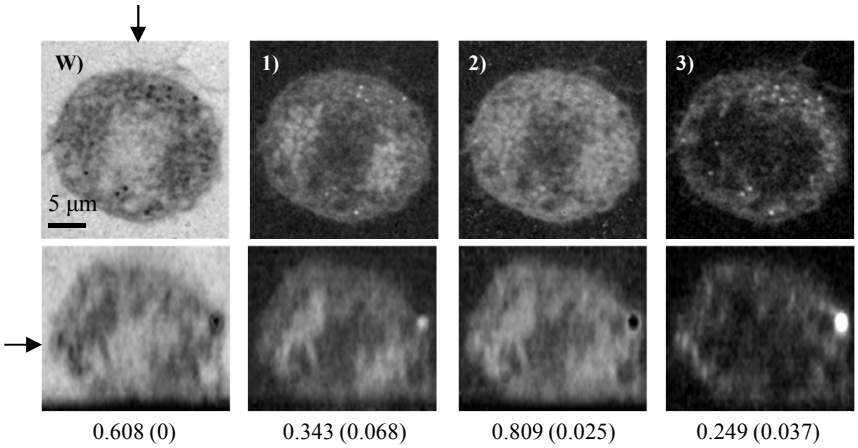

Figure 4.22: FSC^3 concentrations of a U-2OS cell in anaphase. W,1,2,3 are attributed to sum water, protein, chromatin and lipid respectively. Panel description and component spectra the same as in Fig. 4.21.

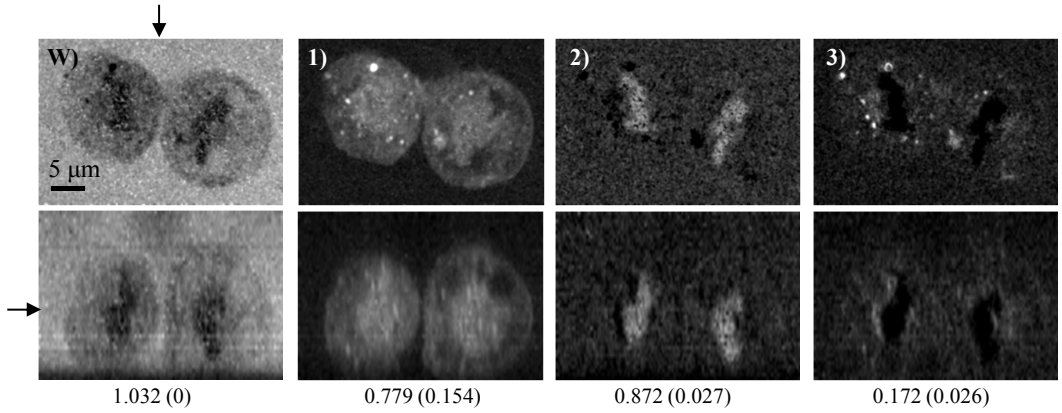

Figure 4.23: FSC^3 concentrations and spectra of U-2OS cells in cytokinesis. W,1,2,3 are attributed to sum water, protein, chromatin and lipid respectively. Panel description and component spectra the same as in Fig. 4.21.

Calculations to estimate the mass of components 1-3 were made as described for the other simultaneous factorization shown in the previous section. The IFD range over which the water subtracted FSC^3 spectra were integrated was 2800 - 3050 cm^{-1} for $\mathcal{C}_{1,3}$ and 2890 - 3050 cm^{-1} for $\mathcal{C}_2$. The results of the volumetric analysis of this simultaneous factorization are summarized in Table 4.7 and Table 4.8 for analysis over the nuclear and full cell volumes respectively. Note that in these results, three organic components have been factorized, compared to the four components in the previous factorization. Such differences in factorization are typical of measurements taken on systems containing components with small signal/noise ratios. On making volumetric calculations, we find that the results are different from the previous factorization, which reiterates our claim of incomparability of any two factorizations on these measurements. Notwithstanding the differences in the two factorizations, we find consistent results correlating the mass of intranuclear protein with the mitotic stage of the cell i.e., maximum intranuclear protein in metaphase, as shown in Table

4.7.

Data	$\mathcal{C}_i$	γ_{dry}	$V_i \pm \Delta V_i$ (μm^3)	V_i/V_{ROI} (%)	Mass (pg)	Localization
Fig. 4.21	1	0.198	35.04 ± 0.06	3.57	45.6	Protein
(Metaphase)	2	0.031	7.5 ± 0.1	0.77	11.3	Chromatin
	3	0.150	2.81 ± 0.01	0.29	2.5	Lipid
Fig. 4.22	1	0.198	21.94 ± 0.04	3.25	28.5	Protein
(Anaphase)	2	0.031	8.4 ± 0.1	1.24	12.5	Chromatin
	3	0.150	4.64 ± 0.02	0.69	4.1	Lipid
Fig. 4.23∗	1	0.198	19.8 ± 0.5	6.25	25.8	Protein
(Cytokinesis)	2	0.031	2.60 ± 0.06	0.82	3.9	Chromatin
	3	0.150	0.591 ± 0.004	0.19	0.6	Lipid

Table 4.7: Results of the volumetric calculations of $\mathcal{C}_1, \mathcal{C}_2$ and $\mathcal{C}_3$ of labelled U-2OS cells in various stages of mitosis, over the nuclear volume. * indicates that the values reported are in units of value/cell as there is more than one cell in the field of view.

Data	$\mathcal{C}_i$	γ_{dry}	$V_i \pm \Delta V_i$ (μm^3)	V_i/V_{ROI} (%)	Mass (pg)	Localization
Fig. 4.21	1	0.198	156.1 ± 0.3	3.16	202.9	Protein
(Metaphase)	2	0.031	26.7 ± 0.4	0.54	39.9	Chromatin
	3	0.150	22.60 ± 0.08	0.46	20.1	Lipid
Fig. 4.22	1	0.198	112.1 ± 0.2	2.34	145.8	Protein
(Anaphase)	2	0.031	47.2 ± 0.7	0.99	70.7	Chromatin
	3	0.150	38.2 ± 0.1	0.80	33.9	Lipid
Fig. 4.23∗	1	0.198	118.5 ± 0.5	4.23	154.1	Protein
(Cytokinesis)	2	0.031	11.2 ± 0.3	0.40	16.8	Chromatin
	3	0.150	10.28 ± 0.07	0.37	9.1	Lipid

Table 4.8: Results of the volumetric calculations of $\mathcal{C}_1, \mathcal{C}_2$ and $\mathcal{C}_3$ of labelled U-2OS cells in various stages of mitosis, over the full cell volume. * indicates that the values reported are in units of value/cell as there is more than one cell in the field of view.

Further, regardless of the differences between any two factorizations, CARS microscopy represents a valuable tool for generating label-free morpho-chemical contrast of the constituent chemical species in a quantitative way. In other words, while the FSC^3 components designated as protein/lipid/chromatin in this work are not correlated with pure chemical species, the method itself is useful in quantitatively comparing biological materials on an absolute scale in terms of the factorized FSC^3 components.

4.5 CARS microscopy of U-2OS cells treated with anti-cancer drugs

The FSC^3 analysis of unstained U-2OS cells as shown in section 4.3 demonstrated the capability of CARS microscopy and HIA to discriminate protein (cytosol), lipid and genetic/nuclear components of fixed cells. By using DAPI fluorescent staining, we have also demonstrated that a chemical component is colocalized within and originates from the intracellular nuclear compartment or DNA (see section 4.4).
From the point of view of drug discovery and delivery, and treatment viability, the study of cell populations following treatment with various drugs is a topic of great interest. In this section, we show the results of application of CARS microscopy to study the effects of drugs on a cellular level long after they are withdrawn from the system. The relevant questions that biochemistry studies of cellular response to treatment with anti-cancer drugs like Taxol and ICRF-193 can answer, will influence the development of future treatment methods in the event of cancer relapse, or other diseases. CARS microscopy was used to study two types of fixed U-2OS cell samples which were treated with drugs prior to fixation (well plates D1 and D2, see Table 4.1). The first set of samples in well plate D1 was treated with 5 nM Taxol for 24 hours and then fixed after washing with PBS. The second set of samples was treated with 2 μg/ml of ICRF-193 for 24 hours and subsequently fixed after various time lengths following treatment (0 hours, 120 hours and 168 hours), in well plate D2.

4.5.1 CARS imaging of cells treated with Taxol

4.5.1.1 Background

Reported in 1971 by Wani et al. [148], Taxol is a derivative of the bark of the Pacific Yew (*Taxus brevifolia*) and possesses antileukemic activity. Taxol promotes polymerization of tubulin to form microtubules in vitro [149] and *in vivo* [17, 18, 150]. At low concentrations, Taxol interferes with microtubule dynamics and prevents the attachment of kinetochores to the spindle apparatus resulting in cell cycle arrest in metaphase by activation of the spindle assembly checkpoint [151]. The arrested cells show misalignment of chromosomes off the metaphasic plate [152]. With specific reference to U-2OS (HeLa) cells treated with 5 nM Taxol, 46 % (93%) respectively of the total population of the arrested cells either die in mitosis or eventually escape the mitotic stage and die within 10 hours [153].
Due to its efficacy in arresting the cells in metaphase, Taxol is an important component of anti-cancer chemotherapy. However, all the chemically specific knowledge we have about Taxol and its effects on cells is acquired (see references above), was acquired using invasive methods like fluorescence microscopy at best and destructive methods like Western blotting / electron cryomicroscopy at worst. With its chemical specificity and sensitivity, CARS microscopy can shed light on the biochemical effects of drug treatment on cells, in a non-invasive, non-destructive and label-free way. The effect of Taxol on U-2OS cells was investigated using CARS microspectroscopy, the results of which are shown in the next section.

4.5.1.2 Results

In this section, the results of FSC^3 analysis of one control (not drug treated, well plate B) and two Taxol treated cells from well plate D1 (see section 4.1.1) will be

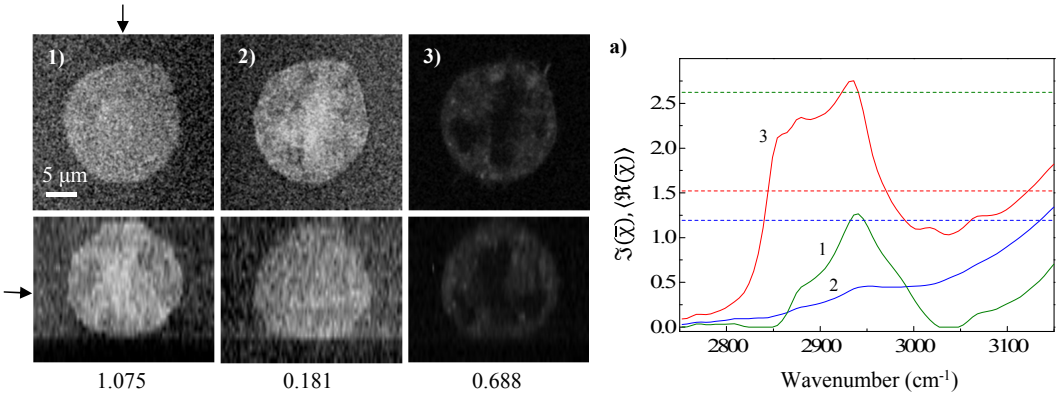

Figure 4.24: FOV 9: FSC^3 analysis of a Taxol treated cell showing xy and xz sections of three concentrations (1-3) corresponding to protein, mixed protein-chromatin, and lipid respectively, with their FSC^3 spectra in a). Grayscales as in Fig. 4.4.

shown. The FSC^3 analysis for these three datasets did not converge to a factorization into all the cell components corresponding to protein, chromatin and lipid which have been consistently found in all previous analyses. As an example, a factorization of one of the Taxol treated cells is shown in Fig. 4.24. Three components (from a total of eight) colocalized intracellularly are shown along with their FSC^3 spectra corresponding to one component of protein which is homogeneous over the whole cell volume ($\mathcal{C}_1$), one component of mixed protein and nuclear material showing a more concentrated distribution in the nuclear region but generally distributed over the entire cell ($\mathcal{C}_2$) and one component corresponding to lipid ($\mathcal{C}_3$). The factorization settings are given in Table D.9, and the other five components corresponding to water (one), glass (one) and glass/water interface (three) are shown in Fig. D.13. A modification of the factorization method, the guided FSC^3 was then used in which a set of FSC^3 spectra are added as additional voxels to form guides (with user defined weights) to 'suggest' to the factorization algorithm the component spectra. The weights $\mathcal{W}$ of the guide spectra in this method correspond to the relative volume fraction of the guides with respect to that of the data being analyzed. The guide spectra are shown in Fig. 4.25.

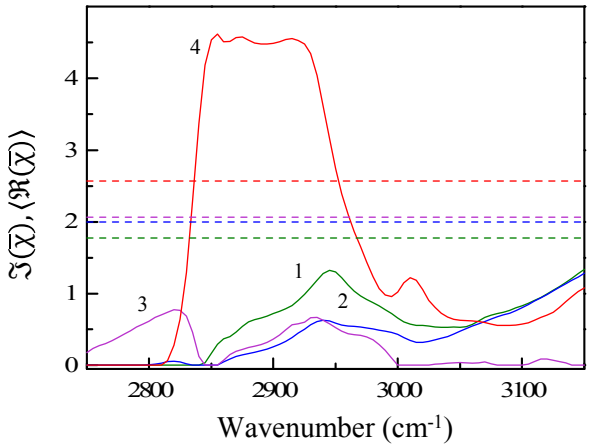

Figure 4.25: Spectra used as guides in the guided factorization method. The factorization from which these guides were obtained is shown in Fig. D.15.

The factorization settings and spatial distributions of concentrations of these guide spectra are given in section D.1.4.1.

The guide spectra were used to guide the following factorizations shown in this section over an IFD range of 2750 - 3150 cm^{-1}.
Fig. 4.26 shows an FSC^3 analysis ($\mathcal{W} = 2.6\%$ for all guides) of a prometaphase cell (control). Of the seven FSC^3 components, the relevant ones corresponding to sum water (W), protein (1), nucleus (2) and lipid (3) are shown here. The other components corresponding to the water (three) and glass are shown in Fig. D.16. The factorization settings are summarized in Table D.12. Fig. 4.27 and Fig. 4.28 show FSC^3 analysis of Taxol treated cells, showing incomplete alignment of the chromosomes on the metaphasic plate, a characteristic effect of Taxol. The cell shown in Fig. 4.27 (analyzed using $\mathcal{W} = 2.5\%$ for all guides) shows an abnormal metaphase wherein the chromosomes appear aligned (see image 3) in a circular contour in contrast to normal metaphase which shows a linear arrangement of the chromosomes on the metaphasic plate of the cell. Additionally, a lipid rich region in the centre of

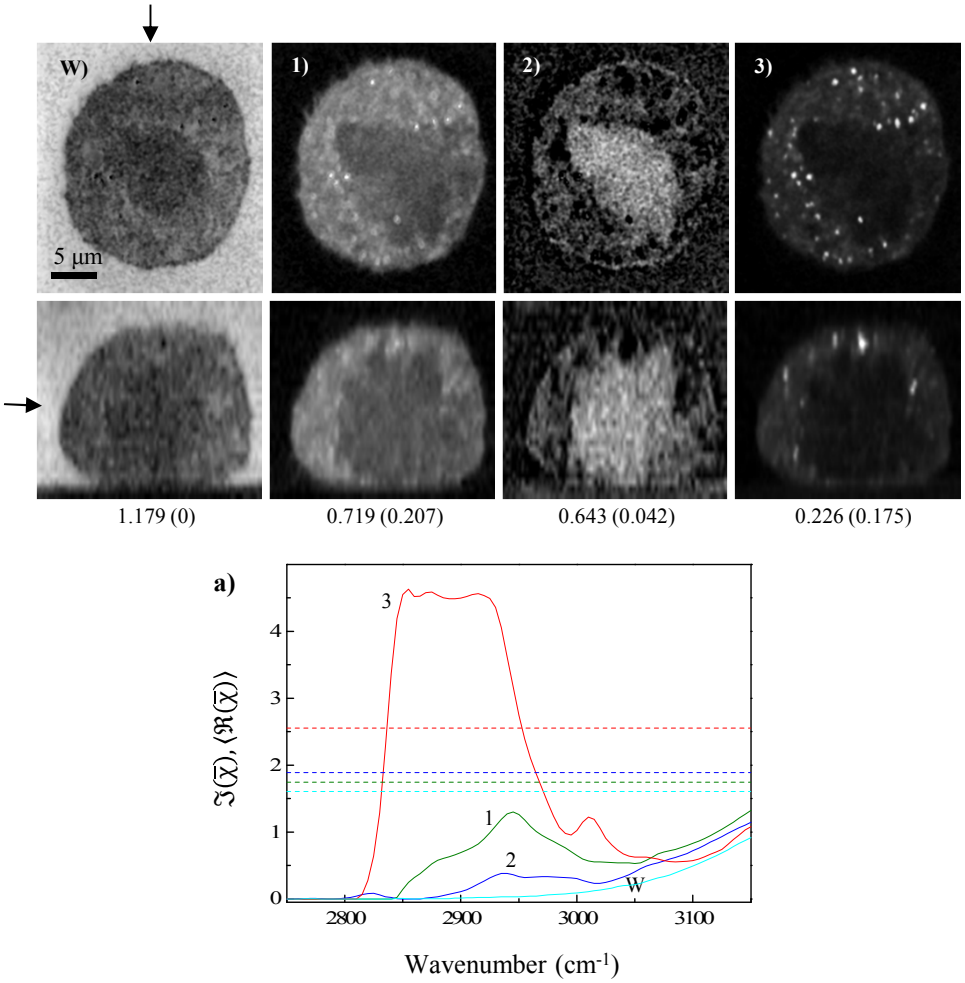

Figure 4.26: FOV 10: FSC^3 analysis of a U-2OS cell (control sample). Images show *xy* and *xz* sections of FSC^3 concentrations (attributed to sum water, protein, chromatin and lipid respectively), with their corresponding spectra in a). This data was acquired with a *z* step size of 0.7 μm. Grayscales as in Fig. 4.4.

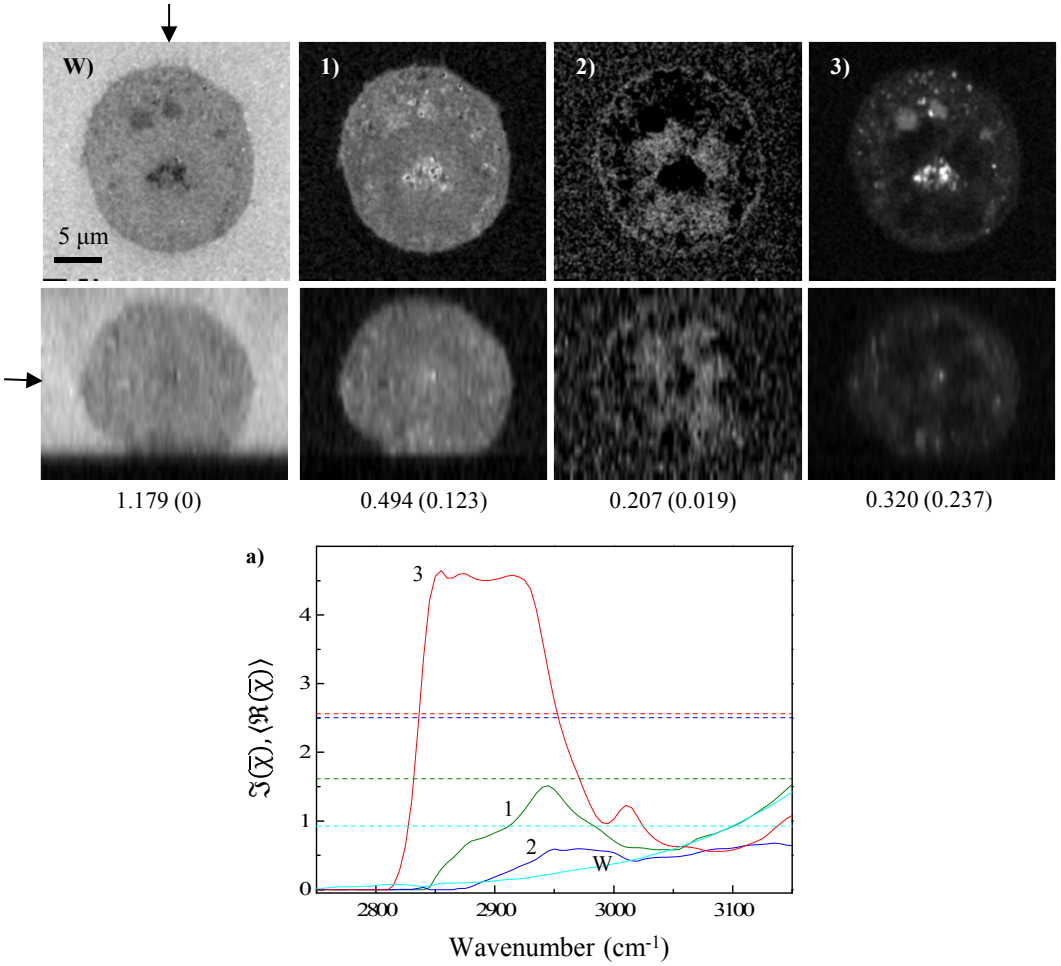

Figure 4.27: FOV 11: FSC^3 analysis of a Taxol treated U-2OS cell. Images W,1,2,3 show xy and xz sections of FSC^3 concentrations corresponding to sum water, protein, chromatin and lipid respectively. Grayscales as in Fig. 4.4 This data was acquired with a z step size of 1 μm. a) shows the component spectra.

the chromosome distribution, corresponding to the clumping of the membranes, is also seen (see images 1 and 3). This feature was not observed before for labelled or unlabelled samples in TPF (mitotracker-orange and DAPI) or CARS microscopy respectively. This data was analyzed using eight FSC^3 components (settings in Table D.13). The five components not shown here are attributed to water (three), glass and systematics. Fig. 4.28 (analyzed using $\mathcal{W} = 1.1\%$ for all guides) shows another Taxol treated cell, with a linear distribution of chromosomes in the equatorial plane of the cell, with some misalignment seen in the mid-left region of the cell in image 2. This factorization was done using eight FSC^3 components (analysis settings in Table D.14) and the FSC^3 components not shown here, corresponding to water (three), glass and systematics are given in Fig. D.18.

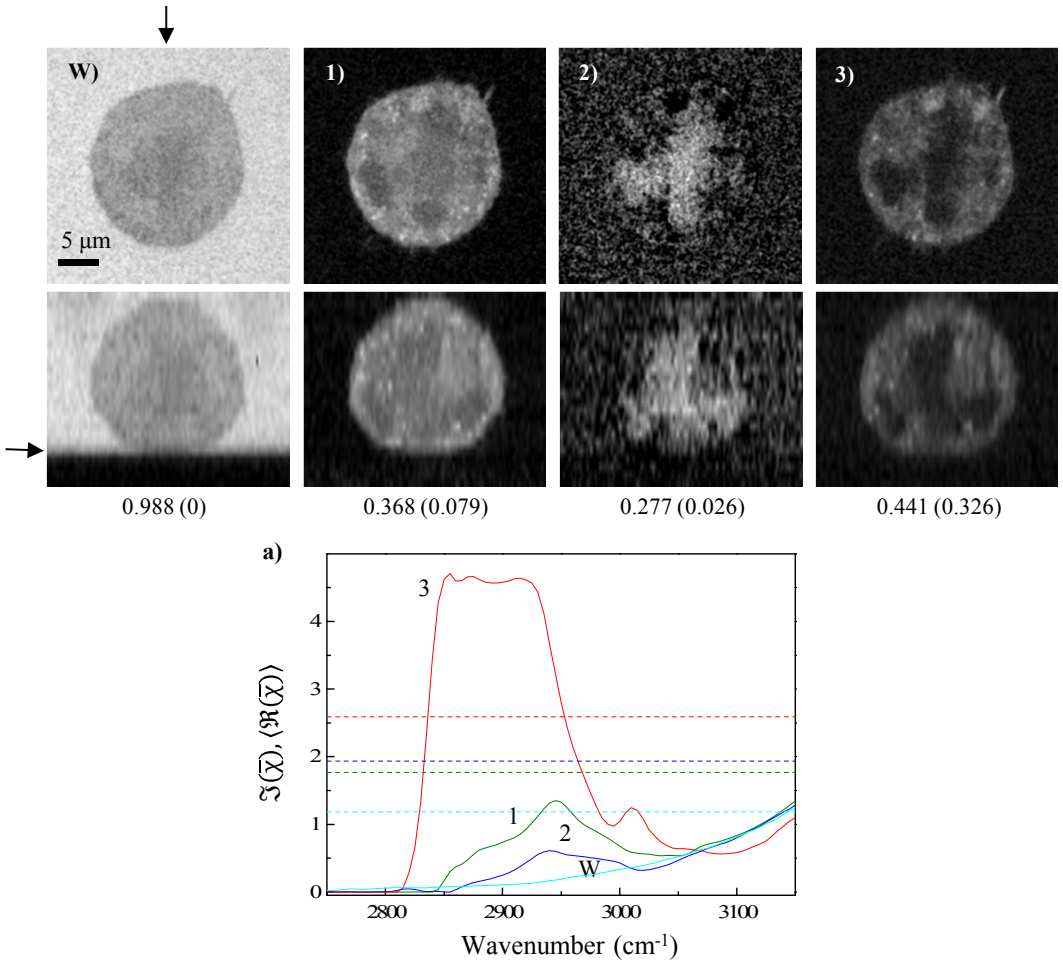

Figure 4.28: FOV 9: FSC^3 analysis of a Taxol treated U-2OS cell. Images W,1,2,3 show *xy* and *xz* sections of FSC^3 concentrations (attributed to sum water, protein, chromatin and lipid respectively) and their corresponding spectra in a). This data was acquired with a z step size of 1 μm. Grayscales as in Fig. 4.4.

Volumetric calculations over the nuclear region and the whole cell were made on all the three cells shown. The IFD ranges over which the water subtracted FSC^3 spectra were integrated to calculate (as described in section 4.4.2.1) the dry factors were 2800 - 3050 cm^{-1} for $\mathcal{C}_{1,3}$ and 2850 - 3030 cm^{-1} for $\mathcal{C}_2$.
The results are tabulated in Table 4.9 and Table 4.10 respectively.
Since the FSC^3 spectra of the components are different for all the cells, the volumes and masses of these components cannot be compared. While we have not observed strong evidence of correlation between Taxol treatment and the lipid content of the cell, the mass of protein confined to the nuclear region is higher in the control sample compared to one Taxol treated cell (by a factor of 7 in the cell shown in Fig 4.27). This result may be significant and warrant further investigation if proven on a larger sample set. Otherwise, as expected, in the nuclear region, protein and chromatin are the most prolific components, followed by lipid. The results over the full cell ROIs show no significant correlation with the status of drug treatment of the cells, but the dominating component (mass/mass) is protein, followed by lipid and chromatin. On examining the factorization results, we observe that the treatment of cells with Taxol prior to fixation causes no detectable spectral changes (in the IFD range mea-

Data	$\mathcal{C}_i$	γ_{dry}	$V_i \pm \Delta V_i$ (μm^3)	V_i/V_{ROI} (%)	Mass (pg)	Localization
Fig. 4.26	1	0.288	99 ± 2	7.11	128.5	Protein
(Control)	2	0.065	26 ± 1	1.87	38.9	Chromatin
	3	0.773	22.78 ± 0.04	1.64	22.8	Lipid
Fig. 4.27	1	0.248	51 ± 1	5.05	65.8	Protein
(Taxol treated)	2	0.095	6.2 ± 0.9	0.62	9.3	Chromatin
	3	0.741	23.1 ± 0.1	2.30	20.6	Lipid
Fig. 4.28	1	0.217	38.5 ± 0.3	3.45	17.8	Protein
(Taxol treated)	2	0.098	13.7 ± 0.3	1.23	37.2	Chromatin
	3	0.739	24.8 ± 0.2	2.23	22.2	Lipid

Table 4.9: Results of the volumetric calculations of $\mathcal{C}_1, \mathcal{C}_2$ and $\mathcal{C}_3$ of Taxol treated cells and control sample over the nuclear volume.

Data	$\mathcal{C}_i$	γ_{dry}	$V_i \pm \Delta V_i$ (μm^3)	V_i/V_{ROI} (%)	Mass (pg)	Localization
Fig. 4.26	1	0.288	392 ± 8	7.52	509.2	Protein
(Control)	2	0.065	32 ± 2	0.62	48.5	Chromatin
	3	0.773	110.2 ± 0.2	2.12	98.6	Lipid
Fig. 4.27	1	0.248	255 ± 1	4.84	331.6	Protein
(Taxol treated)	2	0.095	18.3 ± 0.6	0.35	27.4	Chromatin
	3	0.741	168.2 ± 0.8	3.19	150.5	Lipid
Fig. 4.28	1	0.217	151 ± 1	3.63	196.9	Protein
(Taxol treated)	2	0.098	28.8 ± 0.6	0.69	43.1	Chromatin
	3	0.739	128.2 ± 0.8	3.07	114.8	Lipid

Table 4.10: Results of the volumetric calculations of $\mathcal{C}_1, \mathcal{C}_2$ and $\mathcal{C}_3$ of Taxol treated cells and control sample over the whole cell volume.

sured) in comparison to the untreated, control samples, but induces variations in the spatial distribution of the chromatin component as evident by the circular and the off-metaphasic plate arrangement of this component. This is a result of the effect of Taxol on microtubule dynamics.

In this section we have demonstrated differences in Taxol treated and untreated cells with respect to the concentration distribution of various FSC^3 components without the need for exogenous labels. This is an important result which merits further investigation on a statistically significant number of samples in order to shed light on the effect of Taxol on chromosome dynamics and possibly also the protein content (due to the action of Taxol on microtubules which are dominantly composed of proteins) in a more direct way. The trends which at present are not visible due to the small number of samples studied, along with the difficulty in factorization may also become more apparent by studying a larger number of samples. The avenue of studying the effect of Taxol on live cells, using CARS microscopy remains uncharted and is an interesting future investigation to this project.

4.5.2 CARS imaging of cells drugged with ICRF-193

4.5.2.1 Background

ICRF-193 is an anti-cancer drug that inhibits DNA topoisomerase II, a nuclear enzyme which regulates DNA topology by introducing breaks in both the strands of the DNA molecule. These breaks reduce the mechanical stress on the molecule during the process of replication [69]. However, even in the absence or denaturation of topoisomerase II, DNA replication is not interrupted, suggesting that another class of topoisomerases belonging to the topoisomerase I family (which can break only one DNA strand) are able to modulate the mechanical stress in DNA molecule in the process of replication. The role of topoisomerase II is critical and unique in the final steps of decatenation of the duplicated DNA at the end of the process of DNA replication, condensation and chromosome segregation [154, 155]. Inspite of the abnormal chromosome dynamics due to topoisomerase inhibition, cells treated with ICRF-193 continue to progress through the cell cycle by undergoing an unusual mitotic phase called 'absence of chromosome segregation' or ACS-M phase [19, 155] or bypass mitosis [21]. Therefore, while the genetic content of the cells gets duplicated in the S phase, in the absence of normal topoisomerase II activity the segregation of the sister chromatids fails to occur. Since the CDK-cyclin mechanism of the cells remains intact despite topoisomerase II inhibition, the cells complete ACS mitosis by regeneration of the nuclear membranes without splitting into identical daughters [19] or bypass mitosis altogether. These cells may progress onto subsequent cell cycle(s), resulting in reduplication of their genetic content (endoreduplication). As a result, polyploid cells showing multinucleation in interphase [19, 155] are formed. These polyploid cells may eventually recover from topoisomerase II inhibition after removal of the drug from the system and through subsequent divisions, restore the normal diploid state of the genetic content.
Given the capability of CARS microspectroscopy to discriminate nuclear content as shown in the previous results, the effects of ICRF-193 on fixed U-2OS cells were studied using CARS microscopy. This was done because of a general knowledge gap with regards to the applications of CARS microscopy to *in vivo* drug interactions, as well as a strong motivation to acquire a better understanding of the effect of ICRF-193 on cell nuclei, with chemical specificity. The cells were treated with ICRF-193 for 24 hours to induce polyploidy (well plate D2, see section 4.1.1). The drug treated cells in different wells of the well plate were given specific recovery times- i.e., sample A was given no recovery time before fixation (well plates 1 and 2), sample B was given 5 days to recover from the drug treatment (well plates 3 and 4), and sample C was given 7 days of recovery time following drug treatment (well plates 5 and 6). The results of CARS microscopy and HIA analysis of these cells are given in the following section.

4.5.2.2 Results

Due to the large size of polyploid cells, these data were acquired with 10 times faster speed than all the other CARS data shown in this work, i.e., with a pixel dwell time of 1 μs or 1 MHz pixel rate, for faster acquisition of data, which is critical for biological samples. Imaging such large fields of view with a lower pixel dwell time causes cell damage because of longer exposure to high intensity excitation fields.
FSC^3 analysis for two cells - one each from samples A and B was done using the guided FSC^3 method as described in the previous section. This method was used

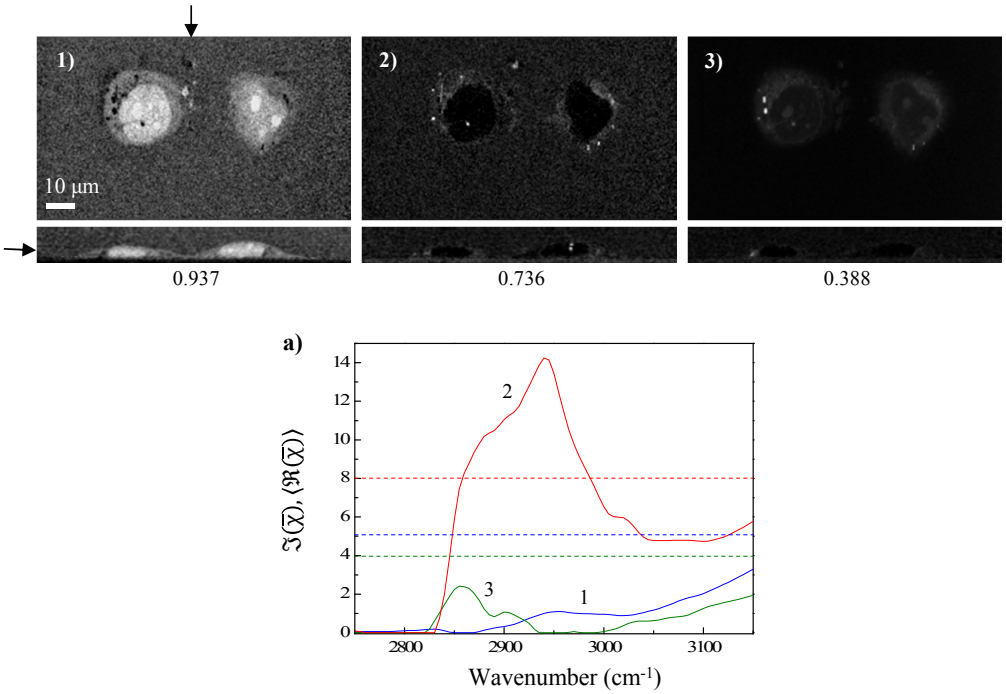

Figure 4.29: FOV 12: FSC^3 analysis of ICRF-193 treated cells. Images 1-3 show *xy* and *xz* sections of FSC^3 concentrations attributed to protein-chromatin (1), and lipids (2,3) respectively. Grayscales as in Fig. 4.4. a) shows the FSC^3 spectra corresponding to images 1-3.

to analyze the data shown in this section because the unsupervised analysis does not result in a separation of all the components of the cells. As an example, in Fig. 4.29 an FSC^3 analysis of an ICRF treated cell which was fixed after 5 days of treatment is shown. From a total of nine FSC^3 components, only three are shown. The other components correspond to water (three), glass (one) and systematics (two) as shown in Fig. D.19. In Fig. 4.29, image 1 is the FSC^3 concentration of the component corresponding to protein and nuclear material. The two chemical species are not well factorized but mixed in $\mathcal{C}_1$. Components 2 and 3 shown in images 2,3 correspond to lipids. The factorization settings used in this analysis are given in Table D.15. To compare the different samples, it is imperative that the data are factorized simultaneously on the same spectral basis or give similar spectra if factorized individually. While for the cells treated with Taxol, neither of these conditions could be satisfied, for the cells treated with ICRF, the data were successfully factorized to similar spectral bases by using the guided factorization method.

The guide spectra used for the analysis (with $\mathcal{W} = 0.4\%$ for all guides) in Fig. 4.30 are shown in Fig. 4.25. Other analysis settings are shown in section D.1.4.2. Due to the large field of view, some vignetting is seen as bright contrast at the bottom of image 2 ($\mathcal{C}_2$) of sample A and the right half of the same component's concentration map for sample B in Fig. 4.30. These regions were excluded from the analysis. Additionally, the regions around the cells were cropped before performing FSC^3 analysis to exclude most of the water dominant area in the field of view. Fig. 4.30 shows the simultaneous analysis of cells from samples A and B. From a total of seven FSC^3 components used in this factorization, only three corresponding to protein (1),

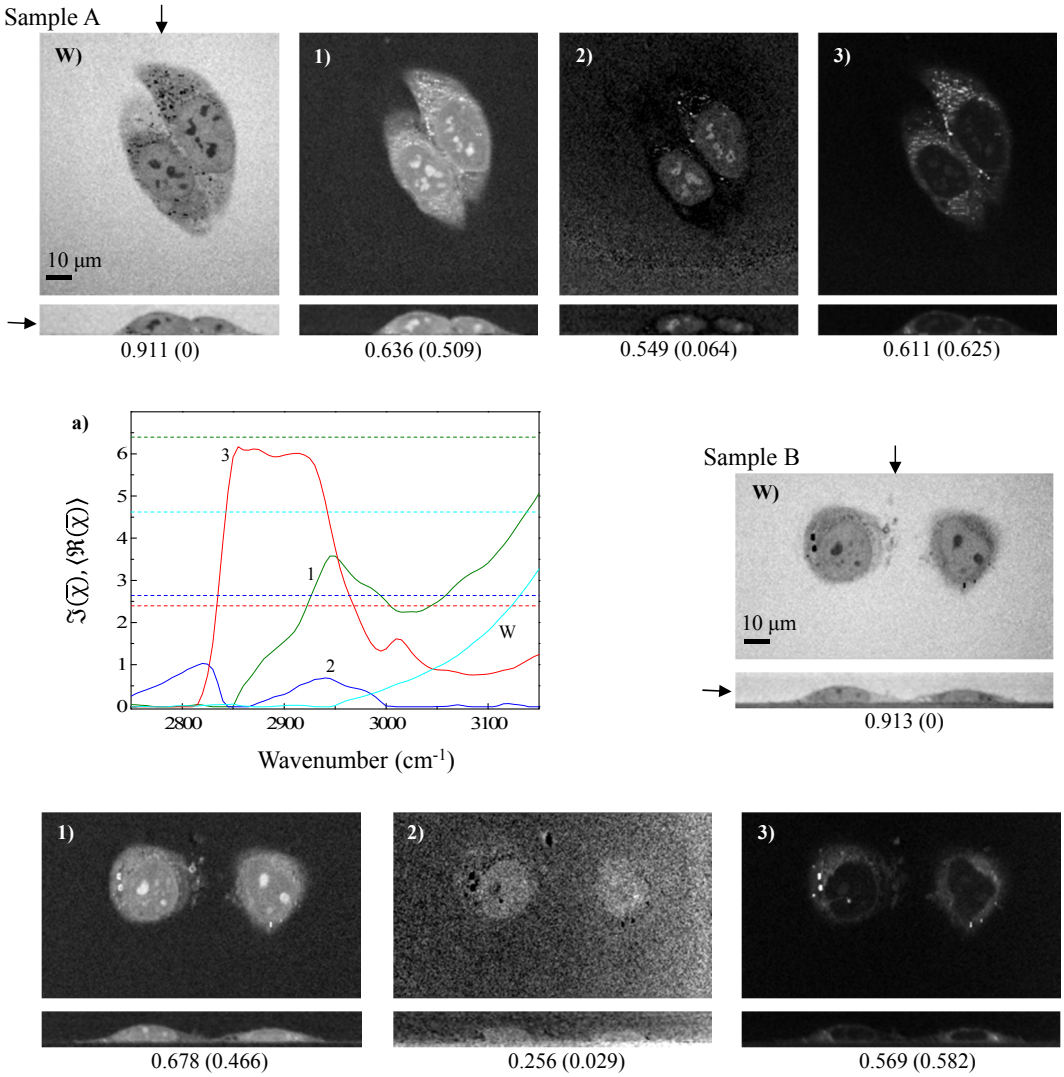

Figure 4.30: FOV 13, 14: Images W,1,2,3,4 show *xy* and *xz* sections of FSC^3 concentrations (attributed to sum water, protein, nuclear material and lipid respectively) of two fields of view- sample A, B. Grayscales as in Fig. 4.4. a) shows the FSC^3 spectra corresponding to the images. The data of sample A was acquired with a z step size of 0.7 μm.

nuclear material (2) and lipid (3) are shown, along with their FSC^3 spectra in a). The sum water component, W is also given. The other components attributed to water (three) and glass are shown in Fig. D.20.

Spectra corresponding to $\mathcal{C}_1, \mathcal{C}_2$ and $\mathcal{C}_3$ in Fig. 4.30 were used as guides (with $\mathcal{W} = 1.7\%$ for all guides) to factorize the data from two cells, one each from sample C and the control. In this factorization, a total of seven FSC^3 components were used and the analysis settings are given in Table D.17. The results of this analysis are shown in Fig. 4.31. Components corresponding to sum water (W), protein (1), nuclear material (2) and lipid (3) are shown along with their FSC^3 spectra. The guided factorization has reproduced well the cell components seen in Fig. 4.30 spectrally. Some particularly interesting features of these analyses include the punctate appearance of interphase nucleoli, visible as bright intranuclear spots in concentrations maps corresponding to $\mathcal{C}_2$, in samples A and control cells. The distribution of protein

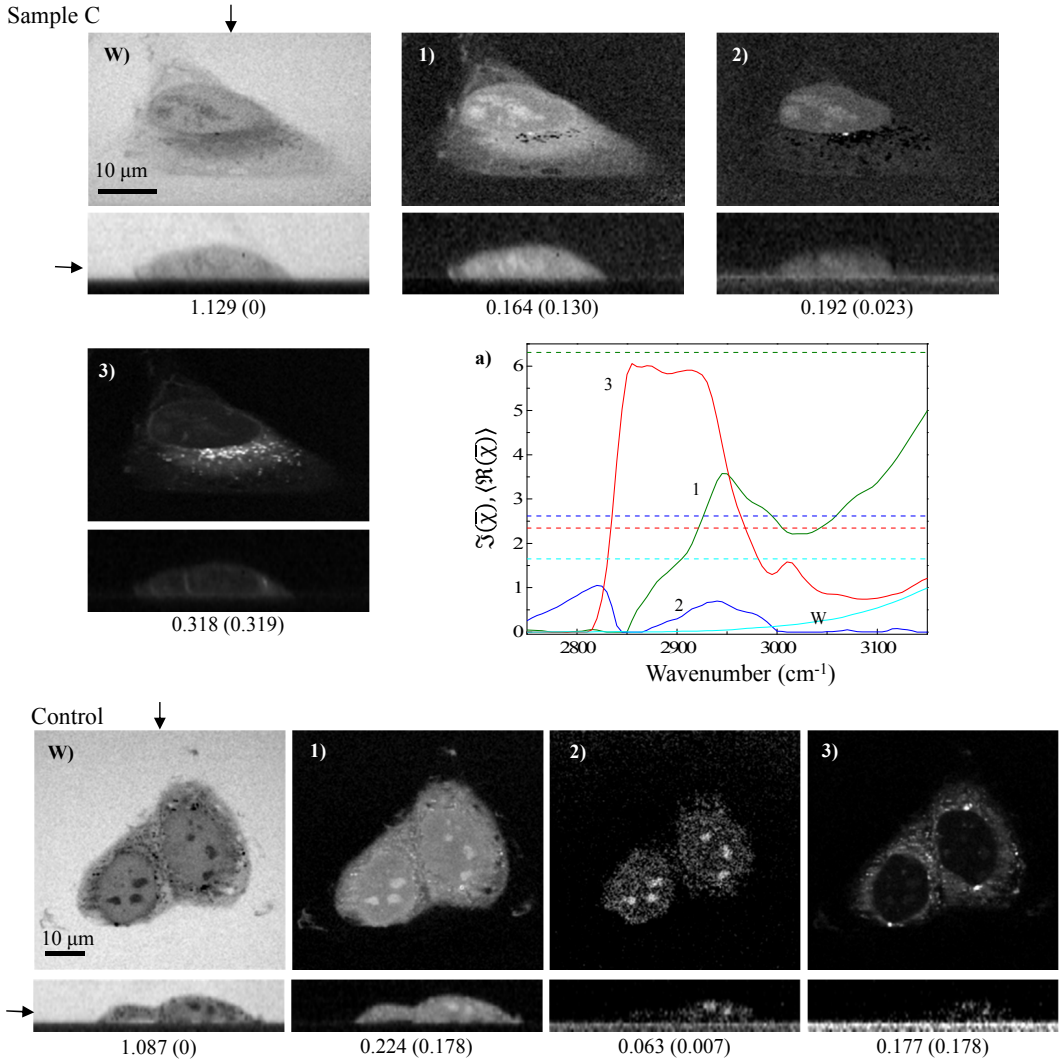

Figure 4.31: FOV 14, 15: FSC^3 analysis of ICRF-193 treated and control sample. Images W,1,2,3 show *xy* and *xz* sections of FSC^3 concentrations (attributed to sum water, protein, nuclear material and lipid respectively) of sample C and the control, with their corresponding spectra in a). Grayscales as in Fig. 4.4. The data of sample C was acquired with an *xy* step size of 200 nm and the control sample was imaged with a *z* step size of 0.7 μm. Other acquisition settings as described in section 4.1.2.

and lipids is as expected, localized with the cytosol and the lipid droplets/organelle membranes respectively. The samples which were given recovery time after drug treatment and before fixation do not show punctated nuclei. The components not shown here are attributed to water (three) and glass as given in Fig. D.21.

The volumetric analysis of these cells over nuclear and whole cell volumes is summarized in Table 4.11 and Table 4.12 respectively. The dry factors for these data were calculated using the steps outlined in section 4.4.2.1. The IFD ranges over which the water subtracted FSC[3] spectra were integrated to calculate the dry factors were 2800 - 3050 cm^{-1} for $\mathcal{C}_{1,3}$ and 2850 - 3010 cm^{-1} for $\mathcal{C}_2$.

Data	$\mathcal{C}_i$	γ_{dry}	$V_i \pm \Delta V_i$ ($\mu\mathrm{m}^3$)	V_i/V_{ROI} (%)	Mass (pg)	Localization
Fig. 4.30	1	0.799	382 ± 16	23.64	496.8	Protein
Sample A∗	2	0.116	16.64 ± 0	1.03	24.9	Nuclear material
No recovery	3	1.023	94.0 ± 0.3	5.82	84.1	Lipid
Fig. 4.30	1	0.799	223 ± 9	23.44	290.2	Protein
Sample B∗	2	0.116	10.44 ± 0	1.09	15.7	Nuclear material
5 days recovery	3	1.023	51.7 ± 0.2	5.43	46.3	Lipid
Fig. 4.31	1	0.794	32 ± 2	7.20	42.2	Protein
Sample C	2	0.118	3.15 ± 0	0.69	4.7	Nuclear material
7 days recovery	3	1.005	18.61 ± 0.08	4.13	16.7	Lipid
Fig. 4.31	1	0.794	83 ± 4	9.12	107.6	Protein
Control∗	2	0.118	1.00 ± 0	0.11	1.5	Nuclear material
	3	1.005	17.59 ± 0.08	1.94	15.7	Lipid

Table 4.11: Results of the volumetric calculations of $\mathcal{C}_1, \mathcal{C}_2$ and $\mathcal{C}_3$ of ICRF-193 treated cells and control sample over the nuclear volume. * indicates that the values reported are in units of value/cell as there is more than one cell in the field of view.

The masses of the component corresponding to nuclear material progressively decrease in the cells in the order of the duration of time following drug treatment prior to fixation. The mass of this component can be treated as a measure of polyploidy, which is directly related to the amount of DNA/chromatin in a cell. From the calculations, we observe that the samples which were fixed immediately on removal of ICRF-193 show the maximum nuclear content, with the control samples showing the least amount of nuclear material, as expected. Moreover, we observe that the amount of nuclear material decreases as the recovery time given to the cells prior to fixation increases. These findings support the known action of ICRF-193 in inducing polyploidy, from which the cells recover over time. More importantly, we have demonstrated that CARS microscopy, applied in the form presented in this project is capable of determining the relative ploidy of cells based on their nuclear content. As an estimate, treating the control sample as diploid (2x), sample A (no recovery time) is 30x , B is 10x (five days recovery time) and C (seven days recovery time) is 6x. The masses of protein within nuclear ROIs appear uncorrelated with the recovery times given to the cells prior to fixation. However, the lipid content within nuclear volumes shows a progressive decline, with the sample given no recovery time showing the highest lipid content, while the samples given five and seven days of recovery progressively showing reduced levels of lipids, converging towards those in the control sample. On using the full cell ROIs, we observe that the protein and lipid contents in the cells given no recovery time and the ones given seven days recovery are of the same order. The masses of protein and lipid in sample A (no recovery) was found to be $\sim$1.5 times that in sample B (five days recovery). We also observe that sample C, which was given seven days recovery before fixation, is,

Data	$\mathcal{C}_i$	γ_{dry}	$V_i \pm \Delta V_i$ (μm^3)	V_i/V_{ROI} (%)	Mass (pg)	Localization
Fig. 4.30	1	0.799	1605 ± 68	19.61	2086.7	Protein
Sample A∗	2	0.116	46.02 ± 0	0.56	69.03	Nuclear material
No recovery	3	1.023	636 ± 2	7.77	568.9	Lipid
Fig. 4.30	1	0.799	1064 ± 45	16.22	1383.2	Protein
Sample B∗	2	0.116	74.85 ± 0	1.14	112.3	Nuclear material
5 days recovery	3	1.023	436 ± 1	6.65	390.2	Lipid
Fig. 4.31	1	0.794	115 ± 5	4.67	149.8	Protein
Sample C	2	0.118	12.16 ± 0	0.49	18.24	Nuclear material
7 days recovery	3	1.005	94.9 ± 0.4	3.84	84.9	Lipid
Fig. 4.31	1	0.794	243 ± 11	4.95	315.8	Protein
Control∗	2	0.118	5.40 ± 0	0.11	8.1	Nuclear material
	3	1.005	83.9 ± 0.4	1.71	75.1	Lipid

Table 4.12: Results of the volumetric calculations of $\mathcal{C}_1$,$\mathcal{C}_2$ and $\mathcal{C}_3$ of ICRF-193 treated cells and control sample over the whole cell volume. * indicates that the values reported are in units of value/cell as there is more than one cell in the field of view.

as expected, similar in its protein and lipid content, to the control samples rather than the samples given lesser or no recovery time. The masses of the protein and lipid components in sample C are approximately 10 and 20 times smaller than that of sample B and A respectively. The masses of the nuclear component (which is the noisiest of the three components) over the full cell volumes are not correlated with the duration of recovery given to the cells, due to the inclusion of noise outside the nuclear region in this calculation.

Another interesting feature of these cells was made apparent by factorizing the cells individually using guided factorization. In these analyses, in the control sample (factorized with $\mathcal{W} = 8.6\%$ for all the guides), an additional FSC^3 component colocalized with the nucleus, showing a negative contrast in the punctate regions was also observed (shown in image 2 of Fig. 4.32, and also $\mathcal{C}_{1,2}$ in Fig. D.21) The total number of components in this factorization was nine of which only four are shown here. Images 1-4 correspond to protein, nuclear material (similar FSC^3 spectrum and concentration distribution to the chromatin component in cells not treated with ICRF-193), the nuclear material specific to the puncate regions (similar FSC^3 spectrum and concentration distribution to image 2 in Fig. 4.30 and Fig. 4.31) and lipid respectively. The analysis settings for this factorization are given in Table D.18 and the FSC^3 components not shown here are given in Fig. D.22, attributed to glass (one) and water (four).

The spectral differences between cell populations given recovery time compared to those fixed directly after drug treatment constitute exciting findings, which suggest that the chemical composition of the cells once treated with ICRF-193 shows marked differences from the untreated cells, a knowledge which is useful in studying drug resistance and possible reactions of ICRF-193 treated cells to other therapies.

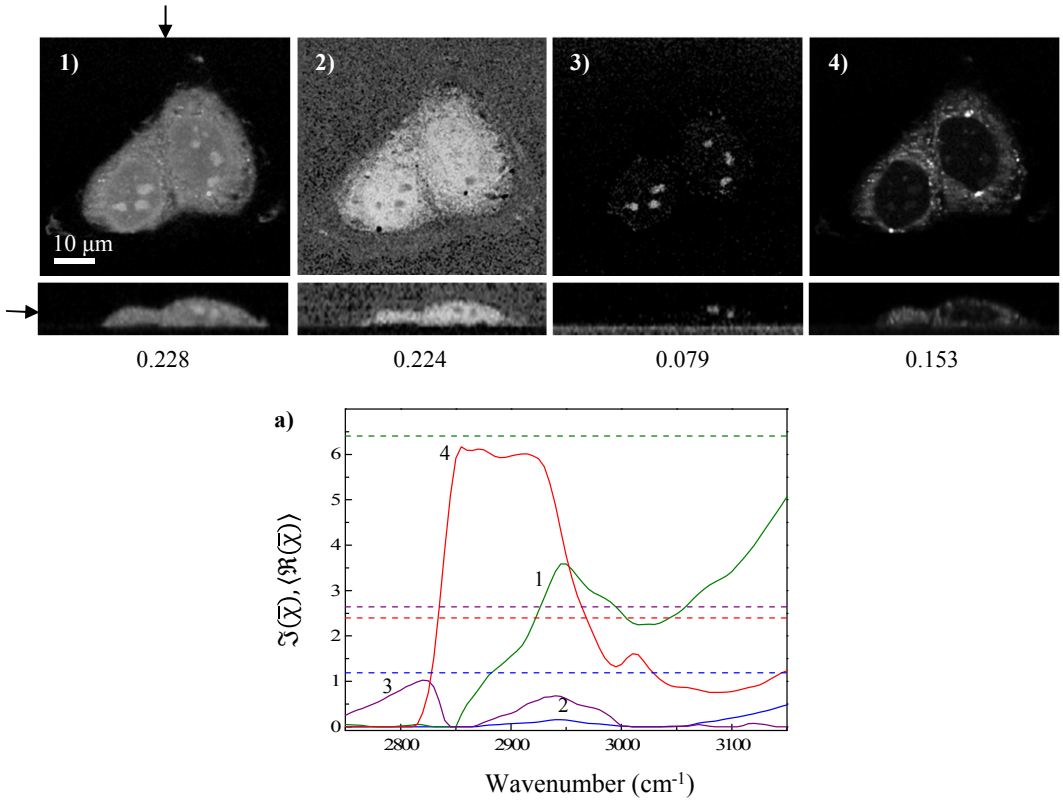

Figure 4.32: FOV 15: Images 1-4 show *xy* and *xz* sections of FSC^3 concentrations attributed to protein, chromatin, nuclear material (punctates) and lipids respectively. Grayscales as in Fig. 4.4. a) shows the FSC^3 spectra corresponding to images 1-4.

4.6 Discussion

In this chapter, we have described a novel, straight-forward method of counting fluorophore molecules and consequently, their target (of the fluorophore) molecules using fluorescence images of U-2OS cells labelled with cyc B1 targetting eGFP. In literature, most examples of such work have been reported to require relatively complicated methods such as Western blotting [141] and flow cytometry. The purpose of this exercise was to acquire expertise in identifying mitotic cells from a larger population on the cover-slips. These cells were imaged using CARS microscopy to determine whether mitotic cells bear characteristic differences at different stages of mitosis. We found a correlation between the intranuclear protein content and the mitotic stage of the cells, consistent with the known biological facts as discussed in this chapter.

As the main work in this project, we have shown that CARS microscopy is a novel and effective method of generating morpho-chemical contrast in fixed U-2OS cells in a label-free way. Additionally, the specific method of analysis demonstrated in this project allows volumetric determination of weights of the various components in the cells using this method of analysis. On testing the factorization algorithm several times, we discovered that FSC^3 does not yield consistently reproducible results in multiple trials due to the fact that the amount of organic material in these cells (not lipid rich since this cell line originates from osteosarcoma) is small, which translates

into a smaller signal/noise ratio compared to lipid rich systems which are typically studied with CARS microscopy. Despite these technical difficulties associated with studying osteosarcoma cells and the non-reproducibility of results using FSC^3 we could differentiate at least three major macromolecular mixtures (as three distinct components) in the cells, using this analysis method in all the samples studied. To our knowledge, this project is the first report in which hyperspectral data in 3D has been acquired and analyzed using CARS microscopy with factorized spectra and quantitative volumetry on cells. Furthermore, the novel ideas of excluding the water peak in the analysis to facilitate the detection of components with small signal/noise ratios, and using guided factorization are the innovations brought forth by this project, which enhance the sensitivity, reproducibility and accuracy of this analysis method. We reiterate that the results of volumetric analysis depend on the factorization used for the calculations and may not necessarily reproduce the chemical composition of cells as documented in literature. This is due to the fact that the factorized components are not pure. In fact, it is appropriate to say that each factorization represents a different way of understanding the chemical composition of the cells imaged and analyzed. The calculations of the masses of different components factorized using FSC^3 was done with an assumption that the components designated as protein, chromatin and lipid are pure and not mixtures of other materials. This is a rather simplistic way of formulating this model of calculations because cytosol in mitotic cells is not entirely protein but also contains RNA and numerous small vesicles which are primarily made of lipids from the membranes of the original organelle (see the discussion on organelle inheritance in section 2.2.2). However, the relative concentrations of protein, RNA and lipids in this component are unknown. In the absence of pure protein, lipid and RNA spectra measured on our set-up, and the uncertainty in the make-up of this component, we consider it to be pure protein in each factorization. Similarly, the FSC^3 component corresponding to chromatin contains protein and DNA but the calculation of dry factors and the factors F for this component were based on the assumption that chromatin contains 2:1 ratio of protein (equal amounts of histone and non-histone proteins) and DNA, which is again a simplified view because in reality, chromatin contains equal masses of DNA and histone proteins, with non-histone proteins in mass ratio between 1-2 times the mass of DNA [80]. Moreover, not all of the chromatin is getting detected in the same component in some factorizations. In the analyses shown in this chapter, some protein contrast is seen in the nuclear region, which is a possible indication that the FSC^3 component designated as chromatin is an underestimate of the chemical species in the cell, a part of which is detected in the protein channel. Another important aspect to be considered while interpreting these results is that the volumetric estimates of different FSC^3 components depend on the factorization used. This means that the results of different factorizations cannot be compared. Despite these issues, we observed definite trends in the masses of proteins localized within the nuclear volumes, consistent with the known role of proteins in DNA condensation during metaphase.

In a medically relevant application, cells treated with Taxol and ICRF-193 prior to fixation were also studied using CARS microscopy. We found no spectral, but concentration distribution differences in the cells treated with Taxol compared to the control (undrugged) samples, as expected. Some interesting quantitative results have been pointed out and discussed in the main text. However, as demonstrated in the case of cells treated with ICRF-193, once factorized simultaneously, we can

differentiate between the cells on the basis of their nuclear content. This is an important result which allows label-free sorting of cells into different categories depending on the recovery time given to the cells prior to fixation. Differences in the nuclear signature of ICRF-193 drugged cells compared to that of the control samples is another potentially path-breaking discovery, furthering the knowledge of the effects of this drug on cellular nuclei. The impact of this discovery can be completely ascertained only after studying a statistically significant number of samples. The findings, nevertheless, are promising for further studies involving phenotype mapping prior to and following drug treatment.

4.7 Conclusions

In this chapter, intracellular cyc B1 concentrations in fixed U-2OS cells transfected with a stable G_2-M eGFP marker have been quantified using epi-fluorescence imaging, which is a simple and novel method of such quantitative analysis. Using the knowledge of mitotic cell morphology acquired by imaging eGFP fluorescence, mitotic cells among a population of label-free cells on a coverslip were identified for further studies with CARS microscopy. In this project, CARS microscopy has been applied to image fixed mitotic U-2OS cells and the discrimination between protein, chromatin/nuclear material and lipid components has been shown. Correlative TPF imaging of mitotracker-orange and DAPI have revealed that the FSC^3 component corresponding to protein and $\mathcal{C}_{1,4}$ corresponding to lipid are not specific to the nucleus or mitochondria. However, in some samples - indicated appropriately in text, (not investigated with other methods), the golgi apparatus of the cells is visible as a lipid distribution. On the other hand, $\mathcal{C}_3$ was found to be colocalized with the nucleus, thus establishing the suitability of CARS microscopy to image nuclei in a chemically specific and sensitive manner. Effects of two anti-cancer drugs, Taxol and ICRF-193 in clinically significant concentrations were studied. Taxol treated cells appeared spectrally similar to untreated samples. However, the morphology of chromatin and its intracellular distribution in Taxol treated cells are characteristically different from the control samples. The Taxol treated cell shown in Fig. 4.27 arrested in metaphase shows chromatin fragments arranged in a circular pattern, and another Taxol treated cell (Fig. 4.28) shows an off-equatorial plate distribution of the chromosomes. The differences in the abnormalities in chromosome distribution and chromatin structure are apparent using CARS microscopy, applied to unlabelled cells. In comparison to fluorescence microscopy, CARS microscopy offers a label-free way to image such morphological differences (for example, the distribution of chromatin which ordinarily requires dyes such as DAPI, Hoechst, etc.) within cell populations without the need to introduce exogenous labels in the samples. In contrast to the treatment with Taxol, ICRF-193 treatment appears to change the chemical composition of the nucleus. Studying the effects of drug treatment with ICRF-193 on cell population phenotypes is an interesting further application of CARS microscopy. Statistically significant samples of such cells can be studied and conclusive inferences drawn with chemically quantitative and specific information obtained from CARS microscopy.

The purpose of this project was to demonstrate the suitability of CARS microscopy for quantitative imaging of label-free cell populations. As already discussed in section 2.3.1, CARS microscopy has been applied by other research groups around the world to study a wide range of biological processes taking place at cellular and tissue

level. The novel aspects of the work presented in this thesis can be summed up in the following points.

1. For the first time in our knowledge, we have imaged cells in 3D with spectral information over a wide range of IFDs i.e., 2400 - 3600 cm^{-1}.

2. We have successfully discriminated between three organic components of cells, i.e., protein, lipid and chromatin. Using correlative TPF imaging, we have shown that the chromatin component does indeed originate from the nucleus. The lipid and protein components are not correlated with any one sub-cellular compartment. Additionally, in some factorizations, the lipids are further discriminated as either saturated or unsaturated.

3. We have quantitatively determined the volumes and masses of each of the organic components of the cells.

4. We have used the morpho-chemical contrast generated by the CARS response of the cells to differentiate between Taxol treated and control cells, albeit without strongly supported quantitative correlation between the different samples, purely because of our inability to factorize all the data to the same spectral basis. This is attributed to small differences in the chemical composition of the cells.

5. The most promising results of this work from an application point of view in biomedical chemistry prove (even though not on a statistically significant population) spectral differences between ICRF-193 treated cells and the control samples. Additionally, differences in the chemical composition of the intra-nuclear material of the cells given different recovery times before fixation have also been shown. These results are possibly representative of path-breaking research on the effects of ICRF-193 on cellular nuclei, with calculations of the nuclear content masses and volumes serving as quantitative indicators of polyploidy induced by topoisomerase poisoning, which in turn can be used to map cell population phenotype pre and post treatment with ICRF-193.

The results of this project as enumerated above, have decisively shown that CARS microscopy is applicable in a quantitative way to studies involving systems containing a concentration of organic material in the few percent range, with chemical specificity and sensitivity in the CH-stretch region. Moreover, this technique also has potential practical applications in studies centered around drug treatment and its effects on cells in general and the nuclei in particular. These and other specifics as discussed in the course of this chapter have pushed CARS microscopy in its present form, to biomedical/biochemistry studies. Furthermore, applications of this technique to more complex systems such as organoids have been explored and are discussed in the next chapter.

Chapter 5

CARS imaging of organoids

5.1 Background

In the previous chapter, a detailed description of cytological studies using CARS microscopy has been given and results of FSC^3 analysis have been demonstrated, establishing the technique's suitability to interrogate biological systems at the single cell level in a label-free way. The hierarchical order of the biological scheme of organization with increasing complexity in structure and function is cells, tissues, organs and organ systems. *In vivo* studies of biological components are often challenging and pose restrictions on the quality and quantity of experimental data that can be collected. In contrast, *in vitro* measurements allow researchers to exercise greater control and flexibility in experimental design, expanding the scope of applications of such studies. Typically, 2D cultures of tissue are used for *in vitro* studies which restrict the scope of the research undertaken due to the loss of clonal nature and structure in these cultures. Recently, various labs have reported success in producing 3D model organs [156, 157, 158] grown as buds in petridishes from pluripotent stem cells in medium enriched with various growth factors such as Wnt and fibroblast growth factor (FGF) which play a role in tissue patterning. The use of progenitor cells in production of various organoids in culture has also been demonstrated [159, 160]. Various research groups have developed methods and/or reported the production of gut, kidney, liver, brain and retinal organoids [161].
By studying these 3D models of organs and tissue which recapitulate the functionality and cellular diversity of *in vivo* samples, we have come a step closer to answering questions of biomedical relevance such as organogenesis, physiology, disease, drug delivery and effects, by studying organoids *in vitro*, using powerful techniques to provide spatio-temporal resolution.
In an exploratory application of CARS microscopy to live organoids, three types of organoids were studied as described in the following section.

5.2 CARS imaging of organoids

The motivation to study organoids using label-free CARS microscopy was to demonstrate the applicability of the technique to complex biological systems such as dense tissues and organoids. The unlabelled organoids in Matrigel were imaged in 35 mm dishes, placed within a temperature controlled environmental chamber with an influx of CO_2 maintained at 37° C. The imaging was done using the dry optics. 2D CARS data was acquired using IFD scans (2600 - 3300 cm^{-1}) of selected z-planes

with a pixel dwell time of 10 μs. 3D data (located in the data DOI) to provide full spatial information about the organoid morphology were collected at specific IFDs. All the data have been analyzed by FSC^3 over a spectral range of 2750 - 3100 cm^{-1}. The samples of mouse intestinal and liver organoids were prepared by Dr. A. Offergeld in School of Biosciences, Cardiff University. The human colorectal cancer organoid samples were prepared by Dr. A. Hollins in School of Biosciences, Cardiff University. The CARS images of these samples were acquired by Dr. I. Pope and Dr. A. Offergeld (School of Biosciences, Cardiff University).

5.2.1 Mouse crypt intestinal organoids

Crypts and villi are the most noticeable features of the small intestine. The crypts contain various kinds of cells which perform specialized functions such as secretion of specific hormones and/or enzymes pertinent to the gut functionality. Each crypt contains 4 to 6 stem cells, a description of their position and identity is attempted by two models i.e., the +4 position model and the stem cell zone model. According to the +4 position model, slow cycling stem cells are located at position +4 above the crypt bottom. The stem cell zone model proposes that a second type of stem cells, the crypt base columnar (CBC) cells [162] lie interspersed between the Paneth cells. Fig. 5.1 shows the crypt structure according to both these models.
More recently, it has been discovered that the CBCs and +4 stem cells produce each other in a mutually compensatory fashion [164] with the former requiring Wnt signalling to undergo cell turnover. The CBCs express the gene Lgr5 which is a receptor for R-spondin, a known Wnt activator. The method followed for produc-

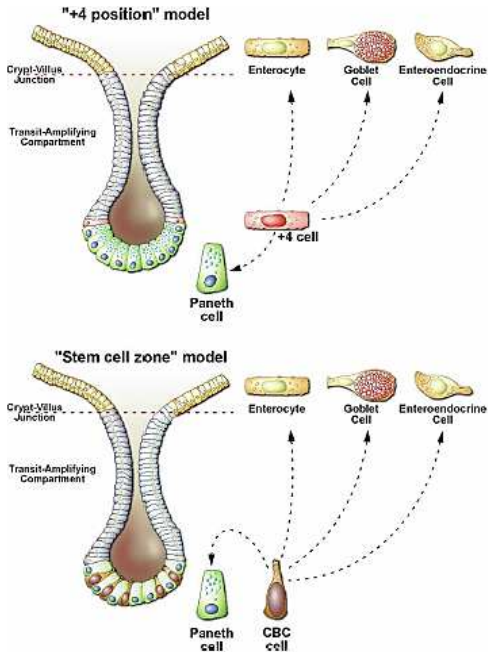

Figure 5.1: Cartoon of intestinal crypt and villus structure according to two models. Note that while the +4 position model considers the position of stem cells to be 4 cells above the bottom of the crypt at either side, the stem cell zone model regards the crypt base columnar cells as the stem cells, lying interspersed between the Paneth cells. Reprinted from [163] with permission from Cold Spring Harbor Library.

tion of mouse intestinal organoids was adapted from Sato et al. [157] who have reported that crypt-like 3D organoids can be generated in long term cultures, from $Lgr5^+$ CBCs, maintaining the compartmental morphology and functionality of *in vivo* crypts. Crypts from a mouse intestine are cultured and allowed to expand and differentiate in media as described in detail in section 5.2.2.
A fluorescence microscopy image of mouse intestine organoid [23] is given in Fig. 5.2 showing anti-lyzosome fluorescence indicating the location of the Paneth cells which are specialized epithelial cells responsible for antimicrobial secretions. The authors also used phalloidin to label F-actin, indicating the position of spindle fibres; and höechst to label the nuclei in the said organoid.

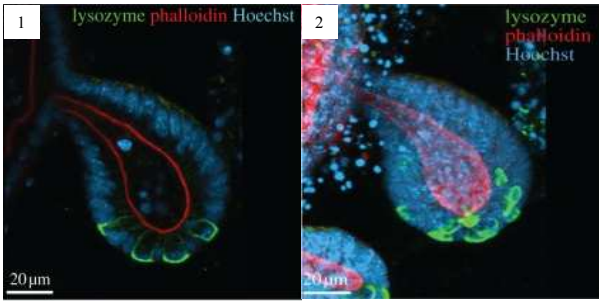

Figure 5.2: Confocal fluorescence imaging of a mouse intestinal organoid stained with höechst (blue channel), anti-lyzosome antibodies (green channel) and phalloidin (red channel). (1) shows the image of a single z-slice (2) shows a maximum intensity projection across the z-stack. Reprinted from [23] with permission from The Royal Society Publishing.

In Fig. 5.3 an FSC^3 analysis of a mouse intestinal organoid is shown. The analysis settings used are given in Table D.19. This data was factorized into a total of five components, of which the components shown in spatial concentration maps W,1,2,3 correspond to sum water (W), protein, chromatin and lipid respectively. The bright green spots in the colour overlay (see also the grayscale distribution map of $\mathcal{C}_1$) in Fig. 5.3 are attributed to the goblet cells responsible for secreting mucus which are found in the epithelial lining of respiratory and intestinal organs. $\mathcal{C}_3$ shows the location of chromatin in epithelial cells, located towards the outer edge of the crypt, imitating *in vivo* organization of the intestine. The central lumen (visible in $\mathcal{C}_1$) is the location of apoptotic cells and other debris. The two components not shown here correspond to water and are given in Fig. D.23. With this analysis, we have demonstrated that CARS microscopy can be used to differentiate between cells in complex organoids, with sub-cellular resolution. The lipid signature is an important observation in these samples due to the specifics of lipid metabolism in various types of cancers [165, 166]. In the remaining parts of this chapter, we show some more organoids (of different types and at different stages of growth) imaged using CARS microscopy.
Fig. 5.4 shows the results of FSC^3 analysis of an intestinal organoid , at a more advanced growth stage than of the organoid in Fig.5.3. The dense tissue, typical of organoids in advanced stages of growth, in the top right quarter of the field of view was excluded from the analysis and then reprojected. The reprojection of the data excluded from the analysis is done by expressing the data in terms of the factorized spectra (calculated without the excluded regions), and then imposing the concentration constraint using one NMF iteration such that the concentration at

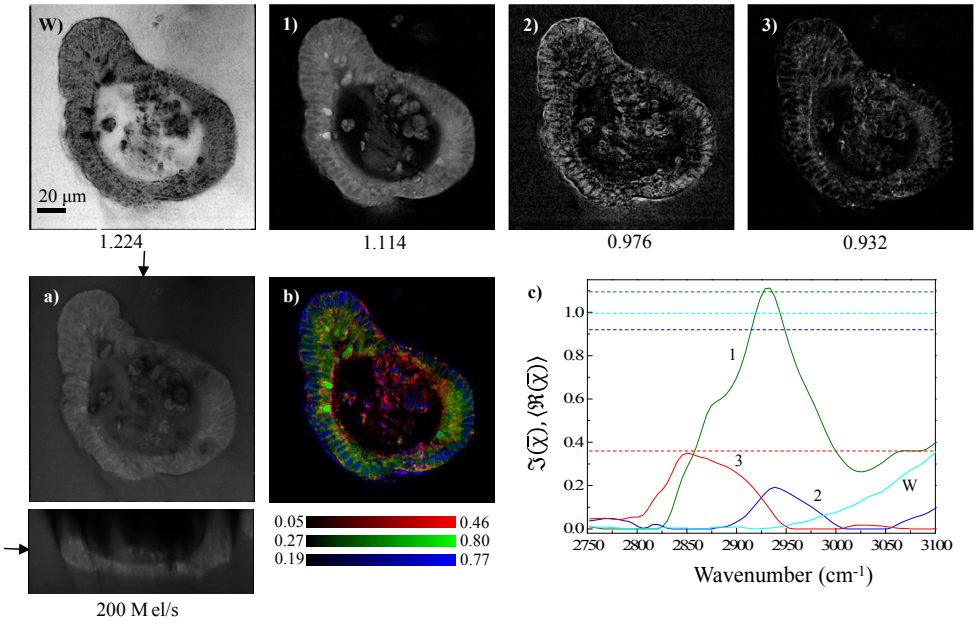

Figure 5.3: FSC^3 analysis of a mouse intestinal organoid. The images show the concentrations W,1,2,3 with spectra in c). Grayscales as in Fig. 4.4. a) shows the xy and xz sections of CARS intensity at $2835\,\mathrm{cm}^{-1}$. b) is a colour overlay showing $\mathcal{C}_3$ in red, $\mathcal{C}_1$ in green and $\mathcal{C}_2$ in blue channels, with the concentration ranges as indicated.

each spatial point ≥ 0.

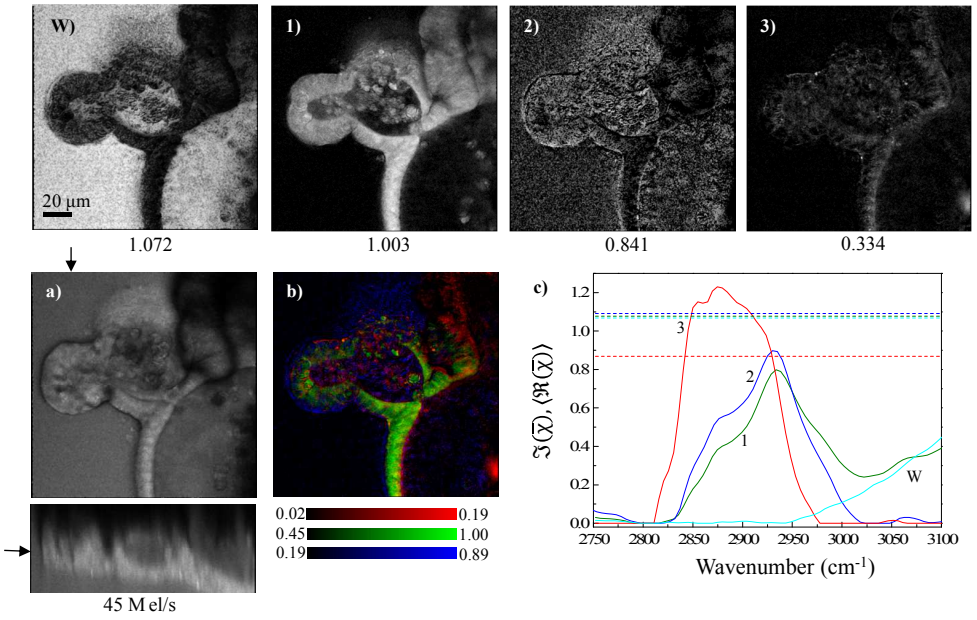

Figure 5.4: FSC^3 analysis of a matured mouse intestinal organoid. Concentrations are shown in images W,1,2,3 with spectra in c). Grayscales as in Fig. 4.4. a) shows the xy and xz sections of CARS intensity at $2835\,\mathrm{cm}^{-1}$. b) is a colour overlay showing $\mathcal{C}_3$ in red, $\mathcal{C}_1$ in green and $\mathcal{C}_2$ in blue channels, with the concentration ranges as indicated.

The FSC^3 analysis factorized the chemical composition of the crypt into seven components (settings in Table D.20) of which three corresponding to protein (1), chromatin (2) and lipid (3) are shown, along with the sum water component (W). The components not shown here include three corresponding to water and one corresponding to the systematics, given in Fig. D.24. We note that the factorized spectra of both the intestinal organoids are similar in their peaks. However, small differences in the lipid spectra are observed, indicating that the lipid composition in the two organoids are different, pointing to the possibility of using the lipid make-up of an organoid to determine its age.

5.2.2 Mouse liver organoids

The preparation method followed to produce mouse liver organoids in culture was adapted from Huch et.al [160]. The organoids were grown by culturing adult stem cells ((Lgr5$^+$, taken from intrahepatic bile duct) in Matrigel (Corning) with a Wnt activator i.e., R-Spondin as medium to promote self renewal. The growth of the organoids in this medium is called the expansion stage of the culture. Some of the organoids from the expansion medium (EM) were allowed to differentiate into their hepatic lineage, with hepatocyte functionality, by culturing them with Notch and TGF-β inhibitors and low Wnt activation (differentiation medium, DM).
The FSC^3 results of CARS imaging performed on two liver organoids, one in the expansion and one in the differentiation stage of growth, are shown. The analysis settings are given in Table D.21. In Fig. 5.5, an FSC^3 analysis of a mouse liver organoid grown in EM is shown.

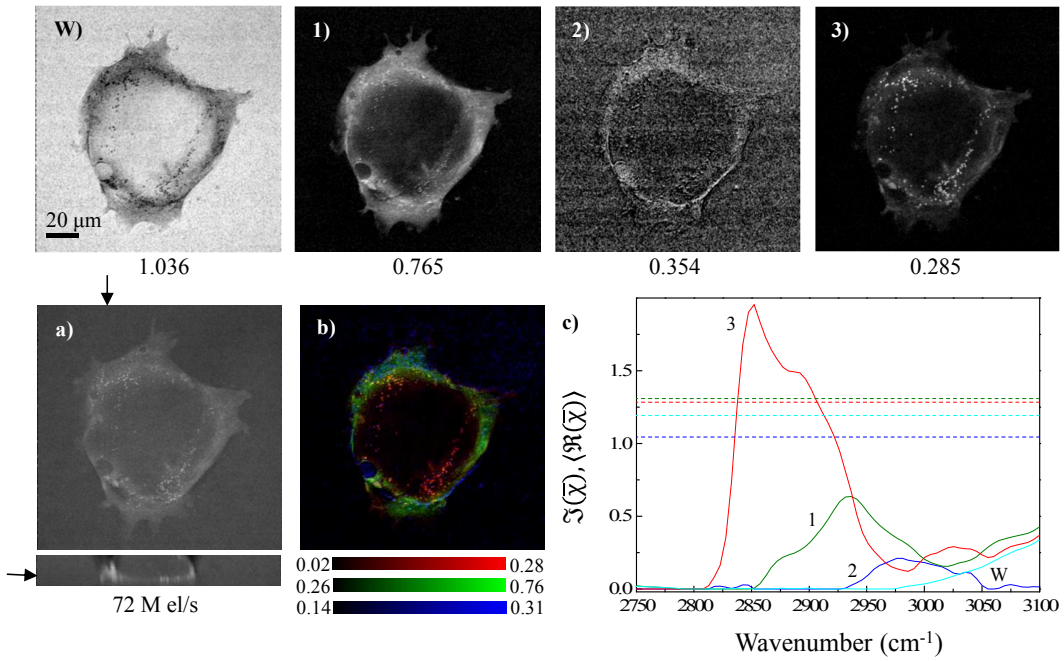

Figure 5.5: FSC^3 analysis of a mouse liver organoid grown in EM. Concentrations (images W,1,2,3) and component spectra (c) are shown. Grayscales as in Fig. 4.4. a) shows the *xy* and *xz* sections of CARS intensity at 2835 cm^{-1}. b) is a colour overlay showing FSC^3 components 3, 1 and 2 in red, green and blue channels respectively.

Three FSC^3 components (out of total six) corresponding to protein (1), chromatin (2) and lipid (3) are shown in the figure as well as the sum water component (W). A lack of organization/structured units is observed in the organoids grown in these culture conditions. The four components not shown here are attributed to water (two) and one to systematics (see Fig. D.25).
Following growth in the DM, the liver organoids attain a morphology and functionality similar to hepatocytes. An FSC^3 analysis of one such organoid grown in DM is shown in Fig. 5.6. The settings used for this analysis are given in Table D.22. A total of five FSC^3 components were obtained corresponding to water (1), protein (2,3) and lipid (4, 5) are shown in Fig. 5.6. The cellular organization of the organoid is visible in $\mathcal{C}_2$ and $\mathcal{C}_3$ corresponding to protein and chromatin respectively. The lumen is also discriminated as negative (positive) contrast in $\mathcal{C}_2$ and $\mathcal{C}_3$ ($\mathcal{C}_1$), located along the left edge of the images shown. In the figure, $\mathcal{C}_1$ is attributed to water and $\mathcal{C}_4$ to lipid.
These are interesting results which show characteristic differences between the lipid spectra in the organoids grown in expansion and differentiation media, reaffirming the capability of CARS microscopy to ascertain the age of an organoid. Moreover, we observe that there is chemical homogeneity in the samples which have only undergone expansion, without differentiating into functionally specialized aggregates.

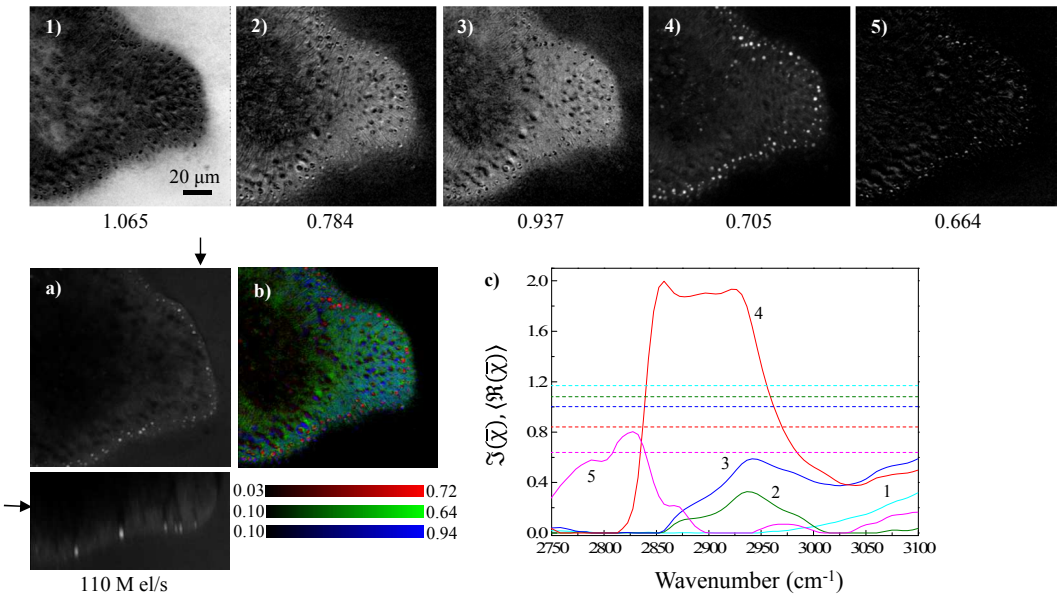

Figure 5.6: FSC^3 analysis of a differentiated mouse liver organoid. Concentrations are shown in images 1-5, with grayscales as in Fig. 4.4. The component spectra are given in c). a) shows the *xy* and *xz* sections of CARS intensity at 2835 cm^{-1}. b) is a colour overlay showing FSC^3 components 4, 2 and 3 in red, green and blue channels respectively.

5.2.3 Human colorectal cancer organoids

Human colorectal organoids prepared using tumour organoids generated in Cardiff from human colorectal samples from the Wales Cancer Bank employing a protocol adapted from Sato et. al [167] were studied with CARS microscopy. These organoids are particularly interesting to the biomedical community because they make patient specific modelling of disease and studying targetted treatment plans possible, which are often complicated or impossible to achieve *in vivo*.
In Fig. 5.7, FSC^3 results of CARS imaging of a primary colorectal cancer organoid are shown. The analysis settings are given in Table D.23. A total of four components were used in this factorization, of which two (in addition to sum water, W) corresponding to protein (1) and lipid (2) are shown. $\mathcal{C}_2$ shows localised distribution, while the $\mathcal{C}_1$ demonstrates the globular appearance of the cancer. The two components not shown in this figure correspond to water and are given in Fig. D.27.

On advancing from the primary state, tumours might develop metastatic capabilities which allow them to spread from primary site of growth to other parts of the body. Fig. 5.8 shows the chemically specific and sensitive FSC^3 analysis of CARS data from a metastatic human colorectal cancer organoid, demonstrating THE structural organization of a metastatic tumour. The factorization settings are given in Table D.24. Of the total five components used in this analysis, three attributed to (in addition to sum water, W), protein (1), chromatin (2) and lipid (3) are shown. The two components not shown here correspond to water and are given in Fig. D.28. Interestingly, we observe that the lipids in the metastatic colorectal cancer tumour are spectrally

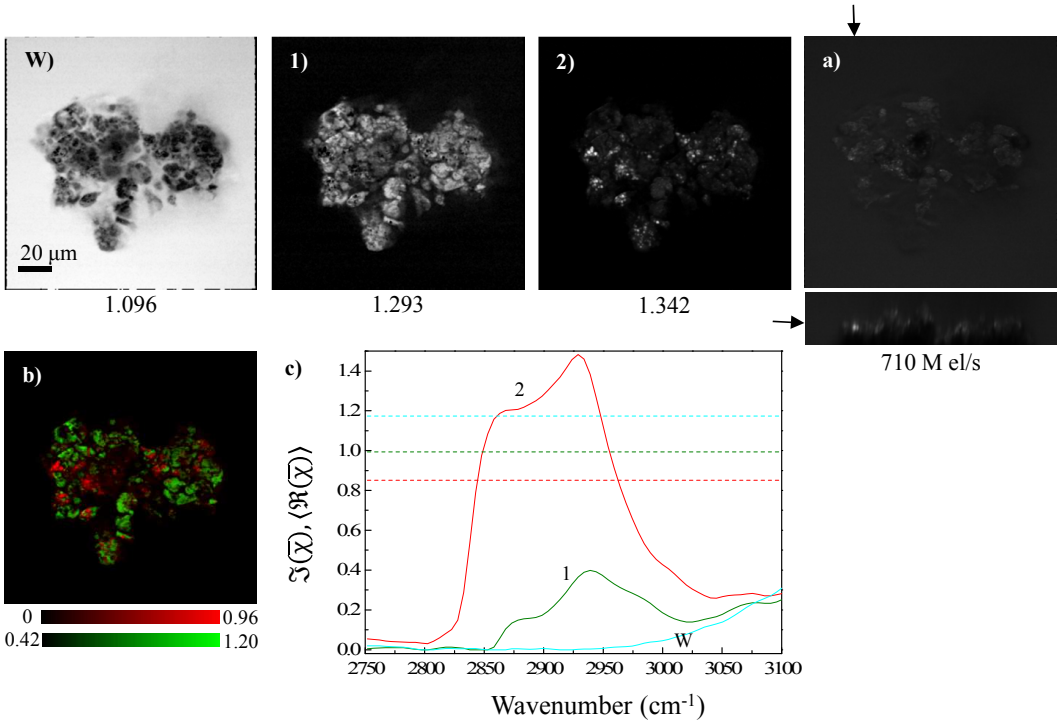

Figure 5.7: FSC^3 analysis of a primary human colorectal cancer organoid. Concentrations (images W,1,2) and their corresponding spectra (c) are shown. Grayscales as in Fig. 4.4. a) shows the xy and xz sections of CARS intensity at 2835 cm^{-1}. b) is a colour overlay with $\mathcal{C}_1$ in green and $\mathcal{C}_2$ in red channels.

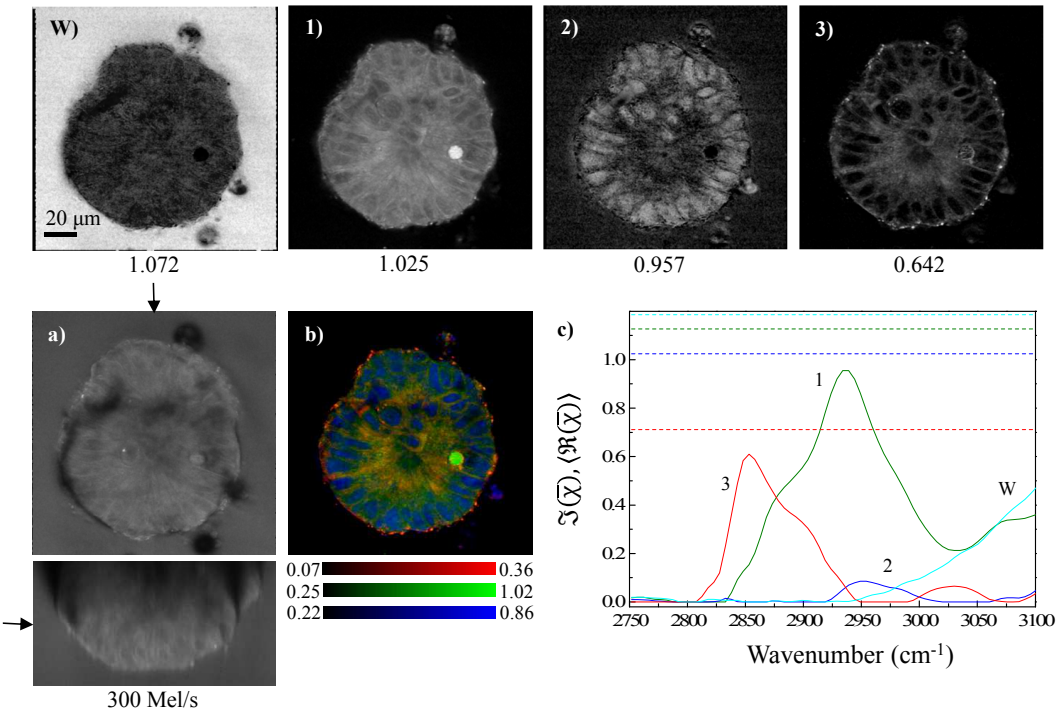

Figure 5.8: FSC^3 analysis of a metastatic human colorectal cancer organoid. FSC^3 concentrations (images W,1,2,3) and their spectra (c) are shown. Grayscales as in Fig. 4.4. a) is a colour overlay showing $\mathcal{C}_3$ in red, $\mathcal{C}_1$ in green and $\mathcal{C}_2$ in blue channels. b) shows xy and xz sections of CARS intensity at 2835 cm^{-1}.

similar to those in the mouse liver organoid grown in EM. On the other hand, the lipids in the primary colorectal cancer tumour are similar to those in the differentiated liver organoid, suggesting that the metastatic cancers are different from not only the primary cancers as expected, but also the functionally specialized healthy DM organoids. However the primary cancers are similar to healthy DM organoids, with respect to their lipid composition.

5.3 Conclusions

In this chapter, the applicability of quantitative, chemically specific CARS microscopy to higher levels of biological organization (organoids) has been demonstrated for three kinds of organoids at various stages of their development. Differences in the organoids with respect to their stage of growth have been determined, with organoids in primary and expansion stages of growth not demonstrating independent CARS discernible concentrations of chromatin whilst those in advanced stages of development are well factorized into three expected components of cellular chemistry corresponding to protein, lipid and chromatin.
Using the same techniques, CARS microscopy has been demonstrated to study the time-dependent lipid composition in live human adipocytes [125]. In the analysis shown in this chapter, the FSC^3 spectra corresponding to lipid ($\mathcal{C}_3$) show peaks at 2850 cm^{-1} and a broad shoulder at $\sim$2930 cm^{-1} along with a peak at $\sim$3010 cm^{-1} in the FSC^3 analyses of the mouse liver organoid (EM) (Fig. 5.5) and the metastatic human colorectal cancer organoid (Fig. 5.8). These peaks are characteristic of unsaturated lipids [125]. On the other hand, the lipid spectra of the mouse intestinal

organoids (shown in Fig. 5.3, Fig. 5.4), the mouse liver organoid (DM) shown in Fig. 5.6 and the primary human colorectal cancer organoid shown in Fig. 5.7 do not show the peak at $\sim 3010\,\mathrm{cm}^{-1}$. The role of lipid metabolism in cancer growth and metastases has been reported in literature [165, 166]. CARS microscopy with its demonstrated chemical specificity and sensitivity can be employed to examine 3D models i.e., organoids of cancer to further our understanding of the underlying causes and possibly identify methods of treatment targeting specific lipid metabolisms.
It is important to acknowledge that the results shown in this chapter are also, not statistically significant, but nevertheless present promising evidence to warrant further investigation using faster imaging methods such as sparse sampling [120], or 100 KHz scans (which have been demonstrated for the data on anti-cancer drug treated U-2OS cells in the previous chapter), in order to acquire full hyperspectral information to enable quantitative volumetry of the composite organic materials. These could present valuable information which could represent clear trends specifically in lipid composition in different stages of growth of tissues/organoids and metastases of tumours.
As briefly discussed in the introduction to this chapter, studies on organoids present important scope for *in vitro* applications to biomedical and biochemistry research at organ level in 3D, along with capabilities to research treatment methodologies for various cancers on a case by case basis, drug interactions and delivery [24, 25, 168]; applications which are typically researched using fluorescence microscopy. Due to the already mentioned drawbacks of invasive microscopy techniques, and the benefits of chemical specificity offered by CARS, the work shown in this chapter opens up an interesting and powerful future outlook for organoid research.

Summary and Outlook

CARS microspectroscopy with a suited subsequent analysis as used in this work (phase corrected Kramers-Kronig (PCKK) and factorization into concentrations of chemical components (FSC^3), see section 3.3) provides chemically specific and quantitative information about the materials under study with three-dimensional spatial resolution in the sub-micrometer range. To verify the volumetric accuracy of the method, polymer beads of known sizes were imaged and their volumes determined from the FSC^3 components were found to be in close agreement with their actual volumes (section 3.4.2). The imaging optics and the refractive index of the samples were found to have no bearing on the accuracy of this quantitative analysis. This project focussed on studying cell division which is responsible for the evolution of life from its unicellular origins to multicellularity. However, if cell division is not regulated, it can lead to diseases like cancer. This necessitates studies on cell division to reveal clues pertinent to the nature of the cancer itself, which can aid in the development of cancer treatments. In this project, CARS microscopy was used to study fixed U-2OS (ATCC HTB-96) osteosarcoma cells transfected with a G2M Cell Cycle Phase Marker (GE Healthcare, UK), eGFP to label cyclin B1 which is expressed during the mitotic phase of the cell cycle.

Starting with feasibility studies to demonstrate the usability of CARS in detecting the chemical contrast between different cell components i.e., chromatin, protein and lipid, the origins of various FSC^3 components was established using correlative TPF. While the chromatin component is certainly nuclear in its origin, the components corresponding to protein and lipids are not colocalized to any one organelle. The suitability of CARS to image the cells in a quantitative way has been demonstrated through volumetric estimations of the relevant FSC^3 components, determining the dry masses of the lipid, protein and chromatin components. Furthermore, the effects of two types of anti-cancer drugs on the cells have been studied. We found that although Taxol produces no detectable differences in the cell's CARS component spectra, the changes in the morphology and intracellular distribution of chromatin induced due to Taxol treatment, are discernible. In this way, we have probed the indirect effect of Taxol on microtubules which play an important role in the movement/distribution of chromosomes during mitosis. This is a new way of studying the action of this drug on cells, without the need for introducing exogenous labels. Along with Taxol, another drug, ICRF-193, a topoisomerase II poison forms an important part of chemotherapy against osteosarcoma. The effects of both these drugs on cellular function have been documented in literature as discussed in chapter 4. In this project, we discovered, in the first CARS based study of its kind, that ICRF-193 changes the FSC^3 component localized within the nucleus both spectrally and in its spatial distribution. In these cells, the distribution of the FSC^3

component corresponding to chromatin is confined/more pronounced in the intranuclear punctate regions of the control sample (see Fig. 4.31) while this component is homogeneously distributed over the nuclei in drug treated cells. Additionally, on analyzing the control sample not aiming to find a common spectral bases for the drug treated and the control cells, we observe in addition to the nuclear component corresponding to the punctates, another nuclear component similar in its spectrum and spatial distribution to the nuclear component in non-drug treated cells. This is an important result, which if proven on statistically significant populations of cells and on live cells, opens up an interesting application of CARS microscopy to study drug treated populations and their phenotype post treatment.
Going from single cells to interacting cell assemblies, 3D models of organs, organoids grown in lab were also imaged using CARS and a similar chemical specificity was observed for these samples as for the cells, revealing their three-dimensional organization and chemical composition in a label-free way.

Outlook

From the technique point of view, CARS microscopy with full 3D hyperspectral information is a time-consuming method, both with respect to image acquisition and analysis. These acquisition times (approx. 20-30 minutes for full data) are incompatible with live cell imaging or indeed, for imaging a statistically significant sample set. High throughput methods such as multiplex CARS- flow cytometry as demonstrated by Camp et al. [169] or sparse sampling algorithm shown by Masia et al. [120] are significant and possible next steps in order to study statistically significant populations of live samples. Furthermore, improvements in CRS imaging techniques by using lasers of longer wavelength (0.9-1.3 μm) would increase the penetration depth and reduce photo damage and therefore make it possible to image dense tissue. Development and use of compact laser systems would contribute towards making CRS microscopy portable and practical in the field of biomedical imaging. SRS, a type of CRS scattering first reported in 2007 is also being rapidly applied to bio-chemical systems, with the advantage of background free single frequency detection. CRS techniques can be used to probe structural information (ordering) by using polarization resolved CRS methods.
The work shown in this thesis has possible applications to biomedical and biochemistry research avoiding the introduction of extraneous labels in the system at both the single cell and organ level. As already mentioned in the introduction of this thesis and in chapter 4, traditionally, invasive methods have been used to study the effects of drugs on cells. In this work, we have demonstrated that CARS microscopy reveals specific markers of drug treatment in a label-free, non-invasive way. Statistically significant sample sets will prove with definite conclusion the results of this work. Several other applications of CARS microscopy in studying the effects of various drug based therapies as well as imaging other biological processes such as necrosis can be envisioned.
The data shown in this work, in chapter 5 (organoids) is an indicator of the quality of the chemical specificity of CARS microscopy even in thicker, more advanced samples (than cells). These model organs present exciting possibilities of discovering the effects of drugs on an organ (represented by the organoid) as a whole rather than limiting the study to single cells. Such results would enable biomedical scientists to devise lines of treatment with a better understanding of the drugs' interaction with the disease, perhaps even on a case-by-case basis.

Overall, this project is only the tip of the iceberg, with many more applications, both in-depth (further data collection and analysis to acquire a deeper understanding of the findings shown) as well as breadth-wise (expand CARS to new applications including other samples and other applications on live cells).

Appendix A

A.1 Optics

The data shown in this thesis were acquired on our home-built microscope using the objective and condenser combinations which are called immersion or dry optics in this thesis. The specifications of the optics are given in this section. The fill factors were calculated as described in section 3.4.1.

Lens	**Specifications**	**Nikon Code**	**Immersion**	**Fill factor (Tube lens multiplication factor)**
Nikon CFI Plan Apochromat λ series	Objective 20 ×, 0.75 NA	MRD00205	Air	0.55 (1.0) 0.83 (1.5)
Nikon CFI Plan Apochromat IR λS series	Objective 60 ×, 1.27 NA	MRD70650	Water (1.33)	0.98 (1.0) 1.43 (1.5)
Nikon CLWD	Condenser 0.72 NA	MEL56100	Air	
Nikon HNAO	Condenser 1.4 NA	MEL41410	Oil (1.52)	

Table A.1: Immersion and dry optics.

Appendix B

B.1 Epi-fluorescence detection efficiency

In section 4.2, epi-fluorescence imaging of $54 \pm 7\,\mu$M eGFP solution filled in a sealed chamber of height $120\,\mu$m is described. In the following two sections, we show the calculations of detection efficiency of the dry objective and the illumination power density.

B.1.1 Detection efficiency

The detection efficiency E_D is defined as a function of the transmission of the optics T_o, the camera quantum efficiency E_{CCD} and the normalized angular range of collection given by $\Theta/(4\,\pi)$

$$E_D = T_o \times E_{CCD} \times \Theta/(4\,\pi) \tag{B.1}$$

Substituting the values of the opening angle for the dry objective, 0.60 rad corresponding to solid angle Θ=1.09 sr, and T_o and E_{CCD} as 0.6 each in equation B.1, we calculate a detection efficiency of 3.1%.

B.1.2 Illumination power density

The illumination power density incident on the sample is calculated as follows. We calculate the number of fluorophore molecules per camera pixel, N_p as

$$N_p = n \times A_0 \tag{B.2}$$

where n is the number of fluorophore molecules/area calculated using equation 4.2 and A_0 is the pixel area. On substituting $n = 3.9 \times 10^{18}$ /m^2 and $A_0 = 0.104\,\mu$m^2, we get $N_p = 4.1 \times 10^5$ molecules/pixel.
The number of photoelectrons/molecule, N'_p is given by

$$N'_p = \frac{N_e}{t\,N_p} \tag{B.3}$$

where N_e is the number of photoelectrons per pixel and t is the exposure time. $N_e = \Gamma \times \overline{I}$, where Γ is the camera gain, 4.45 electrons/count, and $\overline{I} = 2385$ counts is the mean pixel value over the eGFP solution in the epi fluorescence image. The exposure time was 0.6 ms. This results in 1.9×10^7 photoelectrons/second.
By substituting the values of photoelectrons emitted/second in equation B.3 and using N_p calculated previously, we get N'_p= 46 photoelectrons/molecule. We then

use the detection efficiency to calculate the emission rate E; 1.5×10^3 photons/s (see equation B.4)

$$E = N'_{\mathrm{p}}/\mathrm{E_D} \tag{B.4}$$

The photoelectron emission rate is related to the photon absorption rate, $\mathrm{A_p}$ through the quantum efficiency of the fluorophore, $\mathrm{Q_f} = 0.6$ as

$$\mathrm{A_p} = \mathrm{E}/\mathrm{Q_f} \tag{B.5}$$

giving $\mathrm{A_p} = 2.5 \times 10^3$ photons/second.
Using the extinction coefficient β and the number of fluorophores/volume, n calculated from the molarity of the eGFP solution, we obtain an absorption cross section $\sigma = \beta/n$ of $1.6 \times 10^{-16}/\mathrm{cm}^2$.
The photon flux calculated as $\mathrm{A_p}/\sigma$ is $1.6{\times}10^{19}$ photons/cm^2/s; resulting in an illumination power density of 6 W/cm^2 using 488 nm as the wavelength of absorption.

Appendix C

C.1 Raman active bonds in biomolecules

In this section, some examples of counting Raman active bonds in biomolecules like protein, DNA and oleic acid are given. Referring to the database of Raman peaks [170], we know that in addition to the OH, the CH and NH-N bonds are Raman active in the CH stretch region over which the data in this thesis have been acquired. Since we exclude the water resonance in the analysis, we count the number of CH and NH-N bonds in order to determine the bonds/weight for the various FSC^3 components. The following discussion in this section is based on the structures of the various biomolecules given in [171].

C.1.1 DNA

The DNA is made of two strands helically coiled around each other comprising purine (adenine, guanine) and pyrimidine bases (thymine and cytosine) attached to a pentose sugar (deoxyribose). The sugar-base unit is called nucleoside. Several nucleosides (with purine bases) are connected by phosphate bonds to form one strand of DNA. The complementary strand of nucleosides comprises pyrimidine bases (adenine pairs with thymine and cytosine pairs with guanine). The two DNA strands are held together by NH-N bonds. Therefore, there are as many NH-N bonds as there are base-pairs, i.e., 3.2 billion [172]. The CH bonds are counted by considering the structure of the four types of nucleosides. As an example, the structure of the nucleoside with adenine base is given in Fig. C.1 a). We count for this nucleoside, 8 CH bonds (2 CH from the base, 6 CH from the sugar). The structures of other nucleosides are given in [171] and the number of Raman active bonds in the other nucleosides (named after the base) are cytosine (8), thymine (10) and guanine (7). Considering the four types of nucleosides in equal proportions and the N-H-N bonds, the total number of Raman active bonds in DNA is 57.75 billion. This corresponds to 18.05 bonds/base-pair. The atomic mass of one base pair is 650 a.m.u.

C.1.2 Proteins

Proteins are long chains of amino acids bonded such that the acidic moiety of one amino acid is linked to the amino moeity of the other, through a peptide bond (-CO-NH-) lacking Raman active CH/N-H-N bonds. There are 20 amino acids in all, of which we show the most abundant amino acid, leucine in Fig. C.1 b) containing 10 CH bonds.
The number of CH bonds, b in all the amino acids are listed in Table C.1.

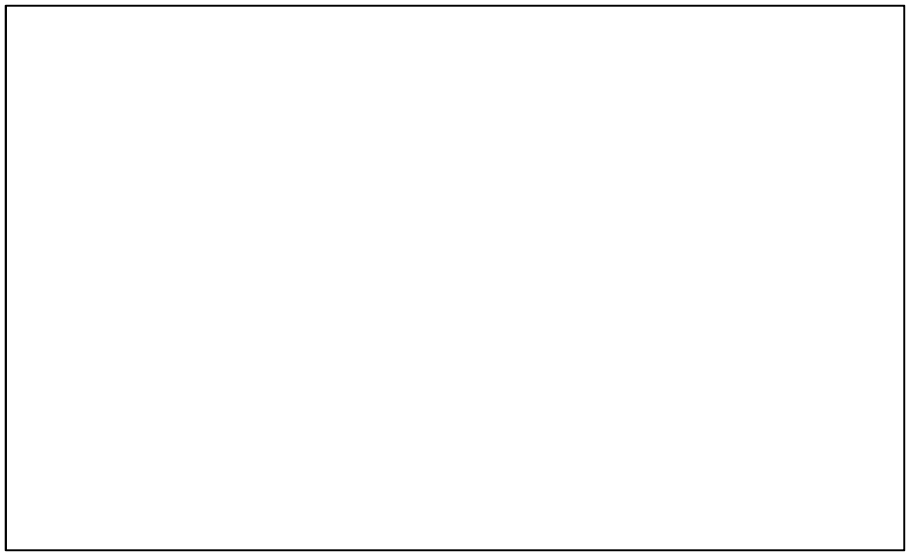

Figure C.1: a) Molecular structure of adenine nucleoside comprising a pentose sugar attached to adenine. b) Molecular structure of amino acid Leucine. This figure (appearing as Figures 2.13 and 2.14 in reference [171]) has been redacted for copyright reasons.

Amino acid	b	mass (a.m.u)	Amino acid	b	mass (a.m.u)
Alanine	5	89	Arginine	7	174
Asparagine	3	132	Aspartic acid	3	133
Cysteine	3	121	Glutamic acid	5	147
Glutamine	5	146	Glycine	2	75
Histidine	5	155	Isoleucine	10	131
Leucine	10	131	Lysine	9	146
Methionine	7	149	Phenylanine	8	165
Proline	7	115	Serine	3	105
Threonine	5	119	Tryptophan	10	204
Tyrosine	7	181	Valine	8	117

Table C.1: Number of Raman active bonds in, and the relative abundance of various amino acids [143].

The relative abundances of the various amino acids [143] were considered and the number of Raman active bonds in an average protein was calculated as 6.06.

C.1.3 Oleic acid

The molecular formula of oleic acid is $CH_3\,(CH_2)_7\,CH\,=\,CH\,(CH_2)_7\,COOH$ comprising 33 CH bonds. The molecular mass of oleic acid is 282.5 a.m.u.

C.2 Dry factors calculation parameters

The areas and other parameters used to determine the dry factors for the volumetric calculations shown in this thesis are given in this section.

C.2.1 Simultaneous factorization of the cells labelled with DAPI and mitotracker-orange

The parameters for the calculation of dry factors of the intracellular FSC^3 components of the factorization shown in Fig. 4.15 - Fig. 4.17 are given in Table C.2.

$\mathcal{C}_i$	α	IFD range (cm^{-1})	A_i (cm^{-1})
$\mathcal{C}_1$	1.04	2750 - 3050	27
$\mathcal{C}_2$	1.04	2750 - 3050	163
$\mathcal{C}_3$	0	2860 - 3050	21
$\mathcal{C}_4$	2.3	2750 - 3050	290

Table C.2: Calculation parameters corresponding to the FSC^3 components 1-4 shown in Fig. 4.15 - Fig. 4.17.

C.2.2 Alternative simultaneous factorization of the cells labelled with DAPI and mitotracker-orange

The parameters for the calculation of dry factors of the intracellular FSC^3 components of the factorization shown in Fig. 4.21 - Fig. 4.23 are given in Table C.3.

$\mathcal{C}_i$	α	IFD range (cm^{-1})	A_i (cm^{-1})
$\mathcal{C}_1$	1.02	2800 - 3050	90
$\mathcal{C}_2$	0.8	2890 - 3050	14
$\mathcal{C}_3$	0.4	2800 - 3050	119

Table C.3: Calculation parameters corresponding to the FSC^3 components 1-3 shown in Fig. 4.21 - Fig. 4.23.

C.2.3 Factorization of the cell shown in Fig. 4.26

The parameters for the calculation of dry factors of the intracellular FSC^3 components of the factorization shown in Fig. 4.26 are given in Table C.4.

$\mathcal{C}_i$	α	IFD range (cm^{-1})	A_i (cm^{-1})
$\mathcal{C}_1$	1.5	2800 - 3050	131
$\mathcal{C}_2$	1.28	2850 - 3030	29
$\mathcal{C}_3$	1.15	2800 - 3050	616

Table C.4: Calculation parameters corresponding to the FSC^3 components 1-3 shown in Fig. 4.26.

C.2.4 Factorization of the cell shown in Fig. 4.27

The parameters for the calculation of dry factors of the intracellular FSC^3 components of the factorization shown in Fig. 4.27 are given in Table C.5.

$\mathcal{C}_i$	α	IFD range (cm^{-1})	A_i (cm^{-1})
$\mathcal{C}_1$	1.05	2800 - 3050	112
$\mathcal{C}_2$	0.5	2850 - 3030	43
$\mathcal{C}_3$	0.75	2800 - 3050	590

Table C.5: Calculation parameters corresponding to the FSC^3 components 1-3 shown in Fig. 4.27.

C.2.5 Factorization of the cell shown in Fig. 4.28

The parameters for the calculation of dry factors of the intracellular FSC^3 components of the factorization shown in Fig. 4.28 are given in Table C.6.

$\mathcal{C}_i$	α	IFD range (cm^{-1})	A_i (cm^{-1})
$\mathcal{C}_1$	5	2800 - 3050	363
$\mathcal{C}_2$	0	2850 - 3010	52
$\mathcal{C}_3$	1.2	2800 - 3050	815

Table C.6: Calculation parameters corresponding to the FSC^3 components 1-3 shown in Fig. 4.28.

C.2.6 Simultaneous factorization of the cells shown in Fig. 4.30

The parameters for the calculation of dry factors of the intracellular FSC^3 components of the factorization shown in Fig. 4.30 are given in Table C.7.

$\mathcal{C}_i$	α	IFD range (cm^{-1})	A_i (cm^{-1})
$\mathcal{C}_1$	1.6	2800 - 3050	363
$\mathcal{C}_2$	0	2850 - 3010	52
$\mathcal{C}_3$	0.4	2800 - 3050	815

Table C.7: Calculation parameters corresponding to the FSC^3 components 1-3 shown in Fig. 4.30.

C.2.7 Simultaneous factorization of the cells shown in Fig. 4.31

The parameters for the calculation of dry factors of the intracellular FSC^3 components of the factorization shown in Fig. 4.31 are given in Table C.8.

$\mathcal{C}_i$	α	IFD range (cm^{-1})	A_i (cm^{-1})
$\mathcal{C}_1$	5	2800 - 3050	361
$\mathcal{C}_2$	0	2850 - 3010	53
$\mathcal{C}_3$	1.2	2800 - 3050	801

Table C.8: Calculation parameters corresponding to the FSC^3 components 1-3 shown in Fig. 4.31.

Appendix D

This Appendix gives the factorization settings and the FSC^3 components not shown in chapters 4 and 5. The errors in concentration and spectrum (E_C and E_S) are also given.

D.1 Analysis settings and FSC^3 components

The settings used for analyzing the CARS data shown in this thesis are given in this section. The analysis settings common to all the factorizations are given in Table D.1. The settings which were different for each data analyzed are given in the following sections.

SVD components	10	PCKK amplitude filtering	3 ps
PCKK phase filtering	0.1 ps	Real part factor	1
Solver	BP	Concentration constrain	Yes
Target	0.1	# Iterations defining divergence	3

Table D.1: Analysis settings common to all the factorizations shown in this thesis .

D.1.1 Polymer Beads

The hyperspectral CARS data of polymer beads of various sizes, shown in chapter 3 was SVD denoised using 5 SVD components and FSC^3 analyzed using single tolerance settings in Table D.2.

Components	2	Min. iterations	100
Max. iterations	100	Stop criterion	Tolerance
Spatial correlation $(\sigma_x, \sigma_y, \sigma_z)$	N/A	Guided factorization weights	N/A

Table D.2: Analysis settings for all the polymer beads shown in section 3.4.1.

D.1.2 Unlabelled fixed U-2OS cells

The simultaneous factorization shown in Fig. 4.4 - Fig. 4.7 was obtained using the FSC^3 settings given in Table D.3. The FSC^3 components corresponding to water (4 components), glass and systematics- one component each which were not shown in Fig. 4.4 to Fig. 4.7 are given in Fig. D.1 to Fig. D.3. Components 4, 6, 7 and 8 correspond to water while components 5 and 9 are attributed to glass and systematics respectively.
Fig. D.2 and Fig. D.3 show these FSC^3 components for the cell shown in Fig. 4.6 and Fig. 4.7 respectively.

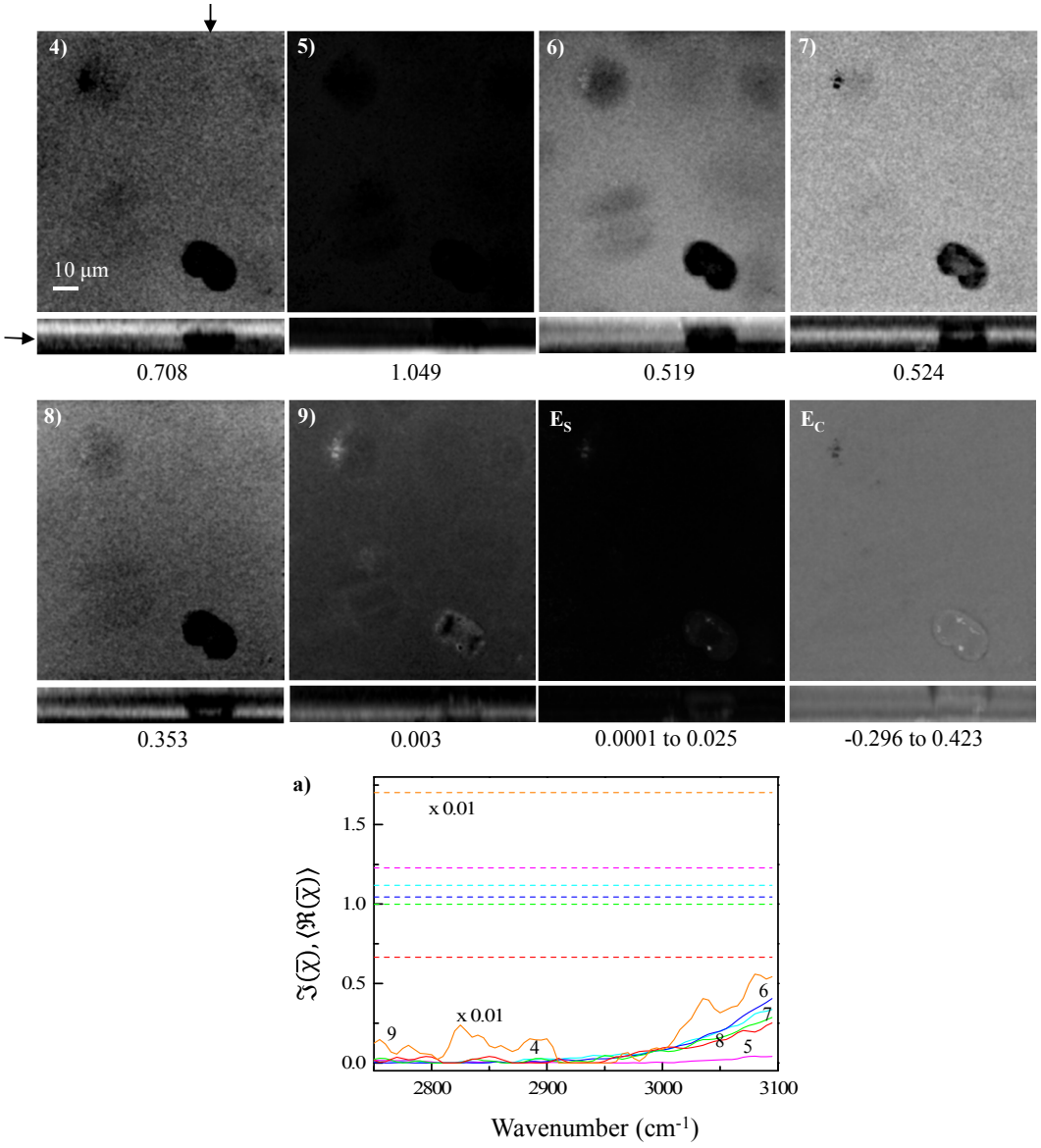

Figure D.1: *xy* and *xz* sections of FSC^3 components (4-9) previously not shown in Fig. 4.4. Grayscales as in Fig. 4.4. a) shows the component spectra of 4-9 in cyan, magenta, blue, green, red and orange respectively. Component 9 spectra are rescaled by a factor of 0.01.

Components	9	Min. iterations	100
Max. iterations	1000	Stop criterion	Tolerance
Spatial correlation $(\sigma_x, \sigma_y, \sigma_z)$	N/A	Guided factorization weights	N/A

Table D.3: Analysis settings for the simultaneous factorization shown in Fig. 4.4 to Fig. 4.7.

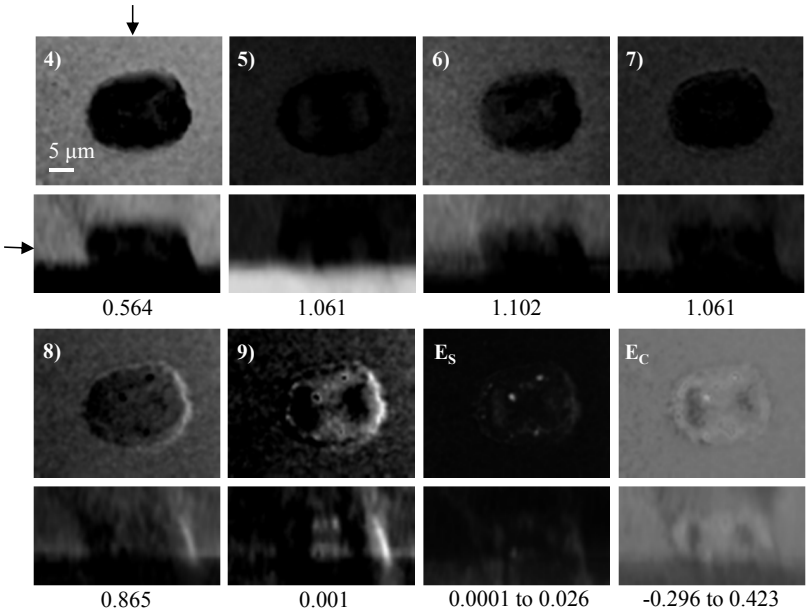

Figure D.2: *xy* and *xz* sections of FSC³ components (4-9) previously not shown in Fig. 4.6. Grayscales as in Fig. 4.4. The component spectra are shown in Fig. D.1 a).

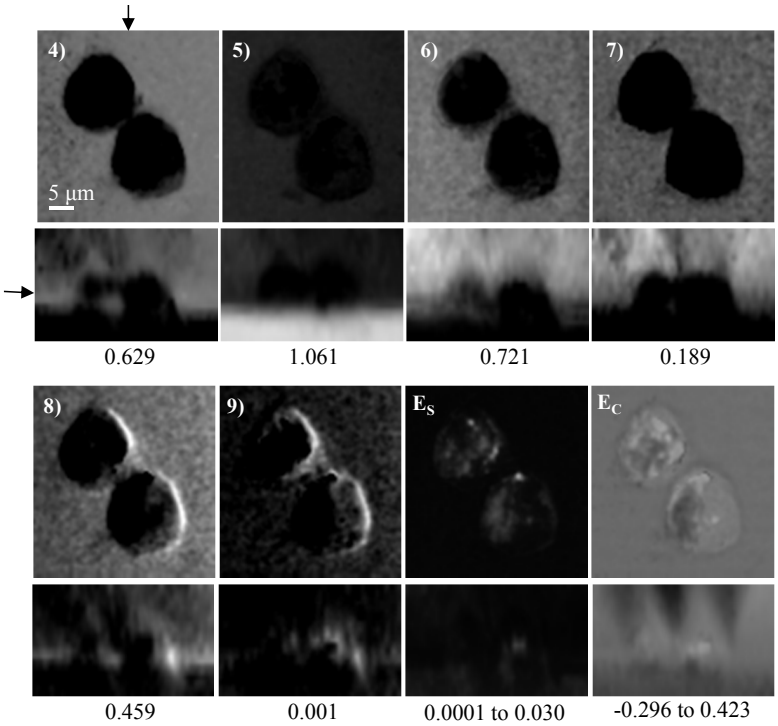

Figure D.3: *xy* and *xz* sections of FSC³ components (4-9) previously not shown in Fig. 4.7. Grayscales as in Fig. 4.4. The component spectra are shown in Fig. D.1 a).

The settings used to analyze the data shown in Fig. 4.8 are given in Table D.4. In this analysis, a modification, referred to as spatial correlation was used in the factorization procedure. In spatial correlation, the concentrations, C and data, D are smoothed by applying a Gaussian filter in the first step of every loop of the NMF, for the calculation of the spectra, S. In the analysis, $\sigma_{x,y,z}$ are the widths along the x, y and z axes of the Gaussian filter in the same units as the pixel scaling (μm).
The five FSC^3 components corresponding to three components of water ($\mathcal{C}_6, \mathcal{C}_7, \mathcal{C}_{10}$) and the others corresponding to systematics are shown in Fig. D.4.

Components	10	Min. iterations	100
Max. iterations	1000	Stop criterion	Tolerance
Spatial correlation $(\sigma_x, \sigma_y, \sigma_z)$	0.175, 0.175, 1	Guided factorization weights	N/A

Table D.4: Analysis settings for Fig. 4.8

Table D.5 shows the FSC^3 settings used to factorize the data shown in Fig. 4.9. The three FSC^3 components corresponding to water which were not shown in Fig. 4.9 are given in Fig. D.5.

Components	6	Min. iterations	100
Max. iterations	100	Stop criterion	Tolerance
Spatial correlation $(\sigma_x, \sigma_y, \sigma_z)$	N/A	Guided factorization weights	N/A

Table D.5: Analysis settings for Fig. 4.9

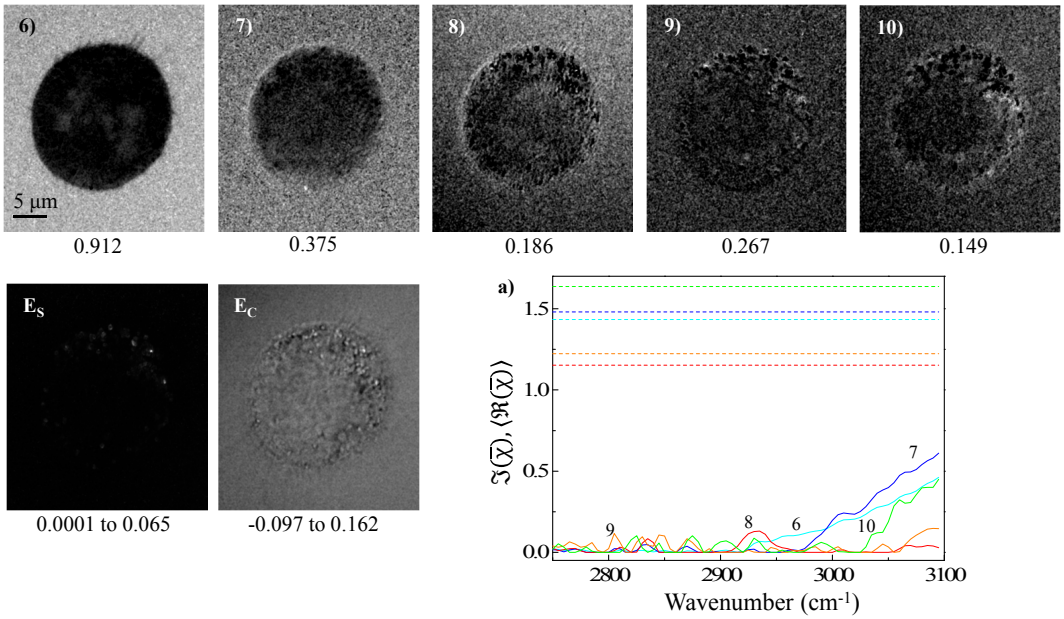

Figure D.4: *xy* and *xz* sections of FSC^3 components (previously not shown in Fig. 4.8) with their spectra shown in a), in cyan (6), blue (7), red (8), orange (9) and green (10). Grayscales as in Fig. 4.4.

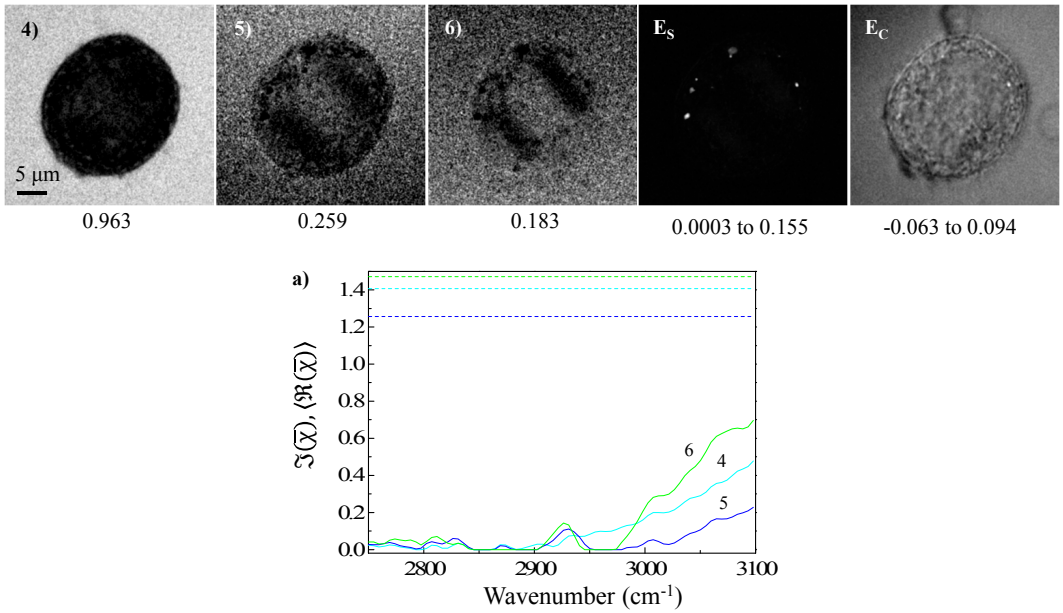

Figure D.5: *xy* and *xz* sections of FSC³ components (previously not shown in Fig. 4.9) with their spectra shown in a). Grayscales as in Fig. 4.4.

D.1.3 Labelled fixed U-2OS cells

D.1.3.1 Factorization over extended spectral range

The factorization settings used to analyze the data shown in Fig. 4.13 over the extended spectral range are given in Table D.6. The four FSC^3 components not shown

Components	8	Min. iterations	10
Max. iterations	1000	Stop criterion	Error
Spatial correlation $(\sigma_x, \sigma_y, \sigma_z)$	0.2, 0.2, 0.5	Guided factorization weights	N/A

Table D.6: Analysis settings for Fig. 4.13

in Fig. 4.13, corresponding to water are given in Fig. D.6.

D.1.3.2 Simultaneous factorization of cells in metaphase, anaphase and cytokinesis in spectral range 2750 - 3200 cm^{-1}

Settings for the first simultaneous factorization analysis shown in Fig. 4.15 - Fig. 4.17 are given in Table D.7. The three FSC^3 components not shown in Fig. 4.15 - Fig. 4.17 with two corresponding to water $(\mathcal{C}_5, \mathcal{C}_6)$ and one corresponding to glass $(\mathcal{C}_7)$ are given in Fig. D.7 - Fig. D.9.

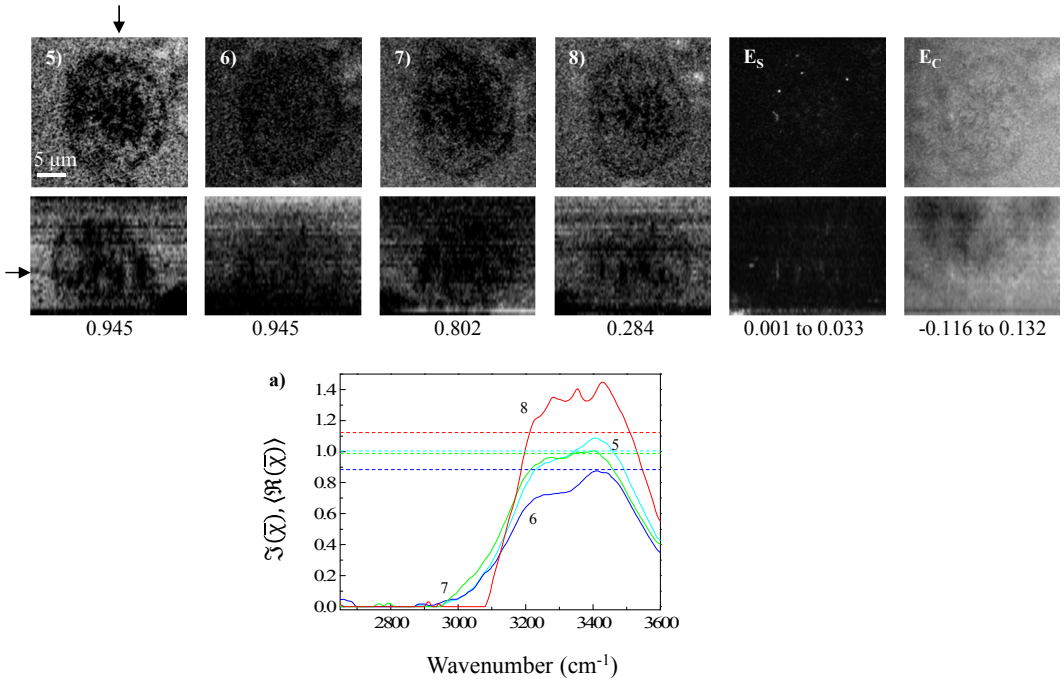

Figure D.6: *xy* and *xz* sections of FSC^3 components (previously not shown in Fig. 4.13) with their spectra shown in a). Grayscales as in Fig. 4.4

.

Components	7	Min. iterations	10
Max. iterations	1000	Stop criterion	Tolerance
Spatial correlation $(\sigma_x, \sigma_y, \sigma_z)$	0.2, 0.2, 0.75	Guided factorization weights	N/A

Table D.7: Analysis settings for the simultaneous factorization of data shown in Fig. 4.15-Fig. 4.17.

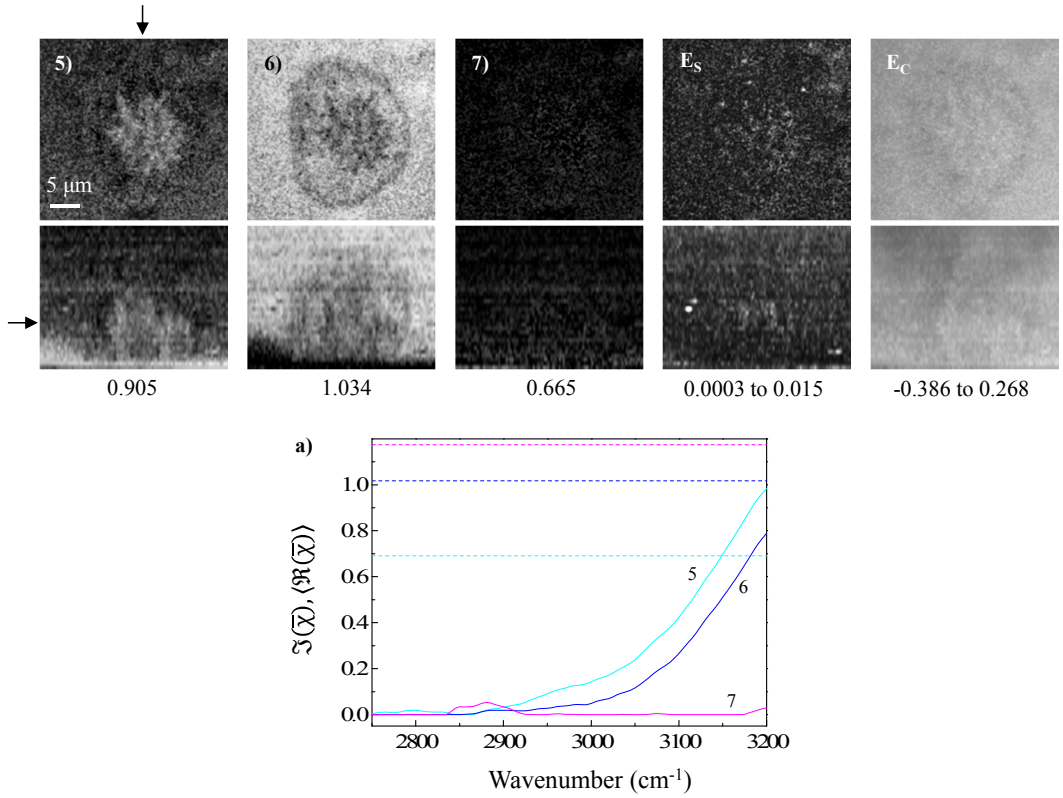

Figure D.7: *xy* and *xz* sections of FSC^3 components (previously not shown in Fig. 4.15) with their spectra shown in a). Grayscales as in Fig. 4.4.

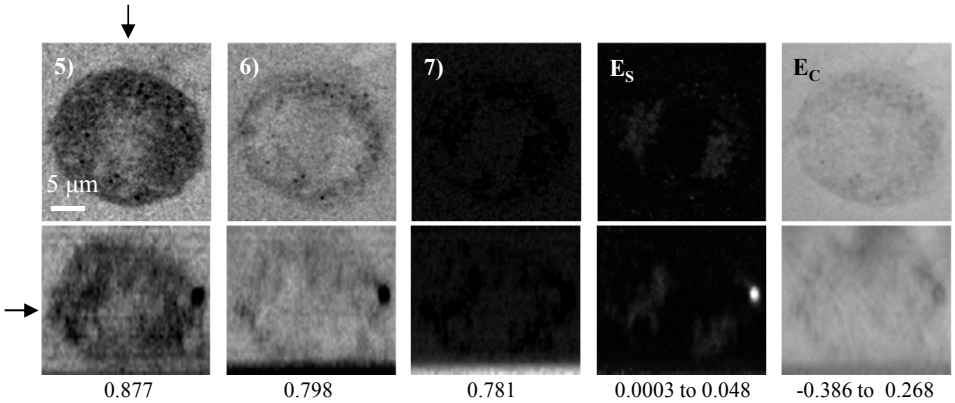

Figure D.8: *xy* and *xz* sections of FSC^3 components (previously not shown in Fig. 4.16) with their spectra shown in Fig. D.7 a). Grayscales as in Fig. 4.4.

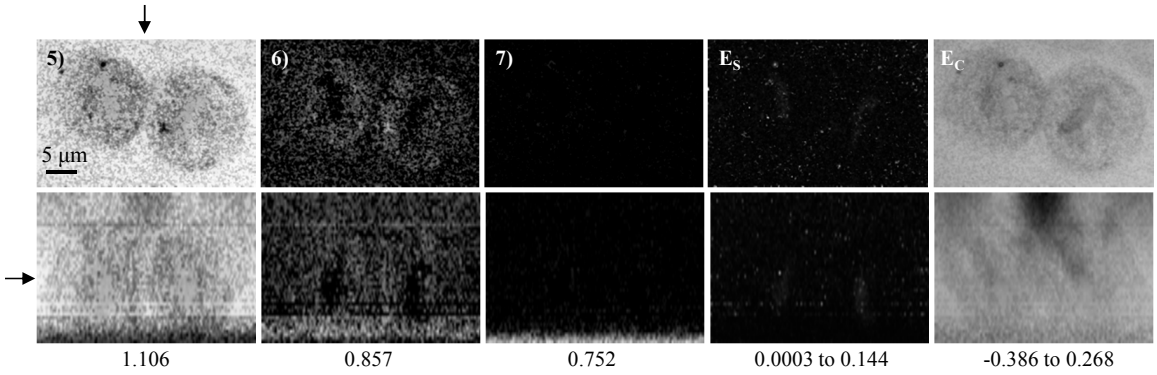

Figure D.9: *xy* and *xz* sections of FSC^3 components (previously not shown in Fig. 4.17) with their spectra shown in Fig. D.7 a). Grayscales as in Fig. 4.4.

D.1.3.3 Alternative simultaneous factorization of the cells in spectral range 2700 - 3150 cm^{-1}

Table D.8 shows the settings of the second simultaneous factorization shown in Fig. 4.21 - Fig. 4.23. The four FSC^3 components ($\mathcal{C}_4, \mathcal{C}_6$) corresponding to water, $\mathcal{C}_5$ to glass and $\mathcal{C}_7$ to systematics along with their spectra are shown in Fig. D.10 - Fig. D.12.

Components	7	Min. iterations	100
Max. iterations	1000	Stop criterion	Tolerance
Spatial correlation $(\sigma_x, \sigma_y, \sigma_z)$	0.2, 0.2, 0.75	Guided factorization weights	N/A

Table D.8: Analysis settings for the simultaneous factorization of data shown in Fig. 4.21-Fig. 4.23.

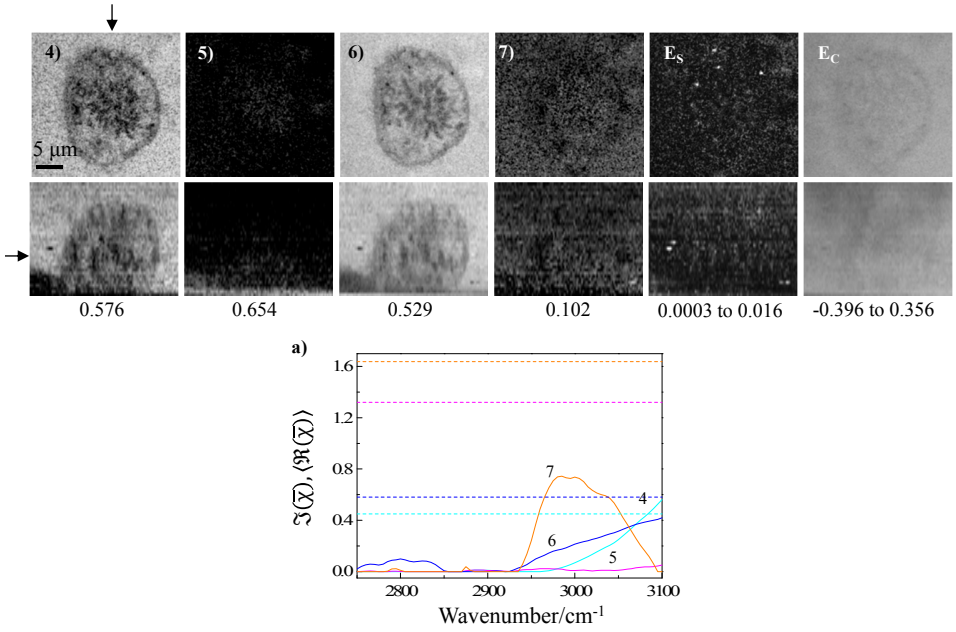

Figure D.10: *xy* and *xz* sections of FSC^3 components (previously not shown in Fig. 4.21) with their spectra shown in a). Grayscales as in Fig. 4.4.

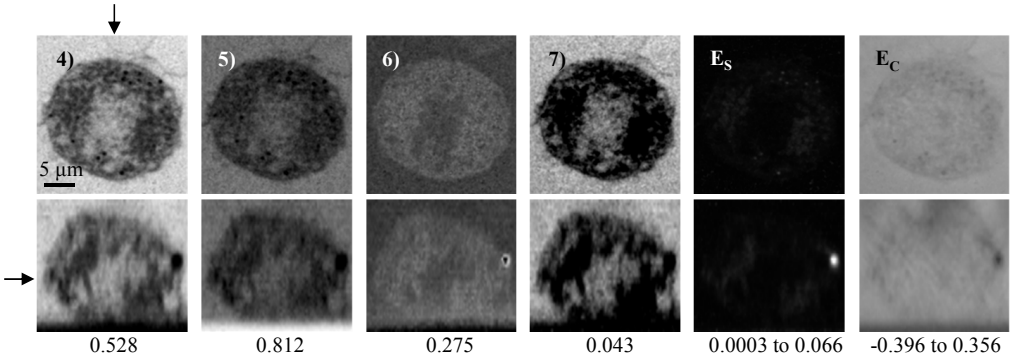

Figure D.11: *xy* and *xz* sections of FSC^3 components (previously not shown in Fig. 4.22) with their spectra shown in Fig. D.10 a). Grayscales as in Fig. 4.4.

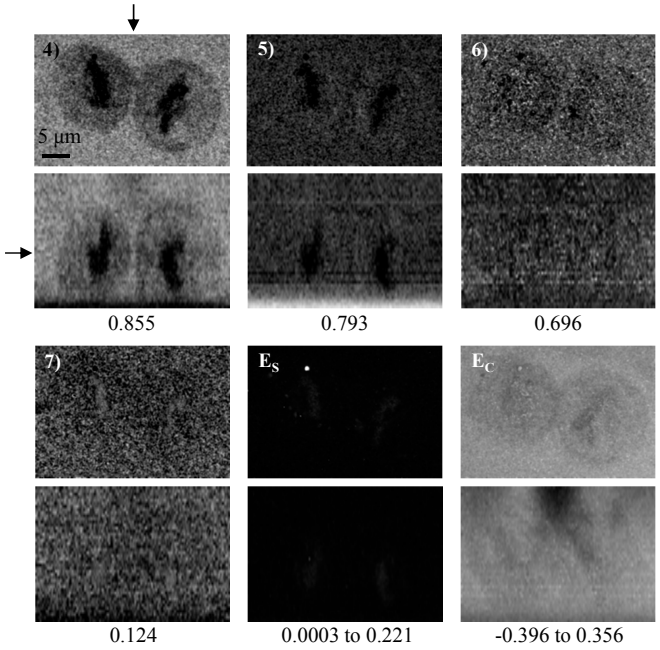

Figure D.12: *xy* and *xz* sections of FSC^3 components (previously not shown in Fig. 4.23) with their spectra shown in Fig. D.10 a). Grayscales as in Fig. 4.4.

D.1.4 Drug treated U-2OS cells

D.1.4.1 Taxol treated cells

The factorization settings used to analyze the data shown in Fig. 4.24 are given in Table D.9.

The five FSC^3 components not shown in Fig. 4.24 are attributed to water (4), glass (5) and interface (6-8). These are given in Fig. D.13.

Components	8	Min. iterations	100
Max. iterations	100	Stop criterion	Error
Spatial correlation $(\sigma_x, \sigma_y, \sigma_z)$	N/A	Guided factorization weights	N/A

Table D.9: Analysis settings for the factorization shown in Fig. 4.24.

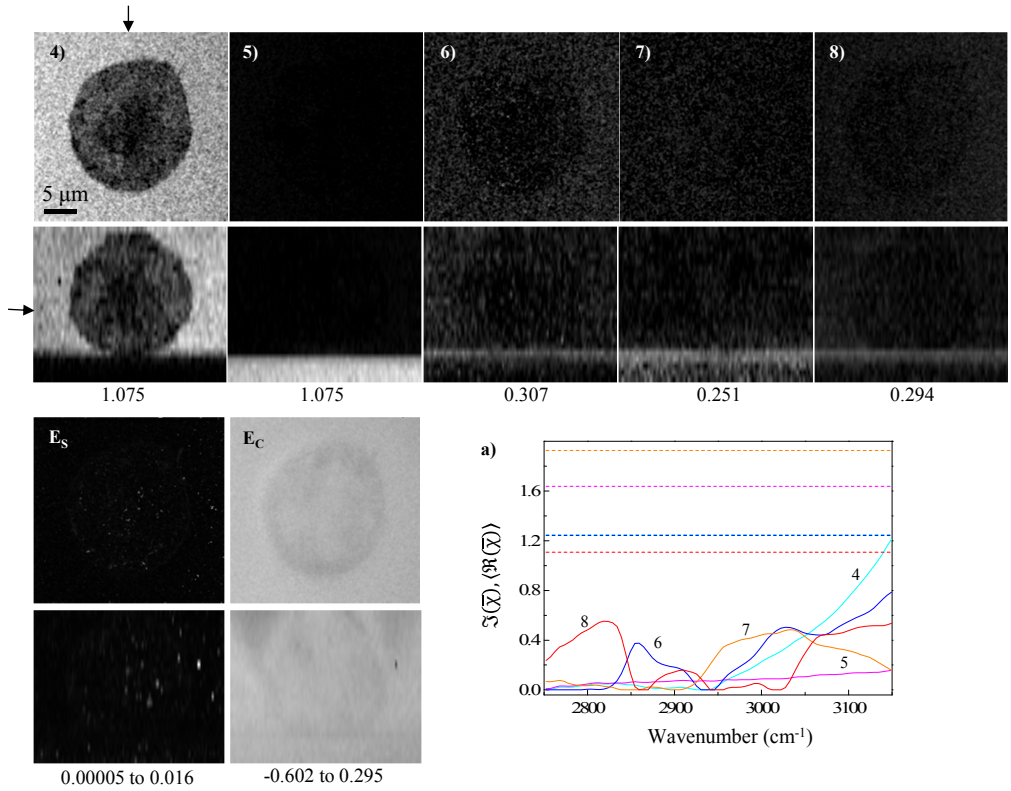

Figure D.13: *xy* and *xz* sections of FSC^3 components (previously not shown in Fig. 4.24) with their spectra shown in a). Grayscales as in Fig. 4.4.

Obtaining guide spectra for guided factorization

Fig. D.14 shows an FSC^3 analyis of an ICRF-193 treated cell (7 days growth following 24 hours of drug treatment prior to fixation, sample C). Components $\mathcal{C}_2, \mathcal{C}_3$, and $\mathcal{C}_4$ shown in Fig. D.14, correspond to protein, chromatin and lipid respectively. The other components correspond to water $(\mathcal{C}_1, \mathcal{C}_5, \mathcal{C}_7, \mathcal{C}_8)$, glass $(\mathcal{C}_6)$ and systematics $(\mathcal{C}_9)$. The analysis settings for this factorization are given in Table D.14.

Components	9	Min. iterations	100
Max. iterations	100	Stop criterion	Error
Spatial correlation $(\sigma_x, \sigma_y, \sigma_z)$	N/A	Guided factorization weights	N/A

Table D.10: Analysis settings for the factorization shown in Fig. D.14.

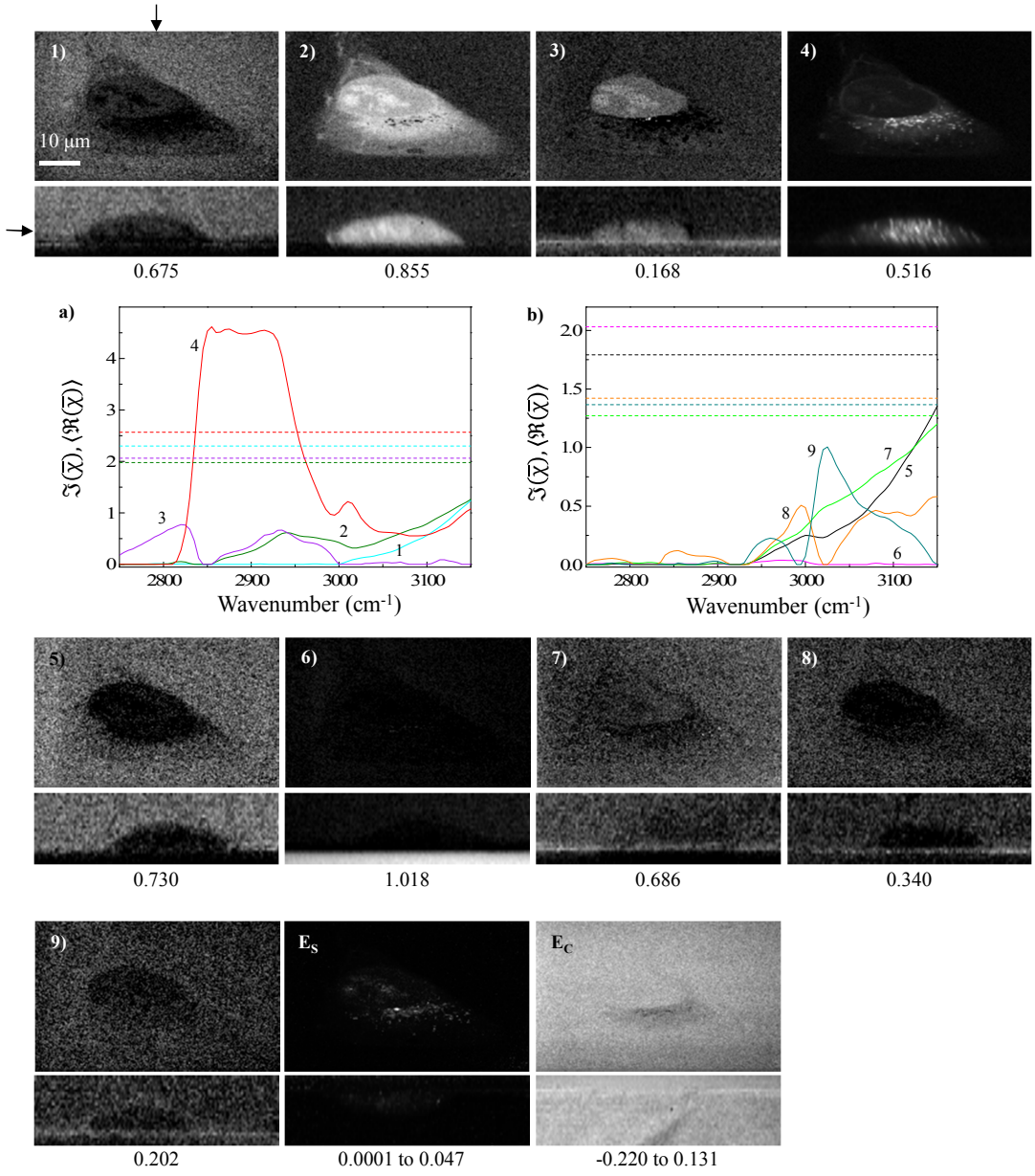

Figure D.14: *xy* and *xz* sections of nine FSC^3 concentrations (1-9) with their corresponding spectra in a). Grayscales as in Fig. 4.4.

$\mathcal{C}_1 - \mathcal{C}_4$ shown in Fig. D.14 were used as guide spectra (the weight used for all the guide spectra was 25%) to factorize the data shown in Fig. D.15, with analysis settings as given in Table D.11.

Components	8	Min. iterations	100
Max. iterations	100	Stop criterion	Error
Spatial correlation $(\sigma_x, \sigma_y, \sigma_z)$	N/A	Guided factorization weights	25% for $\mathcal{C}_1 - \mathcal{C}_4$ in Fig. D.14

Table D.11: Analysis settings for the factorization shown in Fig. D.15.

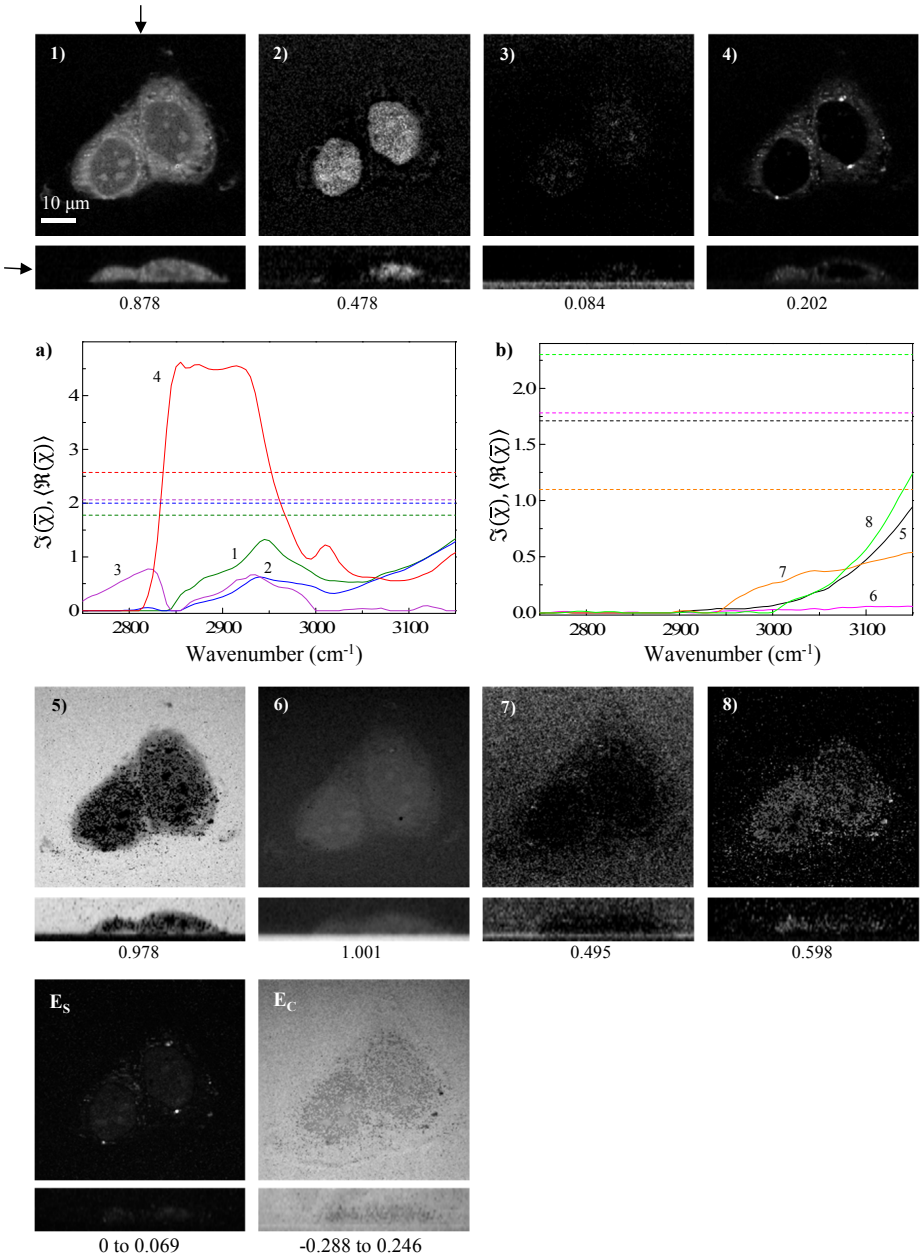

Figure D.15: *xy* and *xz* sections of the eight FSC^3 concentrations (1-8) with their corresponding spectra in a). Grayscales as in Fig. 4.4.

In Fig. D.15, in addition to $\mathcal{C}_1$ and $\mathcal{C}_4$ corresponding to protein and lipid respectively, we also have two components, $\mathcal{C}_2, \mathcal{C}_3$ which are both intranuclear in their localization. From spatial concentrations, $\mathcal{C}_3$ corresponds to nucleoli while $\mathcal{C}_2$ is homogeneous over the nuclear region. The other components correspond to water $(\mathcal{C}_5, \mathcal{C}_7, \mathcal{C}_8)$ and glass $(\mathcal{C}_7)$.

Analysis settings for guided factorizations shown in section 4.5.1.2

Components $\mathcal{C}_1 - \mathcal{C}_4$ from the analysis in Fig. D.15 were used as guide spectra for the analysis shown in Fig. 4.26 - Fig. 4.28. The analysis settings are given in Table D.12 - Table D.14.

Components	7	Min. iterations	100
Max. iterations	100	Stop criterion	Error
Spatial correlation $(\sigma_x, \sigma_y, \sigma_z)$	N/A	Guide factorization weights	2.6% for $\mathcal{C}_1, \mathcal{C}_2$ and $\mathcal{C}_4$ in Fig. D.15

Table D.12: Analysis settings for the factorization shown in Fig. 4.26.

The FSC³ components not shown in Fig. 4.26 are given in Fig. D.16 and are attributed to water $(\mathcal{C}_4, \mathcal{C}_5, \mathcal{C}_7)$ and glass $(\mathcal{C}_6)$.

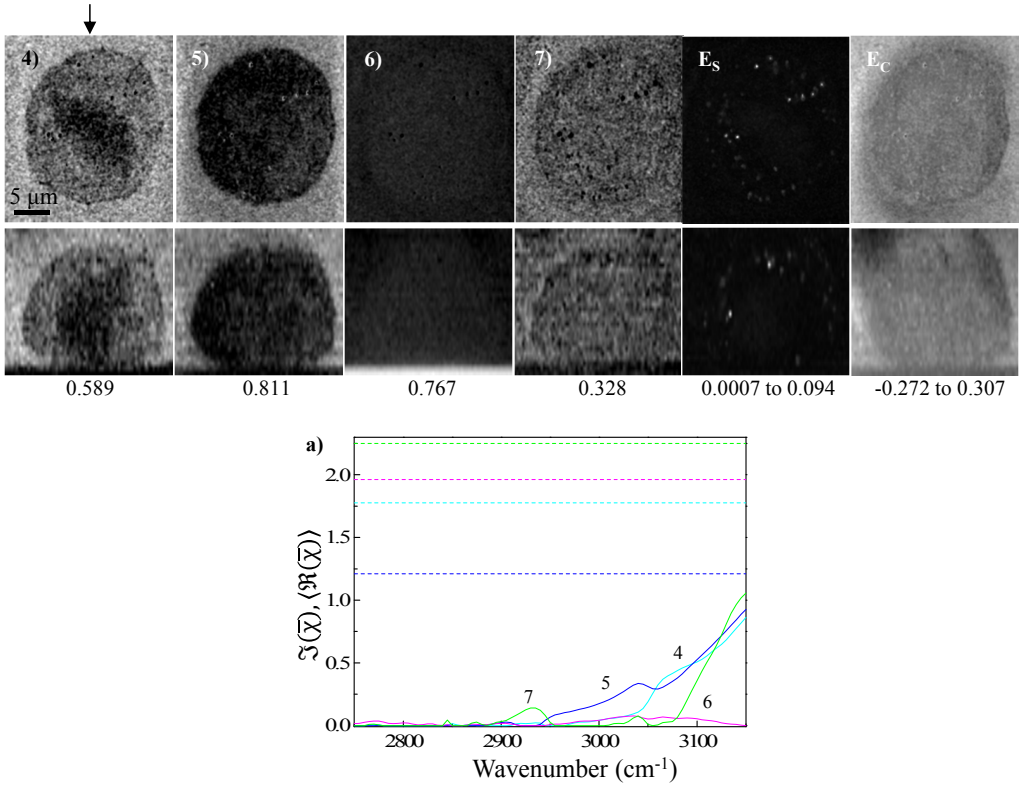

Figure D.16: *xy* and *xz* sections of FSC³ components (previously not shown in Fig. 4.26) with their spectra in a). Grayscales as in Fig. 4.4.

The analysis settings of the data shown in Fig. 4.27 are given in Table D.13. Fig. D.17 shows the components not given in Fig. 4.27.

Components	8	Min. iterations	100
Max. iterations	100	Stop criterion	Error
Spatial correlation $(\sigma_x, \sigma_y, \sigma_z)$	N/A	Guide factorization weights	2.5% for $\mathcal{C}_1, \mathcal{C}_2$ and $\mathcal{C}_4$ in Fig. D.15

Table D.13: Analysis settings for the factorization shown in Fig. 4.27.

The FSC^3 components not shown in Fig. 4.27 are given in Fig. D.17, and are attributed to water ($\mathcal{C}_4, \mathcal{C}_6, \mathcal{C}_7$), glass ($\mathcal{C}_5$) and systematics ($\mathcal{C}_8$).

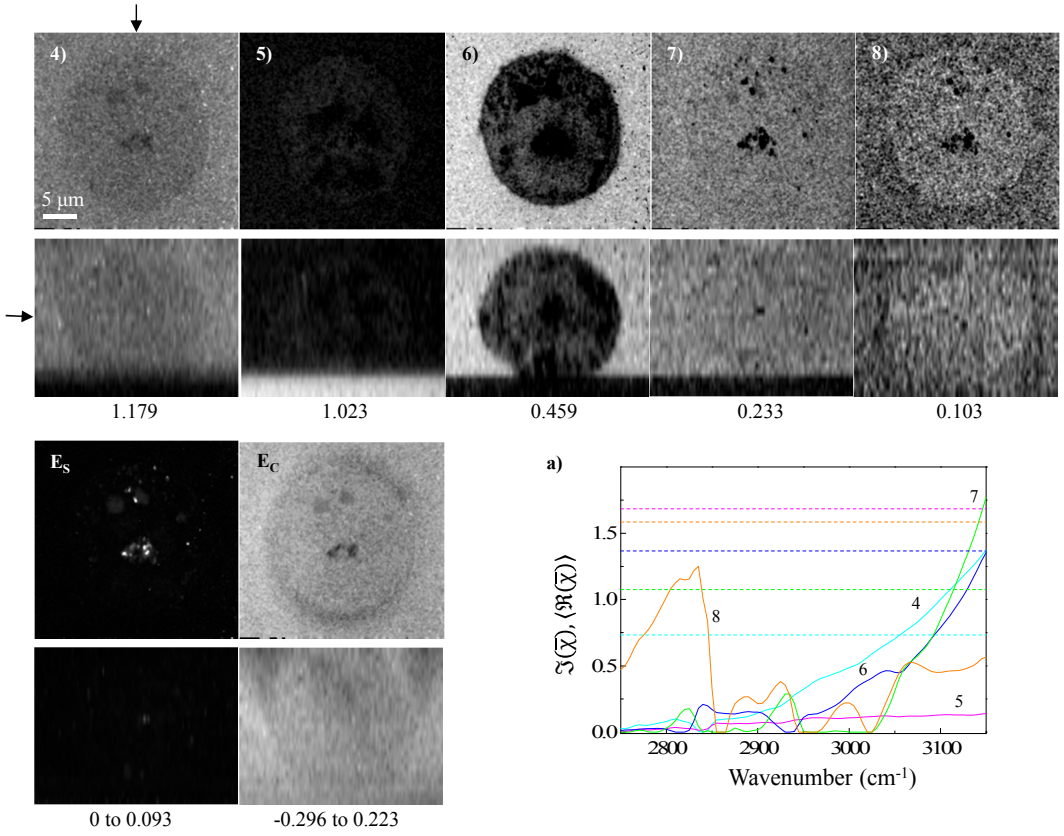

Figure D.17: *xy* and *xz* sections of FSC^3 components (previously not shown in Fig. 4.27) with their spectra in a). Grayscales as in Fig. 4.4.

The analysis settings of the data shown in Fig. 4.28 are given in Table D.14. Fig. D.18 shows the components not given in Fig. 4.28.

Components	8	Min. iterations	100
Max. iterations	100	Stop criterion	N/A
Spatial correlation $(\sigma_x, \sigma_y, \sigma_z)$	N/A	Guide factorization weights	1.1% for $\mathcal{C}_1 - \mathcal{C}_4$ in Fig. D.15

Table D.14: Analysis settings for the factorization shown in Fig. 4.28.

The FSC³ components not shown in Fig. 4.28 are given in Fig. D.18, and are attributed to water ($\mathcal{C}_4, \mathcal{C}_5, \mathcal{C}_7$), glass ($\mathcal{C}_6$) and systematics ($\mathcal{C}_8$).

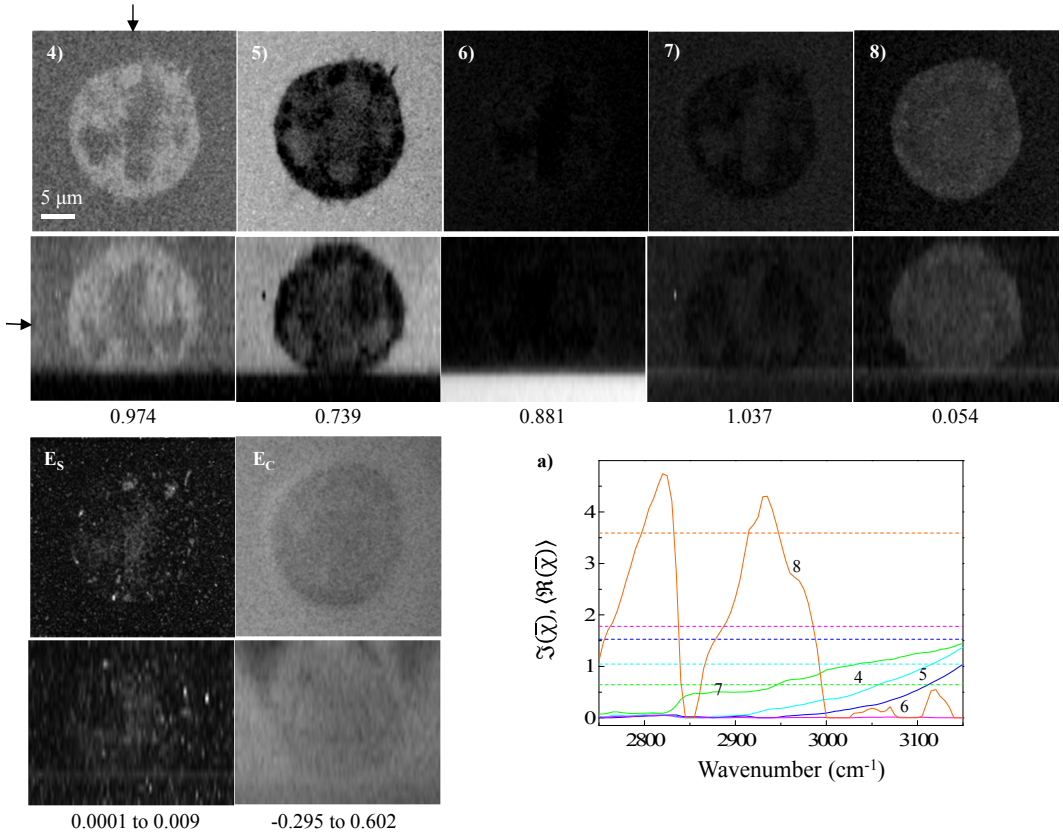

Figure D.18: *xy* and *xz* sections of FSC³ components (previously not shown in Fig. 4.28) with their spectra in a). Grayscales as in Fig. 4.4.

D.1.4.2 ICRF-193 treated cells

The analysis settings of the data shown in Fig. 4.29 are given in Table D.15.

Components	9	Min. iterations	100
Max. iterations	100	Stop criterion	Error
Spatial correlation $(\sigma_x, \sigma_y, \sigma_z)$	N/A	Guided factorization weights	N/A

Table D.15: Analysis settings for the factorization shown in Fig. 4.29.

The FSC^3 components not shown in Fig. 4.29 are given in Fig. D.19, and are attributed to water $(\mathcal{C}_4, \mathcal{C}_5, \mathcal{C}_7)$, glass $(\mathcal{C}_6)$ and systematics $(\mathcal{C}_8, \mathcal{C}_9)$.

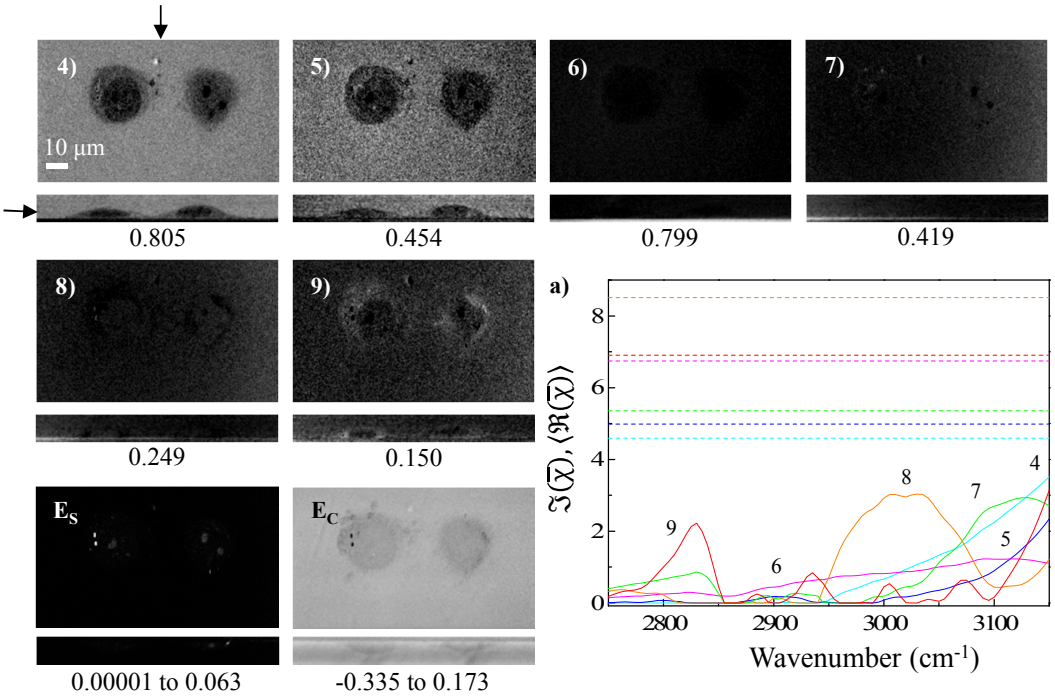

Figure D.19: *xy* and *xz* sections of FSC^3 components (previously not shown in Fig. 4.29) with their spectra in a). Grayscales as in Fig. 4.4.

The analysis settings of the data simultaneously factorized (samples A and B) shown in Fig. 4.30 are given in Table D.16. Fig. D.20 shows the components not given in Fig. 4.30.

Components	7	Min. iterations	100
Max. iterations	100	Stop criterion	Error
Spatial correlation $(\sigma_x, \sigma_y, \sigma_z)$	N/A	Guide factorization weights	0.4% for $\mathcal{C}_1 - \mathcal{C}_4$ in Fig. D.15

Table D.16: Analysis settings for the factorization shown in Fig. 4.30.

The FSC^3 components not shown in Fig. 4.30 are given in Fig. D.20, and are attributed to water $(\mathcal{C}_4 - \mathcal{C}_6)$ and glass $(\mathcal{C}_7)$.

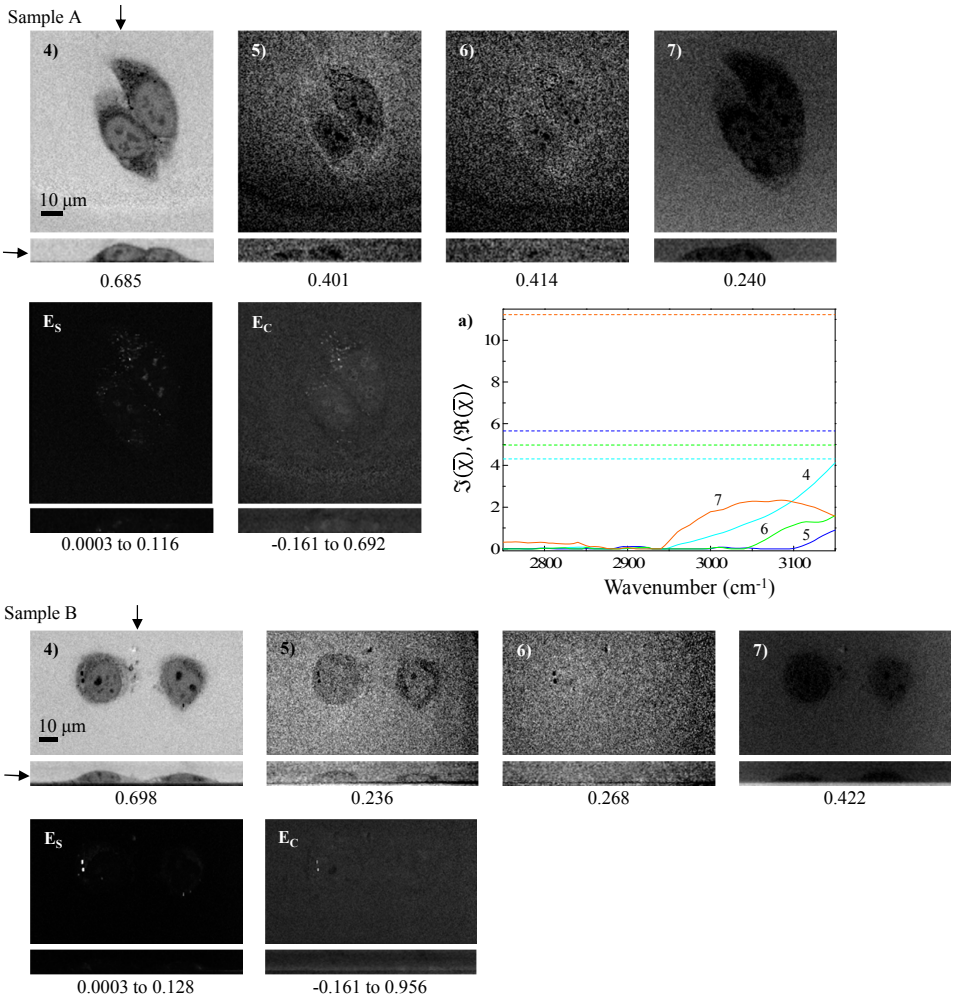

Figure D.20: *xy* and *xz* sections of FSC³ components with their spectra in a) (previously not shown in Fig. 4.30). Grayscales as in Fig. 4.4.

The analysis settings for the simultaneous factorization shown in Fig. 4.31 are given in Table D.17. Fig. D.21 shows the components not given in Fig. 4.31.

Components	7	Min. iterations	100
Max. iterations	100	Stop criterion	Error
Spatial correlation $(\sigma_x, \sigma_y, \sigma_z)$	N/A	Guide factorization weights	1.7% for $\mathcal{C}_2 - \mathcal{C}_4$ in Fig. 4.30

Table D.17: Analysis settings for the factorization shown in Fig. 4.31.

The FSC³ components not shown in Fig. 4.31 are given in Fig. D.21, and are attributed to water $(\mathcal{C}_4, \mathcal{C}_5, \mathcal{C}_7)$ and glass $(\mathcal{C}_6)$.

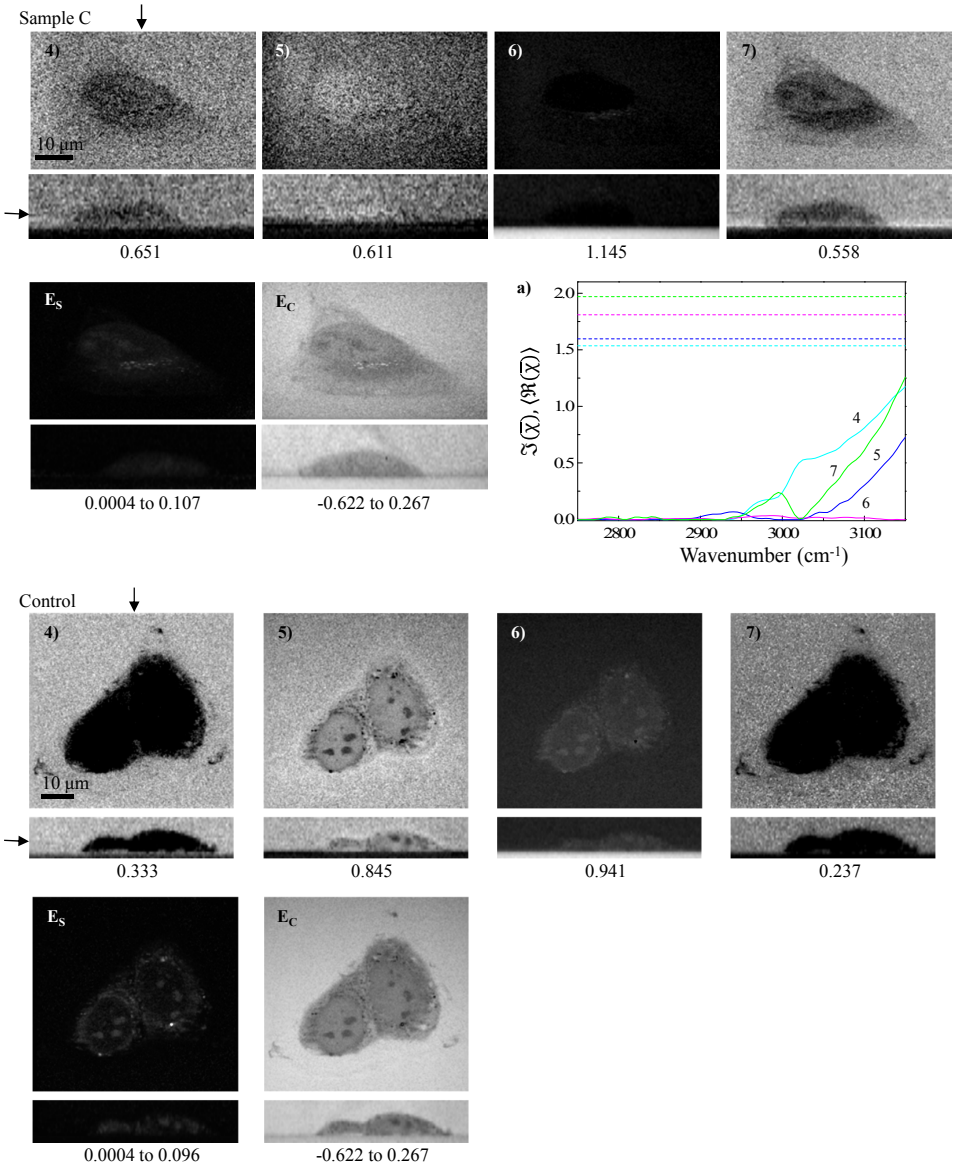

Figure D.21: *xy* and *xz* sections of FSC^3 components with their spectra in a) (previously not shown in Fig. 4.31). Grayscales as in Fig. 4.4.

The analysis settings for the factorization of the control sample shown in Fig. 4.32 are given in Table D.18.

Components	9	Min. iterations	100
Max. iterations	100	Stop criterion	Error
Spatial correlation $(\sigma_x, \sigma_y, \sigma_z)$	N/A	Guide factorization weights	8.6% for $\mathcal{C}_2 - \mathcal{C}_4$ in Fig. 4.30

Table D.18: Analysis settings for the factorization shown in Fig. 4.32.

The FSC^3 components not shown in Fig. 4.32 correspond to glass ($\mathcal{C}_4$) and water ($\mathcal{C}_{6-9}$) in Fig. D.22.

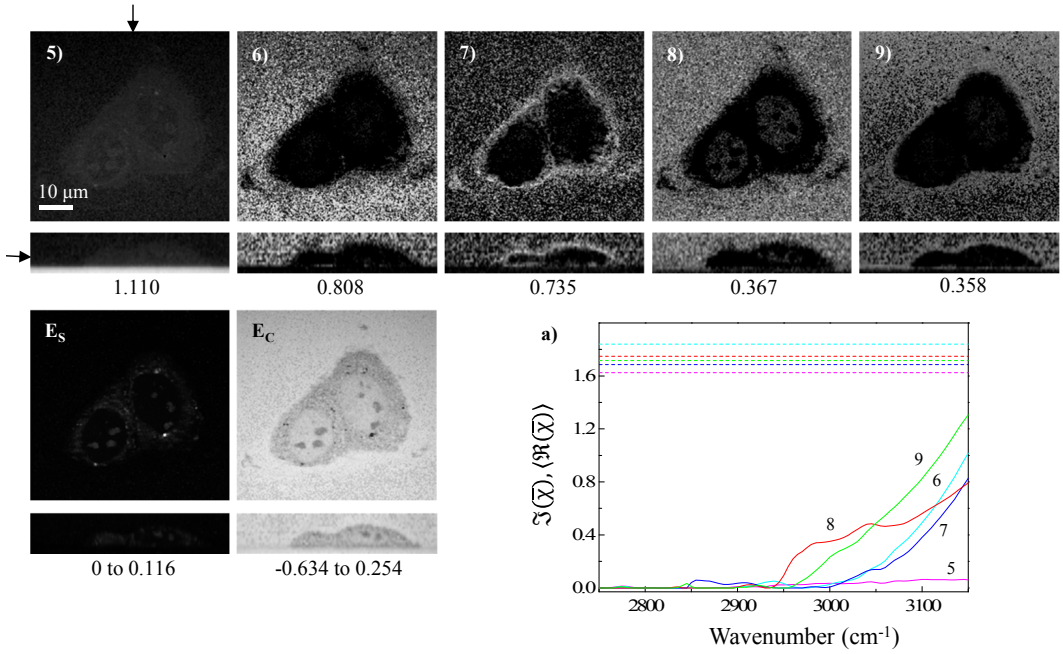

Figure D.22: *xy* and *xz* sections of FSC^3 components with their spectra in a). Grayscales as in Fig. 4.4.

D.1.5 Organoids

In addition to the settings given in Table D.1, the CARS ratio was calculated with glass/water ratio extended over the IFD range of 2600 - 3600 cm^{-1}. The CARS ratio is extended assuming that the dominating spectrum in the range not measured (we measured over 2750 - 3100 cm^{-1}) of the spectrum is water. The water spectrum (in the range not measured) calculated from the glass/water ratio renormalized to be continuous at the edges is added to the data.

D.1.5.1 Mouse crypt intestinal organoids

Table D.19 summarizes the settings used to analyze the mouse intestinal organoid shown in Fig. 5.3. The FSC^3 components not shown in Fig. 5.3 are given in Fig. D.23, corresponding to water.

Components	5	Min. iterations	100
Max. iterations	1000	Stop criterion	Tolerance
Spatial correlation $(\sigma_x, \sigma_y, \sigma_z)$	N/A	Guided factorization weights	N/A

Table D.19: Analysis settings for Fig. 5.3.

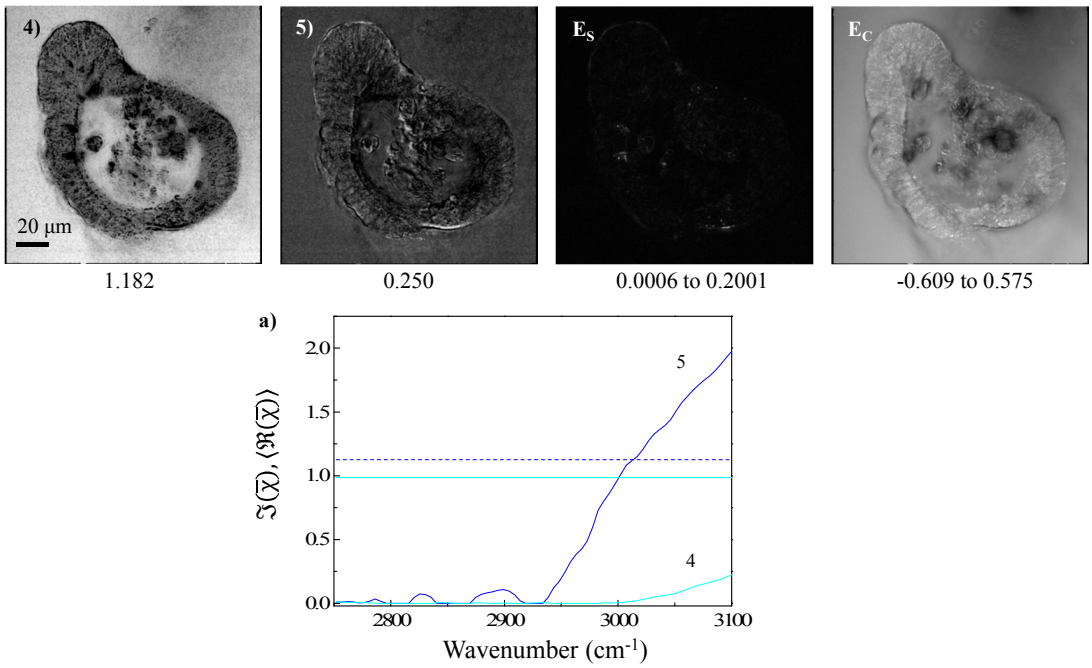

Figure D.23: FSC^3 concentrations (4,5), and component spectra (previously not shown in Fig. 5.3) in a). Grayscales as in Fig. 4.4.

In Table D.20, FSC^3 settings used for factorizing the data shown in Fig. 5.4 are given.

Components	7	Min. iterations	100
Max. iterations	1000	Stop criterion	Tolerance
Spatial correlation $(\sigma_x, \sigma_y, \sigma_z)$	0.4, 0.4, 1	Guided factorization weights	N/A

Table D.20: Analysis settings for Fig. 5.4, shown in chapter 5.

Four FSC^3 components including two components corresponding to water (4,5,6), and one to systematics (7) which were not shown in Fig. 5.4 are given in Fig. D.24.

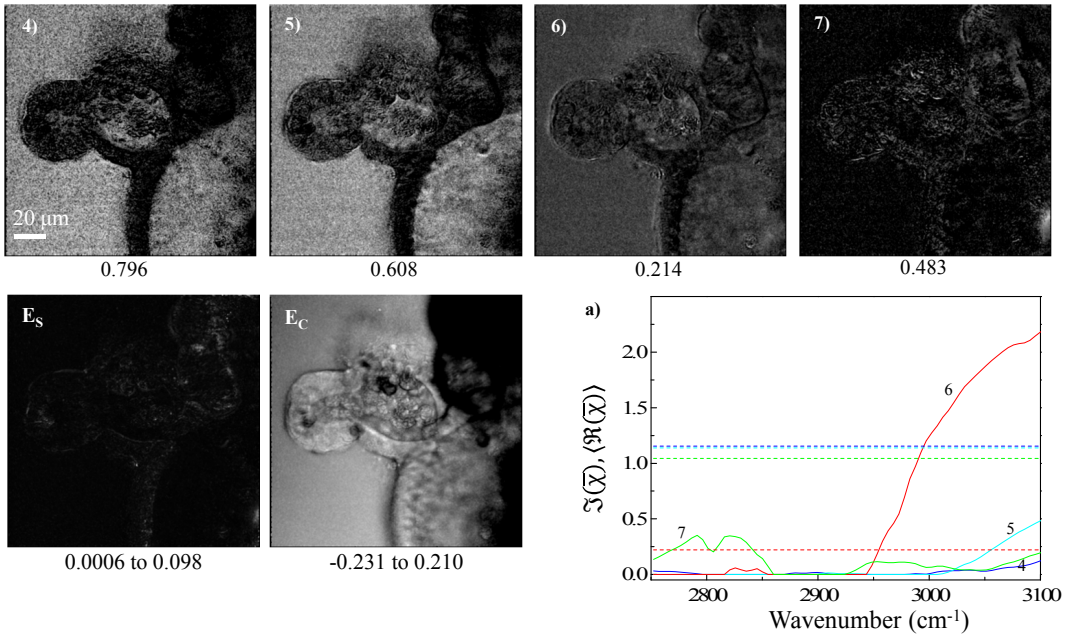

Figure D.24: FSC^3 concentrations (4-7), and component spectra (previously not shown in Fig. 5.4) in a). Grayscales as in Fig. 4.4.

D.1.5.2 Mouse liver organoids

The mouse liver organoid shown in Fig. 5.5 was analyzed using the settings given in Table D.21. The three FSC^3 components not shown in Fig. 5.5 are given in Fig. D.25. The concentrations 4 and 5 correspond to water while 6 is attributed to systematics.

Components	6	Min. iterations	100
Max. iterations	1000	Stop criterion	Tolerance
Spatial correlation $(\sigma_x, \sigma_y, \sigma_z)$	N/A	Guided factorization weights	N/A

Table D.21: Analysis settings for Fig. 5.5, shown in chapter 5.

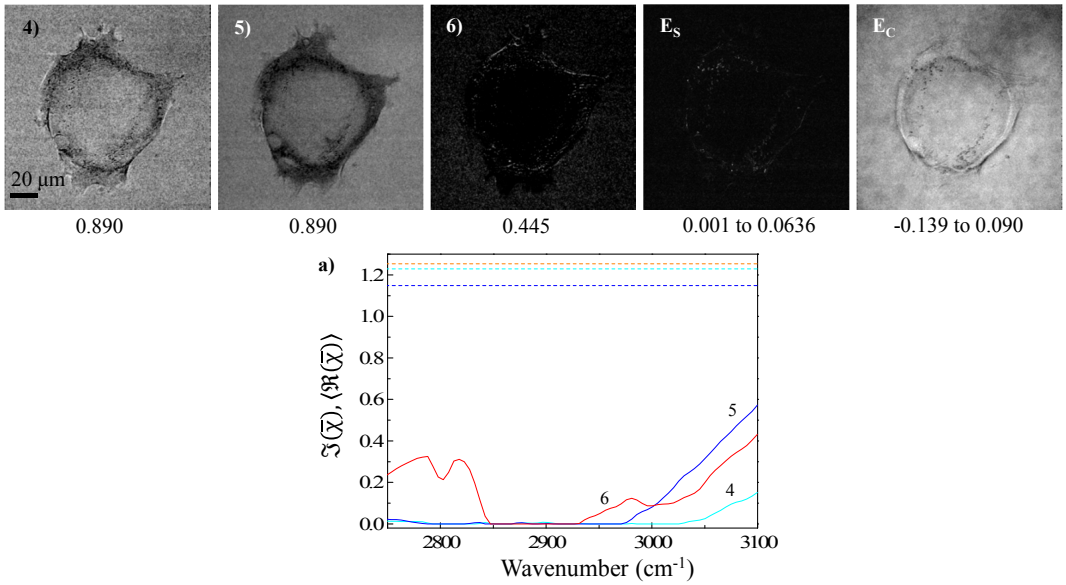

Figure D.25: FSC^3 concentrations (4-6) and their corresponding spectra (previously not shown in Fig. 5.5) in a). Grayscales as in Fig. 4.4.

The mouse liver organoid in differentiation medium, shown in Fig. 5.6 was FSC^3 analyzed using the settings given in Table D.22.

Components	5	Min. iterations	100
Max. iterations	1000	Stop criterion	Tolerance
Spatial correlation $(\sigma_x, \sigma_y, \sigma_z)$	N/A	Guided factorization weights	N/A

Table D.22: Analysis settings for Fig. 5.6, shown in chapter 5.

In Fig. D.26, the errors E_C and E_S of the factorization shown in Fig. 5.6 are given.

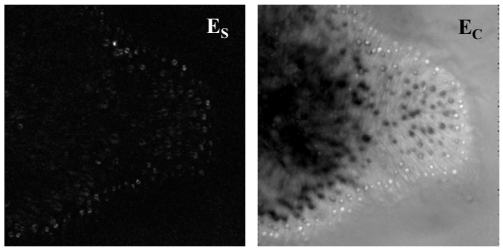

Figure D.26: E_C and E_S of the factorization in Fig. 5.6. Grayscales as in Fig. 4.4.

D.1.5.3 Human colorectal cancer organoids

The FSC^3 analysis of primary human colorectal cancer shown in Fig. 5.7 was done using the settings given in Table D.23. The two FSC^3 components corresponding to water not shown in Fig. 5.7 are given in Fig. D.27.

Components	4	Min. iterations	100
Max. iterations	1000	Stop criterion	Tolerance
Max. iterations	1000	Stop criterion	Tolerance
Spatial correlation $(\sigma_x, \sigma_y, \sigma_z)$	N/A	Guided factorization weights	N/A

Table D.23: Analysis settings for Fig. 5.7, shown in chapter 5.

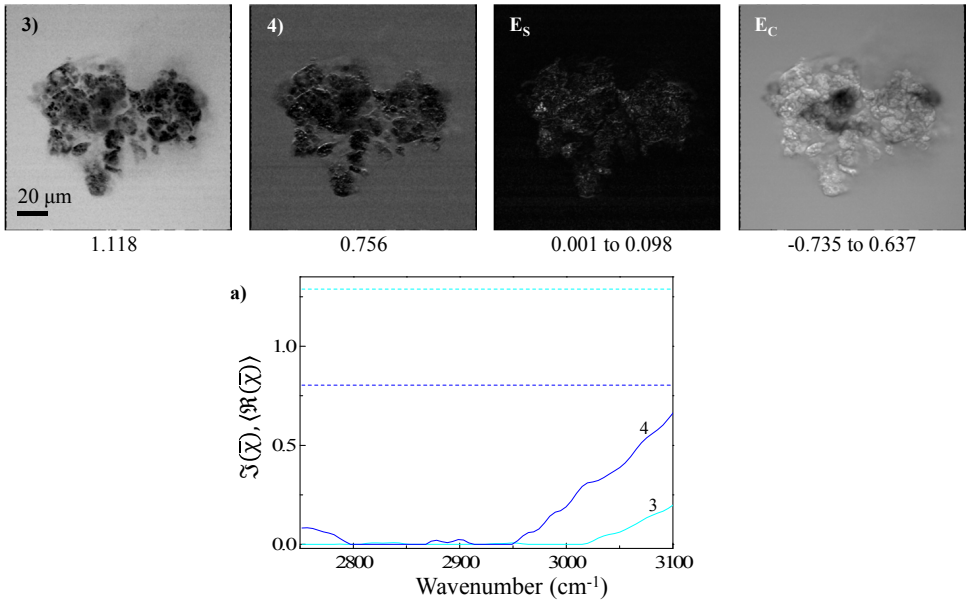

Figure D.27: FSC³ concentrations and their corresponding spectra (previously not shown in Fig. 5.7) in a). Grayscales as in Fig. 4.4.

The metastatic human colorectal cancer organoid shown in Fig. 5.8 was analyzed using the settings given in Table D.24. Fig. D.28 shows the FSC³ components attributed to water which were not shown in Fig. 5.8.

Components	5	Min. iterations	100
Max. iterations	1000	Stop criterion	Tolerance
Spatial correlation $(\sigma_x, \sigma_y, \sigma_z)$	N/A	Guided factorization weights	N/A

Table D.24: Analysis settings for Fig. 5.8, shown in chapter 5.

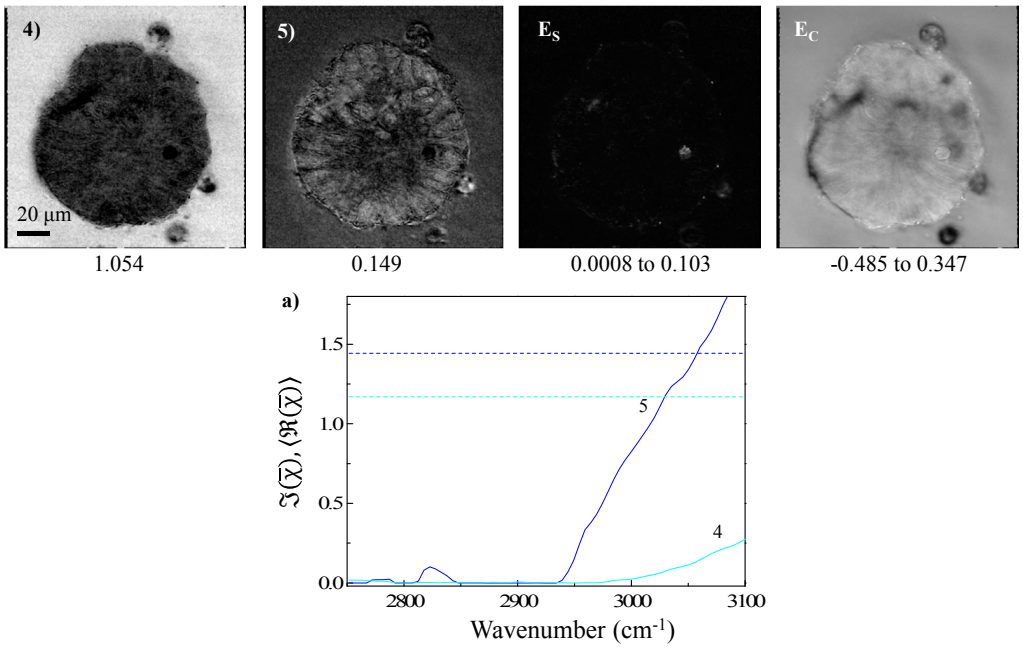

Figure D.28: FSC^3 concentrations and their corresponding spectra (previously not shown in Fig. 5.8) in a). Grayscales as in Fig. 4.4.

Publications

Parts of this work have been published in the following works either in journals or at conferences as listed below.

Articles

Parts of this work have been presented in the following articles.

1. **A. Karuna**, F. Masia, P. Borri and W. Langbein. Hyperspectral volumetric coherent anti-Stokes Raman scattering microscopy: quantitative volume determination and NaCl as non-resonant standard. Journal of Raman Spectroscopy, DOI: 10.1002/jrs.4876, published online, 2016.

2. F. Masia, **A. Karuna**, P. Borri and W. Langbein. Hyperspectral image analysis for CARS, SRS and Raman data. Journal of Raman Spectroscopy, Vol. 46 (8), 727-734, DOI: 10.1002/jrs.4729, 2015.

Conferences

1. **A. Karuna**, F. Masia, I. Pope, M. Wiltshire, R. Errington, P. Borri and W. Langbein, 'Quantitative hyperspectral coherent anti-Stokes Raman scattering (CARS) microscopy of somatic cell mitosis', *Poster presentation*, Bio-Nano-Photonics symposium, Cardiff University, U.K. (2015).

2. W. Langbein, F. Masia, C. DiNapoli, P. Watson, **A. Karuna**, S. Chappell, R. Errington and P. Borri, 'Quantitative CARS microscopy: hyperspectral image analysis of cells', *Oral presentation*, Bio-Nano-Photonics symposium, Cardiff, U.K. (2015).

3. W. Langbein, F. Masia, C. DiNapoli, P. Watson, **A. Karuna**, S. Chappell, R. Errington and P. Borri, 'Quantitative label-free chemical imaging of cell compartments using hyperspectral CARS microscopy', *Oral presentation*, Focus on Microscopy, Gottingen, Germany (2015).

4. **A. Karuna**, F. Masia, S. Chappell, M. Wiltshire, R. Errington, P. Borri and W. Langbein, 'Label-free imaging of cell compartments and the cell cycle using quantitative coherent anti-Stokes Raman scattering (CARS) microscopy', *Poster presentation*, Photon14, Imperial College of London, U.K. (2014).

5. W. Langbein, F. Masia, C DiNapoli, P. Watson, **A. Karuna**, S. Chappell, R. Errington and P. Borri, 'Unsupervised quantitative chemical analysis of hyperspectral coherent antiStokes Raman scattering images', Photon 14, London, U.K (2014).

6. **A. Karuna**, F. Masia, S. Chappell, R. Errington, P. Borri and W. Langbein, 'Label-free imaging of cell compartments and the cell cycle using quantitative coherent anti-Stokes Raman scattering (CARS) microscopy', *Poster presentation*, MicroCOR winter school on chemical imaging by coherent Raman and non-linear microscopy, Ecole De Physique, Les Houches, France (2014).

7. W. Langbein, F. Masia, C DiNapoli, P. Watson, **A. Karuna**, S. Chappell, R. Errington and P. Borri, 'Label-free imaging of cell compartment using quantitative hyperspectral CARS microscopy', *Poster presentation*, Frontiers in CRS, Heidelberg, Germany (2014).

8. W. Langbein, F. Masia, I. Pope, **A. Karuna**, P. Stephens, A. Glen, R. Errington and P. Borri, 'CARS hyperspectral imaging using a single 5 fs Ti:Sapphire laser: Quantitative chemical analysis', *Oral presentation*, Bio-Nano-Photonics symposium, Cardiff, U.K. (2013)

Bibliography

[1] Kurt Thorn. A quick guide to light microscopy in cell biology. *Molecular biology of the cell*, 27(2):219–222, 2016.

[2] Paolo Mazzarello. A unifying concept: the history of cell theory. *Nature Cell Biology*, 1:E13–E15, 1999.

[3] E. Boucrot and T. Kirchhausen. Mammalian cells change volume during mitosis. *PLoS One*, page e1477, 2008.

[4] Conly L. Rieder and Alexey Khodjakov. Mitosis through the microscope: Advances in seeing inside live dividing cells. *Science*, 300(5616):91–96, 2003.

[5] Martin Josef Winterhalder and Andreas Zumbusch. Beyond the borders - biomedical applications of non-linear raman microscopy. *Advanced Drug Delivery Reviews*, 89:135–144, 2015.

[6] Dan Fu, Gary Holtom, Christian Freudiger, Xu Zhang, and Xiaoliang Sunney Xie. Hyperspectral imaging with stimulated raman scattering by chirped femtosecond lasers. *The Journal of Physical Chemistry B*, 117(16):4634–4640, 2013.

[7] Xu Zhang, Maarten B. J. Roeffaers, Srinjan Basu, Joseph R. Daniele, Dan Fu, Christian W. Freudiger, Gary R. Holtom, and X. Sunney Xie. Label-free live-cell imaging of nucleic acids using stimulated Raman scattering microscopy. *ChemPhysChem*, 13(4):1054–1059, 2012.

[8] Yasuyuki Ozeki, Wataru Umemura, Yoichi Otsuka, Shuya Satoh, Hiroyuki Hashimoto, Kazuhiko Sumimura, Norihiko Nishizawa, Kiichi Fukui, and Kazuyoshi Itoh. High-speed molecular spectral imaging of tissue with stimulated raman scattering. *Nature Photon.*, 6:845–851, 2012.

[9] P. D. Maker and R. W. Terhune. Study of optical effects due to an induced polarization third order in the electric field strength. *Phys. Rev.*, 137:A801–A818, 1965.

[10] A. Zumbusch, G. R. Holtom, and X. Sunney Xie. Three-dimensional vibrational imaging by coherent anti-stokes raman scattering. *Phys. Rev. Lett.*, 82:4142, 1999.

[11] Luis G. Rodriguez, Stephen J. Lockett, and Gary R. Holtom. Coherent anti-stokes raman scattering microscopy: A biological review. *Cytometry Part A*, 69A(8):779–791, 2006.

[12] Ji-Xin Cheng, Y Kevin Jia, Gengfeng Zheng, and X Sunney Xie. Laser-scanning coherent anti-stokes raman scattering microscopy and applications to cell biology. *Biophys J.*, 83:502–509, 2002.

[13] Ranjana Mitra, Olivia Chao, Yasuyo Urasaki, Oscar B Goodman, and Thuc T. Le. Detection of lipid rich prostrate circulating tumour cells with cars microscopy. *Biomedcentral Cancer*, 12(540), 2012.

[14] Thuc T. Le, Shuhua Yue, and Ji-Xin Cheng. Shedding new light on lipid biology with coherent anti-stokes raman scattering microscopy. *J. Lipid Res.*, 51:3091–3102, 2010.

[15] Sapun H. Parekh, Young Jong Lee, Khaled A. Aamer, and Marcus T. Cicerone. Label-free cellular imaging by broadband coherent anti-stokes raman scattering microscopy. *Biophys. J.*, 99:2695 – 2704, 2010.

[16] Artem Pliss, Andrey N. Kuzmin, Aliaksandr V. Kachynski, and Paras N. Prasad. Nonlinear optical imaging and raman microspectrometry of the cell nucleus throughout the cell cycle. *Biophysical Journal*, 99(10):3483–3491, 2010.

[17] Mary Ann Jordan, Robert J. Toso, Doug Thrower, and Leslie Wilson. Mechanism of mitotic block and inhibition of cell proliferation by taxol at low concentrations. *Proc. Natl. Acad. Sci. USA*, 90:9552–9556, 1993.

[18] Peter B. Schiff and Susan Band Horwitz. Taxol stabilizes microtubules in mouse fibroblast cells. *Proc. Natl. Acad. Sci. USA*, 77(3):1561–1565, 1980.

[19] Ryoji Ishida, Makoto Sato, Toshiharu Narita, Kazuhiko R. Utsumi, Takeharu Nishimoto, Takashi Morita, Hiroshi Nagata, and Toshiwo Andoh. Inhitbition of dna topoisomerase ii by icrf-193 induces polyploidy by uncoupling chromosome dynamics from other cell cycle events. *The Journal of Cell Biology*, 126(6):1341–1351, 1994.

[20] Jonathan Kelling, Kevin Sullivan, Leslie WIlson, and Mary Ann Jordon. Suppreession of centromere dynamics by taxol in living osteosarcoma cells. *Cancer Research*, 63:2794–2801, 2003.

[21] Paul J. Smith, Nuria Marquez, Marie Wiltshire, Sally Chappell, Kerenza Njoh, Lee Campbell, Imtiaz A. Khan, Oscar Silvestre, and Rachel J. Errington. Mitotic bypass via an occult cell cycle phase following dna topoisomerase ii inhibition in p53 functional human tumor cells. *Cell Cycle*, 6(16):2071–2081, 2007. PMID: 17721081.

[22] N. Pastor, Maria Jose Flores, I. Dominguez, and F. Mateos, D.and Cortes. High yield of endoreduplication induced by icrf-193: a topoisomerase ii catalytic inhibitor. *Mutation Research*, 516:113–120, 2002.

[23] Aliya Fatehullah, Paul L. Appleton, and Inke S. Näthke. Cell and tissue polarity in the intestinal tract during tumourigenesis: cells still know the right way up, but tissue organization is lost. *Philosophical Transactions of the Royal Society of London B: Biological Sciences*, 368(1629), 2013.

[24] Alex J. Walsh, Rebecca S. Cook, Melinda E. Sanders, Luigi Aurisicchio, Gennaro Ciliberto, Carlos L. Arteaga, and Melissa C. Skala. Quantitative optical imaging of primary tumor organoid metabolism predicts drug response in breast cancer. *Cancer Research*, 74(18):5184–5194, 2014.

[25] Ling Huang, Audrey Holtzinger, Ishaan Jagan, Michael BeGora, Ines Lohse, Nicholas Ngai, Cristina Nostro, Rennian Wang, Lakshmi B. Muthuswamy, Howard C. Crawford, Cheryl Arrowsmith, Steve E. Kalloger, Daniel J. Renouf, Ashton A. Connor, Sean Cleary, David F. Schaeffer, Michael Roehrl, Ming-Sound Tsao, Steven Gallinger, Gordon Keller, and Senthil K. Muthuswamy. Ductal pancreatic cancer modeling and drug screening using human pluripotent stem cell- and patient-derived tumor organoids. *Nature Medicine*, 2015.

[26] Colin N. Banwell and Elaine M. McCash. *Fundamentals of molecular spectroscopy.* Tata McGraw-Hill Publishing Company Ltd., New Delhi, 4 edition, 2008.

[27] Max Diem. *Modern vibrational spectroscopy and micro-spectroscopy: Theory, Instrumentation and Biomedical Applications.* John Wiley & Sons Inc., 2014.

[28] Michiel Müller. *Introduction to confocal fluorescence microscopy.* Shaker Publishing BV, Maastricht, 1 edition, 2002.

[29] Mark Fox. *Optical properties of solids.* Oxford University Press, 2008.

[30] Oliver Howarth. *Theory of spectroscopy.* Thomas Nelson and Sons Ltd., London, 1 edition, 1973.

[31] Michiel Müller. *Introduction to confocal fluorescence microscopy.* SPIE, 2 edition, 2005.

[32] Andreas Zumbusch, Wolfgang Langbein, and Paola Borri. Nonlinear vibrational microscopy applied to lipid biology. *Progress in Lipid Research*, 52:615–632, 2013.

[33] C.V. Raman and R.S. Krishnan. A new type of secondary radiation. *Nature*, 121:501–502, 1928.

[34] Bahaa E. A. Saleh and Malvin Carl Teich. *Fundamentals of photonics.* John Wiley & Sons, Ltd, 2007.

[35] Martin Oheim, Darren J. Michael, Matthias Geisbauer, Dorte Madsen, and Robert H. Chow. Principles of two-photon excitation fluorescence microscopy and other nonlinear imaging approaches. *Advanced Drug Delivery Reviews*, 58(7):788–808, 2006.

[36] Peter TC So. *Encyclopedia of life sciences*, chapter Two-photon Fluorescence Light Microscopy. John Wiley & Sons, Ltd, 2001.

[37] Jessica C. Mansfield, George R. Littlejohn, Mark P. Seymour, Rob J. Lind, Sarah Perfect, and Julian Moger. Label-free chemically specific imaging in planta with stimulated raman scattering microscopy. *Anal. Chem.*, 85:5055–5063, 2013.

[38] George R Littlejohn, Jessica C Mansfield, David Parker, Robert Lind, Sarah Perfect, Mark Seymour, Nicholas Smirnoff, John Love, and Julian Moger. In vivo chemical and structural analysis of plant cuticular waxes using stimulated raman scattering (srs) microscopy. *Plant Physiology*, 2015.

[39] *Monitoring lipid accumulation in the green microalga Botryococcus braunii with frequency-modulated stimulated Raman scattering*, volume 9329, 2015.

[40] Christian Brackmann, Anton Bengtsson, Marie Larsson Alminger, and Annika Enejder. Visualization of β-carotene and starch granules in plant cells using cars and shg microscopy. *Journal of Raman Spectroscopy*, 42(4):586–592, 2011.

[41] Yining Zeng, Brian G. Saar, Marcel G. Friedrich, Fang Chen, Yu-San Liu, Richard A. Dixon, Michael E. Himel, Sunney X. Xie, and Shi-You Ding. Imaging lignin-downregulated alfalfa using cars microscopy. *Bioenerg. Res.*, 2010.

[42] Erik T. Garbacik, Roza P. Korai, Eric H. Frater, Jeroen P. Korterik, Cees Otto, and Herman L. Offerhaus. In planta imaging of $\triangle^9$- tetrahydrocannabinolic acid in cannabis sativa l. with hyperspectral coherent anti-stokes raman scattering microscopy. *Journal of Biomedical Optics*, 18(4), 2013.

[43] Ji-Xin Cheng and Xiaoliang Sunney Xie, editors. *Coherent Raman scattering microscopy*. CRC Press, Taylor and Francis group, 2013.

[44] M. Muller and A. Zumbusch. Coherent anti-stokes raman scattering (cars) microscopy. *Chem. Phys. Chem.*, 8:2156–2170, 2007.

[45] Andreas Volkmer. Vibrational imaging and microspectroscopies based on coherent anti-stokes raman scattering microscopy. *J. Phys. D: Appl. Phys.*, 38(5):R59–R81, 2005.

[46] Conor L. Evans and X. Sunney Xie. Coherent anti-stokes raman scattering microscopy: Chemical imaging for biology and medicine. *Annu. Rev. Anal. Chem.*, 1:883–909, 2008.

[47] International School "Enrico Fermi". *Resonant Nonlinear Optical Microscopy*, volume 181 of *Microscopy Applied to Biophotonics*. IOS Press, 2014. pp. 141 - 173.

[48] M.D. Duncan, J. Reintjes, and T.J. Manuccia. Scanning coherent anti-stokes raman microscope. *Optics Letters*, 7(8):350–352, 1982.

[49] Francesco Masia, Adam Glen, Phil Stephens, Paola Borri, and Wolfgang Langbein. Quantitative chemical imaging and unsupervised analysis using hyperspectral coherent anti-stokes raman scattering microscopy. *Anal. Chem.*, 85(22):10820–10828, 2013.

[50] Hilde A. Rinia, Mischa Bonn, Michiel Müller, and Erik M. Vartiainen. Quantitative cars spectroscopy using the maximum entropy method: The main lipid phase transition. *ChemPhysChem*, 8(2):279–287, 2007.

[51] Yuexin Liu, Young Jong Lee, and Marcus T. Cicerone. Broadband cars spectral phase retrieval using a time-domain kramers-kronig transform. *Opt. Lett.*, 34:1363, 2009.

[52] Erik M. Vartiainen, Hilde A. Rinia, Michiel Müller, and Mischa Bonn. Direct extraction of raman line-shapes from congested cars spectra. *Opt. Express*, 14(8):3622–3630, Apr 2006.

[53] Ji-Xin Cheng, Lewis D. Book, and X. Sunney Xie. Polarization coherent anti-stokes raman scattering microscopy. *Opt. Lett.*, 26(17):1341–1343, 2001.

[54] Andreas Volkmer, Lewis D. Book, and X. Sunney Xie. Time-resolved coherent anti-stokes raman scattering microscopy: Imaging based on raman free induction decay. *Applied Physics Letters*, 80(9):1505–1507, 2002.

[55] Conor L. Evans, Eric O. Potma, and X. Sunney Xie. Coherent anti-stokes raman scattering spectral interferometry: determination of the real and imaginary components of nonlinear susceptibility $\chi^(3)$ for vibrational microscopy. *Optics Letters*, 29(24):2923–2925, 2004.

[56] Eric O. Potma, Conor L. Evans, and X. Sunney Xie. Heterodyne coherent anti-stokes raman scattering (cars) imaging. *Opt. Lett.*, 31(2):241–243, Jan 2006.

[57] Ji-Xin Cheng. Coherent anti-stokes raman scattering microscopy. *Applied Spectroscopy*, 61:197–208, 2007.

[58] Yan Fu, Haifeng Wang, Riyi Shi, and Ji-Xin Cheng. Characterization of photodamage in coherent anti-stokes raman scattering microscopy. *Opt. Express*, 14(9):3942–3951, 2006.

[59] J.-X. Cheng and X.S. Xie. Coherent anti-stokes raman scattering microscopy: Instrumentation, theory, and applications. *J. Phys. Chem. B*, 108(3):827–840, 2004.

[60] Andreas Volkmer, Ji-Xin Cheng, and X. Sunney Xie. Vibrational imaging with high sensitivity via epidetected coherent anti-stokes raman scattering microscopy. *Phys. Rev. Lett.*, 87:023901, 2001.

[61] James Pawley, editor. *Handbook of biological confocal microsocpy*, volume 236. Springer Science & Business Media, June 2006.

[62] Ji-Xin Cheng, Andreas Volkmer, and X. Sunney Xie. Theoretical and experimental characterization of coherent anti-stokes raman scattering microscopy. *J. Opt. Soc. Am. B*, 19:1363, 2002.

[63] Nadia Djaker, David Gachet, Nicolas Sandeau, Pierre-Francois Lenne, and Hervé Rigneault. Refractive effects in coherent anti-stokes raman scattering microscopy. *Appl. Opt.*, 45(27):7005–7011, 2006.

[64] Eric O. Potma and X. Sunney Xie. Cars microscopy for biology and medicine. *Opt. Photon. News*, pages 40–45, 2004.

[65] Ji-xin Cheng, Andreas Volkmer, Lewis D. Book, and X. Sunney Xie. An epidetected coherent anti-stokes raman scattering (e-cars) microscope with high spectral resolution and high sensitivity. *J. Phys. Chem. B*, 105(7):1277–1280, 2001.

[66] Paras N. Prasad. *Introduction to biophotonics.* John Wiley & Sons Inc., 2003.

[67] Gerald Karp. *Cell and Molecular Biology: Concepts and Experiments*. John Wiley & Sons Inc., 6 edition, 2010.

[68] Yuuta Imoto, Yamato Yoshida, Fumi Yagisawa, Haruko Kuroiwa, and Tsuneyoshi Kuroiwa. The cell cycle, including the mitotic cycle and organelle division cycles, as revealed by cytological observations. *Journal of Electron Microscopy*, 60:S117–S136, 2011.

[69] Harvey Lodish, Arnold Berk, Paul Matsudaira, Chris A Kaiser, Monty Krieger, Matthew P. Scott, Lawrence Zipursky, , and James Darnell. *Molecular Cell Biology*. W.H.Freeman, 5 edition, 2003.

[70] Alisa Zapp Machalek. *Inside the Cell*, chapter 1, pages 6–13. Number 05 in 1051. U.S. Department of health and human services, National Institutes of Health, National Institute of General Medical Sciences, September 2005.

[71] Bruce Alberts, Dennis Bray, Karen Hopkin, Alexander Johnson, Julian Lewis, Martin Raff, Keith Roberts, and Peter Walter. *Essential Cell Biology*. Garland Science, 4 edition, 2013.

[72] Bruce Alberts, Alexander Johnson, Julian Lewis, Martin Raff, Keith Roberts, and Peter Walter. *Molecular Biology of the Cell*. New York: Garland Science, 5 edition, 2007.

[73] C.E. Gillett and D.M. Barnes. Demystified.. cell cycle. *Journal of Molecular Pathology*, 51(6):310–316, 1998.

[74] E.D. Israels and L.G. Israels. The cell cycle. *The Oncologist*, 5(6):510–513, 2000.

[75] Kristie Saltsman. *Inside the Cell*, chapter 4, pages 46–15. Number 05 in 1051. U.S. Department of health and human services, National Institutes of Health, National Institute of General Medical Sciences, September 2005.

[76] Edmund B. Wilson. *The Cell in Development and Inheritance*. The Macmillan Company, 2 edition, 1900.

[77] Roger D. Kornberg. Chromatin structure: A repeating unit of histones and dna. *Science*, 184(4139):868–871, 1974.

[78] U.K. Laemmli, S.M. Cheng, K.W. Adolph, J.R. Paulson, J.A. Brown, and W.R. Baumbach. Metaphase chromosome structure: The role of nonhistone proteins. *Cold Spring Harbor Symposia on Quantitative Biology*, 42:351–360, 1978.

[79] K.W. Adolph, S.M. Cheng, J.R. Paulson, and U.K. Laemmli. Isolation of a protein scaffold from mitotic hela cells. *Proc*, 74(11):4937–4941, 1977.

[80] Yrjo Colland and M. Kosma, V. Morphometry in cancer diagnosis. In Alfred L. Goldson, editor, *Cancer management in man*, chapter 10, page 135. Kluwer Academic Publishers, 1989.

[81] Andreas Nebenfuhr. Organelle dynamics during cell division. In DeshPal S. Verma and Zonglie Hong, editors, *Cell Division Control in Plants*, volume 9 of *Plant Cell Monographs*, pages 195–206. Springer Berlin Heidelberg, 2007.

[82] Graham Warren. Membrane partitioning during cell division. *Annual Review Biochemistry*, 62:323–348, 1993.

[83] Graham Warren and William Wickner. Organelle inheritance. *Cell*, 84(3):395–400, 1996.

[84] K.A Schafer. The cell cycle: A review. *Veterinary Pathology*, 35:461–478, 1998.

[85] Katrien Vermeulen, Dirk R. Van Bockstaele, and Zwi N. Berneman. The cell cycle: a review of regulation, deregulation and therapeutic targets in cancer. *Cell Proliferation*, 36(3):131–149, 2003.

[86] David J. Stephens and Victoria J. Allan. Light microscopy techniques for live cell imaging. *Science*, 300(5616):82–86, 2003.

[87] Claire L. Curl, Catherine J. Bellair, Peter J. Harris, Brendan E. Allman, Ann Roberts, Keith A. Nugent, and Lea M.D. Delbridge. Quantitative phase microscopy- a new tool for investigating the structure and function of unstained live cells. *Proceedings of the Australian Physiological and Pharmacological Society*, 34:121–127, 2004.

[88] Gabriel Popescu, YoungKeun Park, Wonshik Choi, Ramachandra R. Dasari, MIchael S. Feld, and Kamran Badizadegan. Imaging red blood cell dynamics by quantitative phase microscopy. *Blood Cells, Molecules, and Diseases*, 41:10–16, 2008.

[89] KyeoReh Lee, Kyoohun Kim, Jaehwang Jung, JiHan Heo, Sangyeon Cho, Sangyun Lee, Gyuyoung Chang, YoungJu Jo, Hyunjoo Park, and Yongkeun Park. Quantitative phase imaging techniques for the study of the cell pathophysiology: From principles to applications. *Sensors*, 13:4170–4191, 2013.

[90] Michael Shribak, James LaFountain, David Biggs, and Shinya Inoue. Quantitative orientation-indepedent differential intereference contrast microscopy coupled with orientation-independent polarization microscopy. *Miscrosopy. and Microanalysis*, 13, 2007.

[91] Murphy Douglas. *Fundamentals of light microscopy and electronic imaging.* John Wiley & Sons Inc., 2 edition, 2013.

[92] W. Denk, J.H. Strickler, and W.W. Webb. Two-photon laser scanning fluorescence microscopy. *Science*, 248:73, 1990.

[93] M. Rubart. Two-photon microscopy of cells and tissue. *Circulation Research*, 95:1154–1166, 2004.

[94] W. Becker. Fluorescence lifetime imaging- techniques and applications. *Journal of Microscopy*, 247:119–136, 2012.

[95] R. Corriden, P.A. Insel, and Junger W.G. A novel method using fluorescence microscopy for real-time assessment of atp release from individual cells. *American journal of physiology cell physiology*, 293:1420–1425, 2007.

[96] Bi-Chang Chen, Wesley R. Legant, Kai Wang, Lin Shao, Daniel E. Milkie, Michael W. Davidson, Chris Janetopoulos, Xufeng S. Wu, John A. Hammer, Zhe Liu, Brian P. English, Yuko Mimori-Kiyosue, Daniel P. Romero, Alex T. Ritter, Jennifer Lippincott-Schwartz, Lillian Fritz-Laylin, R. Dyche Mullins, Diana M. Mitchell, Joshua N. Bembenek, Anne-Cecile Reymann, Ralph Böhme, Stephan W. Grill, Jennifer T. Wang, Geraldine Seydoux, U. Serdar Tulu, Daniel P. Kiehart, and Eric Betzig. Lattice light-sheet microscopy: Imaging molecules to embryos at high spatiotemporal resolution. *Science*, 346(6208), 2014.

[97] Guohong Zhang, Vanessa Gurtu, and Steven R. Kain. An enhanced green fluorescent protein allows sensitive detection of gene transfer in mammalian cells. *Biochemical and Biophysical Research Communications*, 227:707–711, 1996.

[98] M Chalfie, Y Tu, G Euskirchen, WW Ward, and DC Prasher. Green fluorescent protein as a marker for gene expression. *Science*, 263(5148):802–805, 1994.

[99] Gert-Jan Kremers, Sarah G. Gilbert, Paula J. Cranfill, Michael W. Davidson, and David W. Piston. Fluorescent proteins at a glance. *Journal of Cell Science*, 124(2):157–160, 2010.

[100] Yuichiro Hori, Tomoya Norinobu, Motoki Sato, Kyohei Arita, Masahiro Shirakawa, and Kazuya Kikuchi. Development of fluorogenic probes for quick no-wash live-cell imaging of intracellular proteins. *Journal of the American Chemical Society*, 135(33):12360–12365, 2013.

[101] Christian Matthaus, Susie Boydston-White, Milos Miljkovic, Melissa Romeo, and Max Diem. Raman and infrared microspectral imaging of mitotic cells. *Applied Spectroscopy*, 60:1–8, 2006.

[102] Robin J. Swain, Gavin Jell, and Molly M. Stevens. Non-invasive analysis of cell cycle dynamics in single living cells with raman micro-spectroscopy. *Journal of Cellular Biochemistry*, 104(4):1427–1438, 2008.

[103] Katharina Klein, AlexanderÂ M. Gigler, Thomas Aschenbrenner, Roberto Monetti, Wolfram Bunk, Ferdinand Jamitzky, Gregor Morfill, RobertÂ W. Stark, and JÃ¼rgen Schlegel. Label-free live-cell imaging with confocal raman microscopy. *Biophysical Journal*, 102(2):360–368, 2012.

[104] Christian W. Freudiger, Wei Min, Brian G. Saar, Sijia Lu, Gary R. Holtom, Chengwei He, Jason C. Tsai, Jing X. Kang, and X. Sunney Xie. Label-free biomedical imaging with high sensitivity by stimulated raman scattering microscopy. *Science*, 322:1857, 2008.

[105] John Paul Pezacki, Jessie A Blake, Dana C Danielson, David C Kennedy, Rodney K Lyn, and Ragunath Singaravelu. Chemical contrast for imaging living systems: molecular vibrations drive cars microscopy. *Nat. Chem. Biol.*, 7:137–145, 2011.

[106] L. Mortati, C. Divieto, and M.P. Sassi. Cars and shg microscopy to follow collagen production in living human corneal fibroblasts and mesenchymal stem

cells in fibrin hydrogel 3d cultures. *Journal of Raman Spectroscopy*, 43:675–680, 2012.

[107] Paul J. Campagnola, Andrew C. Millard, Mark Teraski, Pamela E. Hoppe, Christian J. Malone, and William A. Mohler. Three-dimensional high-resolution second-harmonic generation imaging of endogenous structural proteins in biological tissues. *Biophysical Journal*, 82:493–508, 2002.

[108] Piotr Kostyk, Shelley Phelan, and Min Xu. Cell cycle imaging with quantitative differential interference contrast microscopy. *Proc. SPIE*, 8587, 2013.

[109] Vassilis Roukos, Gianluca Pegoraro, Ty C. Voss, and Tom Misteli. Cell cycle staging of individual cells by fluorescence microscopy. *Nature Protocols*, 10:338–348, 2015.

[110] Maija Puhka, Helena Vihinene, Merja Joensuu, and Eija Jokitalo. Endoplasmic reticulum remains continuous and undergoes sheet-to-tubule transformation furing cell division in mamalian cells. *Journal of Cell Biology*, 179:895–909, 2007.

[111] Chi-Kuo Hu, Margaret Coughlin, and Timothy J. Mitchison. Midbody assembly and its regulation during cytokinesis. *Molecular biology of the cell*, 23(6):1024–1034, 2012.

[112] Jennifer Lippincott-Schwartz and George H. Patterson. Development and use of fluorescent protein markers in living cells. *Science*, 300(5616):87–91, 2003.

[113] Christian Matthaus, Benjamin Bird, Milos Miljkovic, Tatyana Chernenko, Melissa Romeo, and Max Diem. Infrared and raman microscopy in cell biology. In *Biophysical Tools for Biologists, Volume Two: In Vivo Techniques*, volume 89 of *Methods in Cell Biology*, chapter 10, pages 275 – 308. Academic Press, 2008.

[114] Delong Zhang, Ping Wang, Mikhail N. Slipchenko, and Ji-Xin Cheng. Fast vibrational imaging of single cells and tissues by stimulated raman scattering microscopy. *Accounts of Chemical Research*, 47:2282–2290, 2014.

[115] Israel Rocha-Mendoza, Wolfgang Langbein, and Paola Borri. Coherent anti-stokes raman microspectroscopy using spectral focusing with glass dispersion. *Appl. Phys. Lett.*, 93:201103, 2008.

[116] Wolfgang Langbein, Israel Rocha-Mendoza, and Paola Borri. Coherent anti-stokes raman micro-spectroscopy using spectral focusing: Theory and experiment. *J. Raman Spectrosc.*, 40:800–808, 2009.

[117] Ajoy Ghatak. *Optics*. Tata McGraw-Hill Publishing Company Ltd., New Delhi, 3 edition, 2005.

[118] Iestyn Pope, Wolfgang Langbein, Paola Borri, and Peter Watson. *Methods in Enzymology*, volume 504, chapter Live cell imaging with chemical specificity using dual frequency CARS microscopy, pages 273–291. Burlington, Academic Press, 2012.

[119] Iestyn Pope, Wolfgang Langbein, Peter Watson, and Paola Borri. Simultaneous hyperspectral differential-cars, tpf and shg microscopy with a single 5 fs ti:sa laser. *Opt. Express*, 21(6):7096–7106, Mar 2013.

[120] Francesco Masia, Paola Borri, and Wolfgang Langbein. Sparse sampling for fast hyperspectral coherent anti-stokes raman scattering imaging. *Optics Express*, 22(4):4021–4028, 2014.

[121] Francesco Masia, Arnica Karuna, Paola Borri, and Wolfgang Langbein. Hyperspectral image analysis for cars, srs, and raman data. *J. Raman Spectrosc.*, 46(8):727–734, 2015.

[122] Arnica Karuna, Francesco Masia, Paola Borri, and Wolfgang Langbein. Hyperspectral volumetric coherent anti-stokes raman scattering microscopy: quantitative volume determination and nacl as non-resonant standard. *Journal of Raman Spectroscopy*, 2016.

[123] D. Gachet, F. Billard, N. Sandeau, and H. Rigneault. Coherent anti-stokes raman scattering (cars) microscopy imaging at interfaces: evidence of interference effects. *Opt. Express*, 15:10408, 2007.

[124] Aaron M. Barlow, Konstantin Popov, Marco Andreana, Douglas J. Moffatt, Andrew Ridsdale, Aaron D. Slepkov, James L. Harden, Lora Ramunno, and Albert Stolow. Spatial-spectral coupling in coherent anti-stokes raman scattering microscopy. *Opt. Express*, 21(13):15298–15307, 2013.

[125] Claudia Di Napoli, Iestyn Pope, Francesco Masia, Peter Watson, Wolfgang Langbein, and Paola Borri. Hyperspectral and differential cars microscopy for quantitative chemical imaging in human adipocytes. *Biomed. Opt. Express*, 5(5):1378–1390, 2014.

[126] Fritjof Helmchen and Winfried Denk. Deep tissue two-photon microscopy. *Nature Methods*, 2(12):932–940, 2005.

[127] H. Frijtof and W. Denk. Deep tissue two-photon microscopy. *Nature Methods*, 2(2):932–940, 2005.

[128] Charles H. Camp, Young Jong Lee, and Marcus T. Cicerone. Quantitative, comparable coherent anti-stokes raman scattering (cars) spectroscopy: correcting errors in phase retrieval. *J. Raman Spectrosc.*, 2015.

[129] D. M. Roessler and W. C. Walker. Electronic spectra of crystalline nacl and kcl. *Phys. Rev.*, 166:599–606, 1968.

[130] Robert Adair, L. L. Chase, and Stephen A. Payne. Nonlinear refractive index of optical crystals. *Phys. Rev. B*, 39:3337–3350, 1989.

[131] H. H. Li. Refractive index of alkali halides and its wavelength and temperature derivatives. *J. Phys. Chem. Ref. Data*, 5(2):329–528, 1976.

[132] I. H. Malitson. Interspecimen comparison of the refractive index of fused silica. *J. Opt. Soc. Am.*, 55(10):1205–1209, 1965.

[133] Cecile Cottet-Rousselle, Xavier Ronot, Xavier Leverve, and Jean-Francois Mayol. Cytometric assessment of mitochondria using fluorescent probes. *Cytometry Part A*, 79A(6):405–425, 2011.

[134] J. Kapuscinski. Dapi: a dna-specific fluorescent probe. *Biotechnic and Histochemistry*, 70(5):220–233, 1995.

[135] George H. Patterson, Susan M. Knobel, Wallace D. Sharif, Steven R. Kain, and David W. Piston. Use of green fluorescent protein and its mutants in quantitative fluorescence microscopy. *Biophysical Journal*, 73:2782–2790, 1997.

[136] Hagting Anja, Karlsson Christina, Clute Pail, Jackman Mark, and Pines Jonathan. Mpf localization is controlled by nuclear export. *The EMBO Journal*, 17(14):4127–4138, 1998.

[137] Paul Clute and Jonathan Pines. Temporal and spatial control of cyclin b1 destruction in metaphase. *Nature Cell*, 1:82–87, 1999.

[138] J. Huang and J.W. Raff. The disappearance of cyclin b at the end of mitosis is regulated spatially in drosophila cells. *The EMBO Journal*, 18(8):2184–2195, 1999.

[139] Martin Beck, Alexander Schmidt, Johan Malmstroem, Manfred Claassen, Alessandro Ori, Anna Szymborska, Fran Herzog, Oliver Rinner, Jan Ellenberg, and Ruedi Aebersold. The quantitative proteome of a human cell line. *Molecular Systems Biology*, 7(549), 2011.

[140] Nick Thomas, Mike Kenrick, Theresa Giesler, Gretchen Kiser, Hayley Tinkler, and Simon Stubbs. Characterization and gene expression profiling of a stable cell line expressing a cell cycle gfp sensor. *Cell Cycle*, 4(1):191–195, 2005.

[141] Phyllis S. Frisa and James W. Jacobberger. Cell cycle-related cyclin b1 quantification. *PLOS One*, 4, 2009.

[142] F. Bestvater, E. Spiess, G.A. Stobraw, M. Hacker, T. Feurer, T. Porwol, U. Berchner-Pfannschmidt, C. Wotzlaw, and H. Acker. Two-photon fluorescence absorption and emission spectra of dyes relevant for cell imaging. *Journal of Microscopy*, 208:108–115, 2002.

[143] Joji M. Otaki, Motosuke Tsutsumi, Tomonori Gotoh, and Haruhiko Yamamoto. Secondary structure characterization based on amino acid composition and availability in proteins. *Journal of Chemical Information and Modeling*, 50(4):690–700, 2010.

[144] Arild C Rustan and Christian A Drevon. *Encyclopedia of life sciences*, chapter Fatty Acids: Structures and Properties. John Wiley & Sons, Ltd, 2001.

[145] Ron Milo and Rob Phillips. *Cell biology by the numbers*. Garland Science, 1 edition, December 2015.

[146] PubChem Compound Database. Palmitic acid.

[147] PubChem Compound Database. Stearic acid. Online.

[148] Mansukhlal C. Wani, Harold Lawrence Taylor, Monroe E. Wall, Philip Coggon, and Andrew T. McPhail. Plant antitumor agents. vi. isolation and structure of taxol, a novel antileukemic and antitumor agent from taxus brevifolia. *Journal of the American Chemical Society*, 93(9):2325–2327, 1971. PMID: 5553076.

[149] P. B. Schiff, Jane Fant, and S. B. Horwitz. Promotion of microtubule assembly in vitro by taxol. *Nature*, 277:665–667, 1979.

[150] N. De Brabander, G. Geuens, R. Nyudens, R. Willebrords, and J. De Mey. Taxol induces the assembly of free microtubules in living cells and blocks the organizing capacity of the centrosomes and kinetochores. *Proc. Natl. Acad. Sci. USA*, 78(9):5608–5612, 1981.

[151] Anne-Marie C. Yvon, Patricia Wadsworth, and Mary Jordan. Taxol suppresses dynamics of individual microtubules in living human tumour cells. *Molecular Biology of the Cell*, 10:947–959, 1999.

[152] Mary Ann Jordan and Leslie Wilson. Microtubules as a target for anticancer drugs. *Nature*, 4(4):253–265, 2004.

[153] D.A. Brito and C. L. Rieder. The ability to survive mitosis in the presence of microtubule poisons differs significantly between human nontransformed (rpe-1) and cancer (u-2os, hela) cells. *Cell Motility Cytoskeleton*, 66(8):437–447, 2009.

[154] John L. Nitiss. Investigating the biological functions of {DNA} topoisomerases in eukaryotic cells. *Biochimica et Biophysica Acta (BBA) - Gene Structure and Expression*, 1400:63–81, 1998.

[155] F. Cortes, N Pastor, D. Mateos, and I. Dominguez. Roles of dna topoisomerases in chromosome segregation and mitosis. *Mutation Research*, 543(1):59–66, 2003.

[156] Eiraku Mototsugu, Watanabe Kiichi, Matsuo-Takasaki Mami, Kawada Masako, Yonemura Shigenobu, Matsumura Michiru, Wataya Takafumi, Nishiyama Ayaka, Muguruma Keiko, and Sasai Yoshiki. Self-organized formation of polarized cortical tissues from {ESCs} and its active manipulation by extrinsic signals. *Cell Stem Cell*, 3(5):519–532, 2008.

[157] Toshiro Sato, Robert G. Vries, Hugo J. Snippert, Marc Van de Wetering, Nick Barker, Daniel E. Stange, Johan H. Van Es, Arie Abo, Pekka Kujala, Peter J. Peters, and Hans Clevers. Single lgr5 stem cells build crypt-villus structures in vitro without a mesenchymal niche. *Nature*, 459:262–265, 2009.

[158] Yoshiki Sasai, Mototsugu Eiraku, and Hidetaka Suga. In vitro organogenesis in three dimensions: self-organising stem cells. *Development*, 139(22):4111–4121, 2012.

[159] Chee Wai Chua, Maho Shibata, Ming Lei, Roxanne Toivanen, LaMont J. Barlow, Sarah K. Bergren, Ketan K. Badani, James M. McKiernan, Mitchell C. Benson, Hanina Hibshoosh, and Michael M. Shen. Single luminal epithelial progenitors can generate prostate organoids in culture. *Nature Cell Biology*, 16:951–961, 2014.

[160] Meritxell Huch, Craig Dorrell, Sylvia F. Boj, Johan H. Van Es, Vivian S.W. Li, Marc van de Wetering, Toshiro Sato, Karien Hamer, Nobuo Sasaki, Milton J. Finegold, Annelise Haft, Robert G. Vries, Markus Grompe, and Clevers Hans. In vitro explansion of single lgr5+ liver stem cells induced by wnt- driven regeneration. *Nature*, 494:247–250, 2013.

[161] C. Xinaris, V. Brizi, and G. Remuzzi. Organoid models and applications in biomedical research. *Nephron*, 130:191–199, 2015.

[162] Nick Barker, Johan H. van Es, Jeroen Kuipers, Pekka Kujala, Maaike van Den Born, Miranda Cozijnsen, Andrea Haegebarth, Jeroen Korving, Harry Begthel, Peter J. Peters, and Clevers Hans. Identification of stem cells in small intestine and colon by marker gene lgr5. *Nature*, 449:1003–1009, 2007.

[163] Nick Barker, Marc van de Wetering, and Hans Clevers. The intestinal stem cell. *Genes & Development*, 22:1856–1864, 2008.

[164] Yoshiki Sasai. Next-generation regenerative medicine: Organogenesis from stem cells in 3d culture. *Cell Stem Cell*, 12(5):520–530, 2013.

[165] Franziska Baenke, Barrie Peck, Heike Miess, and Almut Schulze. Hooked on fat: the role of lipid synthesis in cancer metabolism and tumour development. *Disease Models and Mechanisms*, 6:1353–1363, 2013.

[166] Thuc T. Le, Terry B. Huff, and Ji-Xin Cheng. Coherent anti-stokes raman scattering imaging of lipids in cancer metastasis. *BioMed Central Cancer*, 9:1–14, 2009.

[167] Toshiro Sato, Daniel E. Stange, Marc Ferrante, Robert G. J. Vries, Johan H. Van Es, Stieneke Van Den Brink, Winan J. Van Houdt, Apollo Pronk, Joost Van Gorp, and Peter D. Siersema. Long-term expansion of epithelial organoids from human colon, adenoma, adenocarcinoma, and barrett's epithelium. *Gastroenterology*, 141:1762–1772, 2011.

[168] Aliya Fatehullah, Si Hui Tan, and Nick Barker. Organoids as an in vitro model of human development and disease. *Nature Cell Biology*, 18(3):246–254, 2016.

[169] Charles H. Camp Jr., Siva Yegnanarayanan, Ali A. Eftekhar, Hamsa Sridhar, and Ali Adibi. Multiplex coherent anti-stokes raman scattering (mcars) for chemically sensitive, label-free flow cytometry. *Opt. Express*, 17(25):22879–22889, 2009.

[170] M. C. Martin. Characteristic ir band positions. Online. Accessed on 27/04/2016.

[171] Harvey Lodish, Arnold Berk, Paul Matsudaira, Chris A Kaiser, Monty Krieger, Matthew P. Scott, Lawrence Zipursky, and James Darnell. *Molecular Cell Biology*. W.H.Freeman, 5 edition, 2003.

[172] T. A. Brown. *Genomes*, chapter Chapter 1: The Human Genome. Oxford: Wiley-Liss, 2 edition, 2002.